DISSERTATION

submitted to the
Faculty of Chemistry and Earth Sciences
of the University of Heidelberg, Heidelberg, Germany
in partial fulfillment of the requirements for the degree of
Doctor of Natural Sciences (Dr. rer. nat.)

presented by
Dominique Verreault (M.Sc. Biophysics)
born in Amqui (QC), Canada

Oral examination: June 17th, 2011

Investigation of surface charging at the ITO/aqueous solution interface by *in situ* sum-frequency-generation spectroscopy and voltammetry

The dissertation was carried out at the

Institute of Physical Chemistry

University of Heidelberg, Heidelberg, Germany

and reviewed by

Prof. Dr. Michael Grunze
Institute of Physical Chemistry, University of Heidelberg

Prof. (apl.) Dr. Hans-Robert Volpp
Institute of Physical Chemistry, University of Heidelberg

« *Il n'est pas besoin d'espérer pour entreprendre*
ni de réussir pour persévérer. »
M. Pagnol

Publication related to the work in this thesis:

- D. Verreault, V. Kurz, C. Howell, P. Koelsch, "Sample cells for probing solid/liquid interfaces with broadband sum-frequency-generation spectroscopy", *Rev. Sci. Instrum.* **81**, 06311/1 (2010).

Other contributions to publications as a PhD student:

- V. Kurz, D. Verreault, P. Koelsch, "Sum-frequency-generation in layered media: angular and thickness dependence", *manuscript in preparation* (2011).

- D. Düsselberg, D. Verreault, P. Koelsch, C. Staudt, "Synthesis and characterization of novel, soluble sulfur-containing copolyimides with high refractive indices", *J. Mater. Sci.* **46**, 4872 (2011).

- M.-O. Diesner, C. Howell, V. Kurz, D. Verreault, P. Koelsch, "In vitro characterization of surface properties through living cells", *J. Phys. Chem. Lett.* **1**, 2339 (2010).

- R. Jribi, E. Barthel, H. Bluhm, M. Grunze, P. Koelsch, D. Verreault, E. Sondergard, "Ultraviolet irradiation suppresses adhesion on TiO_2", *J. Phys. Chem. C* **113**, 8273 (2009).

Acknowledgements

This project was carried out partly at the Institute of Physical Chemistry at the University of Heidelberg in Heidelberg and at the Institute of Toxicology and Genetics (ITG) at the Karlsruhe Institute of Technology (KIT) - Campus North in Eggenstein-Leopoldshafen. The present work was funded mainly by the Deutsche Forschungsgemeinschaft (DFG).

First and foremost, I would like to thank my advisor Prof. Dr. Michael Grunze for giving me the opportunity to work in the department, for critical comments and fruitful discussions, and for reviewing this thesis. In addition, I would like to thank Prof. (apl.) Dr. Hans-Robert Volpp for kindly accepting the task of second reviewer.

Secondly, but not least, I would like to express my deepest gratitude to Priv.-Doz. Dr. Patrick Koelsch for his encouragement, interest, patience, and invaluable suggestions during the course of this work. His experimental insights have given me over the years a whole other view on applied physics. His relentless passion for research was contagious, motivational, even though at times tremendously exhausting. Not too mention his enthusiasm and franc-parler that have made working in his group a very enjoyable and pleasant experience.

I would like to thank Dr. Johannes Lützenkirchen at the Institute of Nuclear Waster Disposal (INE, KIT - Campus North) for his collaboration with the streaming potential measurements as well as for many fruitful and interesting discussions concerning surface charging on oxide surfaces.

I would like also to thank Prof. Dr. Michael Bruns and his coworkers (Dipl.-Ing. Vanessa Trouillet, Dipl.-Ing. Florian Stemme, Vanessa Hermann and Udo Geckle) at the Institute of Material Research III (IMF-III, KIT - Campus North) as well as Stefan Heissler and Carlos Azucena at the Institute of Functional Interfaces (IFG, KIT - Campus North) for their continuous help with the preparation and characterization of the ITO thin films.

I would also like to take this opportunity to thank all the people working in technical support in Heidelberg, Gunther Meinusch in electronics, Reinhold Jehle in engineering design, and Rainer Schmitt along with his coworkers in fine mechanics. Without their helpful support and availability, it would have been much more difficult to circumvent some of the experimental difficulties that I have encountered during the course of my project.

Furthermore, I would like to thank all my colleagues from the Optical Spectroscopy group (Volker, Caitlin, Mark-Oliver, Christoph, Anna, and Markus) who made our working place very creative and enjoyable. It has been for me challenging and fulfilling to work in such an interdisciplinary group. With them, each day brought me a new question. I wish them sincerely all the best.

Finally, I would like to thank my family for supporting me in all my endeavors and for letting me go so far away and for so long. They knew that getting a PhD degree and going to Germany were two of my dreams. I was just so fortunate to realized them both together.

Summary

Investigation of surface charging at the ITO/aqueous solution interface by *in situ* sum-frequency-generation spectroscopy and voltammetry

Surface charging and ion specificity effects occurring at the metal oxide/aqueous solution interface play a decisive role in various biological, environmental, geophysical, and industrial processes. Despite their importance, the influence of these effects on interfacial water molecules ordering at charged oxide surfaces is not fully understood. In this work, the surface charging and ion specificity at the tin-doped indium oxide (ITO)/aqueous solution interface was investigated using *in situ* vibrational sum-frequency-generation (SFG) spectroscopy in combination with voltammetry. The n-type, wide bandgap semiconductor ITO was chosen as test material because of its good chemical stability, high optical transparency, and low electrical resistivity, which enables simultaneous spectroscopic and controlled voltammetric measurements in aqueous environments. In order to perform these measurements at this interface and other solid/liquid interfaces, the previously existing SFG spectrometer setup was extensively modified, especially with the addition of a Fabry-Perot etalon for pulse shaping and phase-independent measurements, the redesign of the sample stage area for easy manipulation and quick exchange of measuring cells, and the addition of a reference line for absolute intensity measurements. Furthermore, a novel three-electrode spectroelectrochemical cell with ITO-coated IR-transparent prism as working electrode was designed and constructed. The sputter-deposited and annealed ITO thin film was first characterized in terms of structural, electrical, and optical properties using X-ray diffraction, scanning electron microscopy, four-point probe resistivimetry, and optical spectroscopies. An homogeneous, polycrystalline structured surface with low resistivity ($\sim 10^{-2}$ Ω·cm) and high transmissivity (∼80–90%) in the visible range was found. The isoelectric point of ITO ($\mathrm{pH_{iep}} \approx 3$) was determined by streaming potential measurements in water and aqueous salt solutions. The influence of applied potential on water ordering and ion affinity was investigated by SFG measurements at two positions of the bonded-OH region ($\sim$ 3150 cm^{-1} and $\sim$ 3400 cm^{-1}) with deuterated water, normal water, and two series of anionic and cationic salt solutions. The experiments with water revealed the presence of a strong non-resonant contribution from the ITO film which could potentially dominate all resonant contributions, except maybe at high positive potentials. With the anionic and cationic salt solutions, no ion specific effects could be detected but certain soft ions showed a definite propensity for the ITO surface. Surface current density was also recorded in both spectral regions and showed the presence of corrosion effects on ITO, especially important for halogenated salts.

Zusammenfassung

Untersuchung der Oberflächenladung an der ITO/Wassergrenzfläche mittels *in situ* Summenfrequenzgenerations-Spektroskopie und Voltammetrie

Oberflächenladung und ionenspezifische Effekte, die an der Metalloxid/Wassergrenzfläche auftreten, spielen eine entscheidende Rolle in verschiedenen biologischen, ökologischen, geophysikalischen und industriellen Prozessen. Trotz ihrer Bedeutung ist der Einfluss dieser Effekte auf die Anordnung der Wassermoleküle an der Grenzfläche zu geladenen Oxidoberflächen noch nicht völlig verstanden. In dieser Arbeit wurden Oberflächenladung und ionenspezifische Effekte an der ITO/Wassergrenzfläche mit Hilfe von *in situ* Schwingungs-Summenfrequenzgenerations (SFG)-Spektroskopie zusammen mit Voltammetrie untersucht. Der n-Typ ITO-Halbleiter mit großer Bandlücke wurde als Versuchsmaterial wegen seiner guten chemischen Stabilität, hohen optischen Transparenz und seines geringen elektrischen Widerstandes gewählt. Diese Eigenschaften ermöglichen simultane spektroskopische und kontrollierte voltammetrische Messungen in wässeriger Umgebung. Um diese Messungen an dieser Grenzfläche und anderer geladener fest/flüssig Grenzflächen durchzuführen, wurde der vorherige SFG-Spektrometeraufbau substantiell verändert. Im Besonderen wurde ein Fabry-Perot Etalon für die zeitliche Pulsmodifizierung und unabhängige Phasenmessungen hinzugefügt, ebenso wurde der Probenbereich für eine einfache Bedienung und schnelle Wechsel der Messzelle neu gestaltet. Zusätzlich wurde eine Referenzlinie für Messungen absoluter Intensitäten installiert. Außerdem wurde eine neuartige Drei-Elektroden spektroelektrochemische Zelle mit einem ITO-beschichteten und IR-transparenten Prisma als Arbeitselektrode konzipiert und angefertigt. Die dünne aufgedampfte und temperierte ITO-Schicht wurde zunächst bezüglich ihrer strukturellen, elektrischen und optischen Eigenschaften mit Hilfe von Röntgenbeugung, Rasterelektronenmikroskopie, Vierpunktmessungen und optischen Spektroskopien charakterisiert. Eine homogene, polykristallin strukturierte Oberfläche mit geringer Schichtresistivität ($\sim 10^{-2}$ Ω·cm) und hoher Transmission (∼80–90%) im sichtbaren Bereich wurde gefunden. Der isoelektrische Punkt ($\mathrm{pH_{iep}} \approx 3$) von ITO wurde durch Messungen des Strömungspotentials in Wasser und wässerigen Salzlösungen bestimmt. Der Einfluss des angelegten Potentials auf die Anordnung der Wassermoleküle und auf die Ionenaffinität wurde mit SFG-Messungen an zwei Positionen in der Region für gebundenes OH (~ 3150 cm^{-1} und ~ 3400 cm^{-1}) mit Schwerwasser, Wasser und zwei Reihen anionischer und kationischer Salzlösungen untersucht. Die Experimente mit Wasser zeigten das Vorhandensein eines starken nichtresonanten Beitrages der ITO-Schicht, der möglicherweise alle resonanten Beiträge dominieren könnte, außer vielleicht bei hohem positiven Potential. Für die anionischen und kationischen Salzlösungen konnte kein ionenspezifischer Effekt entdeckt werden. Einige weiche Ionen zeigten jedoch eine bestimmte Affinität für die ITO-Oberfläche. Zusätzlich wurde die Oberflächenstromdichte in beiden spektralen Bereichen und die Anwesenheit von Korrosionseffekten auf ITO gemessen, welche besonders auffällig für Halogensalze waren.

Table of Contents

List of Figures

List of Tables

List of Abbreviations

AFM	atomic force microscopy
CE	counter electrode
CFSE	crystal field stabilization energy
CNT(s)	carbon nanotube(s)
CVD	chemical vapor deposition
D	direct (series)
DC	direct current
DFG	difference-frequency-generation
EDL	electrical double layer
EMA	effective medium approximation
FPP	four-point probe (resistivimetry)
FSR	free spectral range
FTIR	Fourier-transform infrared absorption spectroscopy
FWHM	full width at half maximum
I	indirect (series)
IAS	ion affinity series
IEP	isoelectric point
IPR	ideal polarizable region
ITO	tin-doped indium oxide, indium-tin oxide
MD	molecular dynamics
MIR	mid-infrared
MSE	mean-square error
NDFG	narrow difference-frequency generator
NIR	near-infrared
NR	non-resonant
ODF	orientational distribution function
OLEDs	organic light-emitting diode(s)
OPA	optical parametric amplifier, operational amplifier
OR	optical rectification
PEDOT	poly(3,4-ethylenedioxythiophene)
PVD	physical vapor deposition
PZC	point of zero charge
R	resonant
RE	reference electrode
REF	reference
RF	radio-frequency
RH	relative humidity
SE	spectroscopic ellipsometry
SEM	scanning electron microscopy
SFG	sum-frequency-generation
SHE	standard hydrogen electrode
SHG	second-harmonic-generation
TCO	transparent conductive oxide
TIR	total internal reflection

UHV	ultra-high vacuum
UV	ultraviolet
VIS	visible
WE	working electrode
XPS	X-ray photoelectron spectroscopy
XRD	X-ray diffraction
XSW	X-ray standing waves

List of Symbols

α	absorption (or attenuation) coefficient
$\boldsymbol{\alpha}^{(k)}$	k-th order hyperpolarizability
$\alpha^*(i\omega)$	excess polarizability
$\alpha_{\mathrm{w}}(i\omega)$	intrinsic water polarizability
a	ion size, lattice constant
A	area, analyzer
A_k	amplitude of the k-th vertical deviation
A_q	amplitude of the q-th vibrational transition
A_{rms}	root-mean-square amplitude
$\chi^{(1)}$	linear susceptibility
$\chi^{(2)}$	second-order nonlinear susceptibility
$\chi^{(2)}_{\mathrm{eff}}$	effective second-order nonlinear susceptibility
$\chi^{(2)}_{\mathrm{NR}}$	non-resonant contribution to $\chi^{(2)}$
$\chi^{(2),\mathrm{inter}}_{\mathrm{NR}}$	interband NR contribution to $\chi^{(2)}$
$\chi^{(2),\mathrm{intra}}_{\mathrm{NR}}$	intraband NR contribution to $\chi^{(2)}$
$\chi^{(2)}_{\mathrm{R},q}$	q-th resonant contribution
$\chi^{(k)}$	k-th order nonlinear susceptibility
c^*	critical coagulant concentration
C	charge, compensator, bulk ion concentration
C_{Sn}	concentation of Sn dopant
δ	phase of an electric field, phase delay, resolution, retardation
Δ	ellipsometric (phase-related) angle
δ_C	phase delay of C
$\Delta\phi_{qB}$	relative phase between q- and non-resonant bulk contributions
$\Delta\phi_{qr}$	relative phase between q-th and r-th resonant contributions
$\delta^{p/s}_{i/r}$	phase of p/s-polarized electric field of the incident/reflected beam
ΔV	potential difference
d	probing or sampling depth, probe spacing
d_{exp}	experimental interplanar distance
d_{hkl}	theoretical interplanar distance
ε	(bulk) dielectric constant
ε_0	vacuum electric permittivity
e	elementary electronic charge
e_{ijk}	polarization combination factor
E	amplitude of an electric field
E_{at}	atomic electric field
E_c	conduction band edge
$\mathbf{E}_0$	static or interfacial electric field
$E^{p/s}_{0i/r}$	amplitude of p/s-polarized electric field of the incident/reflected beam
E_g	bandgap energy

E_{bind}	binding energy (of inner shell electrons)
E_{kin}	kinetic energy (of photoelectrons)
E_{phot}	energy of photons
ϕ	phase difference, azimuth angle
ϕ_{M}	work function of a material or metal
f	focal length
F	Faraday constant, force (restoring)
F_{eff}	effective finesse
F_{ijk}	Fresnel or angular factor
Γ	relaxation time of a vibrationally excited state
Γ_k	surface concentration of the k-th species
$\Gamma_{s_q g}$	damping constant of the q-th vibrational transition between ground and excited state
$\|g\rangle$	ground state
G	geometrical correction factor
h	hole, Planck constant
$\hbar$	reduced Planck constant
i	atomic or interstitial site
I	current
I_i	i-th ion, incident intensity
I_{ij}	intensity of the j-th peak from the i-th element
I_{in}	input intensity
I_{out}	output intensity
I_t	transmitted intensity
J	total angular momentum
k	extinction coefficient, force or spring constant
λ	wavelength
λ_{ij}	inelastic mean free path (of the photoelectrons)
λ_p	plasma wavelength
l	length
L	lattice site, angular momentum
$\mathbf{L}$	nonlinear Fresnel coefficients (tensor)
l_c	coherence length
L_{ij}	angular asymmetry factor for the j-th orbital of the i-th element
μ	reduced mass
$\boldsymbol{\mu}$	dipole moment operator, induced dipole moment
$\boldsymbol{\mu}_0$	static (or permanent) dipole moment
μ_H	Hall (or charge carrier) mobility
m_e	electronic (rest) mass
m_e^*	effective (electron) mass (ratio)
M	multiplicity
M	metal
M_p	melting point
M_w	molecular weight
ν	frequency
n	refractive index
n_f	electron density in final state f
n_i	concentration of the i-th element, electron density in initial state i
n_w	number of water molecules
N	charge carrier concentration or density, number of dipole moments
N_s	surface density of molecules
$N_{\mathrm{H_2O}}$	number density of water molecules
ψ	twist angle
Ψ	ellipsometric (amplitude-related) angle

ψ_ν	vibrational wave function of a given state ν
P	polarizer
$\mathbf{P}$	polarization field
$\mathbf{P}^{(2)}$	second-order polarization field
$\mathbf{P}^{(3)}$	third-order polarization field
$\mathrm{pH_{pzc}}$	pH value at the PZC
θ	take-off angle (of the photoelectrons), tilt angle
θ_A	azimuthal angle of A
θ_B	Bragg diffraction angle
θ_C	azimuthal angle of C
θ_P	azimuthal angle of P
$\hat{P}$	parity operator
P_{if}	probability for a transition from an initial state i to a final state f
ρ	electrical resistivity, ellipsometric ratio
ρ_C	retardance of C
ρ_e	electronic (number) density
ρ_s	sheet resistivity
r	radius, ionic radius
r_0	Bohr radius
R	Fresnel reflection coefficient, ideal gas constant, reflectance
r_e	equilibrium bond length
r_M	radius of metal ion M
r_O	radius of oxygen ion
$\mathbf{R}_\nu$	IR transition dipole moment for a given state ν
$\mathrm{R}(\phi), \mathrm{R}(\psi), \mathrm{R}(\theta)$	rotation matrices of the three Euler angles
R_s	sheet resistance
σ	standard deviation
$\sigma(0)$	surface charge density
σ_{ij}	photoionization cross-section of the j-th peak of the i-th element
$\lvert s\rangle$	virtual state
S	spin
s_k	surface molar fraction
S_L^C	species on lattice site L and with charge C
τ	(etalon) cavity lifetime
τ_C	transmittance of C
t	thickness, time
T	absolute temperature, transmission function of the XPS analyzer, transmittance
$\mathrm{T}_{ijk}^{\alpha\beta\gamma}$	transformation matrix between molecular- and laboratory-fixed coordinate systems
$\lvert \upsilon\rangle$	excited state
υ	vacancy
V	volume, voltage or potential, potential energy
V_{acc}	accelerating voltage
V_dc	applied potential across the interface
V_O	oxygen vacancy
V_pzc	potential at zero charge
ω	frequency
ω_p	plasma frequency
$\omega_{s_q g}$	frequency of the q-th vibrational transition between ground and excited state
w	full width at half maximum, width
x_k	volumetric molar fraction
ζ	zeta potential
z	ionic charge

1

Introduction

I do not know what I may appear to the world, but to myself I seem to have been only like a boy playing on the sea-shore, and diverting myself in now and then finding a smoother pebble or a prettier shell than ordinary, whilst the great ocean of truth lay all undiscovered before me.

Sir Isaac Newton

1.1 Metal oxide/aqueous solution interfaces

1.1.1 Importance in natural and artificial processes

Metal (hydr)oxide/aqueous solution interfaces can be considered as almost ubiquitous since they can be found in numerous natural and artificial processes. Over the last decades, the interest for these interfaces has increased significantly due to their importance and relevance in a variety of fields ranging from biological to environmental and geochemical sciences (for reviews, see [1–4]). Indeed, these interfaces are host of several natural processes including, for instance, biomolecular and cellular adhesion [5–7], corrosion and passivation of certain metals and their alloys, environmental catalysis and remediation [8–10], mobilization and transport of mineral colloids in ground water systems [11], and sorption of contaminants, pollutants and metal trace elements in soils [12, 13]. In recent years, natural as well as synthesized metal oxides (the latter being frequently prepared in doped or mixed form), have become of great practical interest and have found their way, either as nanoparticles or thin films, in many industrial processes and technological applications such as heterogeneous water phase catalysis [14], photocatalytic water disinfection [15–18] and splitting for hydrogen fuel production [19, 20], stabilization of colloidal systems [21–24], bacterial filtering [25], controlled cellular adhesion and migration [26], pH and chemical sensing [27, 28], ore beneficiation and enrichment by flotation [29], and nuclear waste disposal [30–32], just to mention a few examples.

All these metal oxide/aqueous solution interfaces are usually charged over the pH range of the surrounding aqueous solution (e.g., natural waters, buffers, electrolytic baths), and the amount of this pH-dependent charge is proportional to the concentration and type of dissolved ions. Aqueous ions thus play a decisive role in these processes. In fact, several of them (if not all) even exhibit a well-defined behavior which depends strongly on the ion-specific interactions between dissolved ions and metal oxide surfaces (for an exhaustive and thorough review of ion-specific effects, see [33]).

Table 1.1 gives a list of the currently most studied metal oxides encountered in some common metal oxide/aqueous solution interfaces. Not surprisingly, all of these involve naturally occurring, simple metal oxides, mainly because of their importance to environmental, geochemical, and soil sciences. In addition, studies on these mineral oxides mostly target their interactions with alkaline (Na^+, K^+) and alkaline earth (Ca^{2+}, Mg^{2+}) cations, because of their abundance in natural waters and soils. Other heavier cations (Rb^+, Cs^+, Sr^{2+}, Ba^{2+}), more deleterious to the environment, have also been considered. In contrast, fewer studies have so far been devoted to other, less common, natural (e.g., δ-MnO_2, SnO_2, TiO_2 (anatase), etc.) and synthetic (e.g., In_2O_3, WO_3, ZnO, ZnO:Al, etc.) metal oxides, and that despite their growing technological importance. Nevertheless, fundamental studies about surface charging and ion specificity on these metal oxides in contact with aqueous solutions could be also of great use in understanding the behavior of those previously listed.

Table 1.1: List of metal oxides encountered in common metal oxide/aqueous solution interfaces (adapted from [2]).

Metal oxide	Mineral name	Cation valence	Crystal face studied
Group MO			
α-FeO(OH)	goethite	+3	(110)
MgO	periclase	+2	(100)
Group MO_2			
α-SiO_2	quartz	+2	(0001), (10$\bar{1}$0), (10$\bar{1}$1)
α-TiO_2	rutile	+2	(100), (110), (111)
Group M_2O_3			
α-Al_2O_3	alumina	+3	(0001), (10$\bar{1}$2), (10$\bar{1}$1)
α-Fe_2O_3	hematite	+3	(0001), (10$\bar{1}$2), (10$\bar{1}$1)

1.1.2 Surface charging and ion specificity

Obviously, none of the previously mentioned processes could proceed normally or optimally without *surface charging* of the metal oxide/aqueous solution interface. In fact, whatever which interface may be involved (e.g., soil mineral oxides in contact with ground water, conductive oxides electrodes immersed in an electrolytic bath, etc.), it is generally agreed that whenever a metal oxide comes in contact with an aqueous solution, its surface develops a net (negative or positive) charge, due to water dissociation at the surface and formation of hydroxyl groups to satisfy the bond valence of surface oxygen and metal ions. This pH-dependent surface charging, in addition to short-range van der Waals forces, then drives the sorption of any dissolved inorganic and organic ionic species, as well as changes in the structure and dynamics of both the aqueous and solid phases within a thin (typically, few nanometers) interfacial region [34]. The changes in the aque-

ous phase include many important interfacial phenomena such as the orientation and polarization of vicinal water layers. The pH-dependent surface charging behavior of a given oxide, and especially its point of zero charge (PZC) (or its isoelectric point (IEP) [1]), is a fundamental parameter of metal oxide/aqueous solution interfaces [35, 36]. The PZC can be defined as the pH value of the aqueous solution where the overall charge at the oxide surface equals zero i.e., the pH value at which the charges due to negatively and positively ionized surface groups neutralized one another. In the absence of other charge-determining ions (and any surface defects and impurities), the PZC depends solely on the surface hydroxyl (OH) groups of the metal (hydr)oxide. The pH value at the PZC (pH_{pzc}) is related to the acidity constants of these surface groups, but the exact relationship depends on the model adopted for describing the acid-base behavior of the metal oxide/aqueous solution interface (e.g., 1 site/1 pK, 1 site/2 pK, and multisite models, etc.). The ion specificity on the other hand refers simply to any phenomena where ions of different size but of the same valency, behave differently. Moreover, the ranking or ordering of the relative influence of these ions on the behavior of a given phenomena leads to so-called ion affinity series (IAS) (among which can be found, for example, the well-known Hofmeister and Irving-Williams series).

1.1.2.1 Literature survey of previous experimental studies

The importance of (pH-dependent) surface charging and ionic specificity at metal oxide/aqueous solution interfaces has been recognized already for almost a century. Indeed, based on previous pioneering works by Schulze [37] and Hardy [38], interest for these two phenomena came in the early 1920's with studies on the effect of inorganic salts on coagulation and precipitation of colloidal metal (hydr)oxides dispersions [39–42]. Since then, numerous and various kinds of metal oxides have been investigated experimentally and systematic data on their surface charging and ion specificity behavior has recently become available (for a complete and exhaustive monograph, see [43]).

For the sake of comparison and in order to get an overview, a compilation of PZCs and IAS for selected insoluble metal oxides is presented in Table 1.2. The gathered data has been restricted to metal oxides that have not undergone any physico-chemical surface pre-treatment. The experimental PZC and IAS given here were obtained exclusively with conventional methods such as adsorption, electrokinetics (streaming potential, electrophoresis) or titration (mass, potentiometric) over a definite pH range (typically, pH 2-11) [2] and small to moderate ($\leq$ 0.1 M) ion concentrations [3]. Within this list, metal oxides were organized according to their PZC. Hence, metal oxides with low or high PZC can be classified as *acidic* (high H_3O^+ affinity) or *basic* (low H_3O^+ affinity), respectively. In addition, for each metal oxide, IAS for anions and/or cations have been reported, when available. For these series, the measured quantities, namely, ion uptake, surface charge density (σ_0), zeta potential (ζ), and critical coagulant concentration (c^*), were usually compared at constant ion concentration.

1. The PZC is equivalent to the IEP if there is no specific adsorption of ions other than the potential-determining H^+/OH^- ions at the surface. This is often the case for pristine oxide surfaces in water.

2. Extreme pH values outside this range are usually avoided since many metal oxides lose their chemical stability and become sparingly or completely soluble.

3. At higher concentrations, the activities of different ions in solutions of equal concentration can differ significantly.

Table 1.2: Compilation of PZCs and IAS for selected insoluble metal oxides obtained by conventional methods.

Metal oxide	Mineral name	PZC/IEP	Anion series	Cation series	Series Type	Method	Experimental conditions†	Reference
			Acidic oxides					
Group MO_2								
δ-MnO_2	pyrolusite	NA	—	$Ba^{2+} > Sr^{2+} > Ca^{2+} > Mg^{2+}$	—/D	AD	NP, 5, 10^{-4}–10^{-3} M	[44]
		1.5	—	$Cs^+ > Rb^+ > K^+ > Na^+ > Li^+$	—/D	EK	NP, Cl^-	[45]
		∼2.3	—	$Ba^{2+} > Sr^{2+} > Ca^{2+} > Mg^{2+}$	—/D	AD, TT	NP, 2–8, 10^{-3} M Cl^-, SO_4^{2-}	[46]
		3.3	—	$Ba^{2+} > Sr^{2+} \approx Ca^{2+} > Mg^{2+}$	—/D	AD	NP, 7, Cl^-	[47]
SiO_2	silica	∼2	—	$Rb^+ > K^+ > Na^+ > Li^+$	—/D			[48]
		NA	—	$Cs^+ > K^+ > Li^+$	—/D	TT	NP, 1.8–9.0, 0.1 M Cl^-	[49]
		2.5-3	—	$Cs^+ > Na^+$	—/D			[50]
		NA	—	$Cs^+ > Rb^+ \approx K^+ > Na^+$, $Ba^{2+} > Ca^{2+} > Mg^{2+}$	—/D	RT	4–9	[51]
		NA	—	$Cs^+ > K^+ > Na^+ > Li^+$	—/D	EK	NP, NA, 10^{-3}–10^{-1} M Cl^-	[52]
TiO_2	rutile	5.4-5.8	$Cl^- \approx ClO_4^- \approx NO_3^- > I^-$	$Li^+ > Na^+ > Cs^+$	I/I	AD	NP	[53]
		5.3	—	$Ca^{2+} > Sr^{2+} > Ba^{2+}$	—/I	AC	NP, 7, 0.1 M Cl^-, KNO_3	[54]
		5.9	$NO_3^- > Cl^- > Br^- \approx I^- \approx ClO_4^-$	$Li^+ > Na^+ > K^+ > Cs^+$	I/I	CG	NP, 1.5–12	[55]
		NA	$Cl^- > NO_3^- > ClO_4^-$	$Li^+ > K^+ > Cs^+$	?/I	TT	NP, 0.01, 0.1 M K^+, Cl^-	[56]
TiO_2	anatase	6.2	—	$Ca^{2+} > Sr^{2+} > Ba^{2+}$	—/I	AC	NP, 7, 0.1 M Cl^-, KNO_3	[54]
		NA	$Cl^- \approx Br^- > I^-$	$Li^+ > Na^+ > Cs^+$	I/I	TT	NP, 0.1 M Na^+, Cl^-	[57]
ZrO_2	zirconia	4.0	—	$K^+ > Na^+ > Li^+$ ($pH < pH_{pzc}$)	—/D	TT	NP, 4–10	[58]
Group MO_3								
WO_3	tungstite	∼1.8	—	$Cs^+ > Rb^+ > K^+ > Na^+ > Li^+$	—/D	CG	NP, 2–12	[59]
		1.5	—	$Cs^+ > Rb^+ > K^+ > Na^+ > Li^+$	—/D	EK, TT	NP/TF, 2.0–5.5, 10^{-3}–1 M Cl^-/ 10^{-1} M NO_3^-, ClO_4^-	[60]
			Basic oxides					
Group MO								
ZnO	zincite	8	$Cl^- > Br^- > I^- > NO_3^- > ClO_4^-$	—	I (?)/—	NA	NA	[61]
Group MO_2								
β-MnO_2	pyrolusite	7.3	—	$Li^+ > Cs^+$	—/I	EK	NP	[45]
Group M_2O_3								
α-Al_2O_3	alumina	8.1	—	$Na^+ > K^+ > Cs^+$	—/I	NA	NA	[62]
		6.7	$I^- \approx Br^- > NO_3^- \approx Cl^-$	—	D/—	NA	NA	[63]
α-Fe_2O_3	hematite	8.5	—	$Li^+ > Na^+ > K^+ > Cs^+$	—/I	NA	NA	[64]
		8.5	$F^- > SCN^- > Br^- > NO_3^- > Cl^- > ClO_4^- > I^-$	$Li^+ > Na^+ > K^+ > Cs^+$	D/I	NA	NA	[65]

Legend: † Experimental conditions, when available, include in the following order: oxide form, pH value or range, co-ion(s) concentration; D, direct series ($Cs^+ \rightarrow Li^+/SCN^- \rightarrow SO_4^{2-}$); I, indirect series ($Li^+ \rightarrow Cs^+/SO_4^{2-} \rightarrow SCN^-$); NP, nanoparticle, TF, thin film; AC, adsorption capacity, CG, coagulation, EK, electrokinetics, RT, radiotracing, TT, titration; NA, data not available.

Hence, for two given ions I_i and I_j, putting that $I_i \gtreqless I_j$ means that I_i has higher, comparable, or lower affinity for a metal oxide surface than I_j. In other words, under the same experimental conditions, it means that the values of ion uptake and σ_0 are higher (comparable or lower) and those of ζ (in absolute value) and c^* are lower (comparable or higher) in the presence of I_i than in the presence of I_j. In terms of terminology, a series for which the ion affinity increases (decreases) with increasing (decreasing) *unhydrated* ion radius is called *direct* (D) (*indirect* (I)) [67].

1.1.2.2 Tentative phenomenological interpretations

It is only recently that insoluble metal oxides have been considered [4] (or at least revisited) as an interesting model which can provide some general features about ion specificity [66, 67]. As readily seen from Table 1.2, it can be noted that ion series are different between different metal oxides. As pointed out by Lyklema [67], the main observation is that there is no unique IAS i.e., it depends on the type of surface involved. It appears as though there exists no underlying principle for these systems. Nevertheless, a striking correlation could be made between ion affinity and PZC: for an acidic metal oxides (low pH_{pzc}), the sequence is direct, thus suggesting a preference for larger size ions, whereas for basic oxides (high pH_{pzc}) the series is reversed. Tentative interpretations of ion specificity (as well as non-uniqueness and reversibility) on insoluble metal oxide surfaces have attributed its origin to one of the following effects: (i) ion-induced water structure changes [53, 68], (ii) ion pairing interactions [69, 70], and (iii) dispersive interactions with explicit considerations of ion size and polarizability [71]. Some of these interpretations were developed by extension of similar arguments given for ion specificity in bulk aqueous solutions.

The first of these interpretations assumes that ions perturb the hydrogen bonding network beyond their immediate hydration shells and ascribes the definition of *structure breaking/making* ions depending on the extent of this perturbation. A (perhaps simplistic [5]) definition suggested by Collins [69] considers that large, singly charged ions with low charge density (e.g., SCN^-, $H_2PO_4^-$, HSO_4^-, HCO_3^-, I^-, Cl^-, NO_3^-, NH_4^+, Cs^+, K^+) bind water weakly, whereas small and multiply-charged ions with high charge density (e.g., SO_4^{2-}, HPO_4^{2-}, Mg^{2+}, Ca^{2+}, Li^+, Na^+, H_3O^+, OH^-) bind water strongly relative to the strength of water-water interactions in bulk solution. In contrast, Gierst [68] as well as Berube and de Bruyn [53] gave an "energetic" interpretation of ion specificity on metal oxide surfaces in terms of breaking/forming of hydrogen bonds. This treatment predicts that an entropic attraction will exist between ions and surfaces that promote a similar ordering effect in their local aqueous environments. The structure-inducing behavior of ionic species closely correlates with their hydration enthalpies, with monovalent cations promoting water order in the sequence $Li^+ > Na^+ > K^+ > Cs^+$. However, this interpretation has been considered as unlikely for two reasons [74]: (1) the Gibbs energies involved in the breaking/forming of H-bonds are (in absolute value) at least one order of magnitude too low and thus represents only a fraction of the ion hydration Gibbs energy (for thermodynamic data of ions, see [75]), and (2) it has been shown by molecular dynamics simulation that adjacent to a solid surfaces, a stagnant water layer is formed that behaves like a two-dimensional gel in which the ions can move almost unimpeded [76].

4. Actually, the occurrence of ion specificity on insoluble metal oxides has only been briefly mentioned in [33].

5. Actually, no consensual definition exists on which structural character enables the distinction between these two kind of ions (for critical reviews, see [72, 73])

Hence, this would suggests that upon ion adsorption, no substantial rearrangement of the water molecules adjacent to the solid surfaces would take place, thus pointing to an enthalpic rather than to an entropic driving force. Nevertheless, the water structure breaking/making model predicted correctly cation affinity series on α-alumina obtained at high concentration (1 M) over the entire pH range [77].

The second interpretation invokes so-called inner-sphere or contact ion pairs formation between oppositely charged ions based solely on electrostatic attractive interactions rather than on any specific chemical interactions. As revisited by Collins [69], ion pairing can be predicted through the so-called *law of matching water affinities*, an empirical rule that can be traced back to the *hard–soft acid–base principle* already described in works by Gurney [78] and Pearson [79, 80]. According to this law, inner sphere ion pairs are preferentially formed between oppositely charged ions with matching absolute enthalpies of hydration. In other terms, small ions with high surface charge density, which possess a tightly bound hydration shell (*hard* ions), can pair together because the electrostatic attractive interactions between them is sufficiently strong to squeeze out the hydration shell. Similarly, large ions with lower surface charge density, and thus with a loosely bound hydration shell (*soft* ions), can also pair because the electrostatic interactions, although weaker, is sufficiently strong to expel the hydration shell. In contrast, the pairing of hard and soft ions leads to a mismatch and both ions remains separated by an hydration layer. Returning back to the metal oxides, ion adsorption usually takes place on surface hydroxyl (OH) groups which may become negatively (M–O^-) or positively (M–OH_2^+) charged following deprotonation or protonation, respectively. The radius of the OH group is comparable to that of an OH^- ion in solution ($r(OH^-)$ = 0.140 nm). Hence, by applying the ion pairing law, small (large) ions prefer small (large) ionized surface sites. This trend can also be observed with the activity coefficients of alkali hydroxide salts in solution, where pair formation decreases with increasing cation size [81].

Finally, another, more recent interpretation of ion specificity makes use of non-electrostatic or dispersive ion-surface interactions based on *ab initio* ionic excess polarizabilities with finite ion sizes together with hydration effects [71]. In this model, the electrostatic (self-consistent) potential found in the Boltzmann ion distribution is complemented with a non-electrostatic potential term that contains ion size a and excess polarizability $\alpha^*(i\omega)$ which describes the effect of the water on the polarizability of the ion. The excess polarizability is usually dependent on the intrinsic polarizability of the ion. Hydration effects are included simply by adding to the latter, the intrinsic water polarizability ($\alpha_w(i\omega)$) modulated by the number of water molecules (n_w) in the hydration shell of the ion. In addition, hydrated ion size are considered by taking instead the Stokes radius. It was found that inclusion of the hydrated ion size as well as competing short- and long-range non-electrostatic potentials could explained satisfactorily direct and indirect IAS observed on silica (low pH_{pzc}) and α-alumina (high pH_{pzc}), respectively. However, a major inconvenient of such dispersive models is that the calculated values of polarizabilities depend crucially on the type of model used for the surrounding solvent. For example, it was shown in a comparative study that use of polarizable continuum and point charge solvent models lead to an increase and a decrease in ion polarizability values, respectively [82].

In view of the aforementioned models, the overall conclusion that can be drawn at the moment is that IAS associated with insoluble metal oxides are phenomenologically best

described by ion pairing interactions whose origin are water-mediated and which are to a large extent entropically determined [67]. Nevertheless, recent progress with dispersive models, opens the possibility for a more sophisticated, quantitative model (provided that one exists) that would explicitly include hydration effects and allow for an interplay between electrostatic and non-electrostatics interactions.

1.2 Challenges in the investigation of metal oxide/aqueous solution interfaces

Despite the importance of charged metal oxide/aqueous solution interfaces in the abovementioned processes, a detailed picture of the interfacial architecture, whether at an experimental or a theoretical level, still remains limited. More specifically, one very important, but only partly understood, aspect of these interfaces concerns the pH-dependent surface charging of amphoteric sites such as hydroxyl groups on (1) the molecular ordering (normal and lateral to the surface) or layering of interfacial water relative to bulk water and (2) on the specific adsorption and distribution of dissolved ionic species. Ideally, both experimental and modeling efforts should be directed at better understanding this aspect.

1.2.1 Theoretical challenges

In principle, a complete theoretical description of metal oxide/aqueous oxide interfaces would necessitate a full atomistic description of the metal oxide surface as well as the aqueous phase, a precise knowledge of the interaction potentials between surface groups, dissolved ions, and water, that would take into account the actual acid-base reactions and water dissociation processes, and a functional framework that would enable scaling up microscopic or molecular-based properties to macroscopic observable data.

Unfortunately, this approach has so far been hampered simply due to the formidable complexity behind the atomistic description of the phases and the various chemical interactions involved. For instance, a metal oxide surface is typically far from ideal and is usually characterized by a large set of (often unknown) parameters such as surface roughness at different length scales, number of defects, density and spatial distribution of amphoteric surface OH groups, as well as orientation of their dipoles. In addition, the strength of the non-electrostatic (dispersive) interactions between surface groups and water molecules, is not exactly known. Also, to be realistic, such an approach needs to be applied to large molecular ensembles (e.g., 10^2–10^6 atoms) over different length (1–10 water monolayers) and time scales (1 ns to 1 μs). However, the number of iterations required to obtain sufficient statistics on such simulation cells within a reasonable time frame usually requires high performance computing and long processing times.

Hence, to date, only a few number of theoretical simulations have been carried out on metal oxide/aqueous solution interfaces and these have focused on very different aspects. For example, some studies have used Monte Carlo simulations to investigate the influence of density, spatial distribution, and angular orientation of surface OH groups as well as different types of solid lattices on the interfacial water structure [83, 84]. From these simulations, a certain number of macroscopic parameters such as contact angle, depletion thickness, and density profiles of H and O atoms of water were also deduced.

Other more detailed studies used molecular dynamics (MD) simulations to investigate the interfacial water ordering of pure water and aqueous salt solutions in contact with uncharged and charged metal (hydr)oxides. For example, for pure water in contact with neutral goethite (α-FeOOH) (100) surface, calculations of water density indicated the presence of a layered interfacial region up to $\sim$1.5 nm (i.e., $\sim$4–5 water monolayers) [85]. In this region, the arrangement and orientation of water molecules seems to be dictated directly by the structure of the oxide surface. For a NaCl solution, both Na^+ and Cl^- ions exhibited layering which follows closely that of water. Moreover, water density calculations showed an alternating excess accumulation of Cl^- and Na^+ ions starting at the third and fourth hydration layers which leads to a damped oscillatory pattern of the overall salt distribution. Finally, the presence of a charged surface (either negative or positive) did not affect the pattern of the salt distribution, only the magnitude of the oscillations (i.e., an increase either in Na^+ or Cl^- in the first hydration layer). The presence of a layered distribution, even at a neutral surface, differs significantly from the classical electrical double layer (EDL) theory which instead predicts, beyond the Stern layer, an exponential decay. A further study on the same metal hydroxide then examined the behavior of different salt solutions (NaCl, CsCl, CsF) as function of anions and cations [86]. It was suggested that the strong correlation of ions distribution with fluctuations of water density could be a consequence of water orientation which creates preferred locations for the ions to diffuse to and to reside. It was also found that smaller size ions (Na^+, Cl^-) display stronger adsorption in the layered region in comparison to larger ones (Cs^+, F^-) because the former induce less interfacial water rearrangement. Complementary studies, again with MD simulations, were also performed with pure water and a salt solution at different concentrations in contact with neutral hematite α-Fe_2O_3 (001) surface [87, 88]. As previously, a layered region of water was found but a careful orientational analysis indicated that water molecules in the first and second layer are oriented with their H atoms directed away (*upward state*) and towards (*downward state*) the surface, respectively. Moreover, calculations of residence times showed that water molecules in the first layer are effectively more tightly bound to the surface than those in the second layer. Finally, from water density calculations, Na^+ and Cl^- also showed layering and adsorption as outer-sphere complexes (i.e., water-mediated contact with surface OH groups) in the first two hydration layers. However, Na^+ ions are distributed preferentially in the first layer, while the build-up of Cl^- ions is larger in the second and third layers which are depleted of Na^+.

Recently, more sophisticated MD simulations based on *ab initio* models combined with X-ray experiments were used to study alkaline (Na^+, Rb^+) and alkaline earth (Ca^{2+}, Sr^{2+}) cations adsorption onto uncharged and charged rutile (α-TiO_2) (110) surfaces [89–91]. On a negatively charged surface, the formation of inner-sphere complexes (i.e., direct ion contact) with surface oxygens at specific binding sites was identified for all cations studied. Even at a neutral surface, it was shown that more weakly hydrated cations (Rb^+, Ca^{2+}) still adsorb at the same sites, although at much lower densities, whereas ions that are strongly hydrated (Sr^{2+}, Zn^{2+}) show very weak interactions. The interaction of Cl^- ion for both neutral and negatively charged surfaces was found to be minimal. However, at positively charged surfaces, MD simulations indicate Cl^- adsorption close to the surface and a longer range ordering of ions and water molecules than was observed on neutral or negatively charged surfaces.

As can be seen from these and other similar studies, theoretical simulations constitute an

essential tool towards a more comprehensive picture of metal oxide/aqueous solution interfaces as they can be used to reconsider or extend current phenomenological models. However, a complete description of chemical interactions on an atomistic level, and in turn of phenomena such as ion specificity, has not yet been achieved.

1.2.2 Experimental challenges

Aside from simulations, the investigation of interfacial phenomena at metal oxide/aqueous solution interfaces also poses several experimental challenges. In fact, in order to get information from their direct observation, an experimental method must satisfy a certain number of criteria.

Firstly, since the majority of phenomena occurring at these interfaces (e.g., surface charging through water dissociation, ion adsorption and distribution, and water ordering) are usually confined in a thin (typically, less than 1–2 nm) interfacial region between the solid and aqueous phases, an experimental method must be *surface specific* i.e., its probing depth must be of the same order as the length scale of the interfacial region. This criterion therefore precludes the application of conventional spectroscopic methods such as IR, Raman, or UV spectroscopy which have probing depth in the micrometric range and whose signals derives predominantly from bulk contributions.

Secondly, on the molecular scale, these phenomena generally involve the diffusion of water molecules and ion species within and between hydration layers and, consequently, a continuous rearrangement of the H-bond network which happens on a relatively short timescale. For example, the residence time of water molecules in the first and second hydration layers above a metal oxide is in the range of 100–500 ps, while that in the bulk is about 5 ps [88]. An experimental method thus must be highly *dynamic*. Typically, electron-based scattering and photon-based spectroscopic methods have transition time for a single event in the range 10^{-12}–10^{-15} s^{-1}. This is much faster than the timescale of any ligand exchange, so each event recorded provides only a snapshot of the system in a particular state. However, to obtain a signal or spectrum with a good signal-to-noise ratio sometimes takes from seconds to hours, which means that the resulting signal is a sum over a large number of possible configurations. This results usually in the observation of relatively broad spectral features.

Thirdly, the role of water is of paramount importance in all these phenomena, which means they must be investigated as much as possible in a realistic aqueous environment under relevant conditions (e.g., pressure, temperature, salt concentration, etc.) and, if possible, with minimal external perturbation. Hence, an experimental method must be able to probe this buried interface i.e., must be *applicable in situ* as well as *non invasive*. This prohibits the use of many surface specific electron-based methods such as electron energy loss spectroscopy and X-ray photoelectron spectroscopy, because these works only under ultra-high vacuum (UHV) conditions. It also limits photon-based spectroscopic methods, mainly because of the strong absorption of water in the IR region. However, two different strategies have been employed to overcome this limitation. The first approach uses external reflection on a slab covered with a thin aqueous film. The absorption in the IR range is then reduced by minimizing the aqueous film thickness (typically, less than 1–2 μm). The second approach relies on the condition of total internal reflection (TIR) which allows an IR beam to reach the interface without passing through the aqueous phase.

Finally, an investigation of these interfacial phenomena can only be relevant when the surface charging behavior of the metal oxide associated with the acid-base reactions of its surface groups can be effectively controlled. Unfortunately, an additional complexity inherent to metal oxide/aqueous solution interfaces derives from the fact that most metal oxides behave as insulators such that any voltammetric control of the surface charging is normally inapplicable and needs to be done by varying the pH of the solution.

1.2.3 Literature survey of experimental studies at metal oxide/aqueous solution interfaces

With all the requirements outlined in the previous section, it appears that no single experimental method can alone provide a complete molecular description of metal oxide/aqueous solution interfaces. Nevertheless, significant progresses have been made in recent years in partly unraveling some features of some phenomena occurring at metal oxide/aqueous solution interfaces. This is largely due to the development and application of less conventional, experimental scattering methods such as variable period X-ray standing waves (XSW) (for a review, see [92]) and low-angle X-ray reflectivity (for a review, see [93]), as well as nonlinear optical spectroscopic methods like second-harmonic-generation (SHG) (for a review, see [94, 95]) and sum-frequency-generation (SFG) (for reviews, see Section 2.2.4). The scattering methods can be used to directly probe the substrate surface termination and structure, the atomic arrangement of adsorbed ions, the distribution of ions in the electrical double layer, and the coordination of interfacial water molecules. Total external reflection XSW probes the decay length of the diffuse layer ion distribution, but is insensitive to the condensed layer, whereas XSW generated by Bragg reflection typically has a period in the sub-nanometric range, which is suitable for probing the condensed layer thickness. However, only few results at metal oxide/aqueous solution interfaces have so far been reported, either with total external reflection XWS [96, 97] and Bragg reflection XWS [91, 98–101], mainly because these methods relies on the access to large conventional X-ray synchrotron sources [6].

In contrast, the nonlinear spectroscopic methods can be used to directly probe the substrate surface charging, the interfacial water polarization and net orientation as well as the ion adsorption. These methods both possess intrinsic surface specificity based on nonlinear second-order effects allowed only in a region that lacks inversion symmetry such as an interface. As can be seen from Table 1.3, nonlinear optical methods like SFG and SHG spectroscopy have been particularly useful to unravel many features of the metal oxide/aqueous solution interfaces.

6. However, the recent development of bright and ultrafast, table-top X-ray sources based on laser-driven plasma accelerators opens up new possibilities and potentially wider applicability for these methods [102].

Table 1.3: Compilation of metal oxide/aqueous solution interfaces studied by *in situ* nonlinear spectroscopic methods.

Metal oxide	Mineral name	Surface	IEP/PZC	Solvent	Ion species	Method	Experimental condition†	Reference
Group MO_2								
α-SiO_2	silica	NA	NA	H_2O	Na^+, Cl^-	SHG (TIR)	prism, pH 2–14	[103]
		NA	NA	H_2O	—	SFG (T)	plate, pH 1.5-11.0, 2700–3900 cm^{-1}, *ssp*	[104]
		NA	NA	H_2O	—	SFG (TIR)	plate, pH 2.0–12.0, 2700–3700 cm^{-1}, *ssp*	[105]
		NA	NA	H_2O	Na^+	SFG (TIR)	prism, 1.2–3.0$\times 10^{-3}$ M Cl^-, 2700–3800 cm^{-1}, *sps, ssp*	[106]
		NA	NA	H_2O	Li^+, Na^+, K^+	SFG (T)	plate, pH 5.74, 2800–3900 cm^{-1}, 10^{-1}–10^{-4} M Cl^-, *ssp*	[107]
α-SiO_2	quartz‡	NA	NA	H_2O	Na^+, Cl^-	SFG (TIR)	slab, pH 1.5–12.3, 2500–4000 cm^{-1}, *ssp*	[108]
		NA	NA	H_2O, H_2O/D_2O (1:1)	—	SFG (TIR)	prism, 3000–3700 cm^{-1}, *ppp*	[109]
		(0001)	NA	H_2O	—	SFG (T)	plate, pH 1.5-11.0, 2700–3900 cm^{-1}, *ssp*	[104]
		NA	NA	H_2O, NaOH	—	SFG (NA)	plate, pH 10, 3000–3800 cm^{-1}, *ssp*	[110]
		(0001)	NA	H_2O	—	PS-SFG (T)	plate, pH 1.5–11.5, 2500–4000 cm^{-1}, *ssp*	[111]
		NA	NA	H_2O	Cd^{2+}, Ba^{2+}, Ba^{2+}, NO_3^-	SHG	prism, pH 7, 1–4$\times 10^{-3}$ M Cl^-, 1–60$\times 10^{-5}$ M Na^+	[112]
		NA	NA	H_2O	—	SFG (TIR)	prism, pH 5.7, 2800–3900 cm^{-1}, *ppp, ssp*	[113]
		NA	NA	H_2O	Ca^{2+}, Cd^{2+}, Zn^{2+}	SHG (TIR)	prism, pH 7, 3 $\times$ 10^{-3} M Cl^- + 0.01 M NaCl	[114]
SiO_2	silica (nanoporous)	NA	$\sim$2	H_2O	Na^+, Cl^-	PS-SFG (TIR)	pH 3.0–9.0, 2.0 $\times$ 10^{-3} M, 2900–3700 cm^{-1}	[115]
α-TiO_2	rutile	(110)	5.5	H_2O	—	SFG (TIR)	plate, pH 2.0–12.0, 2700–3700 cm^{-1}, *ssp*	[105]
			4.8$\pm$0.3	H_2O	—	SHG	plate, 3.0–7.5	[116]
Group M_2O_3								
α-Al_2O_3	alumina	(0001)	$\sim$ 8	H_2O, D_2O	—	SFG (TIR)	prism, pH 3-12, 3000–3800 cm^{-1}, *ssp*	[109]
		NA	5–6	H_2O	ClO_4^-, NO_3^-, Cl^-	SHG (TIR)	prism, pH 1.5–12.5, 10^{-1}–10^{-3} M Na^+	[117]
		(0001), (1$\bar{1}$02)	4.1$\pm$0.4, 5.2$\pm$0.4	H_2O	NO_3^-	SHG (TIR)	slab, pH 4.0–7.5, 10^{-1}–10^{-3} M Na^+	[118]
		(1$\bar{1}$02)	$\sim$5.1	H_2O	CrO_4^{2-}, $HCrO_4^-$	SHG (TIR)	prism, pH 5.0–9.0, 10^{-4}–10^{-6} M	[119]
		(0001)	4–5	H_2O	—	SFG (NA)	slab, pH 1.1–14.0, 3000–3800 cm^{-1}, *ssp*	[120]
		(0001)	$\sim$ 6.3	H_2O	—	SFG (TIR)	slab, pH 3.3–9.8, 3000–3800 cm^{-1}, *ppp, sps, ssp*	[121]
		(0001)	$\sim$ 6	H_2O	Na^+, Cl^-	SFG (TIR)	slab, pH 2.7–12.0, 2500–4000 cm^{-1}, *ppp, ssp*	[122]
α-Fe_2O_3	hematite	NA	???	H_2O	—	SHG (NA)	NA	[123]

Legend: † Experimental conditions, when available, include in the following order: sample geometry, pH value or range, co-ion(s) concentration, spectral range, polarization configuration; SHG, second-harmonic-generation, SFG, sum-frequency-generation, PS, phase-sensitive, T, transmission, TIR, total internal reflection; NA, data not available or not applicable. ‡ A distinction was made here between quartz and silica since, in most studies, it was not clearly stated whether the term "quartz" referred to fused silica or crystalline quartz.

SFG spectroscopy can be used to study the influence of metal oxide surface charging on interfacial water molecules ordering. As the amplitude of the SFG response depends on the number of oriented water molecules, then the alignment of these molecules by the electric field generated at a charged aqueous interface should increase that response. For aqueous solutions at hydrophilic solid surfaces such as metal oxides, this SFG response interpreted as a vibrational spectrum generally exhibits in the bonded OH stretching region (3100–3500 cm^{-1}), two peaks[7] at $\sim$ 3150 and $\sim$ 3400 cm^{-1}, which can be understood as a mixture of interfacial water molecules in a highly (3–4 H-bonds with other water molecules) and poorly coordinated hydrogen-bond network, respectively. Early studies with SFG spectroscopy performed at the quartz (α-SiO_2)/water interface have shown that the relative intensities of these peaks change as a function of pH, and it was proposed that the orientation of the interfacial water molecules should change with increasing pH and should go through a minimum at a given pH value, which would correspond to the PZC [108]. Since the PZC of fused silica occurs at pH_{pzc} $\sim$2, then for a solution with pH $>$ pH_{pzc} the surface is negatively charged and water molecules should be oriented with their hydrogen atoms pointing towards the surface (downward state). In contrast, at pH $<$ pH_{pzc}, the surface is positively charged and water molecules reverse their orientation and direct their oxygen atoms towards the surface (upward state). This mechanism was later confirmed by phase-sensitive SFG spectroscopy which enabled to determine the relative phases of each water species [111]. It was found that at low pH the highly and poorly coordinated water species have different orientations; the water species at 3150 cm^{-1} and 3400 cm^{-1} were oriented upward and downward, respectively. As the pH increases, the net orientation of these molecules reversed. This mechanism has been found and confirmed by SFG spectroscopy for various other metal oxides e.g., alumina (α-Al_2O_3) [109, 121, 122] and titania (rutile) (α-TiO_2) [105, 109]. More recently, in an attempt to explain the surface charging behavior of α-Al_2O_3 with pH, it was proposed that water species contributing to the 3400 cm^{-1} peak should have a net polar orientation towards the liquid bulk, while those associated to the 3150 cm^{-1} peak should have one which is more pH-dependent. Hence, pH variations which result from protonation/deprotonation of surface OH groups alter on one hand the average polar orientation of water molecules directly H-bonded to the surface, and on the other hand, also creates an interfacial electric field that reorients the water molecules not directly bonded to the surface. This has led to some speculations about the distribution of the two water species, whether these are evenly distributed throughout the double layer or if one of them has a preferential location e.g., close to the surface [107, 125]. A careful orientational analysis made by SFG spectroscopy of interfacial water ordering at silica/aqueous solution interfaces for different salt concentrations has recently suggested that highly coordinated water species should be rather located at some distance from the interface, while less coordinated ones are closest to the interface [106]. This result strongly supports similar conclusions obtained previously by SFG spectroscopy on interfacial water ordering close to hydrophilic Langmuir monolayers spread on basic aqueous solutions [126].

SFG spectroscopy has also been used to investigate the influence of type and concentration of dissolved ions on interfacial water molecules ordering. In this case, the water acts as an indirect spectroscopic probe of ion effects on its local environment. The adsorption of ions screens the charge of the solid surface and, in turn, reduces the depth of its electric

7. The vibrational origin of these two peaks remains, however, controversial. In fact, it has been suggested that they may be actually caused by a destructive Fermi-like resonance interference with a much broader water band [124].

field, which has for consequence to relax the ordering of interfacial water molecules and to decrease the SFG response accordingly. The extent of this relaxation will depend on the ion concentration as well as on the type of ion. For instance, it was observed that at high pH, the contact of 0.1–0.5 M NaCl solutions with silica surfaces reduces the overall SFG signal intensity (in comparison to pure water) because the Na^+ ions screens the positively charged surface [108]. Nevertheless, an increase in molecular ordering was also noted, particularly for the less coordinated water species. This was attributed to a thinning of the EDL, which in turn leads to an enhancement of the interfacial electric field. A similar effect was found with sodium phosphate buffer in contact with α-TiO_2 (110) [105]. Further studies on silica surfaces have investigated the effects of a series of alkaline cations (Li^+, Na^+, K^+) in a range of concentrations (10^{-4}–10^{-1} M) [107]. It was found that the cation effect can be observed even at the lowest concentration and that it become saturated around 10^{-1} M (Fig. 1.1). It was also found that the peak at 3200 cm^{-1} is the most affected. The screening effect of the different alkaline cation was shown to have some specificity as it followed the series $K^+ > Li^+ > Na^+$ and could be explained by a competitive interplay between effective cationic radii and electrostatics interactions between cations and the surface groups. Interestingly, it was concluded that cations act as the key factor in the perturbation of the water hydrogen-bond network, as no anion effect (with Cl^-, Br^-, and I^-) could be assessed. As of now, no SFG study conducted at metal oxide/aqueous solution interfaces has been undertaken to understand the influence of surface charging on ion distribution nor its relation to ion specificity.

Additionally, SFG spectroscopy in time-resolved mode has been used to reveal the relaxation behavior of the hydrogen-bonding network of interfacial water molecules on the sub-picosecond timescale [127]. Pump-probe experiments conducted at the silica/water interface in the bonded OH region showed that dynamics of interfacial water molecules were similar to those in the bulk with recovery on similar timescales. Moreover, this recovery was mainly dictated by energy transfer, vibrational relaxation, and thermalization of the H-bonding network. Hence, it was concluded that the dynamics was governed more by H-bonding between water molecules than by the configuration or ordering of the whole network.

As for SHG spectroscopy, it is a related surface-selective, nonlinear spectroscopic method whose response, in contrast to SFG, originates from the resonant enhancement of electronic transitions from interfacial molecular species (surface groups, oriented water molecules). In this resonant mode, the intensity of the SHG response depends on the number density and the second-order hyperpolarizability averaged over all molecular orientations of these species. SHG spectroscopy has been used to study the influence of surface charging and dissolved ion concentration on interfacial water molecules ordering. As the amplitude of the SHG response depends on the number of adsorbed species and aligned water molecules, then the ionization of surface groups obtained by varying the pH should increase that response. Also, similarly to SFG, the adsorption of ions screens the charge of the aqueous interface and, in turn, reduces the depth of its electric field, which decreases the SHG response in a concentration-dependent manner. Early studies done at the fused silica/water interface have shown that water gets more strongly aligned with pH variation and that the surface of silica behaves as a diprotic acid with two species of ionizable silanol groups, each with a different pK_a [103]. The determination of the surface potential enabled to calculate the pK_a values and the fraction of each species of silanol groups (pK_a 4.5 and 8.5 for 19% and 81% of the silanols, respectively).

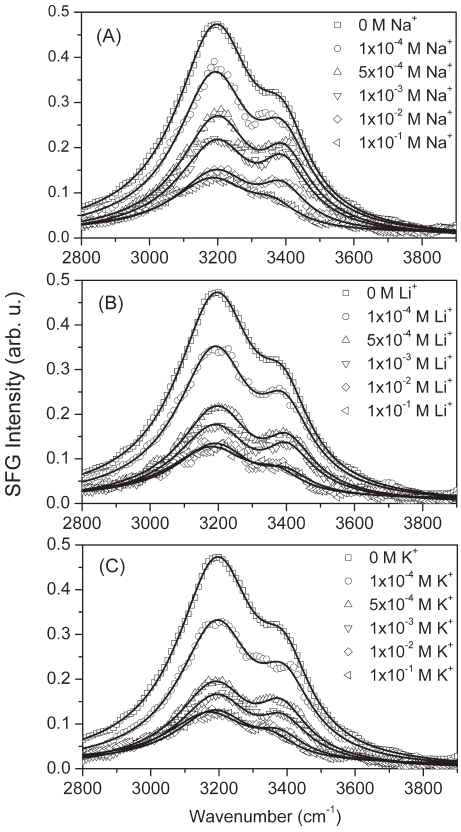

Fig. 1.1: SFG spectra of silica/aqueous solution interface for three alkali chloride solutions at different concentrations. (a) NaCl, (b) LiCl, and (c) KCl. Experimental data (*open symbols*) and fitting curves (*black lines*) are shown (reprinted from [107]).

Another application of SHG spectroscopy has been to monitor in real-time the adsorption and desorption of ions at charged metal oxide/aqueous solution interfaces. A series of studies performed at the fused quartz/aqueous solution interfaces for different large size alkaline earth metal cations (Sr^{2+}, Ba^{2+}, Cd^{2+}) have shown that these ions adsorbs sparsely and in a reversible manner through the formation of outer-sphere complexes to the negatively charged SiO_2 interface (Fig. 1.2) [112, 114]. Adsorption isotherms were also recorded at pH 7 for each ion in a range of concentrations and showed as expected a decrease in the SHG response with increasing ion concentration. The application of an EDL model enabled the calculations of the equilibrium binding constant and free energy of adsorption of these ions to the silica surface. A similar analysis was also reported with the adsorption of Cr^{6+} on alumina [119].

Despite the molecular insights provided by scattering and spectroscopic methods, their application to the study of metal oxide/aqueous solution interfaces remains negligible in comparison to other more common but less sensitive and indirect methods such as electrokinetics methods. Furthermore, most of the experimental evidences gathered so far has been done on natural metal oxides in conditions of geochemical relevance (e.g., moderately to highly concentrated aqueous solutions, definite pH range, specific types of ions, etc.). In contrast, very few data has been given for other less common or syn-

thetic oxides, particularly those heavily involved in industrial and technological applications. In addition, due to their insulating character, the surface charging behavior of metal oxides has been so far possible only by means of an "acidimetric" control of the aqueous solutions. Other types of oxides, more specifically doped, semiconducting oxides, could provide another way of controlling surface charging in a "voltammetric" manner. Nevertheless, it has remain experimentally difficult to provide both electrochemical and molecular insights at these interfaces. The combination of a spectroscopic method such as SFG spectroscopy together with a transparent conducting oxide such as indium-tin oxide (ITO) which enables the voltammetric control as well as the direct access to the charged interface could provide a mean to overcome this difficulty. However, to date, no such work has been undertaken. Assuming ITO as a potentially good candidate for this purpose, its main physico-chemical properties will be briefly reviewed in the following sections.

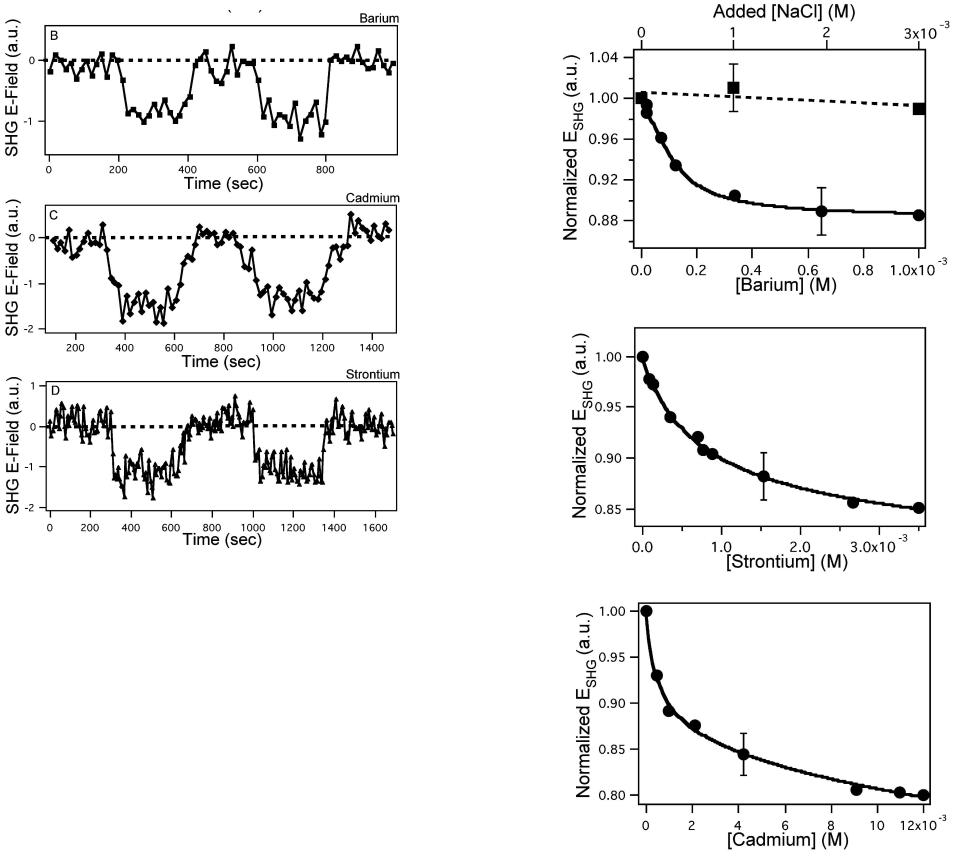

Fig. 1.2: Adsorption behavior of alkaline earth cations at the silica/water interface investigated by SHG spectroscopy. (a) Adsorption/desorption traces of Ba^{2+}, Cd^{2+}, Sr^{2+} ions at silica surfaces recorded at pH 7, (b) Binding isotherms of Ba^{2+}, Cd^{2+}, Sr^{2+} ions at silica surfaces recorded at pH 7 and 10 mM NaCl as background salt. Data (*black point*) and fitting curves (*black curve*) from combined Gouy-Chapman and Langmuir models are shown (reprinted from [112]).

1.3 Indium tin oxide

1.3.1 Applications

Tin-doped indium oxide (In_2O_3 : Sn) or simply ITO is currently, along with ZnO:Sb (ATO), ZnO:Al (AZO), and SnO_2:F (FTO), one of the most studied and widely used transparent conducting oxide (TCO) [8], a class of oxides that combine both the electrical conductivity of metal with the optical transparency of glass [128–131]. Since the 1960's, it has been recognized that ITO, as a degenerated (n-type) semiconductor, possess a low electrical resistivity ($\sim 10^{-4}$ Ω·cm), a large bandgap (~ 3.6 eV), and a plasma frequency in the near-infrared (NIR), which optically make it highly transmissive (>80%) and highly reflective in the visible (VIS) and the mid-infrared (MIR) spectral regions, respectively [132, 133]. Because of these combined properties, ITO thin films have been over the years increasingly used in the form of transparent electrodes in various optoelectronic devices [9] such as flat panel, liquid-crystal and touch-screen displays [135, 136], organic light-emitting diodes (OLEDs) [137–141], and electrochromic panels and windows [142–144]. It can also be found in various types of photovoltaic cells including inorganic [145–152], organic [153–157], and dye-sensitized cells [158–162]. Moreover, the reversible change in the conductivity of porous ITO upon exposure to reducing gases, such as propane and methane, and its high sensitivity towards (often toxic) gases (CO, NO, NO_2) and volatile organic compounds (CH_3OH, CCl_4), has also enabled use of ITO as gas sensors [163–171]. More recently, it has been shown that ITO can be functionalized with various chemical compounds (e.g., amines [172–174], carboxylic [175–177] and phosphonic [178–181] acids, silanes [182–185], thiols [186–188], etc.) which makes it an ideal electrode substrate for interfacial electron transport in organic electroluminescent devices. Finally, ITO can be used as a biosensor or bioelectronic platform acting as a substrate for direct, one-step immobilization of biomolecules (peptides and proteins [189–195], oligonucleotides and nucleic acids [196–200], etc.) through the functional groups of some of the aforementioned linker compounds. It has also been used in electrical control of cell adhesion and migration by reductive release of adsorbed monolayers [26, 201–203]. Finally, and as shown in the present work, it can also be used as transparent conducting electrodes in *in situ* spectroelectrochemistry [204–209].

1.3.2 Preparation

To date, various methods have been used for the deposition and growth of ITO thin films. Depending on the deposition process involved, these methods can be grouped into three types: physical vapor deposition (PVD), chemical vapor deposition (CVD), and wet chemical methods. Among these, PVD methods are by far the most employed methods for the growth of ITO films, especially at the industrial level, because of their large applicability, effectiveness, flexibility, and relatively low costs. Typically, with these methods, ITO material is brought in vaporized form and recondense as a thin film onto a substrate. However, this process requires working at low pressure in an evacuated atmosphere in order to minimize scattering with gas molecules and to reduce material losses. When these requirements are met, ITO films of high quality with definite thickness and optimal

8. In fact, the production of ITO represents the leading end use of indium, accounting yearly for more than 75% of its global consumption.

9. Nevertheless, because of the high cost and limited supply of In, the brittleness and lack of flexibility of deposited ITO films, novel alternatives such as poly(3,4-ethylenedioxythiophene) (PEDOT), carbon nanotubes (CNTs), and graphene are currently being considered for these specific applications [134].

properties (ideal density, non-porous, low resistivity, etc.) can be produced [210, 211]. In addition, the substrate temperature can be easily adjusted, which makes PVD methods adequate for more temperature-sensitive substrate (e.g., polymers) [212].

The most commonly used PVD methods include evaporative (vacuum) deposition [213, 214], electron beam deposition [215, 216], sputter deposition [217–220], and pulsed laser deposition [221, 222], and involve either resistive heating, electron and ion bombardment, plasma discharge, or laser ablation, as means of material evaporation. Each of these methods has its advantages and disadvantages (for a review, see [128, 223]) and ITO film properties produced by them have shown some variations (Table 1.4).

Table 1.4: Comparison of some physico-chemical properties of ITO thin films prepared by different PVD methods [128, 223].

Method	**Deposition parameters**		**Film properties**	
	Substrate temperature [°C]	Growth rate [nm/min]	Resistivity [$\times 10^{-4}$ Ω·cm]	Transmittance [%]
Vacuum evaporation	RT–440	12–40	0.7–12	80–90
DC sputtering	RT–453	25–80	1.2–160	70–90
RF sputtering	RT–450	11.6–120	1.4–7	85–90
Ion-beam sputtering	100–450	—	1.5–5.5	>80

Sputter deposition or simply sputtering is the most applied PVD method for deposition of ITO thin films as it generally produces more homogeneous films. In this process, a target and a substrate are used as cathode and anode, respectively. In the presence of an inert gas, a plasma is created by applying a voltage between the two electrodes. The target is subjected to an intense ion bombardment and material is ejected from the surface of the cathode towards the anode, thus depositing an uniform thin film onto the substrate (a more complete description will be given in Chap. 2). Typically, two powering modes have been used in sputtering systems, namely, direct current (DC) and radio-frequency (RF). The DC mode is restricted to conducting targets, in which a direct voltage is applied between the electrodes. In contrast, the RF mode can be applied to both conducting and non-conducting targets, in which a high frequency generator is connected between the electrodes. These conventional sputtering modes suffer from several disadvantages, for example, low deposition rates and substantial heating of the substrate as a result of the bombardment by secondary electrons from the target. This heating effect, however, can be substantially reduced by employing a magnetic field to confine these electrons to a region close to the target surface. Nowadays, DC and RF sputtering systems employ water-cooled magnetron cathode to obtain high deposition rates with low substrate temperatures [223].

Whatever the method chosen, it has been shown that the quality and, in turn, the physico-chemical properties of sputtered ITO films depends strongly on both sample parameters (Sn doping [224], thickness [225–227]) as well as on deposition and post-deposition conditions (sputtering pressure [228, 229] and rate [230, 231], gas composition [232–234], partial pressure [235–237], and flow rate [238–240], substrate type [241, 242], temperature [243–245], and bias voltage [246–248], target-to-substrate spacing and geometry [249, 250] as well as post-annealing atmosphere and temperature [251]). A precise control and monitoring of these parameters enables the production of films for different purposes.

1.3.3 Crystalline structure

1.3.3.1 Bulk structure

The crystal structure of ITO is based on the bixbyite structure (space group $Ia\bar{3}$, Nr. 206) of the undoped host oxide In_2O_3, which is a body-centered cubic structure with a lattice constant of 1.0117 nm [252] (Fig. 1.3). The crystallographic data of In_2O_3 is summarized in Table 1.5. The bixbyite structure is similar to that of fluorite, with the exception that the former contains $\sim 25\%$ of oxygen vacancies. The In_2O_3 unit cell contains 16 In_2O_3 molecules for a total of 80 atoms i.e., 32 In and 48 O atoms. The In^{3+} cations are located in two different six-fold-coordinated sites which can be described as distorted cubes with six of their eight vertices occupied by oxygen anions (O^{2-}). The two remaining vacant anion sites are located either on opposite vertices (b sites) or along one face diagonal (d sites) (Fig. 1.4) [253, 254]. The b and d sites are occupied by 8 and 24 In^{3+} cations, respectively. All 8 b cations are coordinated to six O^{2-} anions with an In−O bond distance of 0.218 nm (and to two oxygen vacancies), while the 24 d cations exhibit less symmetry, as they are coordinated to six O^{2-} anions at variable In−O bond distances (0.213, 0.219 and 0.223 nm) [255]. The 16 structural oxygen vacancies are located along the four $\langle 111 \rangle$ axes and the other 32 oxygen anions are coordinated to four cations. The oxygen vacancy plays an important role in the defect chemistry of In_2O_3 and ITO because it acts as a diffusion channel for In^{3+} and Sn^{4+} cations.

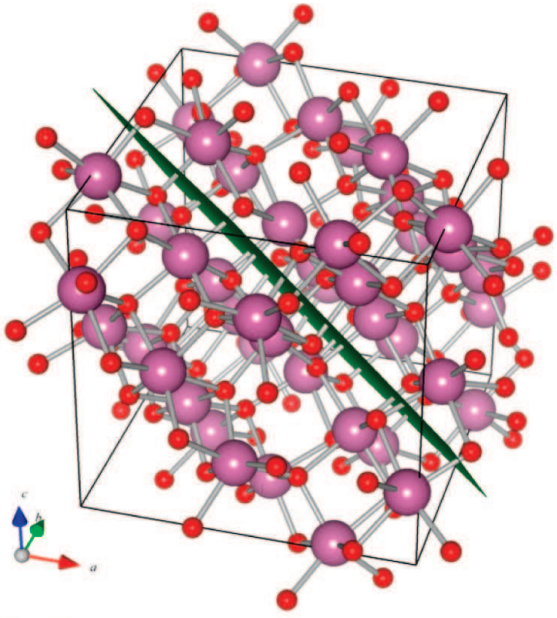

Fig. 1.3: Bulk In_2O_3 unit cell (cubic). The (222) lattice plane (*green*) is highlighted (reprinted from [258]).

ITO is essentially formed by substitutional doping of In_2O_3 i.e., by replacement of a fraction of its In atoms with extrinsic Sn dopant atoms in the cationic sites. The Sn substitution was shown not to alter significantly the bixbyite lattice structure with only a slight reduction of the lattice constant ($a = 1.000$–1.005 nm) [256]. This is due presumably to the smaller effective ion radius of Sn^{4+} ($r(Sn^{4+}) = 69$ pm) in comparison to that of In^{3+} ($r(In^{3+}) = 79$ pm) [257].

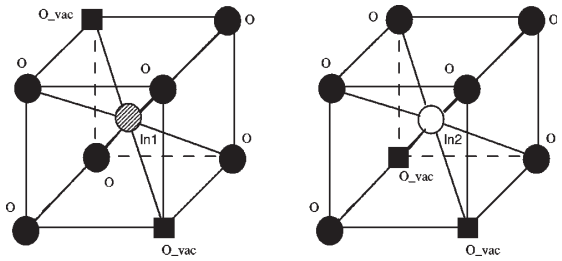

Fig. 1.4: Cationic In sites in the cubic In_2O_3 structure (reprinted from [254]).

Table 1.5: Bulk crystal parameters of In_2O_3 and ITO.

Parameter	In_2O_3	ITO
Crystal structure	cubic (body-centered)	cubic (body-centered)
Space group	$Ia\overline{3}$	$Ia\overline{3}$
Lattice constant [nm]	$a = b = c = 1.0117$	$a = b = c = 1.000$–1.005
b site Cation–O distance [nm]	0.218	0.208
d site Cation–O distance [nm]	0.213, 0.219, 0.223	—
Cell volume [cm^3]	1.0355×10^{-21}	1.000–1.015×10^{-21}
X-ray density [g/cm^3]	7.120	7.120–7.160

1.3.3.2 Surface structure

To date, very few information has been gathered about the actual surface structure of ITO. This is due partly because ITO exhibits many different crystal orientations which depend largely on the sample composition and on the preparation conditions. However, a theoretical characterization, based on density functional theory (DFT), on a model ITO surface has been recently reported [258]. The model selected the (222) lattice plane since its has often been found to be the predominant plane. The optimized surface structure has revealed two types of (potentially) chemically active sites on the ITO surface, namely, under-coordinated metal ions (In, Sn) and surface hydroxyl groups (OH) (Fig. 1.5).

As can be seen from Fig. 1.5, the surface chemical composition of an untreated ITO film is relatively complex because it contains both metal hydroxyl groups (In−OH, Sn−OH) as well as oxygen bridges (In−O−In, Sn−O−In). In addition, it was also shown through XPS measurements that other physisorbed hydroxide and oxy-hydroxide species, which results from the hydrolysis or incomplete hydrolysis of In_2O_3 such as [259]

$$In_2O_3 + 3H_2O \longrightarrow 2In(OH)_3, \tag{1.1a}$$
$$In_2O_3 + H_2O \longrightarrow 2InOOH, \tag{1.1b}$$

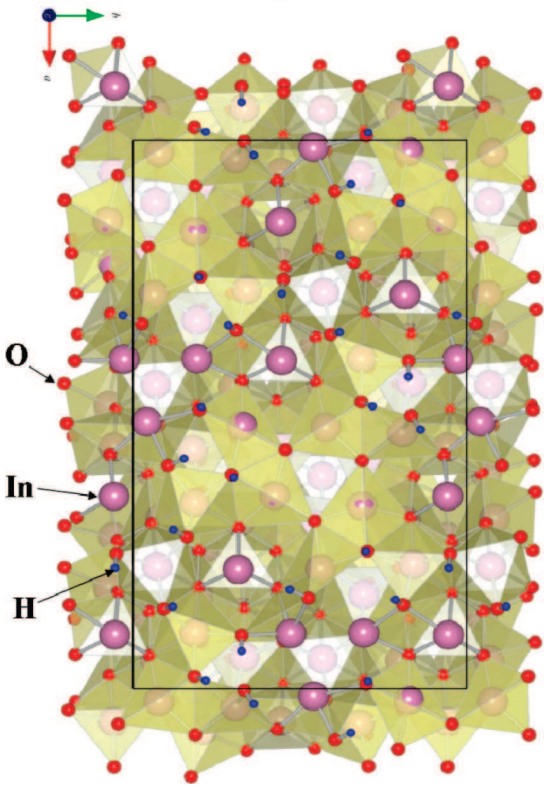

Fig. 1.5: Top view of a rectangular, OH-terminated ITO surface in the (222) plane, optimized at the DFT level. The periodic rectangular supercell is indicated. The chemically active surface sites include under-coordinated metal ions (*pink*) (not shaded by bulk-like coordination polyhedra) and surface OH groups (*red-blue*) (reprinted from [258]).

co-exist in the first molecular layer of the ITO surface [10].

It has been argued that the different deposition methods introduced previously as well as the deposition conditions strongly determine the bulk structure and properties of ITO, but that the surface chemical structure depends essentially on the post-deposition treatments [259]. The commonly employed treatments for removal of trapped particles and surface contaminants include mechanical, wet, and dry cleaning. The mechanical treatment simply involves degreasing with a detergent solution followed by ultrasonication [261, 262]. In contrast, the wet cleaning treatments use either cleaning in organic solvents [263] or, most commonly, heating in acidic or basic solutions in the presence of oxidative reagents such as with piranha (H_2O_2 : H_2SO_4 (1:4)) [259], aqua regia (HNO_3 : HCl : dH_2O (1:3:20)) [261, 262], and RCA (NH_4OH : H_2O_2 : dH_2O_2 (1:4:20)) [259, 261, 262, 264] treatments. Finally, dry cleaning treatments usually employ plasma cleaning such as air plasma [259, 265], Ar plasma [259, 266], H_2 plasma [267, 268], O_2 plasma [266, 269–272], and UV-ozonolysis [186, 273–275].

Each of these treatment removes surface contamination with different levels of efficiency. Moreover, some of these treatments also induce modifications in the surface chemical

10. In fact, stability diagrams of metal oxides show that hydrolysis of In_2O_3 is generally more favored than for SnO_2 at any pH [260].

composition, morphology, and properties (wettability, work function, etc.). For instance, wet cleaning treatments remove relatively well contaminants (although to a lesser degree than dry treatments), but induce surface degradation of ITO by creating an amorphous layer which contains In hydroxide species physisorbed on the ITO lattice. Nevertheless, piranha treatment has been shown to increase significantly the surface coverage of hydroxyl groups. In contrast, dry treatments such as air, Ar, O_2 and UV-ozonolysis have been shown to remove effectively carbonaceous contamination but also to introduce higher concentrations of O^{2-} anions at the surface. However, Ar plasma tends to remove the first surface layer of ITO, thereby decreasing its roughness. On the other hand, O_2 plasma produces new oxygen species through oxidation of surface Sn−OH to Sn−$O^{\cdot}$, while H_2 plasma, although improving surface crystallinity, usually reduces surface metal oxides into metallic In.

1.3.4 Physico-chemical properties

1.3.4.1 Chemical and electrochemical properties

The IEP value of ITO thin films is usually found in the range 4–6 [189, 276] and indicates that ITO should only be dissolved in either strong acidic or basic solutions (Table 1.6). In addition, ITO films were found to be chemically stable during exposure to organic solvents like hexane, toluene, and methanol [277]. However, significant degradation in some of its properties (e.g., increase in surface roughness, resistivity, and transmittance below 300 nm) has been observed after exposure to dichloromethane and also to strong acidic and basic solutions (e.g., 1 M HNO_3 or NaOH) and was attributed, at least partly, to localized chemical attack and film dissolution.

The electrochemical behavior of ITO films was first studied in water. It has been observed, for example, that ITO film immersed in water can be irreversibly destroyed (e.g., dark colored ITO film with poor transparency) if the potential is poised in the hydrogen evolution regime for any extended period of time [278]. It is well known in electrochemistry that around the cathode, hydrogen is generated according to the following electrolysis reaction:

$$2H_2O + e^- \longrightarrow OH^-_{(aq)} + H_{(g)}, \tag{1.2}$$

and that most of the hydrogen thus produced will diffuse out of the water as gaseous hydrogen ($H_{2\,(g)}$) in the form of bubbles:

$$H_{(g)} + H_{(g)} \longrightarrow H_{2\,(g)}. \tag{1.3}$$

However, it has been suggested that some of these hydrogen atoms may instead adsorb on ITO and react with it according to the following mechanism: [278]

$$M{-}O + H_{(g)} \longrightarrow M_{(aq)} + H_2O \qquad (M = In, Sn). \tag{1.4}$$

Table 1.6: Physico-chemical properties of ITO thin films.

Parameter	**Range**[†]
Isoelectric point (IEP)	4–6
Surface OH density [nm^{-2}]	1–3
Electrical	
Sheet resistance (R_s) [Ω]	4×10^{-4}
Electrical resistivity (ρ) [Ω·cm]	2–4$\times 10^{-4}$
Charge carrier concentration (N) [cm^{-3}]	10^{20}–10^{21}
Hall mobility (μ_H) [$cm^2/V \cdot s$]	10–70
Effective (electron) mass (m_e^*/m_e)	0.30–0.35
Optical	
Reflectance (IR region) [%]	80–90
Transmittance (VIS region) [%]	80–95
Bandgap energy (E_g) [eV]	3.0–4.6
Refractive index (n) (VIS region)	1.7–2.1
Extinction coefficient (k) (VIS region)	0.007–0.030
Plasma frequency (ω_p) [cm^{-1}]	8700.9
Coherence length (l_c) [μm]	20.65
Second-order nonlinear susceptibility ($\chi^{(2)}$) [V·m]	1.005×10^{-13}
Third-order nonlinear susceptibility ($\chi^{(3)}$) [$V^2 \cdot m^2$]	2.16–3.36$\times 10^{-18}$

[†] The range given here depends largely on the deposition conditions.

Hence, under anodic polarization (i.e., by the withdrawal of electrons from ITO), In and/or Sn metal ions appear at the electrode surface, which then results in a loss of transparency.

ITO thin film properties are also significantly altered during potential cycling in both 1 M HNO_3 and NaOH. Changes in chemical composition and microstructure occur during the anodic and cathodic polarization of ITO and extend into the film bulk [277]. However, it appears that most of the film degradation occurs during cathodic polarization [11].

The combination of acidic electrolytes, particularly chloride solutions, with anodic polarization also favor ITO film dissolution [279–281]. It was proposed that dissolution of ITO occurs as the result of sequential electrochemical and chemical reactions. At potentials close to the standard redox potential of Cl^-/Cl_2 reaction ($\sim$ 1 V vs SCE [282]), begins the electrochemical oxidation of Cl^- and OH^- ions to $Cl^{\cdot}$ and $OH^{\cdot}$ radicals, which in turn induces the chemical breaking of In–O surface bonds due to electron withdrawing by the radical species. Depending on the pH, this corrosion mechanism would then release

11. Some faradaic effects have been observed between the oxygen and hydrogen evolution regimes, which would suggest that some change in the chemical composition is occurring on the film surface and/or in the bulk and that it could be associated with the reduction of Sn^{4+} oxide to Sn^{2+} or even Sn.

different products. For example, hypochlorous acid (HClO) and indium chloride ($InCl_3$) at low pH, and indium hydroxochloride at high pH. Thus, if an ITO film is subjected to cyclic voltammetry for many cycles in such solutions, then its surface soon becomes etched and it acquires poor resistivity and a hazy appearance. Under cathodic polarization, contributions from oxygen vacancies and O^{2-} anions have been considered as crucial for the electrochemical behavior of ITO [283]. In this regime, metal oxides cations are strongly reduced so that ITO is gradually and irreversibly converted to a metallic mirror with a noticeable decrease of lattice oxygen content.

1.3.4.2 Electrical properties

ITO is a highly degenerate (or metal-like) n-type semiconductor meaning that it has a negative surface charge (see Fig. 1.6 for the band structure). The most commonly used parameters related to the electrical properties of ITO thin films are the electrical sheet resistivity (ρ_s), the sheet resistance (R_s), the Hall or charge carriers mobility (μ_H), and the carrier density (N) (Table 1.5). For a thin conducting film deposited on a semi-infinite insulating substrate, the sheet resistivity is given by (see Section 2.2.3.5)

$$\rho_s = \frac{\pi t}{\ln 2}\left(\frac{V}{I}\right), \tag{1.5}$$

and the sheet resistance by

$$R_s = \frac{\rho}{t} = \frac{\pi}{\ln 2}\left(\frac{V}{I}\right). \tag{1.6}$$

The mobility of charge carriers is related to the carrier density and is given by

$$\mu_H = \frac{1}{\rho_s N e}, \tag{1.7}$$

where e is the elementary electronic charge.

Typically, the resistivity of ITO thin films obtained by sputtering methods falls in the range 1–2$\times 10^{-4}$ Ω·cm, although lower values in the range 7–9$\times 10^{-5}$ Ω·cm have been obtained with less conventional methods [222, 284, 285]. In comparison, the resistivities of gold and silver at 20°C are $\sim 1.6 \times 10^{-6}$ Ω·cm and $\sim 2.4 \times 10^{-6}$ Ω·cm. As for the carrier density of ITO film, it typically falls in the range 10^{20}–10^{21} cm^{-3}.

In the case of ITO, the free carriers, and thus the degeneracy, originate from two main donors: the substitutional Sn dopant cations and the oxygen vacancies (V_O). In the first case, Sn usually forms an interstitial bond with oxygen and exists as SnO_2 with a valency of +4. This leads to the formation of a mixed oxide of the form $(In_{1-x}Sn_x)_2O_3$ where x is the atomic percentage of dopant atoms. Hence, the difference of valency between In^{3+}

and Sn^{4+} results in a maximum number of x free electrons that can be donated [12]. Using Kröger-Vink notation, this can be written conveniently as

$$2\ In_{In}^{\times} + 2\ SnO_2 \longrightarrow 2\ Sn_{In}^{\cdot} + 2\ e' + In_2O_3 + 1/2\ O_{2\ (g)}, \tag{1.8}$$

where the symbol S_L^C defines a given species S (atom, vacancy (v), electron (e), or hole (h)) on a specific lattice site L (atom or interstitial site (i)) with a charge C (relative to the lattice site) which can be zero ($^{\times}$), negative ($'$), or positive ($^{\cdot}$).

In the second case, doubly charged oxygen vacancies act as electron donors which results in an oxygen-deficient oxide of the form $(In_{1-x}Sn_x)_2O_{3-y}$ [256]. Again, using Kröger-Vink notation, this can be written as

$$O_O^{\times} \longrightarrow v_O^{\cdot\cdot} + 2\ e' + 1/2\ O_{2\ (g)}. \tag{1.9}$$

The incorporation of Sn dopant atoms and the presence of oxygen vacancies in the In_2O_3 lattice also changes significantly its electronic band structure. Fig. 1.6 compares the energy band models of undoped and low-doped In_2O_3. It can be seen that doping causes the partial filling of the conduction band of ITO as well as shifts in energy of the valence and conduction bands relative to their location in In_2O_3. As shown in Fig. 1.6, the valence band of ITO is build from low energetic In:$3d^{10}$ core level and a bonding O^{2-}:$2p^6$ level, while the conduction band is made from anti-bonding In:$5s^0$ [288]. The substitution with Sn^{4+} ion creates a two-electron donor level about 0.03 eV below the conduction band edge (E_c). The oxygen vacancies also give supplementary levels. This model has recently been challenged by calculations on ITO electronic band structure which assigns the main contribution to the top of the valence band to O $2p$ states hybridized with In $5d$ (from d sites), whereas the bottom of the conduction band is mainly formed from In $5s$ (from b and d sites) electronic states hybridized with O $2s$ states [254]. This feature is in disagreement with the band model of Fan and Goodenough which suggests rather a gap between the In $5s$ and In $5p$ states (see Fig 1.6).

1.3.4.3 Optical properties

1.3.4.3.1 Linear properties

ITO is optically transparent and essentially colorless when deposited as a thin film on a glassy substrate. The most commonly used parameters related to the optical properties of ITO thin films are the reflectance (R) and/or transmittance (T) [289]. Other optical parameters such as the dielectric constant (ε), the refractive index (n), as well as the extinction (k) and absorption (α) coefficients can also be derived from the latter through

12. The optimal atomic percentage of Sn is not known exactly but it typically ranges between 5 and 10% [256, 286]. Higher percentages lead to point defects build from SnO complexes which promote the formation of negatively charged interstitial O^{2-} anions, capable of neutralizing the cation charge [287].

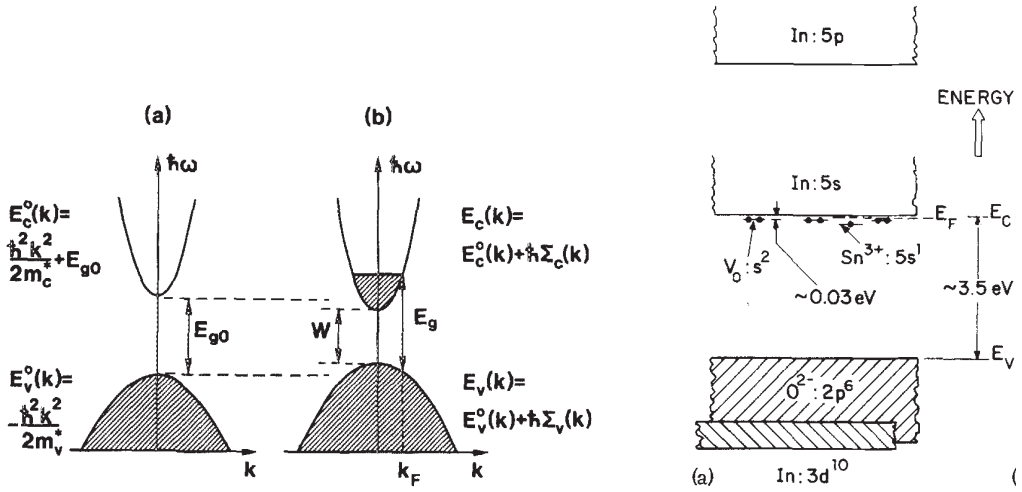

Fig. 1.6: Schematic representation of ITO band structure. (a) Band structure of undoped In_2O_3 and ITO in the region of bandgap. Shaded areas denote occupied states (reprinted from [289]). (b) Energy-band model of ITO for small Sn doping (reprinted from [288]).

standard relations for thin absorbing films on non-absorbing substrates [290]. Most studies published so far have been performed in a range between the UV and NIR regions (with few exceptions in the MIR [289, 291–294]), and were mainly concerned with the effects of sample composition and/or deposition conditions on these optical properties. Fig. 1.7 illustrates the variation of R and T from UV to MIR for an ITO thin film deposited on a CaF_2 substrate. The ITO film shows high transmittance in the VIS and NIR spectral regions as well as high reflectance in the MIR region. The strong absorption at shorter wavelengths ($\lambda \lesssim 0.3$ μm) is due mainly to the electronic interband or bandgap transitions, while that at longer wavelengths ($\lambda \gtrsim 1.2$ μm) comes from intraband transitions in the conduction band. In the UV and IR regions, the slopes of the absorption curve have been used to determine the value of E_g and the electronic (number) density (ρ_e), respectively.

1.3.4.3.2 Nonlinear properties

ITO displays several nonlinear effects, especially observable when deposited as thin film on glassy substrates. The most commonly used parameters related to the nonlinear optical properties of ITO thin films are their second- and third-order nonlinear susceptibilities. These parameters describe the efficiency of nonlinear processes such as, for example, nonlinear refraction, Pockels effect, and SHG, and depends on molecular dipole effects created by the non-centrosymmetric crystal structure. Additionally, Sn doping also causes additional non-centrosymmetry and a redistribution of electronic charge density. Few studies have measured the SHG response of ITO thin films and their dependence on beam incident angle [295, 296] and film thickness [296]. The variation of the SHG response with the beam incident angle was explained by the preferred crystal face orientation taken by the ITO films during deposition. As for the thickness effect, the SHG response was found to increase slowly in the range 75–120 nm, and then sharply from 120–150 nm with approximately a quadratic dependence on thickness (Fig. 1.8). This demonstrates that the observed SHG response is a bulk effect rather than one due to the

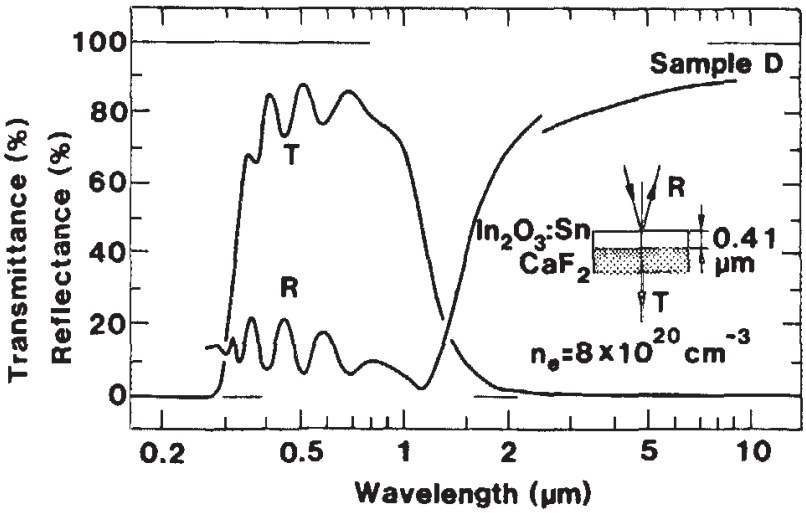

Fig. 1.7: Spectral normal transmittance and near-normal reflectance (p-polarized light) for ITO-coated CaF_2 plate. The ITO film thickness is 410 nm. The incident angle in the reflectance measurements were 10° for $\lambda < 2.5$ μm and 25° for $\lambda > 2.5$ μm (adapted from [289]).

interface between the ITO film and the glass substrate. The values of the second- and third-order susceptibilities ($\chi^{(2)}$, $\chi^{(3)}$) were also determined [296, 297] (Table 1.6). The maximum of the SHG signal is proportional to the square of the coherence length of the ITO sample which for the case of normal incidence (and under non-phase matched condition) was calculated from

$$l_c = \frac{\lambda}{4(n(2\omega) - n(\omega))} \approx 20.6\ \mu\text{m}, \tag{1.10}$$

where λ is the fundamental wavelength ($\lambda = 1.064$ μm) and $n(\omega)$, $n(2\omega)$ represents the refractive index at the fundamental (ω) and second-harmonic (2ω) frequencies.

To date, no study of the SFG response from ITO thin films has been reported, although in virtue of its metal-like properties, it is expected that ITO should generated a nonlinear response similar to those of noble metals (Ag, Au, Pt) [13].

1.4 Objectives

In order to investigate the surface charging and any potential ion-specific effects at the ITO/aqueous solution interface and to partly overcome the previously mentioned exper-

13. In fact, it was reported that the non-resonant response of ITO is allegedly two times higher than that of Au [298].

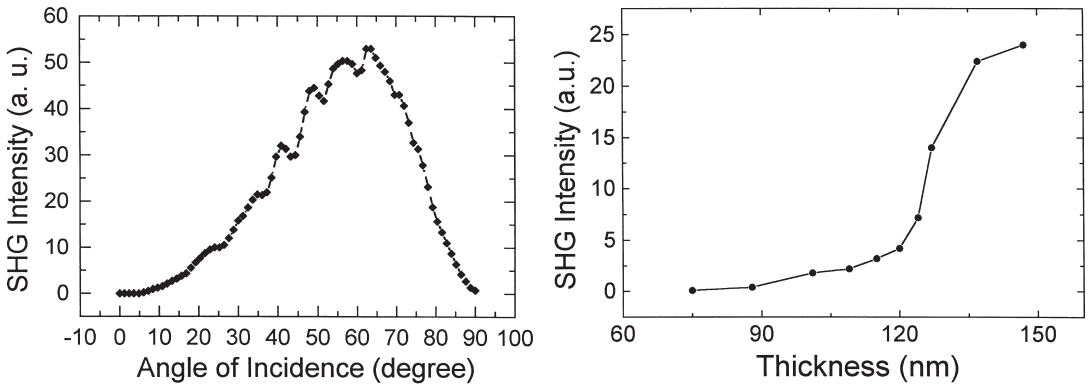

Fig. 1.8: SHG intensity generated from an ITO-coated glass substrate. (a) Dependence of the SHG intensity on the incident angle of the fundamental beam, (b) Dependence of the SHG intensity on the ITO film thickness. The wavelength was set at $\lambda = 1.064$ μm (reprinted from [296]).

imental difficulties linked to this kind of interface, the following objectives were set:

- Design and construction of an adaptable and flexible SFG spectroscopy setup that enables *in situ* probing of various interfaces including the metal oxide/aqueous solution interface under different experimental configurations (incident angle, polarization configuration) and environmental conditions (temperature, humidity). This includes notably implementing an etalon for the pulse shaping of one of the probing beams which enables recording background-subtracted spectrum, a reference beam line to account for the source fluctuations in the quantitative analysis of the SFG signal intensity, a sample stage area that allows easier manipulation and accommodates the fast exchange of various measuring cells, and a purging chamber which permits measurements in water-absorbing spectral regions;

- Design and construction of a three-electrode spectroelectrochemical measuring cell with ITO as the working electrode that enables simultaneously SFG spectroscopy measurements and, if required, voltammetric control of the surface charging at the ITO/-aqueous solution interface under various aqueous phase conditions (pH, salt concentration, temperature);

- Characterization of the deposited and annealed ITO layer i.e., determination of its structural (grain size, morphology, texture, roughness, thickness), electrical (sheet resistivity), and optical (refractive index, extinction and absorption coefficient, bandgap energy) properties;

- Characterization of the ITO/water interface i.e., determination of the SFG response of interfacial water in the bonded OH spectral region (3100–3500 cm^{-1}) and surface current density under different externally applied potentials;

- Characterization of the ITO/aqueous salt solutions i.e., determination of the influence of anionic and cationic salt series on the SFG response of interfacial water in the bonded

OH spectral region (3100–3500 cm^{-1}) and surface current density under different externally applied potentials;

1.5 Outline of the thesis

This thesis is composed of four chapters. Chapter 2 introduces the different materials used, the preparation of the samples and solutions, and the experimental methods used for their characterization. A brief description of the basic experimental arrangement as well as some theoretical background for each of these methods is also given. Chapter 3 presents and discusses the experimental results. Conclusions drawn from the work as well as future outlooks are given in Chapter 4.

2

Materials, Methods, and Instruments

2.1 Materials

2.1.1 Solvents and salts

All organic solvents used (methanol, isopropanol, hexane, toluene) for cleaning were purchased from Sigma-Aldrich (CHROMASOLV® Plus HPLC Grade, ≥99.9%; Germany). All inorganic anionic and cationic salts were purchased from Sigma-Aldrich and are summarized in Table 2.1. Milli-Q water (≥18.2 MΩ·cm at 25°C; Synergy UV, Millipore, Germany) was used for all solutions and was found to be slightly acidic (pH 5–6), owing to dissolved atmospheric CO_2. HCl (*Trace*SELECT®, fuming, ≥37.0%) and NaOH (semiconductor grade, ≥99.99%) were also purchased from Sigma-Aldrich.

2.1.2 CaF_2 plate and prism

CaF_2 was chosen as substrate material for the ITO coating mainly because of its high optical transparency in the VIS and near-IR (0.1-10 μm) spectral regions and its relatively low solubility in water (0.0016 g/100 mL H_2O)[1]. CaF_2 rectangular plates (10 mm×20 mm×2 mm, two-sided optically polished (60/40); MaTecK, Germany) were used for the physicochemical characterization of the ITO coating, while CaF_2 hemicylindrical prisms (RCX-13-20-10CF, $A = 13$ mm×20 mm, $r = 10$ mm; optically polished (10/20); Laser Components, Germany) were used for the *in situ* SFG spectroscopy investigations at the ITO/aqueous solution interface.

2.2 Methods and Instruments

2.2.1 Preparation of samples, solutions, and measuring cell

The spectroelectrochemical measuring cell and all glassware were cleaned by soaking in a hot diluted 0.5% (v/v) Hellmanex® solution (Hellma Analytics, Germany) for 1 h, then soaked in hot Milli-Q water for 1 h, then rinsed thoroughly with Milli-Q water, and finally dried under a stream of purified $N_{2\,(g)}$.

The 10 mM aqueous salt solutions were always freshly prepared by dissolving the appropriate amount of salts in a given volume of Milli-Q water. Prior to any spectroelectro-

1. In fact, CaF_2 offers a compromise between IR transparency and water solubility in comparison to two other commonly used IR-transparent materials, namely BaF_2 (0.1-12.5 μm, 0.161 g/100 mL H_2O) and IR-grade SiO_2 (e.g. Suprasil® 300) (0.1-3.5 μm, virtually insoluble).

Table 2.1: List of inorganic salts for the anionic and cationic salt series.

Salt	M_w [g/mol]	M_p [°C]	**Purity** [%]
	Anionic series		
Na_2CO_3	105.99	851	99.0
Na_2SO_4	142.04	884	99.0
Na_2HPO_4	141.96	240	99.0
NaF	41.99	993	99.0
NaBr	102.89	755	99.0
$NaNO_3$	84.99	306	99.0
NaI	149.89	661	99.0
$NaClO_4{}^a$	140.46	468	99.0
NaSCN	81.07	287	98.0
	Cationic series		
$CaCl_2{}^b$	147.01	772	99.0
LiCl	42.39	605	99.0
NaCl	58.44	801	99.5
KCl	74.55	770	99.0
RbCl	120.92	715	99.0
CsCl	168.36	615	99.5
NH_4Cl	53.49	340	99.5

Legend: ^{a}, monohydrated; ^{b}, dihydrated.

chemical measurement, all solutions were degassed by bubbling $N_{2\,(g)}$ for 30 min.

Prior to any measurement, the top and basal faces, respectively, of the ITO-coated CaF_2 plates and prisms were cleaned by UV/ozonolysis in an UVO cleaner (model 42, Jelight, USA) for 1 h and then kept in Milli-Q water. This cleaning method has previously been shown to be the most efficient in removing adventitious surface contamination [186].

The reference and counter-electrodes of the spectrochemical measuring cell were also unmounted and cleaned before any measurement. The reference electrode was frequently refilled with saturated KCl solution to avoid any contact of the electrode with air bubbles. The counter-electrode was cleaned with a series of organic solvents.

2.2.2 Preparation of ITO films

2.2.2.1 RF magnetron sputtering

RF magnetron sputtering was used to deposit ITO thin films onto the CaF_2 substrates (plates and prisms). Sputtering is a PVD process by which atoms from the surface of a target material are removed and ejected, carried by a plasma, and then condensed and deposited onto the surface of a substrate material under UHV conditions [299, 300]. In a basic DC sputtering system, two plane parallel disk electrodes composed of a target

(cathode) and a substrate (anode) are mounted at a given separation distance from each other in an evacuated chamber. An inert gas (usually Ar) is then fed continuously into the chamber at a low pressure (10^{-5}–10^{-6} bar) and the electrically neutral gas atoms are allowed to flow between the electrodes. A high voltage (10^{2}–10^{3} V) is applied between the electrodes such that initial electrons from the target surface initiate an ionization cascade in the gas i.e., free electrons ionize inert gas atoms which become positively charged, and create secondary electrons, which are then accelerated to the anode substrate, subsequently colliding with additional gas atoms, creating more ions and more free electrons in the process. This results in the formation of a plasma, a hot gas-like phase consisting of electrons and ions. The charged ions found at the edge of the plasma (otherwise, the plasma is considered as electrically neutral) are then accelerated towards the negatively charged target surface. Their collision at high kinetic energies with the target surface ejects neutral atoms by energy transfer, which then travel to the substrate. On their way to the substrate, each ejected target atom hits numerous gas atoms that deflect them and cause energy loss. These low energy target atoms then approach the substrate surface from partially randomized directions, and then settle on it to produce a reasonably uniform thin film across a textured substrate surface. One disadvantage of DC systems is that positive charge will tend to accumulate on the cathode (target), thus requiring higher voltages which could damage both target and produced film. RF sputtering systems circumvent this problem by applying an alternating, high-frequency (typically, 13.56 MHz) voltage which forces the positive ions to stay in the plasma zone, away from the cathode.

With magnetron sputtering, one can enhance the process described above by producing strong magnetic fields (e.g., with permanent magnets) near the target area [301]. This (toroidal-type) field causes traveling electrons to be trapped and to follow cycloidal motions along magnetic flux lines near the target instead of being attracted towards the substrate. This has for advantage to confine the plasma to an area close to the target, without causing damages to the thin film being formed. Moreover, electrons travel over a longer distance, increasing the probability of further ionizing gas atoms. The additional ions created as a result of these collisions lead to a plasma with a higher ion density. More ions means more ejected atoms from the target, therefore, increasing the efficiency of the sputtering process. It also means that the plasma can be sustained at a lower pressure. Finally, a higher ejection rate, and hence a higher deposition rate, minimizes impurities to form in the thin film.

ITO thin films of approximately 100 nm in thickness were sputter-deposited on the top face of CaF_2 plates and on the basal face of hemicylindrical CaF_2 prisms using an home-built RF magnetron sputtering chamber equipped with DC power suppliers and load-lock system (Dr. Michael Bruns; Institute for Materials Research III (IMF-III), KIT - Campus North, Eggenstein-Leopoldshafen, Germany). A special holder was designed and fabricated specifically for the sputtering of the CaF_2 prisms. The sputtering chamber was evacuated down to a base pressure $\leq 5 \times 10^{-6}$ mbar prior to deposition using a turbo-molecular pump backed by a membrane pump. Pressure in the sputtering chamber was measured using digital Pirani-Penning gauge combination. A circular planar magnetron of 3.00" (7.62 cm) in diameter was used as the magnetron cathode. The magnetron target assembly was mounted at the bottom of the sputtering chamber facing the target so that the sputtering can be achieved in the sputter up mode. A continuously variable DC power supply of 750 V and 3 A was used as power source for sputtering. A sintered ITO metal alloy (In_2O_3:SnO_2 (90:10 wt.%), $3.00" \times 0.165"$ (7.62 cm $\times$ 0.42 cm), 99.99%; EJTI-

TOX403A2, Kurt J. Lesker Materials Group, Germany) was used as sputtering target and was mounted on the magnetron holder. A gas mixture of Ar/O_2 (80:20 vol.%) was used as pre-sputtering and sputtering atmospheres. The use of O_2 in the mixture compensates for the oxygen loss from the ITO target. The flow rates of both gases were controlled individually by Tylan mass flow controllers. Before deposition of each film, the target was pre-sputtered for 30 min to remove the passive oxide layer present at its surface. The parameters used for the deposition of the ITO films are summarized in Table 2.2. The sputtered ITO thin films were subsequently annealed in air at 300°C for 3 hrs. Films deposited onto unheated substrate tends to be amorphous and increasing the substrate or annealing temperature usually improves the crystallinity and grain size and decreases the density of structural defects, leading to higher carrier concentration and lower sheet resistivity. The sheet resistance of 50 nm-thick ITO films deposited on Si_3N_4 substrates was observed to be highly dependent on the annealing temperature but less on the annealing time (Fig. 2.1). The sheet resistivity was $\sim 4.5\times10^2$ Ω·cm for a unannealed sample (not shown). The coating preparation was performed in collaboration with V. Hermann (IMF-III, KIT - Campus North).

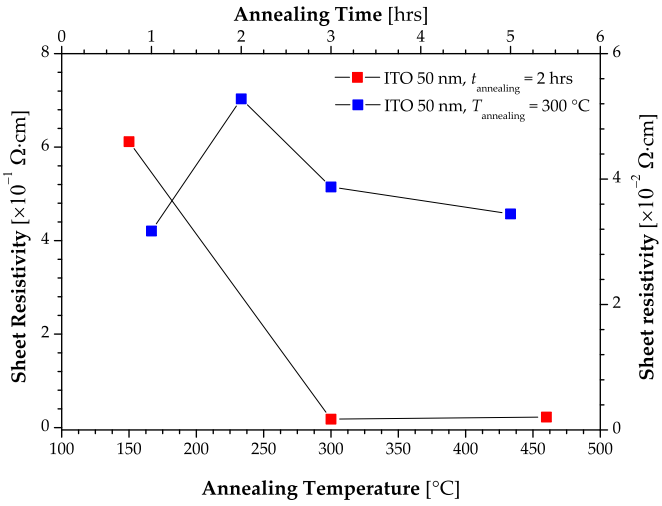

Fig. 2.1: Sheet resistivity of sputtered ITO films annealed in air at different annealing temperatures and for different annealing times (source: V. Hermann (IMF-III, KIT - Campus North)).

2.2.3 Characterization of ITO films

2.2.3.1 X-ray photoelectron spectroscopy

X-ray photoelectron spectroscopy (XPS) is a spectroscopic method used for the quantitative analysis of surface chemical composition [302]. Usually, a XPS spectrum of a single element or of multiple elements is given as function of core level electrons binding energy.

XPS is based on the photoemission process by which inner shell (or core level) electrons of surface atoms irradiated with X-rays, overcome their binding energy, and are emitted out of the surface with a certain kinetic energy. This process is described by the photoelectric effect which relates the energy of emitted photoelectrons to that of the core level

Table 2.2: Deposition and post-deposition parameters for the preparation of ITO thin films.

Parameter	**Condition**
Deposition	
Sputter gas atmosphere	Ar/O_2 (80:20 vol.%)
Base pressure [mbar]	$\leq 5 \times 10^{-6}$
Sputter pressure [mbar]	2.5×10^{-3}
Sputter power [W]	66
Sputter temperature [°C]	60
Target-substrate distance [cm]	10
Target voltage [V]	NA
Target current density [mA/cm^2]	NA
Substrate bias voltage [V]	125–130
Substrate temperature [°C]	22
Gas flow rate [cm^3/min]	14.2 (Ar), 3.5 (O_2)
Film growth rate [nm/min]	1
Post-deposition	
Annealing gas atmosphere	air
Annealing temperature [°C]	300
Annealing duration [hr]	3

Legend: NA, data not available.

electrons such as

$$E_{\mathrm{kin}} = E_{\mathrm{bind}} - (E_{\mathrm{phot}} + \Phi_{\mathrm{M}}), \tag{2.1}$$

where E_{kin} denotes the kinetic energy of the emitted photoelectron, E_{bind}, the binding energy of the inner shell electron, $E_{\mathrm{phot}} = h\nu$, the photon energy of X-rays of frequency ν, and Φ_{M}, the work function of the material. By recording E_{kin} of the emitted photoelectrons, and knowing the X-rays wavelength as well as the work function of the particular element considered, E_{bind} of the inner shell electrons can be determined.

The XPS spectrum of a material contains peaks of the various chemical elements (with the exception of H and He) present on its surface. The binding energy of a particular elemental peak depends not only on the element but also on the chemical environment and energy (oxidation) state of its atoms. Any change of the chemical environment and state, which perturbs the energy level of the atom, will cause a small variation in the peak position or chemical shift in the XPS spectrum. For example, when a given atom is bound to another one, more electronegative, the electron density around the former will decrease

and the effective nuclear charge increases. Therefore, the core level electrons are more strongly attracted by the nucleus, resulting in an higher binding energy. Another effect, spin-orbital (or L-S) coupling of p, d, and f orbitals leads to XPS peak splitting. The total angular momentum (J) of an electron is found by summing its angular (L) and spin (S) momenta ($J = L + S$). The intensity of the doublets is determined by the occupation probability of the two different energy states, which can also be expressed as the multiplicity $M = 2J + 1$. Other features can be observed in an XPS spectrum including, for instance, X-ray satellite peaks, photon-induced Auger electron peaks, shake-up satellites, and valence band features ($E_{\text{bind}} < 30$ eV).

The intensity of XPS peaks, as well as the integrated area under these peaks, are related to the amount of each element. The intensity of a peak j from element i in a spectrum is given by

$$I_{ij} = CT(E_{\text{kin}})L_{ij}(\gamma)\sigma_{ij}\int_0^d n_i(z)e^{-z/\lambda_{ij}(E_{\text{kin}})\cos\theta}dz, \tag{2.2}$$

where C is an instrumental constant, $T(E_{\text{kin}})$ is the transmission function of the analyzer, $L_{ij}(\gamma)$ is the angular asymmetry factor for orbital j of element i, σ_{ij} is the photoionization cross-section of peak j of element i, $n_i(z)$ is the concentration of element i at a distance z below the surface, $\lambda_{ij}(E_{\text{kin}})$ is the inelastic mean free path length of the photoelectron emitted from orbital j of element i with a given kinetic energy, and θ is the take-off angle of the photoelectrons measured with respect to the surface normal. The instrumental constant C is assumed not to vary appreciably under acquisition conditions and time required for XPS measurements. Typically, it can be removed when either elemental ratios or atomic percentages are calculated. The angular asymmetry factor $L_{ij}(\lambda)$ accounts for the type of orbital the photoelectron is emitted from and the angle between the incident X-rays and the emitted photoelectrons. When s orbitals are used for quantification, this factor remains constant and can be ignored. Even for other types of orbitals, the variation is very small and usually neglected.

Assuming that the elemental concentrations are homogeneous (i.e., $n_i = n_i(z)$) within the XPS sampling depth (from 0 to d), a take-off angle normal to the surface ($\theta = 0°$), and a small ratio of wavelength to the photoelectrons mean free path ($d/\lambda \ll 1$)[2], Eq. (2.2) simplifies to

$$I_{ij} = CT(E_{\text{kin}})L_{ij}(\gamma)\sigma_{ij}n_i\lambda_{ij}(E_{\text{kin}}). \tag{2.3}$$

The cross-sections for each element has been calculated and tabulated previously [303].

The basic experimental setup for XPS measurements consists of an ultra-highly evacuated chamber, an X-ray source, an electrostatic guiding lens system, a moderately evacuated sample transfer chamber, a sample holder, an electron energy analyzer, and a multi-

2. For XPS sampling depth $d = 10$ nm, $\lambda \approx 5d$ for photoelectrons with $E_{\text{kin}} = 10$–10^3 eV.

channel detector. The UHV environment enables collecting and analyzing the emitted photoelectrons without interference from collisions with residual gas phase molecules, which would otherwise lead to loss of energy and intensity. It also permits minimizing formation of monolayer from gas molecules adsorbed on the sample. The sample holder is usually mounted on a sample stage which allows for high resolution positioning in the x, y, z and θ directions. The most common X-ray sources employs Al K_α and Mg K_α emission lines because of their relatively high energy (1486.6 and 1253.6 eV) and narrow spectral width (0.85 and 0.70 eV). Hence, X-rays are emitted and directed towards the surface of a sample, then emitted photoelectrons are directed by the electrostatic guiding system through the electron analyzer which uses an electric field between two hemispherical surfaces to disperse the electrons according to their kinetic energy. Faster electrons will impinge on the outer hemisphere, while slower ones will be attracted to the inner hemisphere. Only electrons in a narrow energy region (called the pass energy) will succeed in getting all the way round the analyzer to the detector. Finally, these electrons hit a set of multi-channel plates resulting in an electron cascade that can be recorded by a CCD camera located on the air side.

XPS spectra were obtained for the surface chemical analysis of the ITO samples using a commercial XPS spectrometer system (K-Alpha, ThermoFisher Scientific, United Kingdom). Monochromatic Al K_α radiation was used and focused within an X-ray spot size of 400 μm. Spectra were recorded by combining a 1300 eV low-resolution survey scan and 25 eV high-resolution scans for all relevant peaks (C1s, O1s, In3d5, Sn3d5). The take-off angle was set to $0°$. Data acquisition and processing was done with the Thermo Avantage software (ThermoFisher Scientific). All recorded spectra were background-corrected and referenced to the C1s peak (285.0 eV) originating from adventitious carbon contamination. The elemental peaks were fitted with one or more Voigt profiles ($\Delta E_{\text{bind}} = \pm 0.2$ eV) and their intensity normalized. These measurements were performed in collaboration with V. Trouillet (IMF III, KIT - Campus North).

2.2.3.2 X-ray diffraction

X-ray diffraction (XRD) was used to assess the surface crystallinity, texture (i.e., preferred crystalline orientation), and grain size of the deposited ITO thin films. XRD is a scattering technique that enables to determine the degree of crystallinity of a solid material by scanning its surface with monochromatic X-rays over a wide range of incident angles and studying the diffraction pattern caused by sub-nanometer sized structures [304]. Usually, the scattering intensity I_s is recorded as a function of the detector angle 2θ.

Typically, the basic instrument for X-ray diffraction consists of two arms, an emission arm and a detection arm, arranged on the periphery of a goniometer and a sample holder fixed on its rotational axis. The incident angle of both arms is θ with respect to the normal to the sample surface. The emission arm consists of an X-ray source (X-ray tube), a monochromator (Ni or Ge filter) for wavelength selection, and a set of apertures and slits (diverging, soller, scattering) for beam conditioning and shaping. The detection arm consists also of a set of slits (scattering, soller, receiving) and the detector. Most systems use the so-called Bragg–Brentano (or parafocusing) reflection arrangement. In this configuration, a focusing circle is defined as positioned tangentially to the sample surface. The (para)focusing condition is obeyed only when the X-ray source and detector are positioned on the goniometer circle where it intersects the focusing circle. The goniometer

usually operates in the $\theta - 2\theta$ mode, where the X-ray source remains stationary, but the sample and the detector move simultaneously by an angle θ and 2θ, respectively. The diffraction pattern is then collected by varying the angle of the incoming X-ray beam by θ and that of the scattered beam by 2θ while measuring $I_s(2\theta)$ as a function of the latter.

X-ray scattering is based on the phenomenon known as Bragg diffraction in which X-rays are scattered by the electrons of the lattice atoms without changing their wavelength and undergo constructive interference only when certain geometrical conditions are satisfied. The periodicity of a crystalline solid can be modeled by selective sets of crystallographic lattice planes that are occupied by the atoms of the solid. Any set of lattice planes can be indexed by a triplet of integers (hkl), the so-called Miller indices. These lattice planes are parallel to each other, intersect the edges of the unit cell at specific points $(a/h, b/k, c/l)$, and are separated by an interplanar distance d_{hkl}, which depends on the unit cell parameters such as lattice constants (a, b, c) and angles (α, β, γ). Assuming that these planes are irradiated by X-ray beams incident at an angle θ, a condition of maximum I_s can be satisfied only when the X-ray beams scattered by the lattice planes can interfere constructively i.e., remain in phase when their geometrical path length is equal to an integer multiple of the wavelength. This condition known as Bragg's law, describes the condition for constructive interference from successive crystallographic planes (hkl), and can be written as

$$n\lambda = 2d_{hkl} \sin \theta_B, \tag{2.4}$$

where n is an integer determined by the reflection order considered, λ represents the X-ray wavelength (0.15406 nm for Cu Kα source), and θ_B, the Bragg diffraction angle.

The diffraction pattern of a crystal obtained by measuring the intensity of scattered X-rays as a function of scattering angle is a characteristic of the material. Very strong intensities known as Bragg peaks are obtained in the diffraction pattern when scattered waves satisfy the Bragg condition. Ideally, in the case of random distribution of all possible (hkl) planes, only crystallites having planes parallel to the sample surface will contribute to the reflected intensities [3]. In reality, as in the case of thin polycrystalline films, certain crystallographic planes can occur with a greater probability than others. This phenomenon is known as texture and has a significant influence on the diffraction pattern, where more abundant lattice planes will be associated with more intense Bragg peaks.

From Eq. 2.4, the distance between two adjacent lattice planes can be derived from the experimental peak position by putting

$$d_{exp} = \frac{\lambda}{2 \sin \theta_B}, \tag{2.5}$$

whereas its theoretical value d_{hkl} for a cubic lattice can be calculated from the lattice constant (a) by

3. This is a consequence of the $\theta - 2\theta$ mode which constrains the scattering vector $\mathbf{Q}$ to remain parallel to the surface normal.

$$d_{hkl} = \frac{a}{\sqrt{h^2 + k^2 + l^2}}, \tag{2.6}$$

where hkl are the Miller indices of the given lattice plane.

A characteristic shift towards lower or higher angle compared to the reflection of ideal crystals usually indicates a lattice expansion or contraction (Fig. 2.2). The lattice distortion can be defined as

$$\frac{\Delta d}{d_0} = \frac{(d_{exp} - d_{hkl})}{d_{hkl}}. \tag{2.7}$$

An estimate of the mean crystallite or grain size for a given orientation can be obtained by using the Debye-Scherrer formula given by

$$D = \frac{\lambda}{w \cos\theta} \qquad [\text{nm}], \tag{2.8}$$

where $w = \Delta(2\theta)$ [4] denotes the full width at half maximum (FWHM) (or broadening) of the XRD peak.

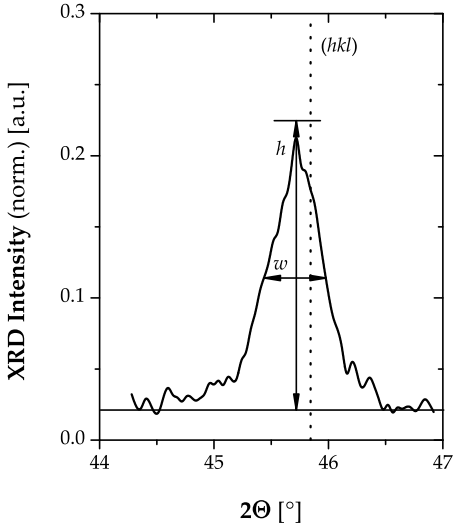

Fig. 2.2: XRD peak originating from the (hkl) plane reflection for a given crystalline film. The position of this peak from an hypothetical reference (*dotted line*) is also shown.

4. Typically, one should also account for the XRD spectrometer resolution (δ) and therefore put instead $w' = \sqrt{w^2 - \delta^2}$. However, for a resolution $\delta \leq 0.01°$, this term is usually neglected.

XRD spectra of unannealed and annealed ITO thin films were recorded with an X-ray diffractometer (XRD D5000, Bruker AXS, Germany) (in a Bragg-Brentano geometry) equipped with a Cu Kα source ($\lambda = 0.15405$ nm) whose radiation was filtered through a Ge crystal primary monochromator (Fig. 2.3). The Cu X-ray tube was operated at 40 kV, 40 mA and cooled by an internal, water-filled recirculating chilling system set at 16 °C and a flow rate of 4–5 L/min. The slit widths were set to 2 mm for the pre- and post-sample slits, and 0.2 mm for the detector slit. The detector used was a standard scintillation counter. The XRD spectra were collected with diffraction angle (2θ) ranging from 20 to 80° in steps of 0.01°. The diffraction spectra was recorded and processed using the DIFFRAC^{plus} software (Bruker AXS). The XRD spectrum of the ITO film was compared to an ITO reference from the Inorganic Crystal Structure Database (ICSD) (ICSD-50858, ICSD, FIZ Karlsruhe - Leibniz Institute for Information Infrastructure, KIT - Campus North). These measurements were performed in collaboration with F. Stemme (IMF-III, KIT - Campus North).

Fig. 2.3: Image of the X-ray diffractometer XRD D5000 from Bruker-AXS/Siemens (source: http://www.bruker-axs.com).

2.2.3.3 Scanning electron microscopy

Scanning electron microscopy (SEM) was used to study the surface morphology (grain shape and size) of the deposited ITO thin films. SEM is a microscopic technique that enables imaging of a sample surface by detecting the emission of electrons and other electromagnetic radiation resulting from the interactions of a focused electron beam with its surface [305, 306].

Typically, in an evacuated chamber, a highly energetic (~ 0.5–50 keV) electron beam is first generated by a field emission gun consisting of a thermally-assisted Schottky type emitter, and then focused onto the surface of a sample by a set of condenser lenses to a nanometric-sized (~ 0.5–5 nm) spot. Finally, the electron beam goes through pairs of deflector plates which direct the beam along the x and y axes, and enable raster scan-

ning over a rectangular area of the sample surface. When the primary electrons interact with the surface, the electrons lose energy by random scattering and absorption within a teardrop-shaped volume, whose extent (0.1–5 μm) depends primarily on the primary electron energy and the material density. The interactions between the electron beam and the sample usually result in the emission of electrons and electromagnetic radiation such as primary back-scattered electrons, low energy (< 50 eV) secondary electrons, and characteristic X-rays, each of which can be detected with specialized detectors. Back-scattered electrons are electrons that are reflected from the sample by elastic scattering, while secondary electrons are electrons ejected from the k orbitals by inelastic scattering with primary electrons. Characteristic X-rays are emitted when the electron beam removes an inner shell electron from the sample, thus causing a higher energy electron to fill the shell. Among all these detection modes, the secondary electrons are generally used for topography imaging.

Due to their low energy, these electrons are emitted within a few nanometers from the sample surface. The detection of secondary electrons is done with a coupled scintillator-photomultiplier system. The secondary electrons are first collected by a low positively-biased grid, and then further accelerated towards a highly positively-biased scintillator where they can be converted to photons through cathodoluminescence. The photons are then guided to a photomultiplier tube for amplification. The amplified electrical signal output is subjected to analog-to-digital conversion and displayed as a two-dimensional intensity distribution that can be viewed on a computer monitor. The brightness of the signal depends on the number of secondary electrons reaching the detector. If the beam enters the sample perpendicular to the surface, then the activated region is uniform about the axis of the beam and a certain number of electrons "escape" from within the sample. As the angle of incidence increases, the "escape" distance of one side of the beam will decrease, and more secondary electrons will be emitted. Thus steep surfaces and edges tend to be brighter than flat surfaces, which results in images with a well-defined, three-dimensional appearance.

SEM micrographs of ITO thin films were recorded with a scanning electron microscope (Zeiss Supra 55, Carl Zeiss NTS, Germany) equipped with a Schottky field emission source (V_{acc} = 0.1-30 kV) and an Everhart-Thornley secondary electron detector (Fig. 2.4). Depending on the chosen resolution (magnification: 10–$10^6\times$), the accelerating voltage was set in the range 5.0–7.5 kV and the working distance in the range 2.9–4.6 mm. The resolution is 1.7 nm at 1 kV. These measurements were performed in collaboration with U. Geckel (IMF III, KIT - Campus North).

2.2.3.4 Atomic force microscopy

Atomic force microscopy (AFM) in contact mode was used to assess the surface roughness and topography of the deposited ITO thin films. AFM is a microscopic technique that enables imaging of a surface by bringing a cantilever parallel to the surface and then measuring the deflections which result from the interaction between its tip and the surface [307, 308].

Typically, the simplest arrangement of an AFM is composed of a light source, a cantilever with a force-sensing tip, a piezoelectric scanner, and a detector. The cantilever has a sharp tip attached to its free end and is brought in proximity to the surface of a sample. As the interaction (either attractive or repulsive) forces between the cantilever tip and the sur-

Fig. 2.4: Image of the scanning electron microscope Supra 55 from Zeiss (source: http://www.zeiss.de).

face varies, deflections (either positive or negative) are produced on the cantilever. The deflections of the cantilever Δz are proportional to the force acting on the tip, derived via Hooke's law, $F = -k\Delta z$, where k is the spring constant of the cantilever. The amplitude of these deflections is measured by means of a laser beam, which is reflected on the back side of the cantilever and detected by a photodiode divided into four quadrants (A, B, C, and D). If the laser beam is displaced vertically between the bottom (C-D) and top (A-B) quadrants, then a bending force is exerted on the cantilever which is due to topography; in contrast, if the beam is displaced horizontally between the left (A-C) and right (B-D) quadrants, then a torsion force is present due to friction of the cantilever with the surface. These deflections can be used to generate either a depth profile that shows the vertical deviations along the surface or, by scanning the sample laterally, a topographic image of the surface. For these two types of measurements, the AFM is usually operated in the contact mode. In this mode, the cantilever is held less than a few angstroms from the sample surface, and the interaction forces between the cantilever and the sample are repulsive. The tip either scans under conditions of constant (but small) height above the surface or of constant force. In the constant height mode, the height of the tip is held fixed, whereas in the constant force mode, the deflection of the cantilever is fixed and the motion of the scanner in the z-direction is recorded.

The amplitude of the vertical deviations is normally used to calculate the surface roughness, which is best described by the root-mean-square amplitude defined as

$$A_{\mathrm{rms}} = \sqrt{\frac{1}{n}\sum_{k=1}^{n} A_k^2}, \tag{2.9}$$

where A_k is the amplitude value of the k-th vertical deviations.

AFM depth profiles and topographic images of the ITO thin films were obtained with a stand-alone AFM (MFP-3D, Asylum Research) (Fig. 2.5). These measurements were performed in collaboration with C. Azucena (IFG, KIT - Campus North).

Fig. 2.5: Image of the atomic force microscope MFP-3D-BIO from Asylum Research (source: http://www.asylumresearch.com).

2.2.3.5 Four-point probe resistivimetry

Four-point probe (FPP) resistivimetry has been applied to determine the sheet resistivity of the ITO thin films. FPP is a technique that permits to obtain the sheet resistance and/or sheet resistivity of a thin film deposited on a substrate, whether it be conductive or insulating, by measuring the potential difference between metallic probes in contact with its surface [309].

Generally, for equally spaced, collinear conducting probes contacting the surface of an uniform conducting film with an infinite lateral extent and thickness t, deposited on an insulating substrate, the sheet resistivity of the film is given by [310, 311]

$$\rho_s = G\frac{\Delta V}{I}, \tag{2.10}$$

where ΔV denote the measured potential difference, I, the injected current, and G is a geometrical correction factor (with units of length) which depends on the measurement geometry i.e., probe spacing (d), lateral dimensions (shape) and thickness of the sample, and the position of the probes relative to the sample edges [312]. For measurements on a sample for which the lateral extent is much larger than the probe spacing, the correction factor is a function only of d and t, with different forms, depending on whether the substrate is, respectively, insulating or conducting.

For films with rectangular dimensions a and b, Eq. (2.10) transforms to [313]

$$\rho_s = 2\pi t G \left(\frac{\Delta V}{I}\right), \tag{2.11}$$

with

$$G(a, b, d, t) = \frac{F(\tau)}{\tau} C \left(\frac{b}{d}, \frac{a}{b}\right), \tag{2.12}$$

and [310, 311]

$$F(\tau) \approx \frac{\pi}{2 \ln\left(\frac{\sinh \tau/2}{\sinh \tau}\right)}, \tag{2.13}$$

where $\tau \equiv t/d$ and C denotes a factor depending on film dimensions.

For thin films ($\tau \ll 1$), larger than the probe spacing ($b/d \gg 1$), Eq. (2.11) reduces to

$$\rho_s = \frac{\pi t}{\ln 2} \left(\frac{\Delta V}{I}\right). \tag{2.14}$$

Equivalently, one can define the sheet resistance such as

$$R_s = \frac{\rho_s}{t} = \frac{\pi}{\ln 2} \left(\frac{\Delta V}{I}\right) \approx 4.532 \left(\frac{\Delta V}{I}\right). \tag{2.15}$$

A typical FPP setup usually consists of a sample platform, an overhead air-pumped lever arm holding a probe head with four collinear, equally spaced, partly retractable metallic tips, and a combined source meter/multimeter connected to the probe head. The probe tips are brought in close contact with the sample and pressed down by the lever. An electrical current is then instantaneously injected between the two outer probes (P_1 and P_4), and the potential is measured between the two inner probes (P_2 and P_3) with a voltmeter with a high input impedance.

The sheet resistance of ITO thin films was measured with a commercial Alessi FPP system (Alessi Industries, USA) equipped with a probe head type 545 with WC probe tips (0.050" (1.27 mm) tip spacing, 0.005" (0.13 mm) tip radius, 40–70 g/tip spring pressure) (Figs. 2.6 and 2.7). The system was calibrated with a one-sided ITO-coated glass wafer (with an intermediate SiO_2 passive layer) of known sheet resistance (CEC020S, Präzision Glas & Optik, Germany; 100 nm ITO, $R \leq 20\ \Omega$, $R_s = 15\ \Omega/\square$). The resistance readout was recorded on a digital multimeter in a four-wire resistance arrangement (Keithley 2001,

Keithley Instruments, Germany; range: 20 Ω–200 kΩ, resolution: 1 $\mu\Omega$–10 mΩ). These measurements were performed at IMF-III (KIT - Campus North).

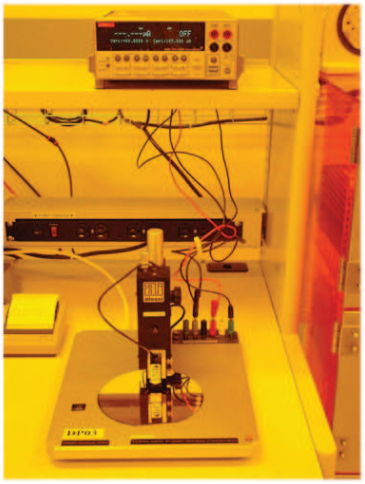

Fig. 2.6: Image of the Alessi FPP system (source: U. Geckel (IMF-III, KIT - Campus North).

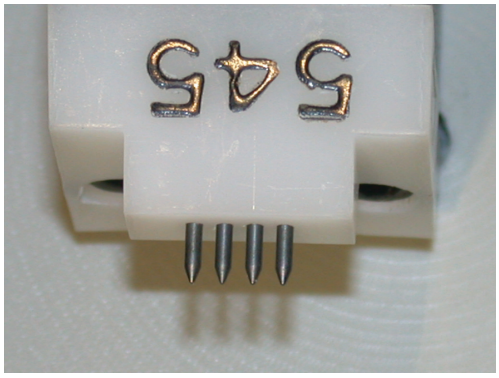

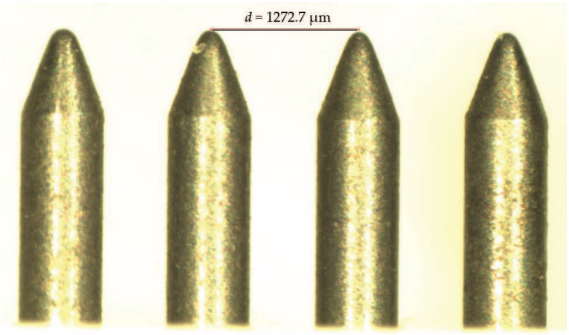

Fig. 2.7: Images of the Alessi FPP probe head. (a) Probe head 545, (b) WC probes with spacing $d = 1272.7$ μm (source: U. Geckel (IMF-III, KIT - Campus North)).

2.2.3.6 Spectroscopic ellipsometry

Spectroscopic ellipsometry (SE) has been used to determine the optical properties (refractive index and extinction coefficient) as well as thickness of deposited ITO thin films. SE is a spectroscopic technique which enables determining the optical properties and thickness of thin films deposited on substrate by measuring in a spectral range extending from the UV to NIR the changes in polarization and intensity of a light beam upon reflection on its surface, provided that the latter is sufficiently reflective [314].

The polarization state of a light beam propagating in a medium can be specified by the orientation taken by its associated electric field at a given point in space. Usually, for

a transversal electric field, the polarization direction is perpendicular to the direction of propagation. The electric field may be oriented or polarized in a single direction (linear polarization) or, more generally, it may rotate with propagation (elliptical polarization). Upon reflection on a surface at the boundary between two different media, the polarization state of a light beam will change. By convention, the plane spanned by the incident and reflected beams is called the plane of incidence. Typically, the polarization state of the light beam incident upon the sample can be resolved into p- and s-polarized components i.e., polarized in a plane parallel and perpendicular to the plane of incidence, respectively.

The electric fields of the incident and reflected beams can then be conveniently represented by a two-component complex vector (also called Jones vector) such as [315]

$$\mathbf{E}_\alpha = \begin{bmatrix} E_{0\alpha}^p e^{i\delta_\alpha^p} \\ E_{0\alpha}^s e^{i\delta_\alpha^s} \end{bmatrix}, \tag{2.16}$$

where $E_{0\alpha}^\beta$ and δ_α^β $(\alpha = i, r; \beta = p, s)$ denote the amplitude and phase of the respective electric fields.

The reflective properties of a sample are given by the so-called Fresnel reflection coefficients. These are complex quantities that account for the changes in amplitude and phase of the reflected fields relative to the incident fields. For a system composed of three isotropic media such as a film (M_j) of thickness (d_j) embedded between an ambient medium (M_i) and a substrate medium (M_k), the global Fresnel reflection coefficients for p- and s-polarized beams can be written such as [316]

$$R^\beta = \frac{r_{ij}^\beta + r_{jk}^\beta e^{-2i\delta}}{1 + r_{ij}^\beta r_{jk}^\beta e^{-2i\delta}} \quad (\beta = p, s), \tag{2.17}$$

with the local Fresnel reflection coefficients given by

$$r_{ij}^\beta = \frac{\tilde{n}_j \cos\theta_i - \tilde{n}_i \cos\theta_j}{\tilde{n}_j \cos\theta_i + \tilde{n}_i \cos\theta_j}, \tag{2.18a}$$

$$r_{jk}^\beta = \frac{\tilde{n}_k \cos\theta_j - \tilde{n}_j \cos\theta_k}{\tilde{n}_k \cos\theta_j + \tilde{n}_j \cos\theta_k}, \tag{2.18b}$$

and the film phase delay given by

$$\delta = 2\pi \frac{d_j}{\lambda} \tilde{n}_j \cos\theta_j, \tag{2.19}$$

where $\widetilde{n}_\gamma = n_\gamma + ik_\gamma$ and θ_γ $(\gamma = i, j, k)$ are the (potentially) complex refractive indices and incident angles in the corresponding medium and λ is the beam wavelength.

The changes in amplitude and phase upon reflection from the ambient-film-substrate system can be defined by the (complex) ellipsometric ratio defined as

$$\rho = \frac{R^s}{R^p} = \tan\Psi e^{i\Delta}, \tag{2.20}$$

where Δ and Ψ represent the so-called ellipsometric angles.

The functional dependence of Δ and Ψ on the optical parameters can be written symbolically such as

$$\tan\Psi e^{i\Delta} = \rho(n_\gamma, k_\gamma, d_j, \theta_i, \lambda) \quad (\gamma = i, j, k), \tag{2.21}$$

or, more explicitly, such as

$$\Psi = \tan^{-1}|\rho(n_\gamma, k_\gamma, d_j, \theta_i, \lambda)| \quad (\gamma = i, j, k), \tag{2.22a}$$
$$\Delta = \arg[\rho(n_\gamma, k_\gamma, d_j, \theta_i, \lambda)], \tag{2.22b}$$

where $|\rho|$ and $\arg(\rho)$ are the amplitude and phase of the complex function ρ.

As can be seen from Eqs. (2.22), in general, for an ambient-film-substrate system, the optical parameters from the film cannot be extracted analytically from the measured angles Ψ and Δ angles. This is the well-known inversion problem of ellipsometry. To circumvent this problem, the system has to be modeled as a layered media in which each individual layer can be define by an optical model which provides the optical constants and thickness parameters. Such models include, among others, Cauchy model for non-absorbing media like glass and crystals, and Drude-Lorentz models for more absorbing media like metals and semiconductors. By keeping fixed the optical constants of the substrate medium which are usually well-known over the chosen spectral range, and by providing a suitable optical model for the specified film, the computational problem reduces to searching iteratively the set of values for the unknown optical film parameters through a least-square minimization or mean-square error (MSE) defined by

$$\mathrm{MSE} = \sqrt{\frac{1}{2N - M}\sum_{k=1}^{N}\left[\left(\frac{\Delta_k^{\mathrm{mod}} - \Delta_k^{\mathrm{exp}}}{\sigma_{\Delta,k}^{\mathrm{exp}}}\right)^2 + \left(\frac{\Psi_k^{\mathrm{mod}} - \Psi_k^{\mathrm{exp}}}{\sigma_{\Psi,k}^{\mathrm{exp}}}\right)^2\right]}, \tag{2.23}$$

where N is the number of data points, M is the number of the fitting parameters, (Δ^{exp}, Ψ^{exp}) and (Δ^{mod}, Ψ^{mod}) are the sets of experimentally measured and modeled ellipsometric angles, respectively, while $\sigma_{\Psi}^{\mathrm{exp}}$ and $\sigma_{\Delta}^{\mathrm{exp}}$ are the standard deviations of the measured ellipsometric angles. The modeled ellipsometric angles are functions of all the fitting parameters which define the multilayer optical models. The values of Δ^{mod} and Ψ^{mod} which best match the experimental data (or which gives the least MSE) provide the optical constants and thickness parameters of the film.

The simplest experimental setup of a spectroscopic ellipsometer consists of two arms, an emission arm and a detection arm, fixed on a goniometer, and a sample holder fixed on its rotational axis. Both arms are fixed at an angle θ with respect to the normal to the sample surface. The emission arm includes a broad light source (covering UV to NIR), a polarizer (P), and a compensator (C) (e.g., a quarter-wave plate), whereas the detection arm includes an analyzer (A), and a detector. The analyzer and polarizer enables transmission or extinction of linearly polarized light, while the compensator introduces a defined phase retardation of one field component relative to the other. In this configuration, the light intensity at the detector is given by [316]

$$I_D(t) \propto \langle |E_{0x}|^2 + |E_{0y}|^2 \rangle, \tag{2.24}$$

with

$$E_{0x} = \cos\theta_A[\cos\theta_C \cos(\theta_P - \theta_C) - \rho_C \sin\theta_C \sin(\theta_P - \theta_C)], \tag{2.25a}$$
$$E_{0y} = \sin\theta_A[\sin\theta_C \cos(\theta_P - \theta_C) + \rho_C \cos\theta_C \sin(\theta_P - \theta_C)], \tag{2.25b}$$

where $\theta_A, \theta_C, \theta_P$ represent the azimuthal angles of A, C and P, and $\rho_C = \tau_C e^{i\delta_C}$ is the retardance of C, and τ_C and δ_C are its associated transmittance and phase delay.

This setup allows for the determination of the ellipsometric angles in various operational modes, among which the nulling mode as the most commonly employed. In this mode, the ellipsometric angles are determined by finding a set of azimuthal angles for A, C, and P such that the light intensity at the detector vanishes. Hence, an incident light beam in any given elliptical state of polarization, which becomes linearly polarized upon reflection, can be completely extinguished with an analyzer. Under the nulling condition ($I_D = 0$), one obtains from Eqs. (2.24) and (2.25) that

$$\rho = \frac{R^p}{R^s} = \frac{E_{0x}}{E_{0y}} = -\tan\theta_A \frac{\tan\theta_C - \rho_C \tan(\theta_P - \theta_C)}{1 - \rho_C \tan\theta_C \tan(\theta_P - \theta_C)}. \tag{2.26}$$

When an ideal quarter-wave plate ($\tau_C = 1, \delta_C = \pi/2 \Rightarrow \rho_C = -i$) is used as compensator and its azimuthal angle is fixed ($\theta_C = \pm 45^\circ \Rightarrow \tan\theta_C = 0$), Eq. (2.26) then simplifies to

$$\rho = \tan\Psi e^{i\Delta} = \mp \tan\theta_A e^{i(\mp 2\theta_P + \pi/2)} \qquad (\theta_C = \pm 45^\circ). \tag{2.27}$$

For each compensator azimuthal angle, two sets of nulling angles can be found, namely, $(\theta_A^{\mathrm{I}}, \theta_P^{\mathrm{I}})$ and $(\theta_A^{\mathrm{III}}, \theta_P^{\mathrm{III}})$ for $\theta_C = -45^\circ$ and $(\theta_A^{\mathrm{II}}, \theta_P^{\mathrm{II}})$ and $(\theta_A^{\mathrm{IV}}, \theta_P^{\mathrm{IV}})$ for $\theta_C = 45^\circ$. These sets are called conjugate zones (I and III, II and IV). Each set is related to the other by the relations

$$\theta_P^{\mathrm{III/IV}} = \theta_P^{\mathrm{I/II}} + 90^\circ, \tag{2.28a}$$

$$\theta_A^{\mathrm{III/IV}} = 90^\circ - \theta_A^{\mathrm{I/II}}. \tag{2.28b}$$

Although a single set of nulling angles can be used to determine ρ, two-zone measurements are usually performed and averaged to eliminate the effects of component imperfections and azimuthal angles errors.

The ellipsometric measurements were performed on ITO thin films with a variable angle spectroscopic ellipsometer (SENpro SE400, SENTECH Instruments, Germany) (Fig. 2.8). Ellipsometric angles Δ and Ψ were acquired at a fixed incident angle (70°) [5] over the spectral range 370–1050 nm in steps of 10 nm. Optical modeling and optical parameters as well as thickness determination were done using SENpro analysis software (SENTECH Instruments).

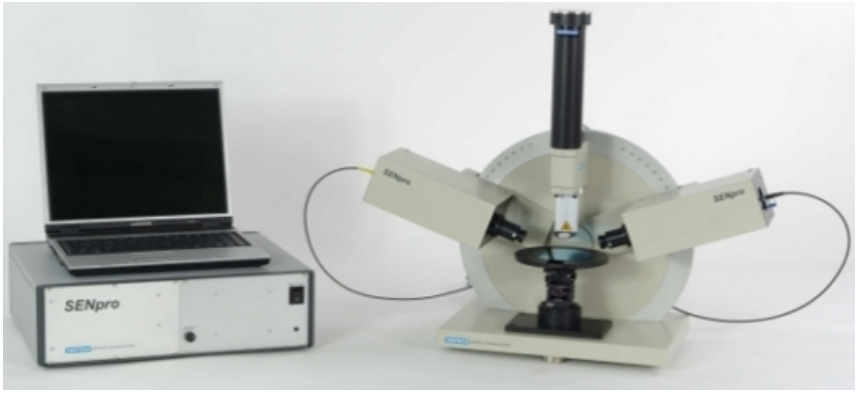

Fig. 2.8: Image of the variable angle spectroscopic ellipsometer SENpro SE400 system from SENTECH Instruments (source: http://www.sentech.de).

2.2.3.7 Ultraviolet-visible-near infrared absorption spectroscopy

UV-VIS-NIR absorption spectroscopy can be used to obtain the absorbance spectrum of a compound in solution or as a solid [317].

5. This angle is best-suited since it is approximately the pseudo-Brewster angle for ITO, where the sensitivity is high since $\Delta \to 90^\circ$.

UV-VIS-NIR spectroscopy considers the absorption of radiation by atoms or molecules as a consequence of transitions among the energy states of their outer shell electrons. Hence, when an atom or molecule absorbs photon energy, electrons are promoted from their ground state to an excited state. In a molecule, the atoms can rotate and vibrate with respect to each other. These vibrations and rotations also generate sets of discrete energy levels, which then stack up on top of each electronic level. In addition, the assembly of a large number of atoms into lattices to form a solid produces a large number of molecular orbitals with small energy differences, which lead to the formation of a continuous bands of energy separated by an energy (band)gap. Several types of electronic transitions exist including those within the same atom (e.g., transitions involving p and s orbitals), between two neighboring atoms (charge transfer transition), and between valence and conduction bands (bandgap transition in semiconductors).

Typically, the UV-VIS spectrum of most molecules and solids consists of a few broad bands rather than sharp absorption lines. These bands indicate that an electronic level transition is usually accompanied by a simultaneous change between the more numerous vibrational levels. In fact, a photon with too low or too high energy for an electronic transition can instead be absorbed for a transition between one of the vibrational levels associated with the lower electronic state to one of the vibrational levels of a higher electronic state. Moreover, the mutual interactions between lattice atoms in a solid or between closely packed molecules bring already numerous energy levels closer together, which results in the broadening of sharp lines into bands. The resulting spectrum is thus dependent on some relevant physico-chemical parameters of the material such as, for example, chemical composition, oxidation state, and band structure.

When a monochromatic light beam passes through a certain thickness of a material, whether it may be a liquid enclosed in a transparent cell or a solid, the intensity of the transmitted beam may be much smaller than that of the incident beam, owing to the absorption of the material. With a change in wavelength, the amount of absorption will also be changed to a lesser or greater extent. The absorption of light by a given material at a particular frequency can be described according to an exponential law given by

$$I_t(\nu) = I_i(\nu)e^{-\alpha(\nu)d}, \tag{2.29}$$

where $I_i(\nu)$ and $I_t(\nu)$ are the incident and transmitted light intensities at frequency ν, respectively, d, the thickness of the material, and α, the absorption (or attenuation) coefficient, characteristic of the material.

The adsorption coefficient $\alpha(h\nu)$ for a given photon energy $E_{\text{phot}} = h\nu$ is given by

$$\alpha(h\nu) = \sum P_{if} n_i n_f, \tag{2.30}$$

where P_{if} represents the probability for a transition from an initial state i to a final state f, while n_i and n_f are densities of electrons in the initial and final states, respectively. The

summation is taken over all possible transitions with an energy difference equal to $h\nu$.

As mentioned previously, the assembly of atoms in a solid leads to the formation of a band structure which consists of a lower (or valence) band and an upper (or conduction) band separated by an energy gap whose extent determines whether the solid is a conductor (metal), semiconductor, or an insulator. The valence band can contain has many states as electrons, and hence can be completely filled, whereas the conduction band may contain no electron at all or fewer electrons than states. For a conductor, no energy gap exists ($E_g = 0$) and the conduction band is densely populated with electrons ($\rho_e \sim 10^{23}$ cm^{-3}), while for semiconductor, $E_g \lesssim 3$ eV and the electron density in the conduction band (or the hole density in the valence band) is slightly lower ($\rho_e \sim 10^{20}$ cm^{-3}). Finally, for an insulator, $E_g \gtrsim 3$ eV and almost no electrons can be found in the conduction band (and practically no holes in the valence band).

For semiconductors, a description of electronic transitions can be adequately described by an energy-momentum (E–$\mathbf{k}$) diagram in which a transition obey both energy and momentum must be conserved. Depending upon the relationship between the momentum in the initial and final states (which, in turn, depends on the energy-momentum profile), direct and indirect transitions occurs. By using a parabolic energy profile, an expression of $\alpha(h\nu)$ for each type of transition is given in the general form

$$\alpha(h\nu) \propto \frac{(E_p - E_g)^n}{h\nu} = \begin{cases} n = 1/2, & \text{direct transition} \\ n = 2, & \text{indirect transition} \end{cases}. \tag{2.31}$$

In both cases, the absorption caused by the electronic interband transition can be used to determine E_g by locating the intercept of the straight line obtained through the plot $[\alpha(h\nu)h\nu]^{1/2}$ vs $h\nu$ (also known as Tauc plot) [318].

A semiconductor usually exhibits minimal optical absorption for photons with energies smaller than the bandgap and high absorption for photons with energies greater than the bandgap. As a result, there is a sharp increase in absorption at energies close to the bandgap that manifests itself as an absorption edge in the UV-VIS absorbance spectrum.

The basic experimental setup of a UV-VIS-NIR spectrophotometer includes interchangeable UV and VIS light sources (usually deuterium and tungsten-halogen lamps), a sample holder, a monochromator based on one or two dispersing elements (e.g., gratings), and a CCD detector. The monochromator works as a diffraction grating that disperses the transmitted light beam into its various wavelengths towards the detector.

The transmittance of the ITO films in the UV to NIR spectral range was measured using a commercial UV/VIS high-resolution spectrophotometer (HR2000+, Ocean Optics, Germany) based on a symmetrical crossed Czerny-Turner design. Input and output UV-VIS light beams are provided by a balanced deuterium tungsten-halogen light source (DH-2000-BAL, Ocean Optics) and transmitted through two steel-jacketed optical fibers (QP400-2-SR-BX, Ocean Optics; 400 μm core diameter) optimized for transmission in the spectral range 200-–1100 nm. All spectra were recorded and processed using the SpectraSuite software (Ocean Optics). The absorbance spectra were taken as the negative

logarithmic ratio of background-corrected signals coming from ITO-coated (sample) and bare CaF_2 plates (reference).

2.2.3.8 Fourier-transformed infrared absorption spectroscopy

Fourier-transformed infrared absorption spectroscopy (FTIR) has been used to measure the transmittance spectrum of the ITO thin films in the NIR to MIR range. FTIR is a linear spectroscopic technique which permits finding the absorption of IR radiation caused by resonance of molecular vibrational modes simply by measuring the intensity of an IR beam before and after its interaction with a sample [319].

IR spectroscopy considers the absorption of IR radiation by molecules at specific frequencies as a consequence of a resonant excitation of some of their bonds. These frequencies are thus related to the strength of the bonds, and to the masses of the atoms that build them. A simplified but adequate description of the vibrations of diatomic molecules is given by the harmonic oscillator model, which assumes atoms as point masses connected by spring-like forces. Hence, for small bond length variations (compression or extension), the bond strength or restoring force obeys Hooke's law given by

$$F(\mathbf{r}) = -\nabla V(\mathbf{r}) = -k\Delta r, \tag{2.32}$$

with the bond variation from the equilibrium bond length r_e defined as

$$\Delta r = r - r_e, \tag{2.33}$$

where V is the potential energy and k denotes the force constant, the magnitude of which reflects the bond strength.

By integration of Eq. (2.32), one obtains the corresponding potential such as

$$V(r) = \frac{1}{2}kr^2, \tag{2.34}$$

which follows a parabolic (or harmonic) profile.

Since these motions happen on a microscopic scale, the possible energy eigenvalues E_ν of the vibrational modes follow the Schrödinger equation given by

$$\widehat{H}\psi_\nu(r) = E_\nu\psi_\nu(r), \tag{2.35}$$

with the quantum-mechanical Hamiltonian operator defined as

$$\widehat{H} = -\frac{\hbar^2}{2\mu}\nabla^2 + V(r), \tag{2.36}$$

where ψ_ν is the vibrational wave function of a given state ν that describes the system.

The energy eigenvalues of the vibrations of the harmonic oscillator can be shown to be

$$E_\nu = \left(n + \frac{1}{2}\right) hc\overline{\nu} \quad (n = 0, 1, 2, \ldots), \tag{2.37}$$

with the vibrational wavenumber given by

$$\overline{\nu} = \frac{1}{2\pi c}\left(\frac{k}{\mu}\right)^{1/2}, \tag{2.38}$$

where $\mu = m_1 m_2/(m_1 + m_2)$ is the reduced mass of the diatomic molecule with masses m_1 and m_2, n, the vibrational quantum number, and h is the Planck constant (6.62610×10^{-34} J·s).

The selection rules of IR spectroscopy state whether a molecule can be excited from one vibrational state to another. The IR transition moment for a transition from a lower to an upper state with vibrational wave functions $\psi^l_\nu(r)$ and $\psi^u_\nu(r)$, respectively, is given by

$$\mathbf{R}_\nu = \int \psi^u_\nu(r)\boldsymbol{\mu}\psi^l_\nu(r)dr, \tag{2.39}$$

where $\boldsymbol{\mu}$ is the dipole moment operator.

For a heteronuclear diatomic molecule, $|\boldsymbol{\mu}| \neq 0$ and it can be expressed as a Taylor series expansion

$$\boldsymbol{\mu}(r) = \boldsymbol{\mu}(r_e) + \sum_k^\infty \frac{1}{k!}\left(\frac{d^k\boldsymbol{\mu}}{dr^k}\right)\Bigg|_{r=r_e} r^k, \tag{2.40}$$

such that the transition moment in Eq. (2.39) becomes

$$\mathbf{R}_\nu = \boldsymbol{\mu}(r_e)\int \psi^{u\,*}_\nu(r)\widehat{\boldsymbol{\mu}}\psi^l_\nu(r)dr + \sum_k^\infty \frac{1}{k!}\left(\frac{d^k\boldsymbol{\mu}}{dr^k}\right)\Bigg|_{r=r_e}\int \psi^{u\,*}_\nu(r)r^k\psi^l_\nu(r)dr. \tag{2.41}$$

Making use of the orthogonality of the wave functions which states that

$$\int \psi_\nu^u{}^*(r)\psi_\nu^l(r)dr = 0 \quad (\nu_l \neq \nu_u), \tag{2.42}$$

the transition moment then simplifies to

$$\mathbf{R}_\nu = \sum_k^\infty \frac{1}{k!}\left(\frac{d^k\boldsymbol{\mu}}{dr^k}\right)\Bigg|_{r=r_e} \int \psi_\nu^u{}^*(r)r^k\psi_\nu^l(r)dr, \tag{2.43}$$

with the first term of the series being non-zero only if $\Delta\nu = \pm 1$, thereby giving the vibrational selection rule.

Accordingly, the intensity of the IR transition moment is given by

$$I_{\mathrm{IR}} \propto |\mathbf{R}_\nu|^2 \approx \left(\frac{d\boldsymbol{\mu}}{dr}\right)^2\Bigg|_{r=r_e}. \tag{2.44}$$

Hence, the intensity of an IR absorption band depends on the change of the dipole moment associated with the vibration.

The basic experimental arrangement of a FTIR spectrometer consists of an IR light source, a Michelson interferometer, and an IR detector. Typically, an IR beam is split into two beams by a partially transmitting mirror, one of them is reflected off a fixed mirror, the other on a moving mirror. The different paths of the two beams introduces a retardation δ and, in turn, a phase difference $\phi = \omega\delta/c$. For a monochromatic light source, the two beams will interfere constructively and destructively when $\delta = n\lambda$ and $\delta = (n+1/2)\lambda \quad (n = 0, 1, 2, \ldots)$, respectively. Hence, the intensity varies as $I(\delta) \propto \cos(2\pi\overline{\nu}\delta)$. For a broadband light source, constructive interference occurs for different optical retardation. The intensity originates from numerous cosine functions of different wavelengths and can be written as

$$I_{\mathrm{IR}}(\delta) = \int_0^\infty I_s(\overline{\nu})[1 + \cos(2\pi\overline{\nu}\delta)]d\overline{\nu}, \tag{2.45}$$

where $S(\overline{\nu})$ is the intensity of the source.

The IR spectrum is then obtained by inverse Fourier transform of Eq. (2.45) such as

$$I_{\mathrm{IR}}(\overline{\nu}) = 2 \int_0^{\infty} I_{\mathrm{IR}}(\delta) e^{-2i\pi\overline{\nu}\delta} d\delta. \tag{2.46}$$

Since both the sample and the light source are contributing to the resulting spectrum, a reference spectrum $I_0(\overline{\nu})$ is usually recorded. The absorbance (A) and transmittance (T) are then calculated by

$$A(\overline{\nu}) = -\log_{10} \frac{I(\overline{\nu})}{I_0(\overline{\nu})} = \log_{10} \frac{I_0(\overline{\nu})}{I(\overline{\nu})} = -\log_{10} T(\overline{\nu}). \tag{2.47}$$

The reflectance and transmittance spectra of deposited ITO thin films in the NIR and MIR ranges were obtained on a FTIR spectrometer (Vertex 70, Bruker Optics, Germany) using p-polarized light and a liquid nitrogen-cooled mercury cadmium telluride (MCT) detector (Fig. 2.9). The variable angle section IRRAS sample stage was usually adjusted to an incident angle of 70°. The IR spectra was recorded and processed with the OPUS software (Bruker Optics).

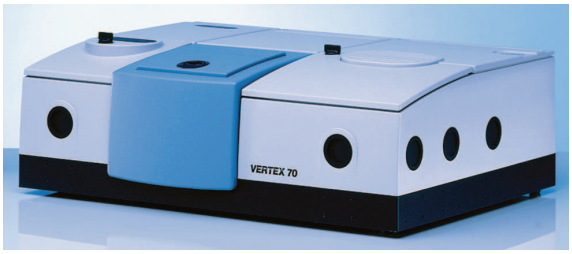

Fig. 2.9: Image of the FTIR spectrometer Vertex 70 from Bruker Optics (source: http://www.brukeroptics.com).

2.2.4 Characterization of ITO/aqueous solution interfaces

2.2.4.1 Vibrational sum-frequency-generation spectroscopy

Vibrational SFG spectroscopy is a surface-sensitive, nonlinear spectroscopic technique in which two intense IR and VIS light beams, coincident spatially and temporally at an interface, generate another light beam at the sum-frequency in a defined direction. In addition, if the frequency of the IR beam corresponds to the frequency of a vibrational mode of adsorbed molecules, then a resonance enhancement of the SFG signal may be observed. Thus, by keeping the frequency of the VIS beam fixed and by scanning that of the IR beam, a surface-specific vibrational spectrum of molecules adsorbed at an interface can be obtained. The selection rules of this second-order nonlinear process dictate that the SFG signal can only be generated in a non-centrosymmetric environment. This feature makes vibrational SFG spectroscopy inherently surface-specific as any signal contribution from the adjacent, bulk isotropic media are to a large extent suppressed.

The existence of SFG and other nonlinear optical processes has been first demonstrated in 1961 by Franken *et al*. [320] followed by others [321–323] in the bulk of dielectric crystals, shortly after the discovery of the ruby laser. The theoretical basis of these processes in the bulk and at interfaces has been laid down also in the 1960's by Bloembergen and Pershan [324, 325]. The first experimental application of the SFG process as a surface vibrational spectroscopy of molecular adsorbates was developed independently by the groups of Shen [326–328] and Harris [329]. Since then, vibrational SFG spectroscopy has been applied to the investigation of various molecules adsorbed to different types of interfaces such as, for instance, gas/solid [330], gas/liquid [94, 331–337], liquid/liquid [338, 339], solid/liquid interfaces [340, 341] as well as buried [342–345] and electrochemical [346, 347] interfaces.

A more detailed treatment on the practical and theoretical aspects of vibrational SFG spectroscopy can be found in numerous review articles [348–355], book sections [356–363], and books [364–370] of nonlinear optics and nonlinear optical spectroscopy. Hence, only a short overview of vibrational SFG spectroscopy will be given here.

2.2.4.1.1 SFG theory

A. Nonlinear optical response and SFG process

When a light beam interacts with the bulk or with the surface of a given medium, the applied electric field polarizes the material i.e., it exerts a force on the valence electrons and displaces them relative to the nucleus, thereby creating induced dipoles. The response of the medium to the applied electric field is called the polarization and can be defined as

$$\mathbf{P} = N\frac{\langle \boldsymbol{\mu} \rangle}{V}, \tag{2.48}$$

where $\langle \boldsymbol{\mu} \rangle$ denote the average induced dipole moment, N, the number of dipole moments, and V, the volume of the medium considered.

The induced dipole moment $\boldsymbol{\mu}$ can be expanded as a power series of the electric field $\mathbf{E}$ such as

$$\boldsymbol{\mu} = \sum_{k=0}^{\infty} \left(\frac{\partial^{(k)} \boldsymbol{\mu}}{\partial \mathbf{E}^{(k)}} \right) \otimes \mathbf{E}^k = \boldsymbol{\mu}_0 + \boldsymbol{\alpha}^{(1)} \cdot \mathbf{E} + \boldsymbol{\alpha}^{(2)} : \mathbf{E}^2 + \boldsymbol{\alpha}^{(3)} \vdots \mathbf{E}^3 + \ldots, \tag{2.49}$$

with

$$\boldsymbol{\alpha}^{(k)} \equiv \frac{\partial^{(k)} \boldsymbol{\mu}}{\partial \mathbf{E}^{(k)}} \otimes \mathbf{E}^k, \tag{2.50}$$

where $\boldsymbol{\mu}_0$ represents the static (or permanent) dipole moment, and $\boldsymbol{\alpha}^{(k)}$ $(k \geq 1)$ represents the k-th order hyperpolarizabilities [6].

By substituting Eq. (2.49) in Eq. (2.48), the polarization becomes

$$\mathbf{P} = \varepsilon_0 \sum_{k=0}^{\infty} \chi^{(k)} \otimes \mathbf{E}^k = \varepsilon_0 \sum_{k=0}^{\infty} \mathbf{P}^{(k)}, \tag{2.51}$$

where $\chi^{(1)}$ is the linear susceptibility and $\chi^{(k)} = \langle \boldsymbol{\alpha}^{(k)} \rangle$ $(k \geq 2)$ are the k-th order nonlinear susceptibilities.

For low intensity beams with weak applied electric fields, the displacement of the electrons is small and confine in a region that can be approximated by an harmonic (or parabolic) potential. In this case, the polarization responds linearly to the applied electric field (either by absorption, Rayleigh, or Raman scattering) and can be written (ignoring any permanent dipole moment) as

$$\mathbf{P}(\omega) = \varepsilon_0 \chi^{(1)} \mathbf{E}(\omega), \tag{2.52}$$

where ε_0 is the vacuum electric permittivity (8.854×10^{12} F/m). In other terms, the induced polarization field oscillates and emits at the same frequency as the input driving electric field.

For intense light beams such as with pulsed lasers with electric fields comparable to the atomic fields ($\sim 10^{10}$–10^{15} V/m)[7], the displacement of electrons becomes large and the polarization is no longer proportional to the electric field such that additional nonlinear terms must be included such as

$$\mathbf{P}(\omega) = \varepsilon_0 \sum_{k=1}^{\infty} \chi^{(k)} \otimes \mathbf{E}^k(\omega). \tag{2.53}$$

The higher order susceptibilities are usually much smaller in magnitude than the first-order susceptibility (typically, $\chi^{(k)} \sim 1/E_{at}^k$ [m/V]^k for $k \geq 2$).

The electron-atom interactions in the linear regime ($E \ll E_{at}$) can be described satisfactorily with a Lorentz model of the atom which considers the binding potential as harmonic. For the nonlinear regime, this model can be extended by including nonlinear terms in the restoring force exerted on the electron. These two regimes are illustrated in Fig. 2.10. For

6. The second- and third-order hyperpolarizabilities $\alpha^{(2)}$ and $\alpha^{(3)}$ are frequently also noted as β and γ. This notation will be used here interchangeably.

7. In comparison, the atomic field strength of an hydrogen atom gives $E_{at} = e/4\pi\varepsilon_0 r_0^2 \sim 10^{11}$ V/m with the Bohr radius as $r_0 = 4\pi\varepsilon_0\hbar^2/m_e e$ and where $\hbar$ is the reduced Planck constant and m_e is the electron (rest) mass [368].

weak applied electric fields, the binding potential remains harmonic and the induced polarization stays proportional to the incident field, while for stronger electric fields, the binding potential becomes anharmonic and the corresponding polarization can be decomposed into higher-order nonlinear components.

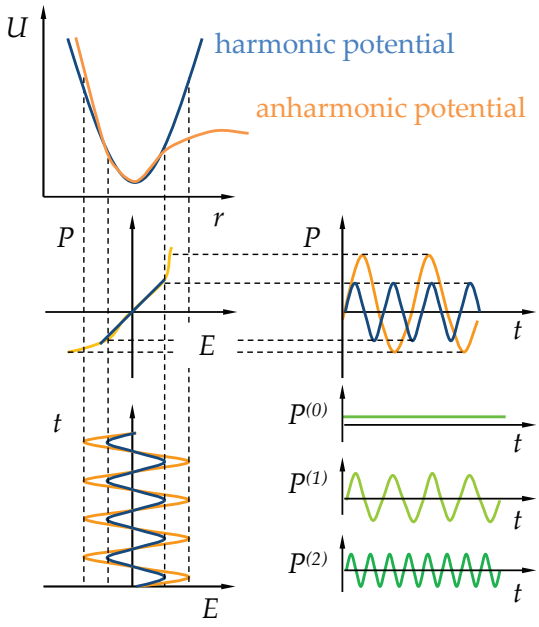

Fig. 2.10: Schematic representation of the nonlinear response of a medium in the linear and nonlinear regimes.

In the case of nonlinear optical processes such as SHG and SFG, the dominant polarization term is of the second-order one and can be written as

$$\mathbf{P}^{(2)}(\omega) = \varepsilon_0 \chi^{(2)} : \mathbf{E}^2(\omega), \tag{2.54}$$

where the second-order nonlinear susceptibility $\chi^{(2)}$ is a third-rank tensor describing the relationship between the applied electric field and the resulting polarization field [8].

An applied electric field with two distinct frequency components incident on a nonlinear optical medium (e.g., two incident laser beams coincident spatially and temporally at an interface) can be written as

8. Generally, the effective polarization field should contain surface as well as volume (bulk) contributions such that $\mathbf{P}^{(2)}_{\text{eff}}(\omega) = \mathbf{P}^{(2)}_S(\omega) + \mathbf{P}^{(2)}_B(\omega)$ with $\mathbf{P}^{(2)}_B(\omega) = \mathbf{P}^{(2)}_D(\omega) - \nabla\cdot\mathbf{P}^{(2)}_Q - (c/i\omega)\nabla\times\mathbf{M} + \ldots$ where $\mathbf{P}^{(2)}_D(\omega)$, $\mathbf{P}^{(2)}_Q(\omega)$, and $\mathbf{M}(\omega)$ are the electric dipolar and quadrupolar polarizations, and magnetization, respectively. Typically, the electric dipole approximation is assumed within which the effects of higher-order electric multipoles and optical magnetic fields can be neglected. However, at a given interface, it is not always known *a priori* whether surface contributions dominate over bulk contributions [371–373].

$$\begin{aligned}\mathbf{E}(\mathbf{r},t) &= \mathbf{E}_1(\mathbf{r},t) + \mathbf{E}_2(\mathbf{r},t) \\ &= (\mathbf{E}_1(\mathbf{r})e^{-i\omega_1 t} + \mathbf{E}_1^*(\mathbf{r})e^{+i\omega_1 t}) + (\mathbf{E}_2(\mathbf{r})e^{-i\omega_2 t} + \mathbf{E}_2^*(\mathbf{r})e^{+i\omega_2 t}),\end{aligned} \tag{2.55}$$

where $\mathbf{E}_\nu \equiv \mathbf{E}(\omega_\nu)$ $(\nu = 1, 2)$.

By substituting Eq. (2.55) in Eq. (2.54), the second-order nonlinear polarization is then given by

$$\mathbf{P}_3^{(2)}(\mathbf{r},t) = \varepsilon_0\chi^{(2)} \begin{bmatrix} 2(\mathbf{E}_1\mathbf{E}_1^* + \mathbf{E}_2\mathbf{E}_2^*) & \text{(OR)} \\ +\mathbf{E}_1^2 e^{-2i\omega_1 t} + (\mathbf{E}_1^*)^2 e^{2i\omega_1 t} & \text{(SHG)} \\ +\mathbf{E}_2^2 e^{-2i\omega_2 t} + (\mathbf{E}_2^*)^2 e^{2i\omega_2 t} & \text{(SHG)} \\ +2(\mathbf{E}_1\mathbf{E}_2^* e^{-i(\omega_1-\omega_2)t} + \mathbf{E}_1^*\mathbf{E}_2 e^{+i(\omega_1-\omega_2)t}) & \text{(DFG)} \\ +2(\mathbf{E}_1\mathbf{E}_2 e^{-i(\omega_1+\omega_2)t} + \mathbf{E}_1^*\mathbf{E}_2^* e^{+i(\omega_1+\omega_2)t}) & \text{(SFG)} \end{bmatrix}. \tag{2.56}$$

As can be seen from Eq. (2.56), several nonlinear optical processes such as optical rectification (OR) (with no frequency dependence) due to static polarization, SHG (at $2\omega_1$ and $2\omega_2$), difference-frequency-generation (DFG) (at $\omega_1 - \omega_2$), and SFG (at $\omega_1 + \omega_2$) contribute to the nonlinear polarization. However, in practice, the predominance or efficiency of any of these nonlinear processes over the others in the generated signal will depend on the so-called phase-matching conditions. When only the SFG process is considered, the SF polarization field can then be written as [9]

$$\mathbf{P}_3^{(2)} = \varepsilon_0\chi^{(2)} : \mathbf{E}_1\mathbf{E}_2, \tag{2.57}$$

where $\mathbf{E}_1$ and $\mathbf{E}_2$ are the two input fundamental electric fields.

B. Inversion symmetry

A simple symmetry consideration reveals that within the dipole approximation, SHG or SFG, cannot occur in a medium with inversion symmetry. This means that the $\chi^{(2)}$ tensor must be invariant under a parity transformation i.e., $\hat{\mathrm{P}}(\chi^{(2)}(\mathbf{r})) = \chi^{(2)}(-\mathbf{r})$ where $\hat{\mathrm{P}}$ is the parity operator defined as $\hat{\mathrm{P}}$: $\mathbf{r} \longmapsto -\mathbf{r}$. In addition, $\chi^{(2)}$ is a polar tensor (a tensor whose components reverse sign with a reversal of coordinates axes) with odd parity, which means that $\chi^{(2)}(\mathbf{r}) = -\chi^{(2)}(-\mathbf{r})$. Therefore, the condition $\chi^{(2)}(-\mathbf{r}) = -\chi^{(2)}(-\mathbf{r})$ needs to be fulfilled for a centrosymmetric medium. Since the only possible solution is $\chi^{(2)} = 0$, it means that in a centrosymmetric medium SFG is forbidden. However, at the interface between two centrosymmetric media (and in the bulk of some non-centrosymmetric crystals), the inversion symmetry is broken and an SFG signal can be generated (Fig. 2.11). For example, adsorbed molecules possess a net orientational order which reflects the asymmetry of the environment. Hence, when probed by SHG or SFG spectroscopy, these

9. Additionally, the factor 2 was removed by taking into account the intrinsic permutation symmetry of the frequencies of the fundamental input electric fields.

molecules generate an inherently surface-specific response.

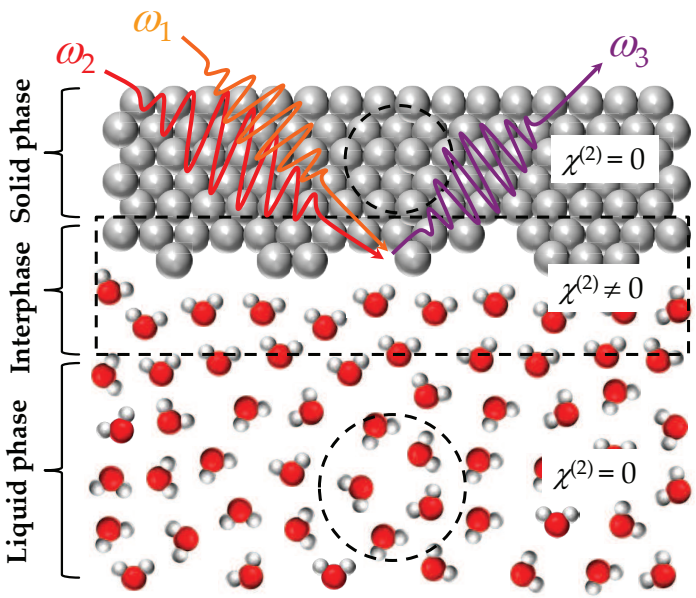

Fig. 2.11: Origin of the nonlinear $\chi^{(2)}$ susceptibility at the solid/liquid interface.

C. Surface SFG phase-matching condition

In order to achieve selectively an SFG process at an interface, the two incident light beams must be coincident spatially and temporally. A coherent SFG signal is subsequently generated at an angle θ_3 to the surface normal, which can be calculated using the conservation of momentum of all three beams parallel to the interface. This rule is known as the phase-matching condition and can be written as

$$k_{3\|} = k_{1\|} + k_{2\|}, \tag{2.58}$$

or, more explicitly, as

$$n(\omega_3)\omega_3 \sin\theta_3 = n(\omega_1)\omega_1 \sin\theta_1 + n(\omega_2)\omega_2 \sin\theta_2, \tag{2.59}$$

where $n(\omega_\nu)$ is the refractive index of the medium for each beam of frequency ω_ν ($\nu = 1, 2, 3$) and θ_ν is the incident or reflected angle relative to the surface normal for each beam. SFG beams are generated in both the reflected and transmitted directions and the more accessible and/or most intense of these two beams is usually detected.

D. Phenomenological models of the interfacial SFG signal

In order to relate the microscopic properties ($\chi^{(2)}$) of any species adsorbed at an interface to the macroscopic experimental data ($I(\omega_3)$), a suitable phenomenological model is required. The problem thus consists in finding a relationship between the intensity of the output SFG field and the intensities of the two input fundamental fields. The first attempt towards this goal was made by Bloembergen and Pershan [325] who considered a nonlinear slab of material, in the limit of zero thickness, as a model for the surface and derived on this basis the nonlinear optical parameters of the interface. Based on this pioneering work, two types of phenomenological models were later developed: interfacial layer models [348, 356, 374, 375] and discrete dipole lattice model [376]. Although the latter model is build rigorously on a molecular level, the level of details provided is not absolutely necessary for an adequate description of SFG.

The main difference between the interfacial layer models is how the thin polarized or dipolar layer responsible for the generation of the nonlinear signal is modeled (Fig. 2.12). In the Heinz-Shen model, the dipolar layer is modeled as an intermediary medium lying between ambient and substrate media, with distinct optical properties. The electric field of the incident beam is calculated within this layer (multiple reflections are usually neglected) and the electric field of the beam generated in the layer is calculated by solving Maxwell equations with the appropriate boundary conditions. The generated beam is then transmitted both in the ambient and substrate media. In contrast, in the Mizrahi-Sipe model, an infinitely thin dipole sheet is assumed to be very close to the interface between two linear media, *but within the substrate medium*. The electric field of the incident beam is then calculated at this position and the one associate with the SFG beam is derived by using a Green function approach. The SFG beam is then reflected and transmitted by the interface towards ambient and substrate media. In the present work, the Mizrahi-Sipe model is privileged because it does not, in contrast to the Heinz-Shen model, introduce an additional medium whose optical properties are not known *a priori*.

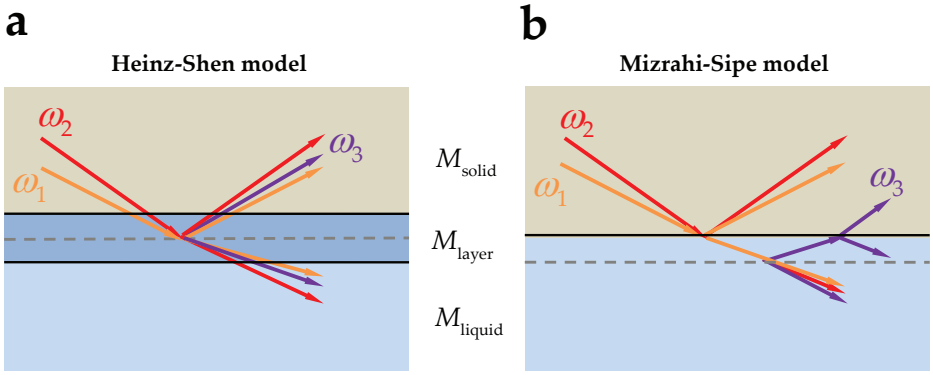

Fig. 2.12: Phenomenological models of the interfacial SFG signal. (a) Heinz-Shen model, (b) Mizrahi-Sipe model.

According to the Mizrahi-Sipe model, the intensity of the output SFG field generated from the interface can be written as

$$I(\omega_3) = \frac{2\omega_3^2 \sec^2\theta_3}{\varepsilon_0 c^3 n_1 n_2^2(\omega_3)} |\chi^{(2)}_{\text{eff}}|^2 I(\omega_1) I(\omega_2), \tag{2.60}$$

where $\chi^{(2)}_{\text{eff}}$ is the effective second-order nonlinear susceptibility, $I(\omega_\nu)$ is the intensity for each beam of frequency ω_ν ($\nu = 1, 2, 3$) and θ_3 is the reflection angle of the output SFG beam. It is related to the actual second-order nonlinear susceptibility $\chi^{(2)}$ through

$$\chi^{(2)}_{\text{eff}} = [\hat{\mathbf{e}}(\omega_3) \cdot \mathbf{F}(\omega_3)] \cdot \chi^{(2)} : [\hat{\mathbf{e}}(\omega_1) \cdot \mathbf{F}(\omega_1)] \cdot [\hat{\mathbf{e}}(\omega_2) \cdot \mathbf{F}(\omega_2)], \tag{2.61}$$

where $\mathbf{F}(\omega_\nu)$ are the nonlinear Fresnel coefficients relating the interfacial electric field components to the incoming fundamental field components in the ambient medium and $\hat{\mathbf{e}}_\nu$ are the unit vectors of each field at frequency ω_ν ($\nu = 1, 2, 3$).

E. Second-order nonlinear susceptibility

The effective second-order nonlinear susceptibility $\chi^{(2)}_{\text{eff}}$ is a third-rank tensor that can be expressed as the sum of $3^3 = 27$ different elements such as

$$\chi^{(2)}_{\text{eff}} = \sum_{i,j,k} \chi^{(2)}_{\text{eff},ijk}, \tag{2.62}$$

with

$$\chi^{(2)}_{\text{eff},ijk} = F_{ii}(\omega_3) F_{jj}(\omega_1) F_{kk}(\omega_2) e_{3i} e_{1j} e_{2k} \chi^{(2)}_{ijk} = F_{ijk} e_{ijk} \chi^{(2)}_{ijk}, \tag{2.63}$$

where $F_{ijk} = F_{ii}(\omega_3) F_{jj}(\omega_1) F_{kk}(\omega_2)$ is the Fresnel or angular factor which includes nonlinear Fresnel coefficients and local field corrections, and which is determined by the SFG geometry. For a fixed geometry, $e_{ijk} = e_{3i} e_{1j} e_{2k}$ can be considered as the polarization combination factor. Generally, changing the SFG experimental geometry (i.e., the incident angles θ_ν of the input fundamental beams) or the polarization angle ρ_ν of each beam may alter the SFG spectral intensity as well as the spectral features. Therefore, SFG spectra are both geometry- and polarization-dependent.

The macroscopic second-order nonlinear susceptibility $\chi^{(2)}$ can be related to the microscopic second-order hyperpolarizability $\alpha^{(2)}$ through the oriented gas model, which states that the susceptibility of a material is given by the summation of the hyperpolarizability of each molecule which constitutes it [377]. Formally, in terms of components, this can be written as

$$\chi^{(2)}_{ijk} = \frac{N_s}{\varepsilon_0} \langle \alpha^{(2)}_{ijk} \rangle, \tag{2.64}$$

where N_s is the surface density of molecules. The angular brackets denote an angular average over the molecular orientational distribution.

The molecular hyperpolarizability can be further expressed as

$$\begin{aligned}\alpha^{(2)}_{ijk} &= \mathrm{T}^{\alpha\beta\gamma}_{ijk}\alpha^{(2)}_{\alpha\beta\gamma} \\ &= \mathrm{T}^{\alpha}_{i}\alpha^{(2)}_{\alpha\beta\gamma}(\mathrm{T}^{\beta}_{j})^{-1}(\mathrm{T}^{\gamma}_{k})^{-1},\end{aligned} \tag{2.65}$$

with

$$\mathrm{T}(\psi,\theta,\phi) = \mathrm{R}(\phi)\mathrm{R}(\psi)\mathrm{R}(\theta), \tag{2.66}$$

and

$$\mathrm{R}(\phi) = \begin{bmatrix} C_\phi & S_\phi & 0 \\ -S_\phi & C_\phi & 0 \\ 0 & 0 & 1 \end{bmatrix}, \tag{2.67a}$$

$$\mathrm{R}(\psi) = \begin{bmatrix} C_\psi & S_\psi & 0 \\ -S_\psi & C_\psi & 0 \\ 0 & 0 & 1 \end{bmatrix}, \tag{2.67b}$$

$$\mathrm{R}(\theta) = \begin{bmatrix} C_\theta & 0 & -S_\theta \\ 0 & 1 & 0 \\ S_\theta & 0 & C_\theta \end{bmatrix}, \tag{2.67c}$$

where $\mathrm{T}^{\alpha\beta\gamma}_{ijk}$ is the transformation matrix connecting the molecular- to the laboratory-fixed coordinate systems, $\mathrm{R}(\phi), \mathrm{R}(\psi), \mathrm{R}(\theta)$ are the rotation matrices of the three Euler angles ϕ (azimuth), θ (tilt), and ψ (twist). The symbols C_X and S_X are a short-hand notation for $\cos X$ and $\sin X$, respectively. The exhaustive list of transformation elements between these coordinate systems has already been tabulated and can be found in [378].

From Eq. (2.64), one can obtained the individual tensor elements of $\chi^{(2)}$ by taking the orientational average of the hyperpolarizability of the adsorbed molecules within a volume defined by the coherence length $l_c = \lambda/4(n(\omega_3) - (n(\omega_1) + n(\omega_2)))$ of the input fundamental beams. Formally, by substituting Eq. (2.65) in Eq. (2.64), one obtains that

$$\chi^{(2)}_{ijk} = \frac{N_s}{8\pi^2\varepsilon_0}\int_\Omega w(\Omega)\mathrm{T}^{\alpha\beta\gamma}_{ijk}\alpha^{(2)}_{\alpha\beta\gamma}(\Omega)d\Omega, \tag{2.68}$$

where $w(\Omega)$ is a (weighting) orientational distribution function (ODF) and $d\Omega = \sin\theta d\theta d\phi d\psi$. Typically, for an isotropic distribution of molecules, the ODF is set to unity, but for other cases, it can take the form of a gaussian or a Dirac delta distribution. For most cases, the number of tensor elements given by Eq. (2.68) can be considerably reduced depending

on the molecular group symmetry and also on the chosen polarization configuration.

F. SFG spectrum

On the molecular level, the hyperpolarizability $\alpha^{(2)}_{\alpha\beta\gamma}$ of the q-th vibrational mode of a given adsorbed molecule can be written as the product of the IR transition dipole moment and the Raman transition polarizability moment such as

$$\alpha^{(2)}_{\alpha\beta\gamma,q} = \frac{N_s}{2\varepsilon_0\omega_q}\sum_{\alpha,\beta,\gamma}\frac{\partial\mu_\alpha}{\partial Q_q}\frac{\partial\alpha_{\beta\gamma}}{\partial Q_q}, \tag{2.69}$$

where Q_q are the classical normal coordinates of the q-th vibrational mode. As such, the vibrational modes can be excited or SFG active only when they are simultaneously IR and Raman active.

A quantum-mechanical expression of $\alpha^{(2)}_{\alpha\beta\gamma}$ can also be derived from perturbation theory [368]. When ω_1 is near a vibrational resonance ω_q and ω_2 remote from any electronic transitions, this can be expressed as

$$\alpha^{(2)}_{\alpha\beta\gamma,q} = \frac{N_s}{2\varepsilon_0\omega_q}\sum_{\alpha,\beta,\gamma}\frac{T_\alpha T_{\beta\gamma}}{(\omega_q-\omega_1-i\Gamma)}, \tag{2.70}$$

with

$$T_\alpha = \langle\nu|\mu_\alpha|g\rangle, \tag{2.71a}$$

$$T_{\beta\gamma} = \frac{1}{\hbar}\sum_s\left[\frac{\langle g|\mu_\beta|s\rangle\langle s|\mu_\gamma|\upsilon\rangle}{(\omega_3-\omega_{sg})} - \frac{\langle g|\mu_\gamma|s\rangle\langle s|\mu_\beta|\upsilon\rangle}{(\omega_2+\omega_{sg})}\right], \tag{2.71b}$$

where μ is the electric dipole operator, $|g\rangle$ and $|\upsilon\rangle$ denote ground and excited states, $|s\rangle$ refers to a virtual state, and Γ is the relaxation time of the vibrationally excited state involved in the resonance. Hence, when $\omega_1 \approx \omega_q$, then $(\omega_q - \omega_1) \to 0$ and the magnitude of $\alpha^{(2)}_{\alpha\beta\gamma,q}$ and, in turn, $\chi^{(2)}_{ijk}$ increases, which then results in a SFG enhancement. A diagrammatic representation of this process is given in Fig. 2.13. It basically shows that a molecular vibration (ω_q) is resonantly excited from its ground state to an intermediary excited state by a first photon (ω_1) and then up-converted by a second photon (ω_2) to a virtual state. These photons are then annihilated by the emission of a photon at a frequency which is the sum of both incoming photons ($\omega_3 = \omega_1 + \omega_2$). The up-conversion and subsequent annihilation thus constitute an anti-Stokes process.

In the vibrational SFG spectroscopy of molecules adsorbed at an interface, the input fundamental field frequencies are usually set at $\omega_1 = \omega_{\mathrm{IR}}$ and $\omega_2 = \omega_{\mathrm{VIS}}$. The output SFG beam intensity is measured by tuning the frequency ω_{IR} over each vibrational mode, which then yields a vibrational SFG spectrum of the adsorbed molecules. This spectrum usually results from the interference between two contributions, a resonant (R) contribution due to interfacial adsorbed molecules organized in a non-centrosymmetric envi-

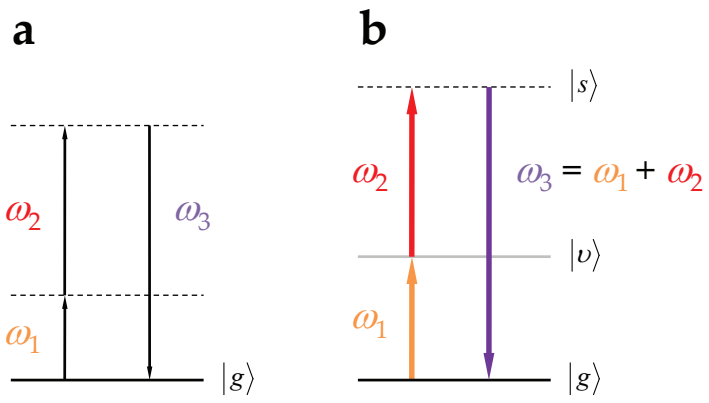

Fig. 2.13: Energy levels diagram of the SFG process. (a) Off resonance, (b) on resonance. The intermediate (*solid line*) and virtual (*dashed line*) levels are shown.

ronment and a non-resonant (NR) contribution which, in the case of some metallic and semiconductor substrates, comes from electronic interband transitions [379]. Both contributions are frequency-dependent, although the latter to a lesser extent.

Accordingly, for molecules with N vibrational modes, the output SFG beam intensity can be expressed as

$$I(\omega_{\mathrm{SFG}}) \propto |\mathbf{P}^{(2)}(\omega_{\mathrm{SFG}})|^2 = |\chi^{(2)} : \mathbf{E}_{\mathrm{IR}}\mathbf{E}_{\mathrm{VIS}}|^2, \tag{2.72}$$

with

$$\begin{aligned}
|\chi^{(2)}|^2 = |\chi^{(2)}_{\mathrm{R}}(\omega_2) + \chi^{(2)}_{\mathrm{NR}}|^2 &= \left|\sum_{q=1}^{N} |\chi^{(2)}_{\mathrm{R},q}| e^{i\delta_{\mathrm{R},q}(\omega_2)} + |\chi^{(2)}_{\mathrm{NR}}| e^{i\delta_{\mathrm{NR}}}\right|^2 \\
&= \sum_{q=1}^{N} |\chi^{(2)}_{\mathrm{R},q}|^2 + |\chi^{(2)}_{\mathrm{NR}}|^2 + 2\sum_{q=1}^{N-1}\sum_{r=q+1}^{N} |\chi^{(2)}_{\mathrm{R},q}||\chi^{(2)}_{\mathrm{R},q+1}|(e^{-(\delta_{\mathrm{R},q}(\omega_2)-\delta_{\mathrm{R},r}(\omega_2))} + e^{(\delta_{\mathrm{R},q}(\omega_2)-\delta_{\mathrm{R},q+1}(\omega_2))}) \\
&\quad + 2\sum_{q=1}^{N} |\chi^{(2)}_{\mathrm{R},q}||\chi^{(2)}_{\mathrm{NR}}|(e^{-(\delta_{\mathrm{R},q}(\omega_2)-\delta_{\mathrm{NR}})} + e^{(\delta_{\mathrm{R},q}(\omega_2)-\delta_{\mathrm{NR}})}) \\
&= \sum_{q=1}^{N} |\chi^{(2)}_{\mathrm{R},q}|^2 + |\chi^{(2)}_{\mathrm{NR}}|^2 + \sum_{q=1}^{N-1}\sum_{r=q+1}^{N} |\chi^{(2)}_{\mathrm{R},q}||\chi^{(2)}_{\mathrm{R},r}| \cos(\delta_{\mathrm{R},q}(\omega_2) - \delta_{\mathrm{R},r}(\omega_2)) \\
&\quad + \sum_{q=1}^{N} |\chi^{(2)}_{\mathrm{R},q}||\chi^{(2)}_{\mathrm{NR}}| \cos(\delta_{\mathrm{R},q}(\omega_2) - \delta_{\mathrm{NR}}) \\
&= \sum_{q=1}^{N} |\chi^{(2)}_{\mathrm{R},q}|^2 + |\chi^{(2)}_{\mathrm{NR}}|^2 + \sum_{q=1}^{N-1}\sum_{r=q+1}^{N} |\chi^{(2)}_{\mathrm{R},q}||\chi^{(2)}_{\mathrm{R},r}| \cos\Delta\phi_{qr}(\omega_2) + \sum_{q=1}^{N} |\chi^{(2)}_{\mathrm{R},q}||\chi^{(2)}_{\mathrm{NR}}| \cos\Delta\phi_{qB},
\end{aligned} \tag{2.73}$$

where $\chi^{(2)}_{\mathrm{R},q}$ and $\chi^{(2)}_{\mathrm{NR}}$ are the (frequency-dependent) q-th resonant and non-resonant contributions of $\chi^{(2)}$, and $\Delta\phi_{qr}$ and $\Delta\phi_{qB}$ denotes the relative phases between q- and r-th resonant contributions and between q-th resonant and non-resonant bulk contributions, respectively.

For dielectrics like glassy and crystalline materials (CaF_2, SiO_2, etc.), $|\chi^{(2)}_{\mathrm{NR}}| \approx 0$. In contrast, for conducting materials like noble metals, NR contributions are non-zero and can be expressed as [380]

$$\chi^{(2)}_{\mathrm{NR}} = \chi^{(2),\mathrm{intra}}_{\mathrm{NR}} + \chi^{(2),\mathrm{inter}}_{\mathrm{NR}}, \tag{2.74}$$

where $\chi^{(2),\mathrm{intra}}_{\mathrm{NR}}$ and $\chi^{(2),\mathrm{inter}}_{\mathrm{NR}}$ denotes the intra- and interband NR contributions originating from the transitions of free (conduction) and bound (valence) electrons, respectively. Low frequencies ($\omega_1 = \omega_{\mathrm{IR}}$) will enable only electronic excitations near the Fermi level, usually involving s orbitals, while for frequencies in the interband range ($\omega_2 = \omega_{\mathrm{VIS}}$), the contribution of d electrons will dominate.

The nonlinear response of the free and bound electrons can be calculated using a free jellium model [381] and a Lorentz oscillator model [380], respectively. According to these models, for a conducting material on which a potential is applied, these contributions are given by

$$\chi^{(2),\mathrm{intra}}_{\mathrm{NR}} \propto \chi^{(3)}(0,\omega_1,\omega_2)(V_{\mathrm{dc}} - V_{\mathrm{pzc}}) = a(V_{\mathrm{dc}} - V_{\mathrm{pzc}}) + b, \tag{2.75a}$$

$$\chi^{(2),\mathrm{inter}}_{\mathrm{NR}} \propto \sum_q \frac{A_q}{(\omega_2 - \omega_{s_q g} + i\Gamma_{s_q g})} = c + id \quad (a,b,c,d \in \mathbb{R}), \tag{2.75b}$$

where V_{dc} and V_{pzc} represents the applied potential across the interface, and the potential of zero charge, respectively. $\chi^{(3)}$ is the third-order nonlinear susceptibility coming from the bulk of the substrate. A_q, $\omega_{s_q g}$, and $\Gamma_{s_q g}$ are the amplitude, frequency, and damping constant of a given q-th oscillator transition between ground and excited state. It is worth noting that only $\chi^{(2),\mathrm{intra}}_{\mathrm{NR}}$ is real and dependent on the applied potential.

At charged solid surfaces such as metal oxide/aqueous solution interfaces, the electric field at the interface can reach values in excess of 10^6–10^7 V/cm. For such strong fields, another SFG signal can be generated following a third-order process, in addition to the second-order process given in Eq. (2.72) [103, 382]. This third-order process, also known as electric field-induced SFG, involves the action of three electric fields on the material, one of which is the static electric field (of zero frequency) due to the charged interface. The output SFG beam intensity can then be rewritten as

$$I(\omega_{\mathrm{SFG}}) \propto |\mathbf{P}^{(2)}(\omega_{\mathrm{SFG}}) + \mathbf{P}^{(3)}(0)| = |\chi^{(2)} : \mathbf{E}_{\mathrm{IR}}\mathbf{E}_{\mathrm{VIS}} + \chi^{(3)} \vdots \mathbf{E}_{\mathrm{IR}}\mathbf{E}_{\mathrm{VIS}}\mathbf{E}_0|^2, \tag{2.76}$$

where $\mathbf{E}_0$ is the interfacial static electric field.

The static electric field extends into the bulk solution and interacts with the water molecules. Hence, the $\chi^{(3)}$ signal is expected to be mainly due to water molecules. In fact, it has contributions that originates from isotropic bulk water molecules as well as from water molecules oriented by the static electric field. Assuming that the dipolar interaction energy is less than the thermal energy ($\mu E_0 \ll k_B T$), $\chi^{(3)}$ can then be expressed as [103, 382]

$$\chi^{(3)} = \chi^{(3)}_{\text{iso}} + \chi^{(3)}_{\text{orient}} = N_{\text{H}_2\text{O}} \left(\alpha^{(3)}_{\text{H}_2\text{O}} + C \frac{\mu_{\text{H}_2\text{O}} \alpha^{(2)}_{\text{H}_2\text{O}}}{k_B T} \right), \tag{2.77}$$

where $N_{\text{H}_2\text{O}}$ is the number density of water molecules, $\alpha^{(2)}_{\text{H}_2\text{O}}$ and $\alpha^{(3)}_{\text{H}_2\text{O}}$ are the second- and third-order electronic polarizability of water, $\mu_{\text{H}_2\text{O}}$ is the permanent dipole moment of water, and C is a constant determined by the particular susceptibility element under consideration.

The third-order term in Eq. (2.76) can also be rewritten in terms of the interfacial potential by considering that all molecules subject to the static electric field can contribute to the $\chi^{(3)}$ signal. Assuming that the density of water molecules does not change significantly from the interface to the bulk, one can integrate over all these contributions and write that

$$\begin{aligned} \mathbf{P}^{(3)}(0) &= \chi^{(3)} \vdots \mathbf{E}_{\text{IR}} \mathbf{E}_{\text{VIS}} \int_0^\infty \mathbf{E}_0(z) dz \\ &= -\chi^{(3)} \vdots \mathbf{E}_{\text{IR}} \mathbf{E}_{\text{VIS}} (\Phi(\infty) - \Phi(0)) \\ &= \chi^{(3)} \vdots \mathbf{E}_{\text{IR}} \mathbf{E}_{\text{VIS}} \Phi(0), \end{aligned} \tag{2.78}$$

where the potential far into the bulk of the solution $\Phi(\infty) = 0$.

In the presence of a salt solution of moderate concentration (< 0.1 M), the Gouy-Chapman model of the charged surface becomes valid and the interfacial potential $\Phi(0)$ can now be written as [103]

$$\Phi(0) = \frac{2 k_B T}{e} \sinh^{-1} \left(\sigma(0) \sqrt{\frac{\pi}{2 \varepsilon k_B T C}} \right), \tag{2.79}$$

where $\sigma(0)$ is the surface charge density, ε is the bulk dielectric constant, and C is the bulk ion concentration.

2.2.4.1.2 SFG spectrometer setup

As mentioned in the previous section, the generation of nonlinear signals from molecules adsorbed at interfaces requires high intensity laser light sources. Therefore, picosecond (ps) and femtosecond (fs) laser setups are most often used in SFG spectroscopy [354]. Ps-based systems usually have a large scanning range (~ 1000 cm^{-1}) with a spectral acquisition time on the order of tens of minutes. A ps-based laser system is tuned within a certain frequency range and an SFG signal is recorded by integrating the intensity at each frequency. In contrast, broadband SFG spectrometers based on fs laser systems are conceptually different. In these, the broad SFG signal is imaged through a spectrometer. This setup allows the detection of SFG signals in a narrower spectral range ($\sim$ 70–200 cm^{-1}) with temporal resolution usually on the order of seconds. Dynamic processes on time scales from seconds to minutes are accessible to both type of systems. However, kinetic measurements obtained by ps systems are restricted to one fixed frequency, while fs systems can record a spectral range.

The IR-VIS SFG spectroscopy setup used in the present work is based on a broad-bandwidth scheme [383, 384] in which broadband, fs IR and narrowband, ps VIS (or NIR) laser beams are mixed at the interface of interest. Aside from the optical tables and the clean room hood, this setup consists of a fs regenerative amplifier (RGA) (Spitfire Pro 35F XP, Spectra-Physics, Germany; sub-35 fs, 1 kHz) seeded by a mode-locked Ti:sapphire oscillator (Tsunami 3941-MS, Spectra-Physics; sub-30 fs, 80 MHz) with a tunable wavelength centered at 800 nm. The regenerative amplifier and seed laser are pumped by frequency-doubled Q-switched Nd:YLF (Empower 30, Spectra-Physics; 30 W, 1 kHz, 527 nm) and Nd:YVO_4 (Millenia Pro 5s, Spectra-Physics; 5 W, 532 nm) solid-state lasers, respectively. The RGA generates 90-fs duration pulses centered at 800 nm with a repetition rate of 1 kHz and an average power of 4 W. The amplified output beam is then split up and the larger fraction ($\sim 80\%$) is used to pump an automated optical parametric amplifier (OPA) (TOPAS-C, Light Conversion) coupled to a non-collinear difference-frequency generator (NDFG) (Light Conversion, Lithuania). This generates broadband (FWHM$\sim$ 70–200 cm^{-1}) IR pulses which can be tuned from 2.6 to 12 μm. The signal and idler beams are spatially separated and spectrally filtered by a Ge plate (Crystec, Germany; OD = 3" (7.62 cm), $d = 5$ mm). The remaining fraction of the output beam ($\sim 20\%$) is fed into an air-spaced Fabry-Perot etalon (SLS Optics, UK; spacing $d = 12.5$ μm, free spectral range FSR = 398.29 cm^{-1}, effective finesse $F_{\text{eff}} = 57.48$ at 790 nm) which gives narrowband (FWHM$\sim$1 nm), time-asymmetric ps VIS pulses. A broadband reference (REF) beam is generated simultaneously by sum-frequency mixing of small portions of the IR ($\sim$1%) and VIS ($\sim$2%) beams in one of the following nonlinear SFG crystals: 0.6 mm-thick $LiIO_3$ (2.7–5 μm, $\theta = 21.4°$, $\phi = 0°$), 0.2 mm-thick $AgGaS_2$ (5–6 μm, $\theta = 71°$, $\phi = 45°$), or 0.2 mm-thick $AgGaS_2$ (6–10 μm, $\theta = 54.4°$, $\phi = 45°$) (TOPAG Lasertechnik, Germany). These crystals were coated with broadband anti-reflection coatings for (0.8–5.0) μm, 800+(5.0–6.0) μm, and 800+(6.0–10.0) μm, respectively, on the front side and (0.6–0.7) μm, (0.65–0.8) μm, and (0.7–0.8) μm, respectively, on the back side. The beam path length prior to the nonlinear reference crystal is the same as the beam path length to the sample stage. This allows for the recording of the exact spectral profile of the incident IR beam on the sample stage which can then be used for the normalization of the SFG signal. Linearly polarized IR, REF, and VIS beams are independently directed and focused on the sample surface with incident angles (relative to the surface normal) of 60°, 68° and 70°, respectively. The overall arrangement of the components on the table is shown in Fig. 2.14.

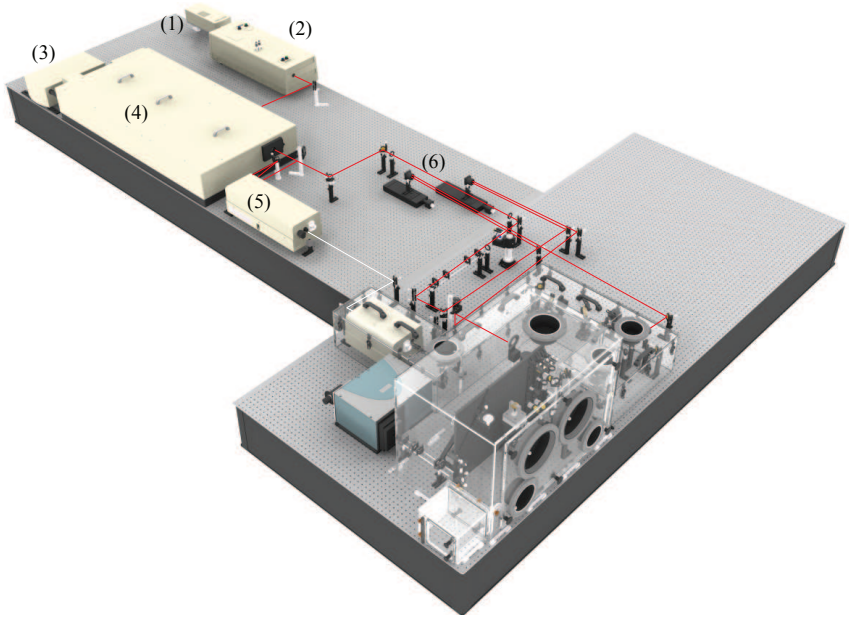

Fig. 2.14: General optical layout of the SFG spectrometer setup. Several components such as the pump laser of the seed laser (1), the seed laser (2), the pump laser of the amplifier (3), the regenerative amplifier (4), the optical parametric amplifier (5), and the delay stages (6) are shown. The VIS (*red line*) as well as signal/idler (*white line*) beams are also represented. For clarity, the beams have been drawn until they reach the purging chamber.

In the following sections, a summary description of some of these components will be given. All other optical (lenses, mirrors, filters) and opto-mechanical (bases, breadboards, holders, linear and rotation stages, mounts, plates, posts, etc.) components were purchased from Laser Components (Germany) and Thorlabs (Germany), respectively, unless otherwise stated.

A broadband SFG beam is produced when the narrowband VIS and broadband IR beams are spatially and temporally overlapped at the sample surface within a spot ~200 μm in diameter. Fig. 2.15 shows the beam profile of the VIS pulse at the sample. The elliptical shape is due to the incident angle. The temporal overlap is accomplished through the use of motorized delay lines which are basically made of hollow retroreflectors (OMNI-Wave; Laser Components; 1" (2.54 cm) clear aperture) mounted on motorized linear stages (NRT100/M and NRT150/M, Thorlabs; travel range: 100 and 150 mm, minimal travel increment: 0.1 μm). The incidence angle of the REF beam is carefully adjusted so that on reflection it propagates collinearly with the SFG beam. Maximum energies of $\sim$ 30 μJ/pulse for the IR beam and $\sim$ 40 μJ/pulse for the VIS beam can be obtained immediately before the sample. Usually, the energy of the incoming beams is adjusted by pinholes to prevent thermal effects such as bubble formation or sample ablation.

The intensity of the reflected REF beam is matched to that of the SFG beam using a variable neutral density filter prior to the sample. The outgoing SFG and REF beams are collimated by lenses, filtered through a short-pass filter (3rd Millenium 770SP, Laser

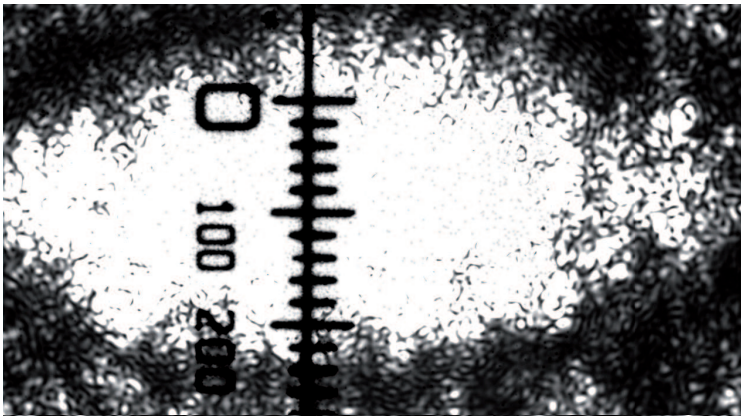

Fig. 2.15: Beam profile of the VIS beam at the sample stage. The VIS beam is incident on a small piece of paper and the image was acquired using a microscope mounted directly above the sample stage. The scale shown is in μm.

Components), and dispersed by an imaging spectrograph (Shamrock SR-301i-B, Andor Technology; focal length $f = 303$ mm, 1200 grooves/mm grating blazed at 500 nm) equipped with both a photomultiplier (R9110, Hamamatsu, Germany) and an air-cooled, back-illuminated high-resolution CCD camera (iDus DU420A-BR-DD, Andor Technology; 254 $\times 1024$ pixels). The SFG and REF beams can thus be simultaneously recorded on the same CCD chip. The focuses of the beams at the entrance slit are tuned with a telescope to match the f-number of the spectrometer, resulting in recorded images only a few pixels in height. The REF beam is tuned to be slightly non-collinear with the SF originating from the sample allowing the clear separation of both signals on the CCD chip (Fig. 2.16). SFG spectra with reasonable signal-to-noise ratio are typically obtained on a time scale of milliseconds to seconds. For alignment purposes, spectra can be recorded within one or two pulses, allowing real-time intensity optimization and frequency adjustment. Spectra are usually taken with an *ssp* polarization combination for the SFG, VIS, and IR beams, respectively. Other polarization combinations (*ppp*, *pss*, and *sps*) are also accessible by rotation of the IR and VIS beams through the use of half-wave plates and/or a periscope.

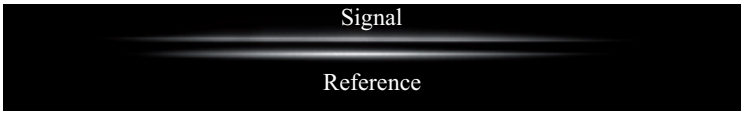

Fig. 2.16: Example of a CCD image showing the (non-resonant) SFG signal generated from a gold-coated surface and the reflected REF beam.

A. Optical tables and clean room hood

All laser and opto-mechanical components were mounted on two optical tables with tuned damping (RS 2000^{TM}, Newport-Spectra Physics, Germany; 150 cm$\times$250 cm$\times$30.5 cm), mounted at a height of 58.5 cm on a set of laminar flow isolators (*Fill and Forget*^{TM}, PL-2000 Series, Newport-Spectra Physics) and arranged in a T-configuration. The ta-

bles as well as the whole SFG spectroscopy setup were enclosed in a free-standing clean room hood (Opta, Germany; section A: 170 cm×240 cm, section B: 170 cm×360 cm) that matches the T-shape contour of the optical tables. The clean room consists of a steel-based frame closed with sliding acrylic glass panes on its upper part, and with overlapping PVC stripes on its lower part. The clean room ceiling is made from melanin-coated chipboard damping plates which support the filtering and ventilation modules. The optical setup is maintained in a constant humidity- and temperature-controlled (typically, RH $\leq 40\%$ and $T = 22 \pm 1°$C) laminar flow.

B. Pulse shaper

The pulse shaper consists of an air-spaced, asymmetric Fabry-Perot etalon (SLS Optics; spacing $d = 12.5$ μm, FSR = 398.29 cm^{-1}, $F_{\text{eff}} = 57.48$ at 790 nm) mounted on a V-shaped clamping mount (C1503, Thorlabs; $\pm 3°$) which allows for fine pitch and yaw adjustment. The whole assembly is fixed through a solid adapter plate on a manual rotation stage with micrometric drive (PR01, Thorlabs).

The spectral resolution of the SFG signal depends on the temporal pulse width of the VIS beam. Fig. 2.17 illustrates this dependency by showing a simulation of the time profile of the VIS beam and the resulting time profile of three typical molecular vibrations. Three Lorentzian oscillators $\chi(\omega_i)$ $(i = 1, 2, 3)$ with equal intensities and widths of 20 cm^{-1} located at 2880, 2925 and 2945 cm^{-1} were used. The time profile of the molecular vibrations was then obtained by taking the Fourier transform of their sum into the time domain. As can be seen from Fig. 2.17, the time profile of the molecular vibrations exceeds several ps, such that the duration of the VIS pulse needs to be on the same order to resolve these vibrations into an SFG spectrum in the frequency domain.

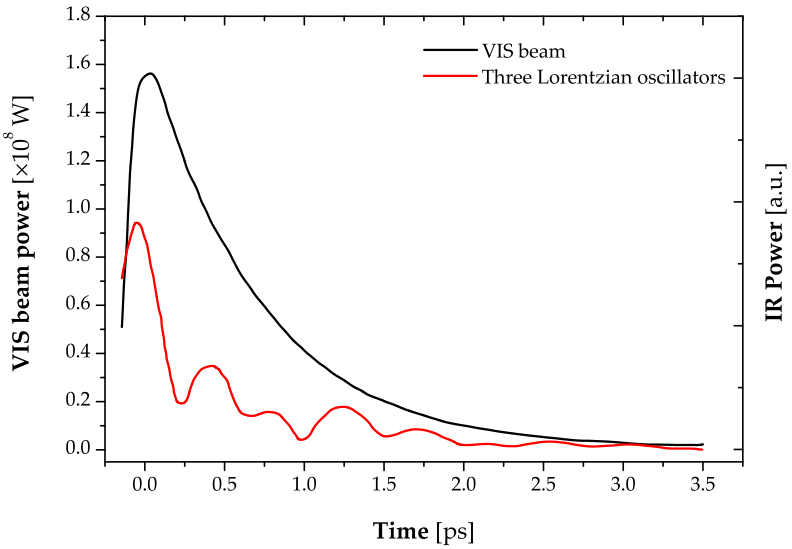

Fig. 2.17: Time profiles of the VIS pulse (*dashed line*) and of three typical CH stretching molecular vibrations (*solid line*) (source: V. Kurz (ITG, KIT - Campus North)).

This pulse duration can be achieved by directing the fs VIS beam through a Fabry-Perot

etalon to obtain a prolonged asymmetric time profile [385]. When the incoming chirped, Gaussian-shaped VIS beam passes through the etalon, it undergoes multiple reflections between its two reflecting surfaces, such that the input intensity gains an additional phase. As such, the output VIS beam intensity can be approximately represented as [10]

$$I_{\text{out}}(\omega_{\text{VIS}}, t) \approx I_{\text{in}}(\omega_{\text{VIS}}, t) * e^{-t\tau}\Theta(t), \tag{2.80}$$

with the cavity lifetime defined as

$$\tau = \frac{1}{\pi\ \text{FSR}}, \tag{2.81}$$

where I_{in} and I_{out} are the time-dependent input and output intensities of the VIS beam, respectively, and FSR is the free spectral range of the etalon. Eq. (2.80) was weighted with an Heaviside function $\Theta(t)$ since no intensity is present in the cavity before the beam reaches the etalon.

C. Sample stage

The sample stage is comprised of a set of input lenses and mirrors (Laser Components), a multi-axial sample holder, and a set of output mirrors (Fig. 2.18). All these components are constrained to the same plane of incidence by direct fixation on an aluminium breadboard (M4560, Thorlabs) positioned vertically on the optical table. Each input beam path consists of a lower mirror/intermediate lens/upper mirror series mounted independently on its own flexible rail system. CaF_2 (or BaF_2) lenses are used for the IR and REF beams, and a BK7 lens for the VIS beam (Laser Components), respectively. The sample holder is made of a 3-axis (xyz) rolling block with manual micrometric drives (RB13M/M, Thorlabs; 13 mm travel) coupled to a 1-axis (θ) manual goniometer (GO90, Owis, Germany; $\pm 15°$ rotation). The rotation axis of the goniometer is coincident with the sample surface. A pair of magnetically-coupled kinematic plates are then used to dock the measuring cells. A bottom base plate is fastened directly on top of the goniometer, while the top mounting plate is fixed to the base of any given measuring cell. This system permits a quick exchange of measuring cells while the position and orientation of the probing plane is preserved. The output beam path is made of a series of three mirrors. The first mirror is larger and acts as a collector for the REF, SFG and VIS beams. It is mounted on an independent rail system that enables the operator to follow the displacement of the beams induced by the goniometer tilting. The two last mirrors guide the REF and SFG beams to the entrance slit of the spectrograph.

D. Purging chamber

In order to prevent IR beam absorption by ambient gaseous H_2O and CO_2, the SFG spectrometer setup was supplemented with a home-built purging chamber (Fig. 2.19). The

10. The exact analytical expression for the output intensity of an incoming chirped, Gaussian beam pulse-shaped by a Fabry-Perot etalon is much more complex and can be found in [386].

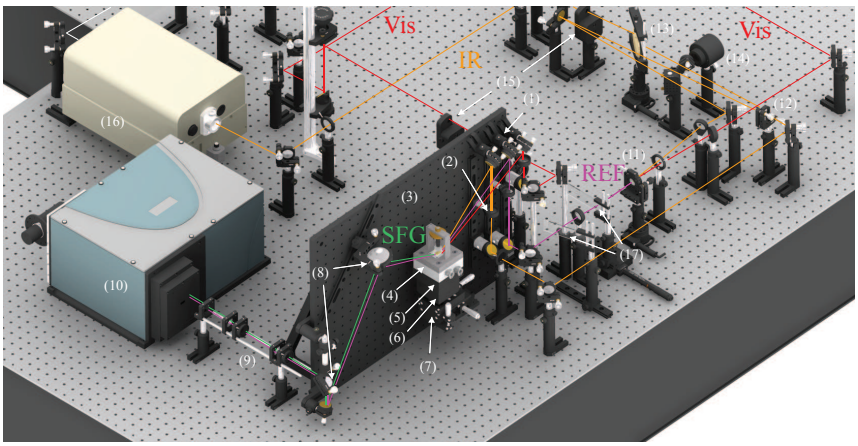

Fig. 2.18: Image (isometric view) of the sample stage area (purging chamber not shown). The input mirrors (1), input lenses (2), breadboard (3), measuring cell (4), kinematic plates (5), 1-axis goniometer (6), 3-axis rolling block (7), output mirrors (8), telescope (9), spectrometer (10), SFG crystal for REF signal (11), BaF_2 beamsplitting plates (12), Ge filtering plate (13), pyroelectric IR pulse energy meter (14), remote shutters (15), NDFG stage (16), and variable density filters (17) are shown. The IR (*orange line*), REF (*purple line*), SFG (*green line*), and VIS (*red line*) beams are also represented. The reflected IR and VIS beams are not shown for clarity.

chamber was designed in collaboration with R. Jehle (Institute of Applied Physical Chemistry, INF 253, University of Heidelberg, Heidelberg, Germany) with Autodesk Inventor Pro software (v. 2009, Autodesk, Germany) and machined at the fine mechanics workshop by R. Schmitt and his coworkers (Institute of Applied Physical Chemistry). This air-proof chamber covers the optical path of the IR beam from the NDFG module to the spectrograph. The enclosure is made entirely of acrylic glass and is divided in two sections: a four-compartment channel ($V \approx 0.14$ m^3) that stretches from the NDFG to the sample stage, and a main chamber ($V \approx 0.30$ m^3) that completely surrounds the sample stage. The channel and the chamber have built-in thin optical BaF_2 and BK7 windows (Laser Components) mounted in Teflon holders to allow entrance of OPA (signal and idler) and VIS beams, respectively. The main chamber is supplemented by a small side chamber with a lockable vertical panel permitting sample transfer without disrupting the air purge. Both channel and chamber are air-dried ($\leq 1\%$ RH) by two FTIR purging gas generators (75-45-12VDC, Parker-Balston, Germany; 14 L/min), each coupled to two additional coalescing pre-filters to remove air particulates and hydrocarbon residues. The humidity and temperature in the chamber are monitored by a thermohygrometer (Hytelog-USB, Hygrosens, Germany) mounted on the top panel. When the chamber is not purged, the optical components in the channel can be accessed through removable covers, while those in the chamber can be reached by removal of the front panel. When the purging chamber is in operation, the mirrors important for beam alignment in the channel and the chamber can be reached externally by built-in small Neoprene® gloves. The entire sample holder area (including the transfer chamber) can be accessed via two pairs of ambidextrous Neoprene® gloves fixed directly to the front panel on fully rotatable circular holders. All other components necessary to adjust IR and REF beam intensity (e.g., Ge plate, REF crystal, variable density filter) are motorized and remotely controlled via T-cube DC servo motor controller (TDC001, Thorlabs). Two independent

side panels, one on the channel and one on the chamber, provide the necessary entry ports for liquid tubing as well as for various electrical cables.

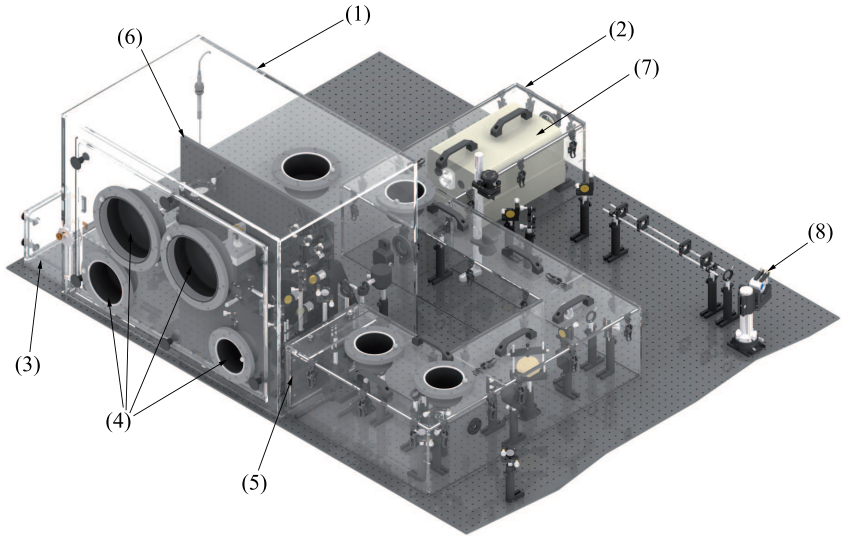

Fig. 2.19: Image (isometric view) of the purging chamber. The main chamber (1), channel (2), transfer chamber (3), Neoprene® gloves (4), vertical lockable flapping door (5), breadboard (6), NDFG (7), and Fabry-Perot etalon (8) are shown.

E. Spectroelectrochemical measuring cell and potentiostat

The three-electrode spectroelectrochemical measuring cell was designed to allow simultaneous *in situ* SFG spectroscopic measurement in total internal reflection (TIR) geometry as well as electrochemical and voltammetric measurements (Fig. 2.20). The cell was designed with Autodesk Inventor Pro software (v. 2009, Autodesk) and machined at the fine mechanics workshop by R. Schmitt and his coworkers (Institute of Applied Physical Chemistry). The cell is composed of five major parts: a square-shaped bottom plate that acts as an adaptor to the sample stage mount and as an isolator for the thermostated reservoir, a cylindrical thermostated reservoir that allows aqueous solutions to be maintained at constant temperature, an intermediary plate acting as the aqueous solution reservoir with six ports (two for the solution inlet/outlet, two for the counter and reference electrodes, and two free ports for pH and temperature sensors), a top plate with a centered rectangular cavity (0.25 cm$\times$1.3 cm$\times$2.0 cm) to support and secure in place the IR-transparent prism, and an overhead bridge which holds a fine threaded rod with an acetal clamp at its lower end which presses down the prism against the top plate to ensure water leakproofness. All parts are made of acetal resin, with the exception of the thermostated reservoir and the overhead bridge which are made of stainless steel. The parts are imbricated one over the other and screwed together from the top plate side. The aqueous solution chamber and the thermostated reservoir are sealed with Viton® fluoropolymer sealing rings. The volume of the solution reservoir is $\sim$ 8 ml. The inlet and outlet of the thermostated reservoir are provided by commercial quick-disconnect acetal couplings (PMCD1002BSPT (valved coupling body) and PMCD2202 (valved in-line coupling insert), Colder, Germany; 1/8" BSPT (0.97 cm) thread) which can be connected to a thermostated bath. The inlet and outlet of the aqueous solutions reservoir are home-

built. The solutions can be provided through Teflon PFA tubing (MedChrom, Germany; 1/16" OD (0.16 cm)) which can be connected to a peristaltic pump.

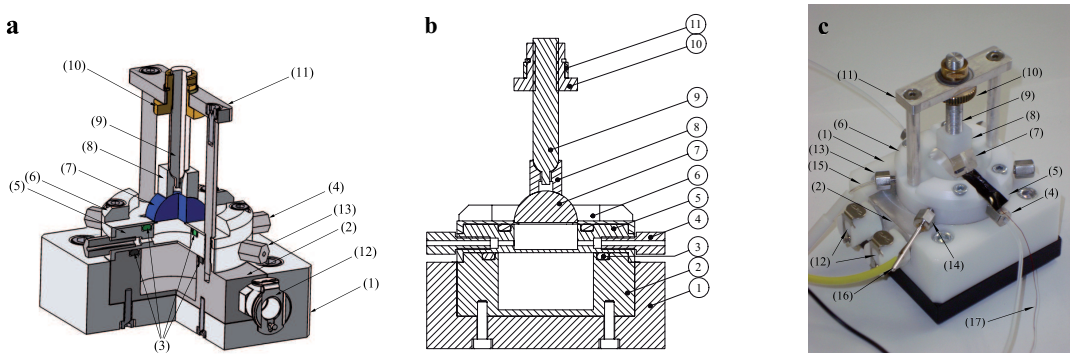

Fig. 2.20: Schematic representation and image of the spectroelectrochemical cell. (a) Three-quarter view (electrodes and tubes not shown). (b) Cross-sectional view. (c) Photograph. The labels denote the bottom plate (1), thermostated reservoir (2), sealing rings (3), solution inlet/outlet with tubes (4), intermediary plate (5), top plate (6), hemicylindrical IR-transparent ITO-coated CaF_2 prism (7), prism adapter (8), threaded rod (9), round nut (10), overhead bridge (11), quick disconnect couplings (12), reference electrode inlet (13), counter electrode inlet (14), Ag/AgCl reference electrode (15), Pt counter electrode (16), and Cu wire with carbon conductive tape (17).

The three-electrode system is made up of a Pt rod (6.1247.010, Metrohm, Germany; $d_{ext} = 0.2$ cm, $l = 6.5$ cm) which acts as counter electrode, an Ag/AgCl wire in a 3 M KCl filling solution enclosed in a barrel with frit tip (MI-402, Microelectrodes, USA; $d_{ext} = 0.2$ cm, $l = 9.5$ cm) as a reference microelectrode. The working electrode is provided by the ITO coating on the basal face of the IR-transparent CaF_2 prism. In addition, a one- or two-sided adhesive (acrylic glue, $R = 0.005\ \Omega$) conducting tape (either C or Cu) (G3939 (C) or G253A (Cu), Plano, Germany; $t = 0.16$ mm, $w = 8$ mm, $l = 20$ m or $t = 0.16$ mm, $w = 6.4$ mm, $l = 16$ m, $\sim 20\ \Omega$ (U. Geckel, private communication)) is fixed to the ITO coating and cover with a thin layer of epoxy glue to prevent any contact with the aqueous solution. The three electrodes are connected to an analog potentiostat. The spectroelectrochemical cell can be employed in two possible measuring modes, an acidimetric or pH-metric mode by which the surface charging is induced by a change of the pH of the underlying solution, and a voltammetric mode by which the surface charging is controlled through an applied potential at the surface of the ITO coating (Fig. 2.21).

2.2.4.1.3 Spectroelectrochemical measurements

The SFG spectrum of water adsorbed at the ITO/aqueous solution interface was measured in the bonded-OH water spectral region (3100-3500 cm^{-1}). In order to cover the complete spectral region, measurements were made in two separate spectral regions centered at ~ 3150 cm^{-1} and ~ 3400 cm^{-1}. The spectrum of the reflected REF beam was simultaneously recorded and could be used to monitor any fluctuations of the laser sources. The ssp polarization configuration was used throughout as it was the only one giving a sufficient signal-to-noise ratio. Independent of the chosen measuring mode (acidimetric or voltammetric), all spectra were recorded for 20 s (10 s$\times$2 accumulations)

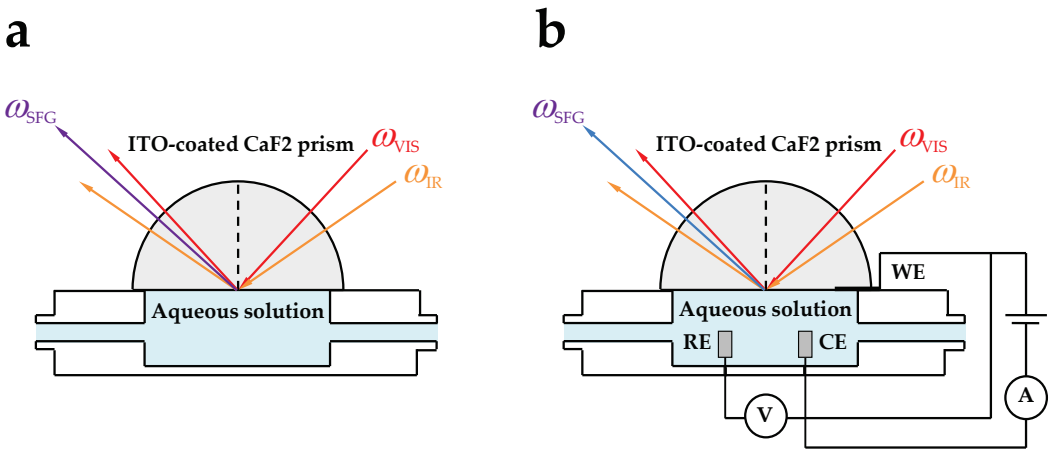

Fig. 2.21: Measuring modes of the spectroelectrochemical cell. (a) acidimetric mode, (b) voltammetric mode.

and background-corrected using the spectrograph software (Andor SOLIS v. 4.12, ANDOR). In order to further minimize the background noise, a region of interest was defined for each signal and the individual spectra was obtained by vertical binning. Prior to any measurement, the intensity of the REF beam was roughly adjusted to that of the SFG beam by using a neutral variable density filter located in its optical path. Using the voltammetric mode, SFG spectra were measured on normal water, deuterated water, and 10 mM salt anionic and cationic salt solutions in the potential range from -1 to +1 V in steps of 0.1 V. Finally, all spectra were processed in the graphing and data analysis software OriginPro (v. 8.5, OriginLab, Germany) using home-built routines.

2.2.4.2 Voltammetry

Voltammetry was used to measure the surface current density at the ITO/aqueous solution interface as the applied potential was varied. Voltammetry is an electrochemical technique which enables to control the potential of an electrode in contact with an analyte (e.g., dissolved ions in an aqueous solution) while measuring the resulting current [387].

The simplest arrangement of a voltammetric setup is given by the three-electrode cell which includes a working electrode (WE), a reference electrode (RE), a counter (or auxiliary) electrode (CE), and a high impedance potentiostat (Fig. 2.22). The working electrode applies the desired potential in a controlled way and facilitate the transfer of charge to and from the solution, while the reference electrode gauge the potential of the working electrode relative to the potential of the standard hydrogen electrode (SHE) (which is by convention established as the potential reference point). For example, an Ag wire dipped in a saturated chloride solution constitutes a simple reference electrode. However, to maintain a stable potential i.e., to obtain a non-polarizable reference electrode, no current is allowed to flow through it. This can be achieved with a counter electrode in which flows enough current to balance the one observed at the working electrode. The potentiostat enables to measure the potential difference between working electrode and reference electrode without polarizing the reference electrode (through a high-impedance feedback loop), and to control the potential difference between the working and counter electrodes

by forcing a current through the counter electrode towards the working electrode. These two functions of a potentiostat essentially relies on the use of a bipolar operational amplifier (OPA) with two inputs, one inverting (-) and one non-inverting (+). For example, if a voltage is fed into the non-inverting input of the OPA, it will produce an amplified voltage (or current) of the same sign. On the contrary, if this voltage is forced into the inverting input, it will produce a voltage (or current) of the same magnitude, but of opposite sign [11]. The fundamental property of the OPA is that the difference between the two inputs will be amplified and inverted. If the loop between output and input is closed, the voltage difference between the two inputs of the OPA will diminish. An increase in the voltage on the inverting input will then force a complementary current on the output, which counteracts the input voltage difference. Using this principle and connecting the working electrode to the non-inverting input, the reference electrode to the inverting input, and the counter electrode to the output, the difference between working and reference electrodes can be directly amplified and inverted by the OPA. A matching current will then be fed to the counter electrode. Since the circuit is closed by the cell, the current passes the electrolyte from the counter electrode to the working electrode. This polarizes the working electrode exactly so that the difference between the reference electrode input and the working electrode input is set to zero. As such, the potential of the working electrode is kept exactly on the potential of the reference electrode. Finally, to vary the potential of the working electrode relative to the reference electrode, only a voltage in series must be inserted between working electrode input and the reference electrode. Similarly, to measure the current through the counter electrode, a resistance must be inserted in the counter electrode wiring, across which a voltage can be measured.

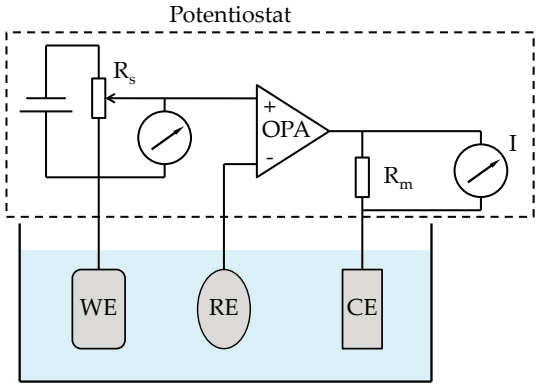

Fig. 2.22: Schematic representation of a three-electrode cell coupled to a potentiostat with potential control.

Different types of voltammetric methods can be used, the most common being linear sweep voltammetry, staircase voltammetry, and cyclic voltammetry. With linear sweep voltammetry, the current at the working electrode is measured while the potential between the working electrode and a reference electrode is ramped linearly in time. The potential at which an adsorbed species begins to be oxidized or reduced is then indicated by a current peak. In the case of staircase voltammetry, the potential is still sweeped lin-

11. It must be mention that the "+" and "–" inputs have nothing to do with polarity but simply indicate the phase relationship between the input and output signals.

early but in a series of small steps. The current is usually measured at the end of each potential step, so that the contribution to the current signal from the capacitive charging current is minimized. In cyclic voltammetry, the working electrode potential is also ramped linearly with time but the sweeping usually ends at a set potential. Then the working electrode potential is inverted and the sweep is ramped again. This cycling between negative and positive potentials can be repeated multiple times resulting in a typical voltamogram trace.

Concomitantly to the SFG spectroscopic measurements, staircase voltammetry was perfomed at the ITO/aqueous solution interface on normal water, deuterated water, and 10 mM salt anionic and cationic salt solutions by varying the applied potential in a range from -1 to +1 V in steps of 0.1 V using an analog potentiostat (Wenking LB 81M, Bank Elektronik, Germany). In addition, the induced current was also measured at each step using a multimeter coupled to the potentiostat. The current was measured at the beginning and the end of each potential step, and the values were averaged and divided by the prism area.

3

Results and Discussion

3.1 Characterization of the ITO layer

Prior to the spectroscopic and electrochemical investigation of the ITO/aqueous solution interface, it becomes also important to characterize the ITO film itself i.e., its structural, electrical, and optical properties in order to assess its quality following sputtering deposition and post-deposition annealing.

3.1.1 Chemical and structural properties

3.1.1.1 Surface chemical composition

The surface chemical composition was obtained by XPS measurements on three ITO thin films sputter-deposited and annealed on CaF_2 plates (untreated (*S1*), pH-treated at pH 3 (*S2*) and pH 9 (*S3*), respectively). As shown in Fig. 3.1a, a low-resolution survey scan of sample *S1* reveals strong In doublet peaks, In($3d_{5/2}$) and In($3d_{3/2}$), at binding energies of ~ 444.8 and ~ 452.3 eV, respectively, as well as Sn doublet peaks, Sn($3d_{5/2}$) and Sn($3d_{3/2}$), at ~ 486.9 and ~ 495.3 eV, respectively. One can also note the O($1s$) peak at ~ 530.5 eV and a C($1s$) peak at ~ 285.0 eV attributable to carbon trace impurities found on the ITO films. The residual carbon contamination ($\lesssim 20\%$) may originate from the brief exposure to air when the sample was transferred from air to vacuum, or from small amount of contamination in the preparation chamber of the XPS system.

A comparison of the peak positions and intensities for untreated and pH-treated ITO thin films can be found in Table 3.1. The binding energy values agree well with those reported in the literature for RF-sputtered ITO thin films with similar Sn doping concentration [288, 388]. From the analysis of the spectrum, the chemical composition of the films can be deduced. Using the atomic concentration given in Table 3.1, a calculated In:Sn ratio of 91.4%:8.6% was found. Thus, within the measurement uncertainty, the chemical composition of this sample is similar to the one from the target.

For sample *S1*, the C($1s$) peak, which arises from traces of adventitious carbon contamination, could be fitted with three contributions coming from CH-, CO^-- and COO^--like carbon species (Fig. 3.1b). As for the O($1s$) peak, it can also be decomposed into three contributions which can be assigned to In_2O_3-like oxygen, to hydroxides and/or oxyhydroxide such as $In(OH)_3$ and InOOH, and finally to adsorbed water and/or some adventitious oxygen-related contaminants [259] (Fig. 3.1c). A fourth contribution due to oxygen atoms adjacent to oxygen deficiency sites is often also seen in the O($1s$) peak

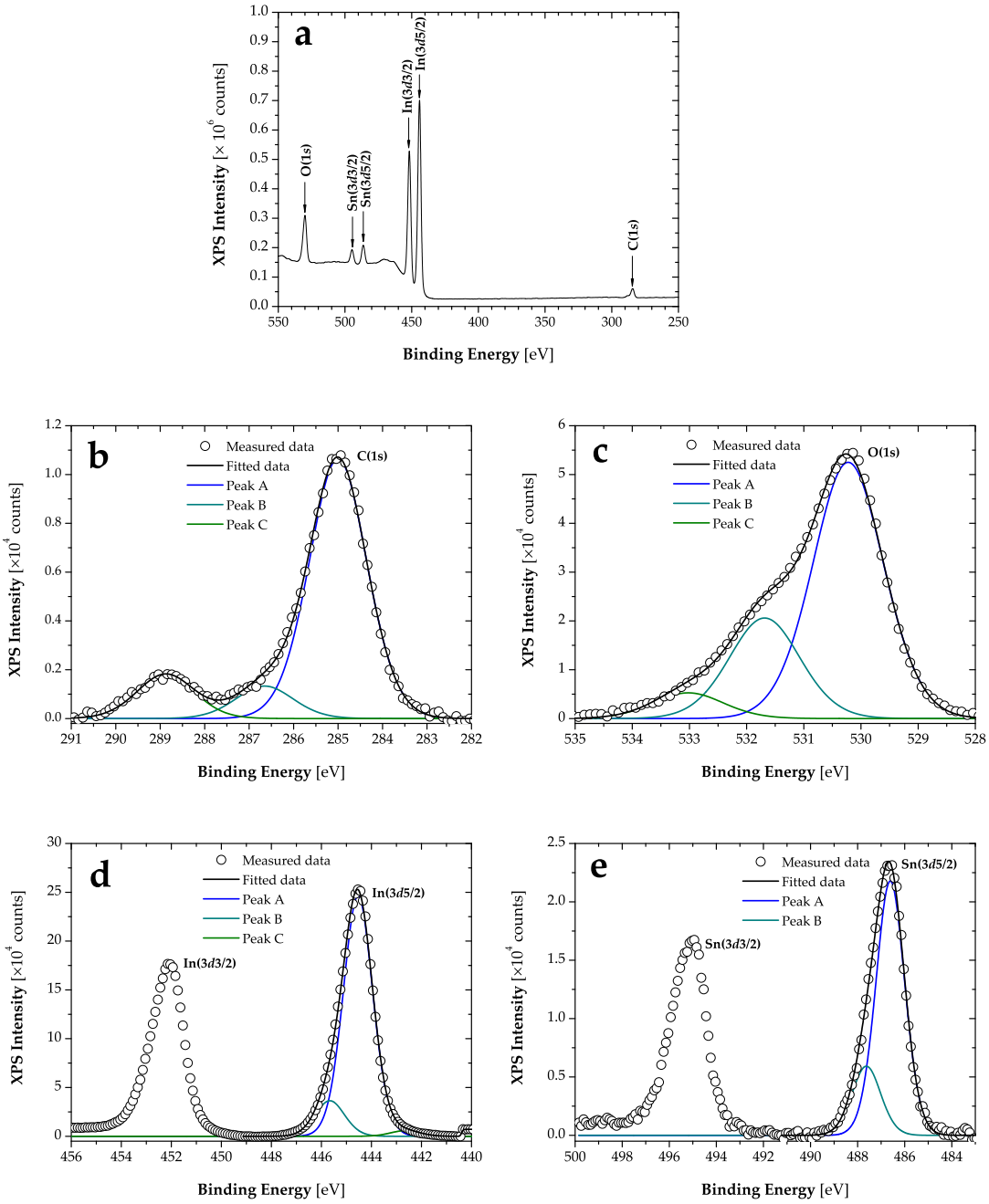

Fig. 3.1: XPS spectra of untreated and pH-treated ITO thin films sputter-deposited and annealed on CaF_2 plates. (a) Low-resolution survey scan, and high-resolution (b) C(1s), (c) O(1s), (d) In(3d), (e) Sn(3d) scans.

(seen as a weak shoulder on the left of Peak A). But this contribution did not appear as significant and was, therefore, left out. The In($3d_{5/2}$) peak in Fig. 3.1d can be fitted with three contributions which are related to In_2O_3- and $In(OH)_3$-like species. A third component remained, however, unidentified. Finally, the Sn($3d_{5/2}$) can similarly be fitted with two components related to SnO_2- and SnOH-like species (Fig. 3.1e). A third contribution,

Table 3.1: XPS peaks of untreated and pH-treated ITO thin films sputter-deposited and annealed on CaF_2 plates.

Peak	**Species**	**Binding energy** [eV]†			**At. %**		
		S1	*S2*	*S3*	*S1*	*S2*	*S3*
C(1*s*)	A: C−H/C−C	285.00	285.00	285.00	15.99	11.87	8.97
	B: C−O^-	286.65	286.81	286.57	2.02	1.87	1.02
	C: COO^-	288.88	288.87	288.68	2.76	2.33	0.93
In(3*d*5)	A: ?	442.59	—	—	0.67	—	—
	B: $In(OH)_3$	444.54	444.38	444.38	27.90	35.56	33.56
	C: ?	445.69	—	—	3.92	—	—
Sn(3*d*5)	A: Sn−O	486.64	486.54	486.44	2.49	3.7	3.20
	B: Sn−OH	487.74	—	—	0.55	—	—
O(1*s*)	A: In−O	530.21	529.87	529.86	29.49	32.80	33.15
	B: $In(OH)_3$	531.64	531.51	531.17	11.26	10.01	13.13
	C: H_2O?	532.86	533.06	532.38	2.97	1.88	6.04

Legend: *S1*, untreated; *S2*, treated at pH 3; *S3*, treated at pH 9; † referenced to C1*s* at 285.0 eV.

usually unidentified, was not used here.

In order to evaluate the effect of pH on the chemical stability of ITO in contact with acidic/basic aqueous solutions, XPS measurements were also done on two ITO-coated CaF_2 plates treated at pH 3 and 9, respectively (data not shown). For all peaks observed, the peak positions remain practically unaltered, regardless of the pH condition. However, the atomic concentration of almost all species undergo some variations (1–8%). This is particularly true for oxygen-related species. The addition of an acid or a base could possibly favor surface hydroxylation which, in turn, influences the amount of surface hydroxide and oxy-hydroxide species. It is known that undoped In_2O_3 has a favorable equilibrium constant for hydrolysis towards these species [389]. Nevertheless, the surface composition remains about the same with calculated In:Sn ratios of 90.6%:9.4% and 91.3%:8.7% at pH 3 and pH 9, respectively.

3.1.1.2 Surface crystallinity, grain size, and texture

The surface crystallinity of unannealed and annealed ITO thin films sputter-deposited on CaF_2 plates was investigated by X-ray diffraction. Fig. 3.2 shows the position of the diffraction peaks for these ITO films before and after annealing as well as those from an ITO reference (ICSD-50858, FIZ, KIT–Campus North). The XRD patterns reveal a cubic bixbyite polycrystalline structure with predominant (211), (222), (226), and (400) diffraction peaks of almost equal intensities. It is well-known that crystallographic orientations of ITO thin films are very different depending upon deposition conditions [390]. Under the applied sputtering conditions (high power, oxygen dilution; see Section 2.2.2), preferred (211), (222), and (400) orientations are usually expected [219]. Moreover, strong (222) and (400) diffraction peaks are indicative of preferred orientations along the $\langle 111 \rangle$ and $\langle 100 \rangle$ directions, respectively [243].

The different crystallographic parameters of the ITO reference as well as of the unan-

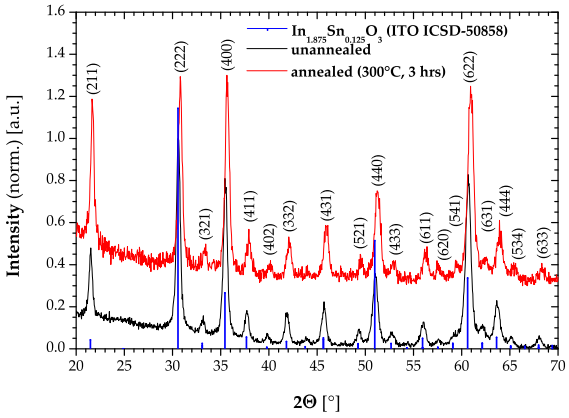

Fig. 3.2: XRD spectra of unannealed and annealed ITO thin films sputter-deposited on CaF_2 plates. The XRD patterns of unannealed (*black line*) and annealed (*red line*) ITO thin films as well as an ITO reference (ICSD-50848) (*blue line*) are shown. The symbols (hkl) denote the Miller indices of the different crystal planes.

nealed and annealed ITO films are summarized in Table 3.2. The calculated lattice constants, plane separations, and lattice distortions indicate a contraction of the ITO lattice for the unannealed and annealed lattices relative to the reference. The lattice contraction for the unannealed film could be explained by the lower Sn doping (10 wt.% compare to 12.5 wt.%), while that of the annealed film is most probably due to restructuring of the lattice during annealing. In this case, the free oxygen from the air reacts with the film and fills the oxygen vacancy sites, which leads to a more perfect structure [391, 392]. The crystallite or grain size given by the Debye-Scherrer equation falls in the range 45–70 nm for the most prominent peaks (e.g., (222) and (400)) and decreases with annealing, which also confirms some kind of lattice restructuration. The texture of ITO thin films (of a given thickness) depends on the method and conditions of deposition. The ratio between the intensity of the (222) peak to the (400) peak ($I(222)/I(400)$) for the unannealed and annealed films indicate a change in texture from the $\langle 111 \rangle$ to the $\langle 100 \rangle$ direction. This texture is often observed for thinner ITO films produced at low sputter power [393].

3.1.1.3 Surface morphology and roughness

The surface morphology of ITO, and especially the grain size and shape, was investigated by SEM (Fig. 3.3). The ITO film exhibits a dense granular structure with a sporadic distribution of grain conglomerates. The grains have irregular shapes and sizes that range from $\sim$ 10 to 20 nm. However, the observed size is lower than that derived from XRD measurements. This discrepancy could be due to the low signal-to-noise ratio obtain with the present XRD measurements. The integration time was probably insufficient ($\sim$ 1 hr) for a proper estimate of the ITO grain size. According to Eq. (2.8), a lower estimated value of w would lead to an overestimation of the grain size D.

The surface roughness of ITO thin films annealed on CaF_2 plates has been studied by means of AFM in tapping mode (Fig. 3.4). The surface was scanned for two different areas, namely, 1.0 μm$\times$1.0 μm and 0.5 μm$\times$0.5 μm. The root-mean-square surface roughness estimated from the latter AFM image was found to be in the range of $\sim$ 4.0–4.5 nm.

Table 3.2: Crystallographic parameters of unannealed and annealed ITO thin films sputter-deposited on CaF_2 plates.

Parameter	**Crystal plane**				
	Reference				
	(211)	(222)	(400)	(440)	(622)
Lattice constant (a_{ref}) [nm]	1.01247	1.01245	1.01248	1.01246	1.01249
Plane separation (d_{ref}) [nm]	0.41334	0.29227	0.25312	0.17898	0.15264
	Unannealed				
	(211)	(222)	(400)	(440)	(622)
Lattice constant (a_{exp}) [nm]	1.01059	1.01118	1.01116	1.01099	1.01087
Plane separation (d_{exp}) [nm]	0.41257	0.29190	0.25279	0.17872	0.15239
Lattice distortion (D) [%]	-0.19	-0.13	-0.13	-0.15	-0.16
Crystallite size (C) [nm]	85.1	68.4	54.3	27.1	23.1
$I(222)/I(400)$			1.225		
Film texture			$\langle 111 \rangle$		
	Annealed				
	(211)	(222)	(400)	(440)	(622)
Lattice constant (a_{exp}) [nm]	1.00139	1.00350	1.00568	1.00621	1.00727
Plane separation (d_{exp}) [nm]	0.40882	0.28968	0.25142	0.17787	0.15185
Lattice distortion (D) [%]	-1.1	-0.9	-0.7	-0.6	-0.5
Crystallite size (C) [nm]	117.1	55.3	46.3	25.5	22.4
$I(222)/I(400)$			0.994		
Film texture			$\langle 100 \rangle$		

This value agrees well with literature values (3.8–3.9 nm) obtained on other RF-sputtered ITO thin films [393], although smaller roughness (1.8–2.2 nm) have also been reported for thin films annealed in the same conditions [391].

3.1.2 Electrical properties

3.1.2.1 Sheet resistivity

The sheet resistivity was measured on ITO thin films of approximately 100 nm thickness annealed on CaF_2 half-cylinders and plates. The average values of sheet resistivity of the ITO films coated on the half-cylinders and plates were 0.0164 ± 0.001 Ω·cm $(n = 2)$ and 0.0239 ± 0.001 Ω·cm $(n = 7)$, respectively. These values fall in the range of sheet resistivity found in literature ($\sim 10^{-2}$–10^{-3} Ω·cm) for other ITO films prepared under similar sputtering (power, gas mixture, substrate temperature) and annealing (atmosphere, annealing temperature and time) conditions [393, 394]. Nevertheless, the sheet resistivity of ITO is $\sim$ 1–2 order of magnitude larger than its bulk resistivity, which is related to the

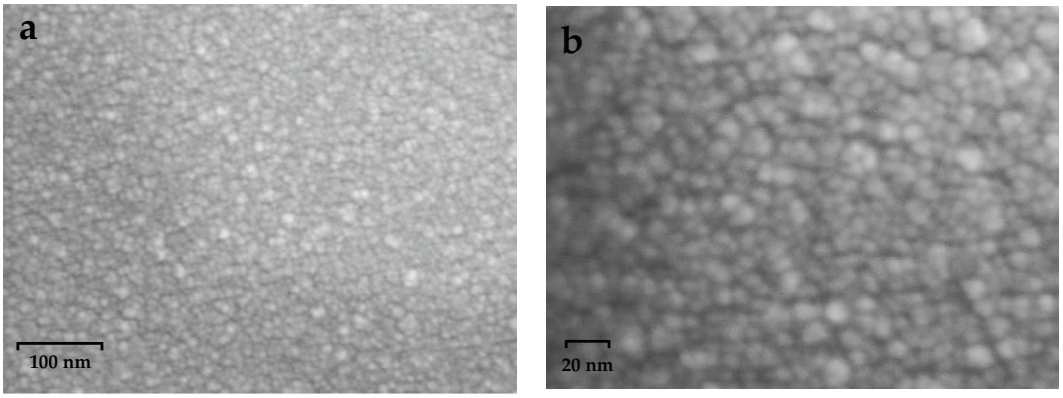

Fig. 3.3: SEM micrographs of ITO layers of unannealed and annealed ITO-coated CaF_2 plates. Surface morphology at (a) 100,000× and (b) 250,000× magnification.

concentration and mobility of charge carriers such as (see Eq. (1.7)) [395]

$$\rho_s = \frac{1}{N\mu_H e} \propto \frac{1}{N^{1/3}e} \quad [\Omega \cdot \mathrm{cm}], \tag{3.1}$$

with $N = 3.0{\times}10^{20} C_{\mathrm{Sn}}$ $[\mathrm{cm}^{-3}]$ and $\mu_H = (4e/h)(\pi/3)^{1/3} N^{-1/3}$ $[\mathrm{cm}^2/\mathrm{V{\cdot}s}]$ where C_{Sn} [at.%] is the atomic concentration of Sn dopant. Hence, for $C_{\mathrm{Sn}} = 10$ at.%, then $N = 3.0 \times 10^{21}$ cm^{-3} such that one obtains $\rho = 4.41 \times 10^{-4}$ Ω·cm $\approx 10^{-2}\rho_s$.

3.1.3 Optical properties

3.1.3.1 Thickness and optical parameters

The film thickness and optical constants of ITO films annealed on CaF_2 plates was determined by SE. Fig. 3.5 shows measured and fitted data for the ellipsometric parameters $\tan\Psi$ and $\cos\Delta$ over the spectral range 370–1050 nm for one of these films. The measured parameters are in good agreement with calculated values obtained from simulated ellipsometric curves from two-layers ITO films [396]. The fits of the ellipsometric data were found acceptable for most part of the VIS spectrum. The discrepancies appear mostly at the adsorption edges ($\lambda < 0.4$ μm and $\lambda > 0.9$ μm) caused by the bandgap transition and the free carriers absorption. The average ITO film thickness was determined to be 91.4 ± 3.2 nm ($n = 3$). The optical constants (n, k) of ITO were modeled using a Cauchy optical model, while those of the substrate CaF_2 were taken from literature [397] and were not allowed to vary during the fitting procedure (Fig. 3.6). The obtained value of the refractive index agrees well with those found in literature (1.4–1.7 $\leq n \leq$ 2.3–2.4) over similar wavelength ranges [398–400]. This model has been found to simulate adequately the refractive index since ITO is nearly transparent (i.e., its extinction coefficient can be neglected) over the VIS spectrum and part of the NIR spectrum [401]. In fact, few ellipsometric studies using more sophisticated optical models of ITO have found

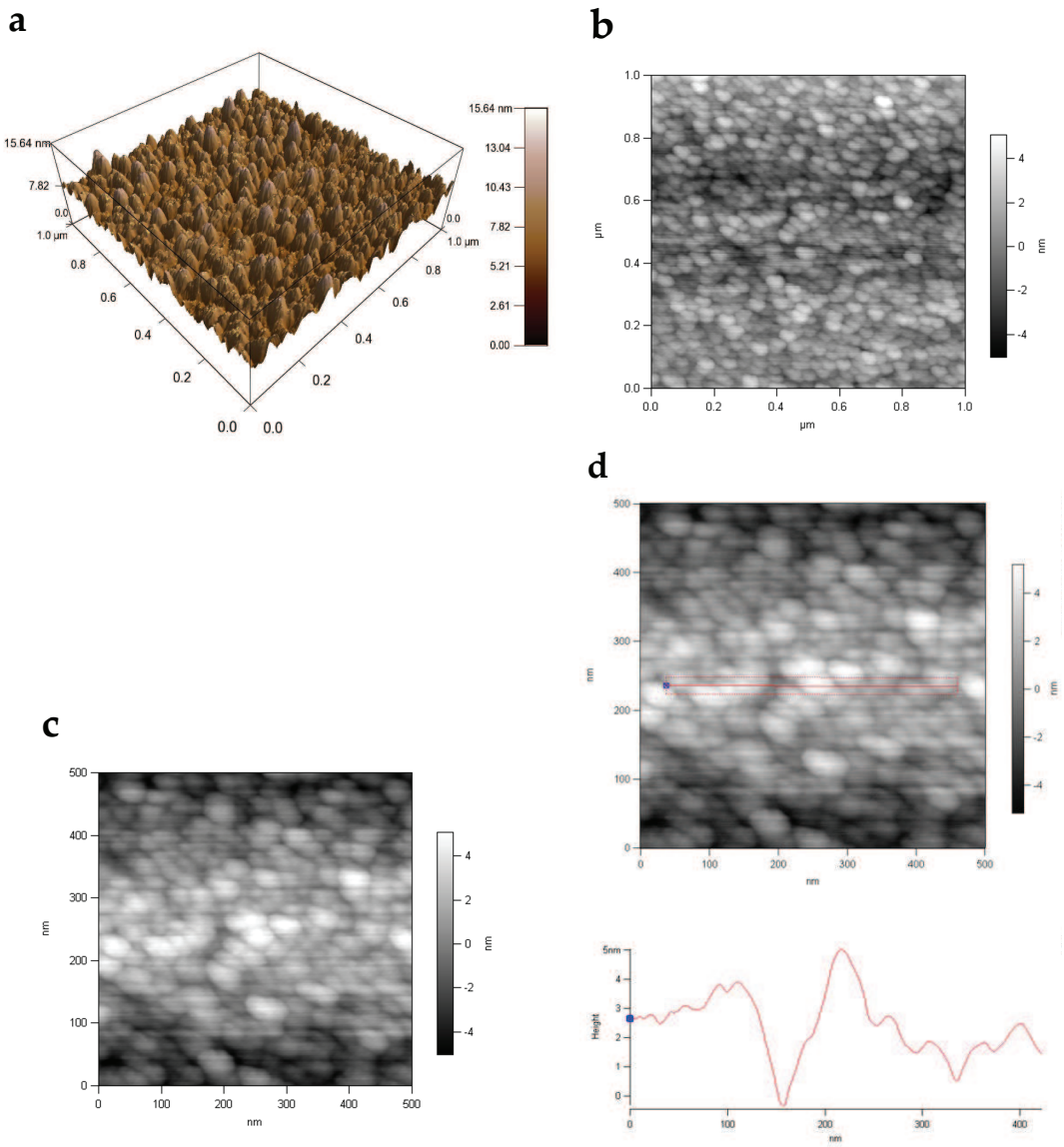

Fig. 3.4: AFM images of ITO thin films annealed on CaF_2 plates. (a) 3D and (b) 2D AFM micrographs over a 1 μm×1 μm scan area, (c) AFM micrograph over a 0.5 μm×0.5 μm scan area, and (d) the profile along the direction shown by the straight line on the same scanned area.

that $0.0 \leq k \leq 0.2$ over the selected wavelength range [398, 400]. However, as shown in Fig. 3.6b, an attempt within the Cauchy model to determine such low k values partly fails as it does not take into account the gradient of refractive index nor the small absorption of the ITO film. For instance, it has been shown that the ITO extinction coefficient is lower at the bottom of the film, suggesting that the film is more conductive near the surface, which is consistent with a graded microstructure [401]. Hence, through the Cauchy model, even a small discrepancy in the fits of the ellipsometric angles in the absorbing regions (e.g. at the bandgap edge) leads to underestimated and unphysical k values. However, this limitation can be overcome by using more complex models such as a two-layers Bruggeman effective medium approximation (EMA) model to account for the gradient structure and

surface roughness, combined with Drude and Lorentz oscillators which consider the free electron and interband transition contributions to the optical absorption [400]. Unfortunately, such complex optical modelings were not readily available within the software of the ellipsometer used in this work.

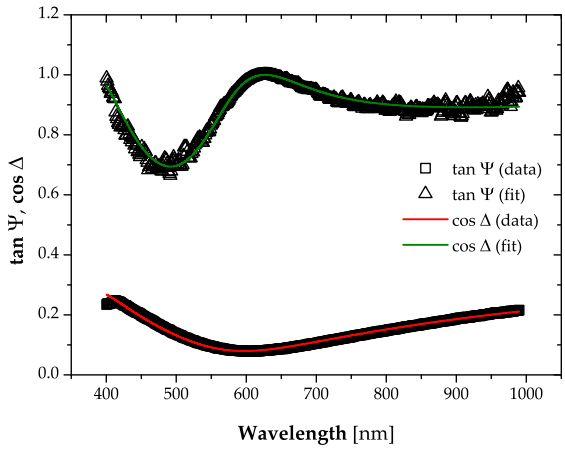

Fig. 3.5: Ellipsometric angles of ITO film annealed on CaF_2 plates. Measured (*open symbols*) and fitted data for both ellipsometric parameters $\tan\Psi$ (*red line*) and $\cos\Delta$ (*green line*) are shown.

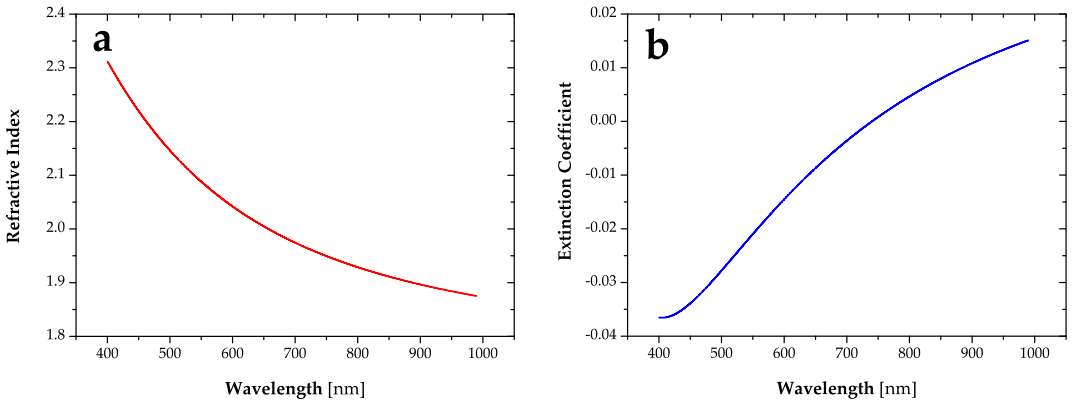

Fig. 3.6: Optical parameters of ITO thin films annealed on CaF_2 plates. (a) refractive index, (b) extinction coefficient.

3.1.3.2 UV-VIS and IR transmittance

The UV-VIS absorbance and transmittance of the ITO films annealed on CaF_2 plates was measured by UV-VIS spectroscopy at near-normal incidence. The optical band gap (E_g) was also derived by using the Tauc plot assuming that ITO behaves as a semiconductor

with direct allowed electronic transitions [318]. Fig. 3.7 shows that the ITO thin film has a transmittance higher than 80% over the whole visible range (0.4–0.8 μm) and part of the NIR range (0.8–1.0 μm) as well as a strong absorption in the near-UV range which indicates the onset of the bandgap transition. The bandgap value can be determined by extrapolation of the linear part of the plot to $\alpha = 0$. For the ITO thin film, the linearity can be seen in the absorption region (250–350 nm) and by extrapolation it was found that $E_g \approx 3.9$ eV, which is typical for a wide bandgap semiconductor and also in good agreement with literature values (E_g = 3.5–4.0 eV) [393, 402, 403].

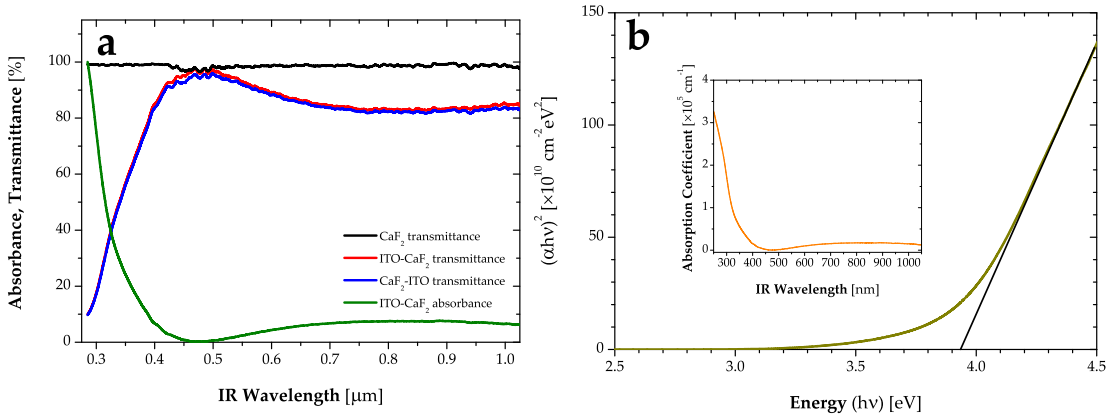

Fig. 3.7: UV-VIS transmittance and optical bandgap of ITO thin films annealed on CaF_2 plates. (a) UV-VIS absorbance and transmittance, (b) Tauc plot (optical bandgap). The spectral distribution of the absorption coefficient (α) is also shown in the inset.

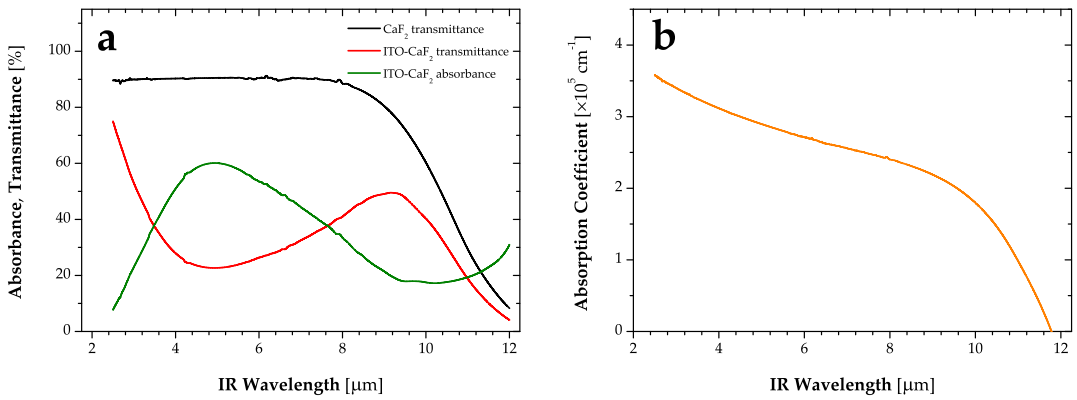

Fig. 3.8: IR transmittance of ITO thin films annealed on CaF_2 plates. (a) IR absorbance and transmittance, (b) absorption coefficient.

Similarly, the MIR absorbance and transmittance of the ITO films annealed on CaF_2 plates was measured by FTIR spectroscopy at near-normal incidence. In this region, the ITO thin film exhibits a rather strong absorption ($\sim$ 60% at most) over a range which extends from 2–8 μm which can be attributed to absorption from free electrons in the conduction band (Fig. 3.8). The onset of this absorption is given by the plasma wavelength (or frequency) which was found experimentally to be at $\lambda_p = 1.4$–1.8 μm [288, 289, 292, 404]. Since $\lambda_p = \omega_p^{-1} = (m_e^* \varepsilon_0 / Ne^2)^{1/2}$, an increase of the Sn content, and in turn, of charge carriers, should cause a blue shift of this wavelength and a concomitant decrease of the IR transmittance. However, in the present work, this onset could not be determined since it is located outside the instrumental range. Moreover, the absorption coefficient is shown to decrease steadily with wavelength from 2–10 μm.

3.2 Investigation of the ITO/aqueous solutions interface

3.2.1 Surface charging with pH at the ITO/water interface

3.2.1.1 Theoretical prediction of the isoelectric point of ITO

The IEP of simple metal oxides can be predicted using an electrostatic model which takes into account the surface charges originating from the dissociation of amphoteric surface M−OH groups and adsorption of the hydrolysis products of $M^{z+}(OH)^{z-}$ [405]. In this model, a theoretical value of the IEP for a given metal oxide can be obtained by putting that

$$\mathrm{pH_{iep}} = A - 11.5 \left(\frac{z}{R} + 0.0029(\mathrm{CFSE}) + B \right), \tag{3.2}$$

with

$$R = 2r_{\mathrm{O}} + r_{\mathrm{M}}, \tag{3.3}$$

where z is the ionic charge, $r_{\mathrm{O}} = 0.141$ nm is the radius of the oxygen ion, r_{M} is the radius of the metal ion, CFSE is the crystal field stabilization energy or correction (assumed to be zero in these calculations), and A and B are parameters depending on the coordination number of the metal ion. Since Sn^{4+} and In^{3+} occupy octahedral interstitial sites in SnO_2 and In_2O_3, the coordination number for these metal ions is 6, and therefore $A = 18.6$ and $B = 0$ [405]. The predicted IEP values obtained for SnO_2 and In_2O_3 are then $\mathrm{pH_{iep}}(SnO_2) = 5.93$ and $\mathrm{pH_{iep}}(In_2O_3) = 9.37$ [405].

For complex oxides such as ITO, the $\mathrm{pH_{iep}}$ can be considered as a mixture of the constitutive simple oxides and can be calculated by putting that [406]

$$\mathrm{pH_{iep}} = \sum_k s_k \mathrm{pH_{iep},}_k, \tag{3.4}$$

where s_k represents the molar fraction of each constituting oxide at the surface. It can be defined by

$$s_k = \frac{x_k^{2/3}}{\sum\limits_k x_k^{2/3}}, \tag{3.5}$$

where x_k is the usual volumetric molar fraction of each constituting oxide.

The commercial ITO target used in the present has a volume $V(\mathrm{ITO}) \approx 14.479\ \mathrm{cm}^3$. Noting that $\rho(\mathrm{ITO}) = 7.21\ \mathrm{g/cm}^3$ gives $m(\mathrm{ITO}) = 104.395$ g. Hence, for an ITO mixture In_2O_3:SnO_2 (90:10 wt.%), this means that $m(\mathrm{In_2O_3}) = 0.9m(\mathrm{ITO}) = 93.955$ g and $m(\mathrm{SnO_2}) = 1{-}m(\mathrm{In_2O_3}) = 10.439$ g. The molar weight of SnO_2 and In_2O_3 are 150.71 g/mol and 277.64 g/mol, respectively, which gives, in turn, $n(\mathrm{SnO_2}) = 0.06927$ and $n(\mathrm{In_2O_3}) \approx 0.33841$. The volumetric molar fractions of SnO_2 and In_2O_3 are then $x(\mathrm{In_2O_3}) \approx 0.83009$ and $x(\mathrm{SnO_2}) = 1 - x(\mathrm{In_2O_3}) \approx 0.16991$ which then gives, using Eq. (3.5), surface molar fractions of $s(\mathrm{In_2O_3}) \approx 0.74221$ and $s(\mathrm{SnO_2}) = 1 - s(\mathrm{In_2O_3}) \approx 0.25779$. By substituting these values in Eq. (3.4) and using the IEP of both constituting oxides, one finally obtains that

$$\begin{aligned} \mathrm{pH_{iep}(ITO)} &= s_{\mathrm{SnO_2}}\mathrm{pH_{iep}(SnO_2)} + s_{\mathrm{In_2O_3}}\mathrm{pH_{iep}(In_2O_3)} \\ &= 0.258(5.93) + 0.742(9.37) \approx 8.48. \end{aligned} \tag{3.6}$$

The IEP value predicted by Eq. (3.6) agrees well with some values given in the literature but is also at variance with some others (Table 3.3). The discrepancy found between these values depends mainly on the measuring method used and also on the form (particle or film) and physico-chemical properties (crystallinity, size, etc.) of the given ITO sample. Moreover, the calculations given above neglect the corrections provided by the CFSE factors, which have been shown to be significant for most divalent and trivalent metal ions [405].

3.2.1.2 Experimental determination of the isoelectric point of ITO

The isoelectric point of ITO has been determined experimentally by measuring the zeta potential at the ITO/aqueous solution interface with solutions at different pHs. Fig. 3.9 shows the electrokinetic curves obtained by doing HCl titration as well as a mixed HCl/-NaOH titration. The effect of added salt on the zeta potential was also tested. As shown in Fig. 3.9, for all titrations, the zeta potential of ITO is negative almost over the whole pH range. As expected, it becomes zero at the IEP which is found at very low pH values. Similar IEP values of $\mathrm{pH_{iep}} \approx 3.2$ and $\mathrm{pH_{iep}} \approx 3.3$ were determined from the HCl and HCl/NaOH titrations, respectively. These results would go in line with the fact that because ITO is a n-type, wide bandgap semiconductor, its surface must be initially negatively charged. Furthermore, from the HCl/NaOH titration, the positive zeta potential measured at the slipping plane (i.e., the plane at the onset of the diffuse layer) at pH values below the IEP ($\mathrm{pH} < \mathrm{pH_{iep}}$) would suggests that the charge of the cations (H_3O^+)

Table 3.3: Comparison of the experimental and theoretical IEP values of ITO.

Method	Form	IEP	Material, Substrate, Solution	Ref.
particle adhesion	TF	4.3±0.3	deposited, In:Sn 90:10 wt.%, soda-lime SiO_2, HNO_3 10 mM/KOH	[276]
streaming potential	TF	2.9±0.2	deposited, 130-140 nm, Si, H_2O	[409]
particle adhesion	TF	∼ 5	deposited, 30–60 nm, glass, 0.34 mM KOH	[410]
zeta potential	NP	8.5	grown, H_2O, EG/HCO_3 dispersant	[411]
zeta potential	NP	7.0-8.0	???	[412]
zeta potential	NP	∼6.0	commercial, 90:10 wt.% (In:Sn), ∼20 nm, H_2O	[408]
zeta potential	NP	4.9	commercial, 90:10 wt.% (In:Sn), ∼60 nm, H_2O	[413]
zeta potential	NP	7.35	grown, 90:10 wt.% (In:Sn), ∼20 nm, H_2O	[414]
UV-VIS spectroscopy	NP	7.42	grown, 90:10 wt.% (In:Sn), ∼20 nm, H_2O	[414]
zeta potential	NP	9.5-10	commercial, 90:10 wt.% (In:Sn), ∼50 nm, H_2O	[415]
			Theoretical	
electrostatic modelling	—	8.5	—	[408]
electrostatic modelling	—	8.03	—	[414]

Legend: NP, nanoparticle; TF, thin film.

adsorbed at the interface exceeds that of the negatively charged surface groups (M−O^-). With addition of NaOH, the amount of H_3O^+ cations decreases because of their neutralization with OH^- anions. The Na^+ co-ions are assumed to remain in the diffuse layer. At the IEP ($pH \approx pH_{iep}$), the lesser amount of H_3O^+ cations barely compensates the negatively charged surface such that the zeta potential equals zero. Finally, at pH values above the IEP ($pH > pH_{iep}$), the amount of negatively charged surface groups increasingly exceeds that of the adsorbed cations, and the zeta potential becomes more negative. A model summarizing the behavior of the zeta potential with pH at the ITO/aqueous solution interface is given in Fig. 3.10.

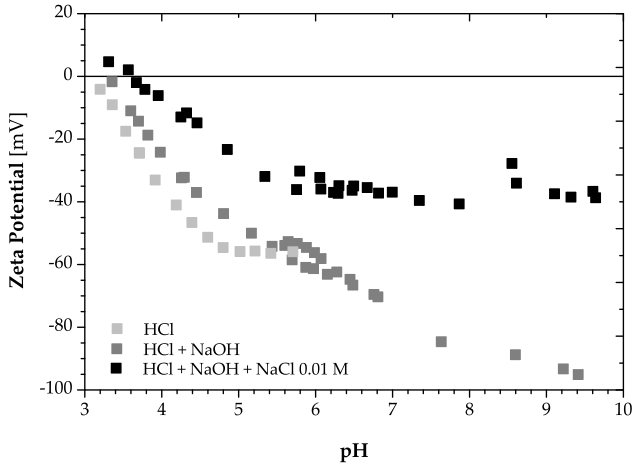

Fig. 3.9: Zeta potential measurements of ITO-coated CaF_2 plates in contact with aqueous solutions (source: J. Lützenkirchen (INE, KIT - Campus North)).

The IEP value of ITO determined in the present work is at variance with other IEP values obtained by zeta potential and found in literature (Fig. 3.11). As can be seen, the

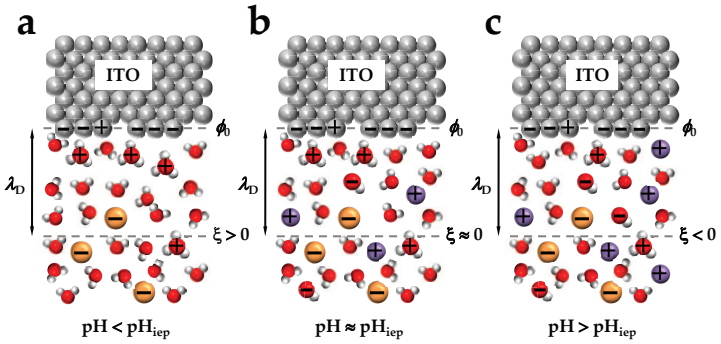

Fig. 3.10: Schematic model of the pH dependency of the zeta potential for a solid charged surface in contact with aqueous solutions.

published IEP values are quite dispersed, ranging from pH_{iep} 3 to 9. As previously mentioned, the discrepancy could depend on the measuring method used and also on the form and physico-chemical properties of the ITO sample. However, when restricted to ITO thin films, the IEP value given here agrees fairly well with experimental values obtained by other methods (Table 3.3).

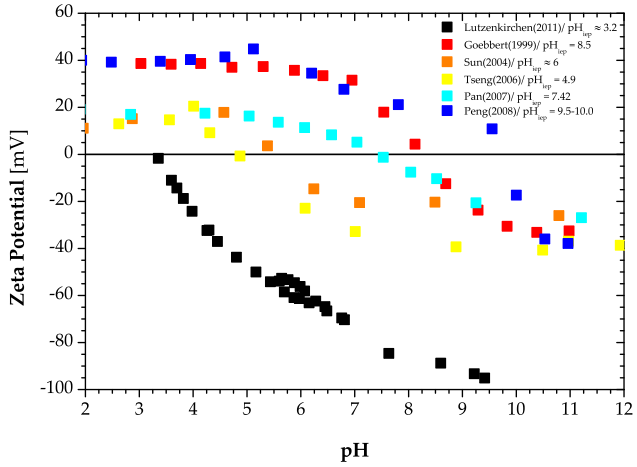

Fig. 3.11: Comparison of electrokinetic curves obtained in the present work and in literature by zeta potential measurements on ITO nanoparticles and thin films in contact with aqueous solutions.

The addition of salt in the titration solution has also an influence on the zeta potential at the ITO/aqueous solution interface. Fig. 3.9 shows, for instance, that adding 10 mM NaCl salt solution effectively reduces the magnitude of the zeta potential. In view of the previously developed model, this would means that a certain amount of Na^+ cations also adsorb at the interface, together with the H_3O^+ cations, therefore further increasing the screening of the negatively charged surface. In addition, one can note that the addition of salt has also for effect to slightly shift upward the IEP ($pH_{iep} \approx 3.6$) which indicate that less H_3O^+ cations are required to overcome the surface negative charge because of the presence of the adsorbed salt cations. Finally, a small peak at pH 8.5–8.6 that could be associated to some corrosive effects of NaCl is also observed.

It can be assumed that the extent by which the negative surface charge of ITO can be compensate through salt addition depends, on one hand, on the salt concentration, and on the other hand, on the type of ion. To investigate these two possibilities, zeta potential measurements were also performed with different chloride salt solutions at several concentrations (Fig. 3.12). As expected, the increase in concentration for any ion substantially reduces the magnitude of the zeta potential. Similarly to NaCl, the accumulation of these cations at the ITO surface compensates its negative charge. Interestingly, although all salts follow the same tendency, the screening efficiency is different for the different type of cations. Indeed, Li^+ cations compensate the surface charge to a lesser extent than K^+ and Rb^+ cations which have a comparable efficiency. This seems to contradict the fact that Li^+ cations should be able to screen more effectively simply because of their high surface charge density. Moreover, it does not support the law of matching water affinities that would favor the interaction between a hard, strongly hydrated surface group ($M{-}O^-$) and a hard, strongly hydrated cation such as Li^+. A possible cause of this contradictory behavior could lie in the different ionic size. In contrast to Li^+, it could be easier for larger cations like K^+ and Rb^+ to compete against and displace H_3O^+ cations from a negatively charged site. This would then render these cations more efficient in screening the surface charge. However, as shown in Fig. 3.12, at higher salt concentrations this distinction disappears since the amount of alkaline cations at the interface exceeds by far that of H_3O^+.

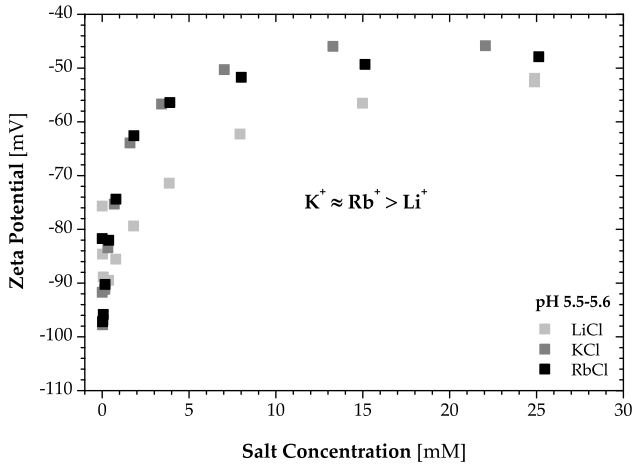

Fig. 3.12: Zeta potential measurements of ITO-coated CaF_2 plates in contact with chloride salt solutions at different concentrations (source: J. Lützenkirchen (INE, KIT - Campus North)).

3.2.2 Surface charging with applied potential at the ITO/aqueous solution interface

3.2.2.1 Surface current density

3.2.2.1.1 Normal and deuterated water

The dependence of surface current density on applied potential was first measured at the ITO/water interface with normal and deuterated water (Fig. 3.13). As can be seen,

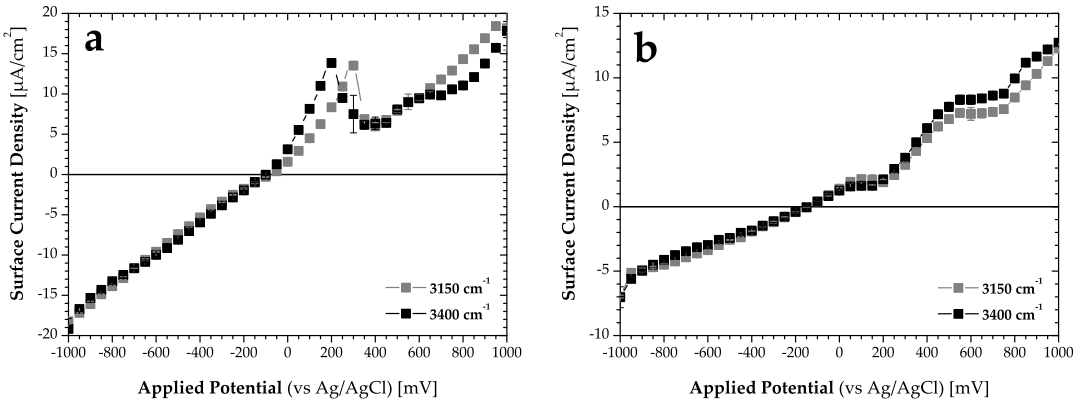

Fig. 3.13: Surface current density of water as function of applied potential associated with the spectroscopic measurements in the 3150 and 3400 cm^{-1} water spectral regions. (a) normal water, (b) deuterated water.

both curves show indications of water electrolysis as well as some small corrosive effects at the ITO thin film surface. This behavior was also reproducible for both spectral regions. Traditionally, with cyclic voltammetry, the surface current density curve can generally be divided into three regions, an ideal polarizable region (IPR) which gives minimal current variations and appears as a plateau, and anodic (positive potential) and cathodic (negative potential) regions which exhibit important faradaic currents responsible for the water electrolysis. This water splitting effect on ITO films in water has already been demonstrated by cyclic voltammetry at high scan rates (100 mV/s) [410]. An IPR was found in the range -450–+800 mV (vs Ag/AgCl) and negative and positive surface current densities of $\sim -25\ \mu A/cm^2$ and $\sim +90\ \mu A/cm^2$ were found in the cathodic and anodic regions, respectively. In the present case, however, no IPR could be observed and smaller current densities were observed in the faradaic regions. This could be explained by the fact that in contrast to cyclic voltammetry, staircase voltammetry allows capacitive charges (or currents) to attain equilibrium at each potential step, thereby reducing their accumulation at the electrodes.

It is well known that electrolysis of water in acidic solution can be expressed by two half-reactions (oxidative and reductive) such as

$$2\,H_2O_{(l)} \longrightarrow O_{2(g)} + 4\,H^+{}_{(aq)} + 4\,e^- \quad \text{(anodic region)}, \tag{3.7a}$$

$$2\,H^+{}_{(aq)} + 2\,e^- \longrightarrow H_{2(g)} \quad \text{(cathodic region)}. \tag{3.7b}$$

Within the anodic region, an oxidative reaction occurs and generates oxygen gas as well as hydronium ions, and gives electrons to the WE which then enter the external circuit. The current (and electric field) are usually defined opposite to the flow of electrons through the external circuit. Hence, the electric field was directed out of the WE into the solution. In contrast, in the cathodic region, a reductive reaction takes place, with

electrons from the WE being given to hydronium ions to form hydrogen gas. Most of the hydrogen gas produced will then diffuse as gas bubbles on the electrode. This gas evolution was readily observed on the ITO surface near the electrode contact, usually at high applied potentials ($|V| \lesssim 1$ V).

Finally, the corrosive effects observed as a current spike at 200–300 mV in the surface density curve of H_2O (but not clearly in that of D_2O) can be explained by noting that in the second half-reaction, a certain amount of monatomic H could be produced and adsorbed on the substrate, where it may react according to Eq. (1.4). The possibility of having some small salt contamination which could come from the normal KCl leakage of the RE also cannot be excluded. Although the aqueous-based reduction reaction of gaseous hydrogen with most metallic oxides usually takes place at high temperatures, it has been reported that hydrogen generated by the electrolysis of water can reduce In−O−In bonds to In even at room temperature based on the high reactivity of the freshly generated hydrogen [278].

3.2.2.1.2 Anionic salt solutions

Fig. 3.14 shows the measured surface current density as function of applied potential for anionic salt solutions with Na^+ as common cation. Similarly to water, the surface density curves of the anions also exhibit gas evolution ($O_{2(g)}$ and $H_{2(g)}$) at large negative and positive potentials. However, bubble formation was not observed for Na_2CO_3, Na_2HPO_4, $NaNO_3$, and NaSCN solutions. All curves were to some extent reproducible in both water spectral regions, with the exception of Na_2CO_3 and NaSCN. The reason for this different behavior remains however unknown. The surface current densities at negative potentials are rather large for most salts (-100– -200 μA/cm^2) but about one order of magnitude lower for Na_2HPO_4 and NaSCN solutions which could indicate some charge compensation through adsorption of these ions. On the other hand, at positive potentials, all salts have about the same current densities ($\leq$50 μA/cm^2).

Some corrosive effects at positive potentials also appear for most of the salt solutions, with the exception of Na_2HPO_4, $NaNO_3$ and NaSCN, which exhibited little to no electroactivity. All other solutions, especially those with an halogenated anion (Br^-, I^-) have pronounced corrosion peaks with an onset in the range of 200–300 mV. Incidently, the anodic dissolution of ITO seems to start at potentials close to the standard redox potentials of some of these salts. For instance, for the Br^-/Br_2 and I^-/I_2 reactions, the redox potentials are ~ 0.87 V and ~ 0.34 V (vs Ag/AgCl), respectively. As was shown for chloride ions, the creation of radicals from these ions could induce a breakdown of the ITO surface structure [280]. This effect is also enhanced by the fact that the salt solutions were slightly acidic (pH 5.2–5.5).

3.2.2.1.3 Cationic salt solutions

The surface current density was also measured for cationic salt solutions with Cl^- as common anion (Fig. 3.15). As expected, the gas evolution is also present for all solutions but bubble formation was observed for none of them, with the exception of CsCl. All curves show a relative reproducibility in both water spectral regions, apart from LiCl and NH_4Cl. Moreover, the surface current densities are comparable at negative (-100– -150 μA/cm^2) and at positive ($\leq$50 μA/cm^2) potentials for all studied cationic salts.

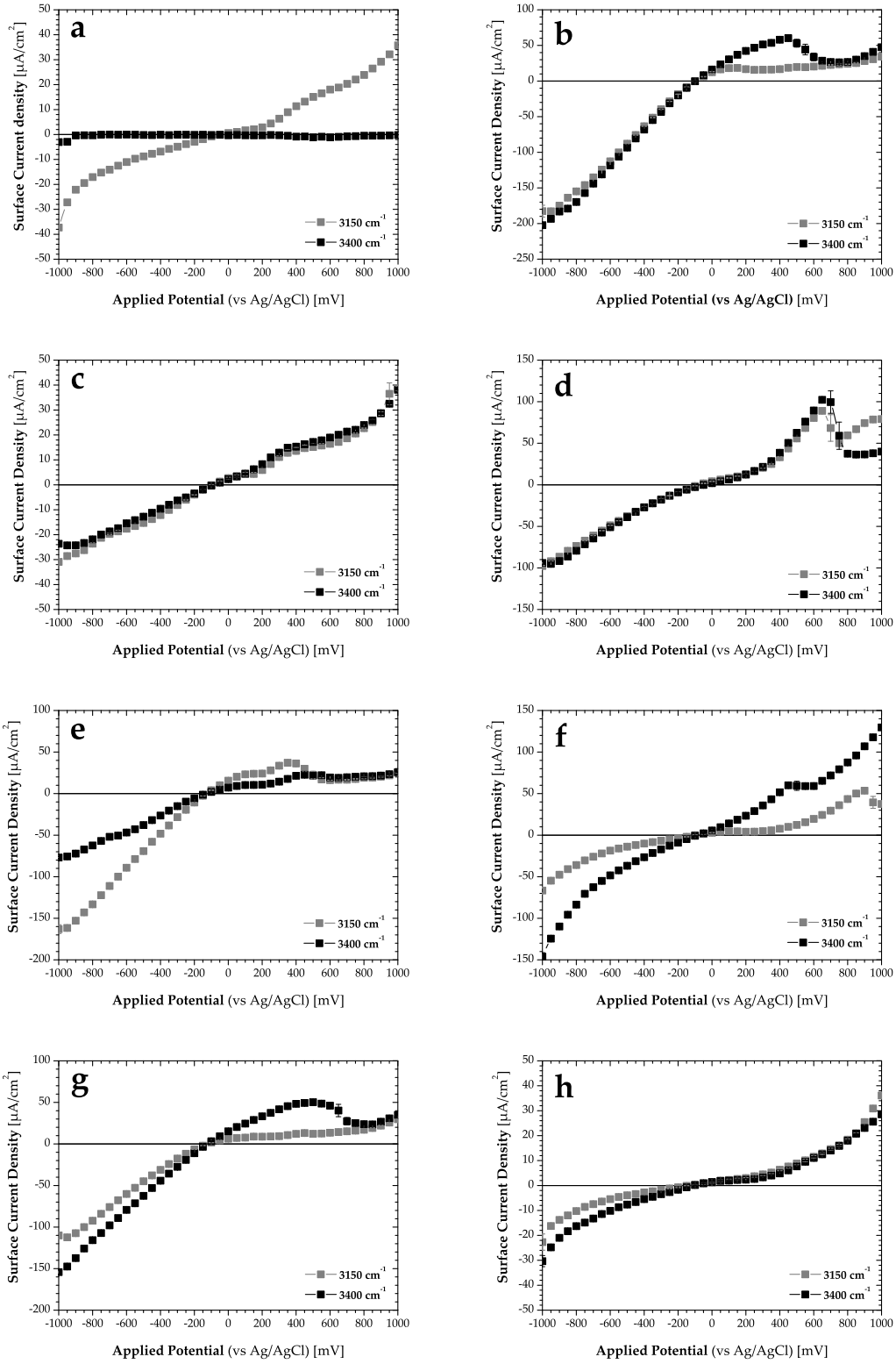

Fig. 3.14: Surface current density of anionic aqueous salt solutions as function of applied potential associated with the spectroscopic measurements in the 3150 and 3400 cm^{-1} water spectral regions. (a) Na_2CO_3, (b) Na_2SO_4, (c) Na_2HPO_4, (d) NaBr, (e) $NaNO_3$, (f) NaI, (g) $NaClO_4$, and (h) NaSCN.

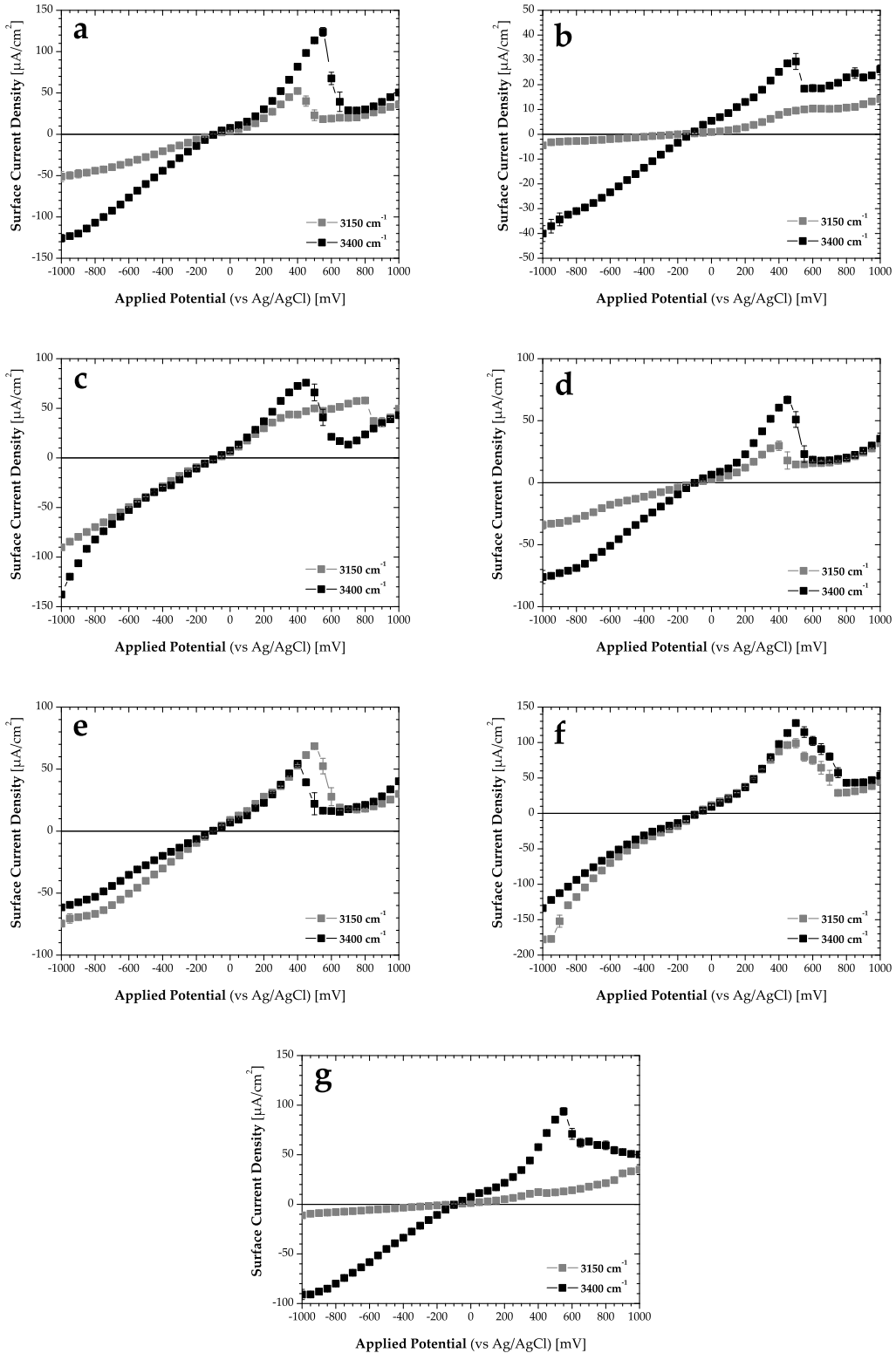

Fig. 3.15: Surface current density of cationic aqueous salt solutions as function of applied potential associated with the spectroscopic measurements in the 3150 and 3400 cm^{-1} water spectral regions. (a) $CaCl_2$, (b) LiCl, (c) NaCl, (d) KCl, (e) RbCl, (f) CsCl, and (g) NH_4Cl.

The corrosive peaks are omnipresent for all chloride salts and their intensity is about two-fold higher than that of the anionic salts. Again the onset of these peaks can be found in the range 200–300 mV. The effect of chloride solutions on ITO dissolution has been documented and models have been proposed to explain it [280]. The standard redox potential of the Cl^-/Cl_2 falls around 1.1 V (vs Ag/AgCl). Cyclic voltamograms obtained at slow scan rates with ITO in contact with chloride solutions have also reported similar corrosion peaks [281].

3.2.2.2 Influence of applied potential on water ordering

3.2.2.2.1 Normal and deuterated water

The SFG response of water as function of applied potential was first measured at the ITO/water interface with normal and deuterated water in the bonded-OH spectral regions at $\sim$ 3150 cm^{-1} (Figs. 3.16–3.17) and $\sim$ 3400 cm^{-1} (Figs. 3.18–3.19). The measurement at the ITO/deuterated water interface was used as the control experiment. By inspection of Figs. 3.16 and 3.17, it can be observed that the SFG signal measured in the $\sim$ 3150 cm^{-1} is fairly different between D_2O and H_2O. For instance, with applied potential, the SFG signal of D_2O follows a slow increase, while that of H_2O exhibits a maximum. However, the position of the maximal SFG intensity for D_2O is shifted more strongly than the one of H_2O. In contrast, in the $\sim$ 3400 cm^{-1} region, both SFG signals show similarities, for example, a steep increase of the SFG signal towards a plateau phase as well as an increase in the frequency shift, but only at positive applied potentials (Figs. 3.18 and 3.19).

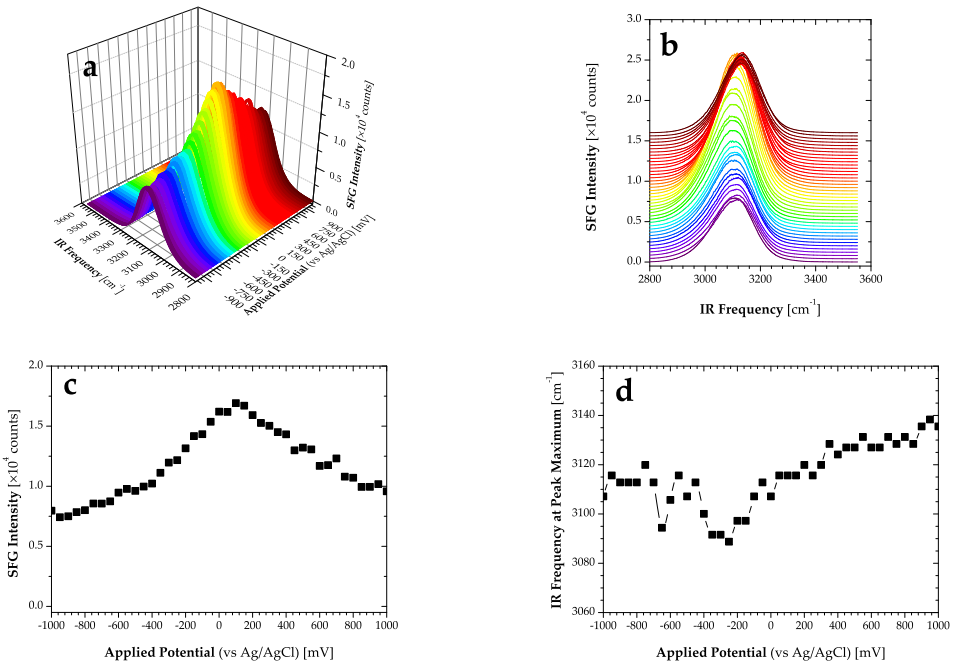

Fig. 3.16: SFG intensity of H_2O as function of applied potential in the 3150 cm^{-1} water spectral region. SFG intensity as function of potential in (a) 3D and (b) 2D representations, (c) SFG intensity at maximum as function of applied potential, and (d) IR frequency shift at maximum SFG intensity as function of applied potential.

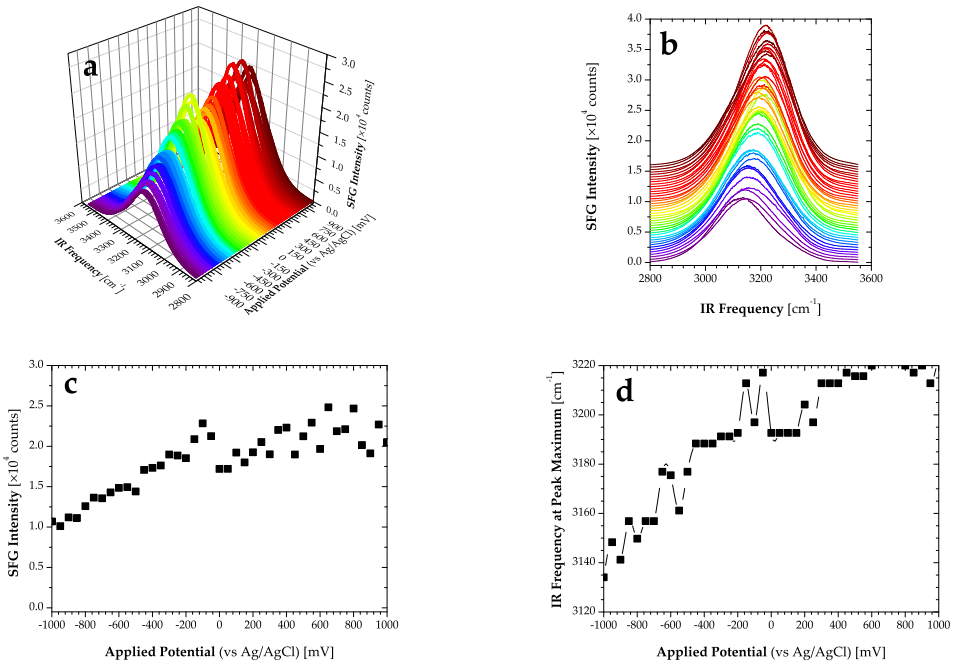

Fig. 3.17: SFG intensity of D_2O as function of applied potential in the 3150 cm^{-1} water spectral region. SFG intensity as function of potential in (a) 3D and (b) 2D representations, (c) SFG intensity at maximum as function of applied potential, and (d) IR frequency shift at maximum SFG intensity as function of applied potential.

A closer comparison of the SFG responses of D_2O and H_2O and their dependency on the applied potential for both bonded-OH spectral regions is given in Fig. 3.20. As mentioned previously, the SFG signal of D_2O serves as control and represents all nonlinear contributions other than those of H_2O, for instance, the NR contributions coming from intra- and interband electronics transitions in the bulk of ITO. As shown in Fig. 3.20, the SFG response of D_2O shows a small dependence on applied potential which would confirm the presence of some potential-dependent, NR response coming from the ITO substrate. In both spectral regions, this signal varies with applied potential by about a factor 2. In contrast, the SFG response of H_2O seems to be dominated by this NR contribution but only up to a given positive potential which could potentially be considered as the potential at zero charge (V_{pzc}). The inflection point of the H_2O curve at 3400 cm^{-1} can be obtained through a sigmoidal Boltzmann fit (data not shown) and is found at ~ 134 mV. Interestingly, this value falls close to the potential at zero charge determined from the work function of the substrate. It is well known that the potential at zero charge and the work function of a conductive material are directly related to each other such as [416]

$$V_{\text{pzc}} = \frac{\Phi_{\text{M}}}{e} - 0.4\alpha - (4.31 + C), \tag{3.8}$$

where α is a dipolar contribution coming from ordered water molecules at the electrode surface and which takes a value between 0 and 1, the constant 4.31 V refers to an absolute electrode potential for the SHE (rescaled to the Ag/AgCl reference electrode), and the

constant C denotes the dipolar contribution of the metal/electrolyte interface (for metals, $C \approx +0.3$ V). With Φ_M(ITO) = 4.75 eV [417], and putting that $\alpha = 0$ and $C = +0.3$ V, one obtains that V_{pzc}(ITO) ≈ 0.14 V or 140 mV.

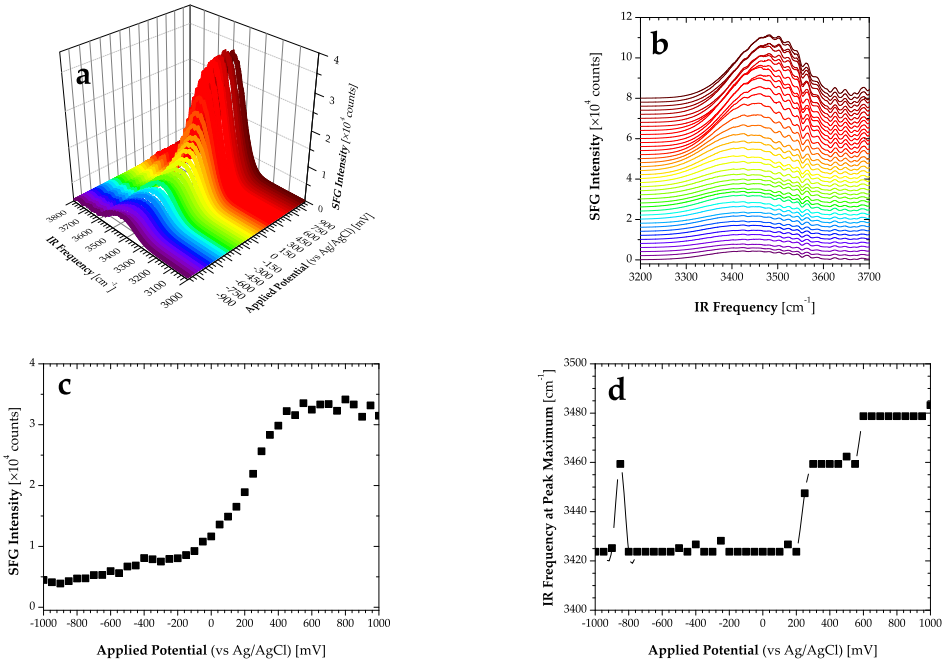

Fig. 3.18: SFG intensity of H_2O as function of applied potential in the 3400 cm^{-1} water spectral region. SFG intensity as function of potential in (a) 3D and (b) 2D representations, (c) SFG intensity at maximum as function of applied potential, and (d) IR frequency shift at maximum SFG intensity as function of applied potential.

At higher applied potentials, the SFG response behaves differently depending on the spectral region. In the 3150 cm^{-1} region, the SFG signal decreases below the level of the corresponding D_2O signal by about a factor 2, whereas for the 3400 cm^{-1} region, the signal increases drastically by a factor 3 up to a plateau. This is only observable when one proceeds to a rescaling of the D_2O response to that of H_2O. However, since both experiments were done separately i.e., for each solution, the incident beams were slightly realigned, the SFG signal maximized, and compared with its own REF signal, it appears difficult to do a strict quantitative comparison between the two sets of data. This could be done only when the ratio between SFG and REF signals for the two data sets is comparable, which was not ideally the case here. Hence, it is difficult from this data to ascertain whether the NR signal from ITO actually dominates the resonant SFG signal from water such that both solutions reflect only NR contributions from the substrate, or if there is an actual increase in the resonant SFG signal of water at positive potentials as suggested [1]. An insight about the importance of the ITO NR response could be gained

1. Independent SFG measurements performed at an incident angle of 45° over the whole bonded-OH water spectral region on an ITO-coated equilateral sapphire prism showed that the SFG response from ITO/D_2O and ITO/H_2O interfaces are fairly similar, thus favoring the first scenario. However, these SFG experiments were conducted under different angular conditions in comparison to the one used here ($\theta \approx 65°$) (M. Bonn and coworkers (AMOLF, The Netherlands), private communication).

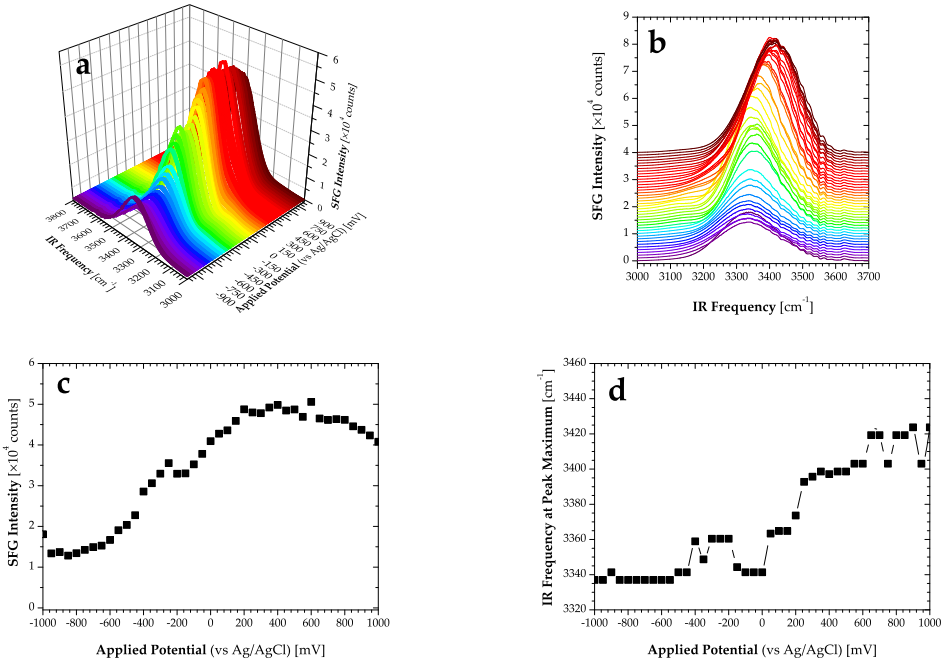

Fig. 3.19: SFG intensity of D_2O as function of applied potential in the 3400 cm^{-1} water spectral region. SFG intensity as function of potential in (a) 3D and (b) 2D representations, (c) SFG intensity at maximum as function of applied potential, and (d) IR frequency shift at maximum SFG intensity as function of applied potential.

by simulating the dependency on angular and polarization configuration conditions of the nonlinear Fresnel coefficients at the ITO/water interface. This could demonstrate whether or not the SFG signal is dominated by the substrate response. Nevertheless, the difference in the SFG response for the two water regions would suggest that the weakly and strongly correlated water species have different distributions in the interfacial region as demonstrated recently at the silica/water interface [106].

3.2.2.2.2 Anionic salt solutions series

Similarly to the SFG measurements with D_2O and H_2O, the SFG response of water as function of applied potential was also measured at the ITO/aqueous solution interface for a series of 10 mM anionic Na^+ salt solutions in the bonded-OH spectral regions at $\sim$3150 cm^{-1} (Figs. 3.21–3.29) and $\sim$3400 cm^{-1} (Figs. 3.30–3.38).

A comparison of the SFG responses of all anionic Na^+ salts and their dependency on the applied potential for both bonded-OH spectral regions is also given (Fig. 3.39). Contrary to the case of H_2O and D_2O, a comparison between the SFG responses of the different salt solutions is, to some extent, possible for most of them since within the complete set of measurements, the ratio between SFG and REF signals was often very comparable. In the 3150 cm^{-1} region, the SFG response has been represented in a potential range from -800 to +400 mV to minimize the influence of faradaic effects as well as some corrosion effects, especially important with halogenated salts. As can be seen in Fig. 3.39a, the

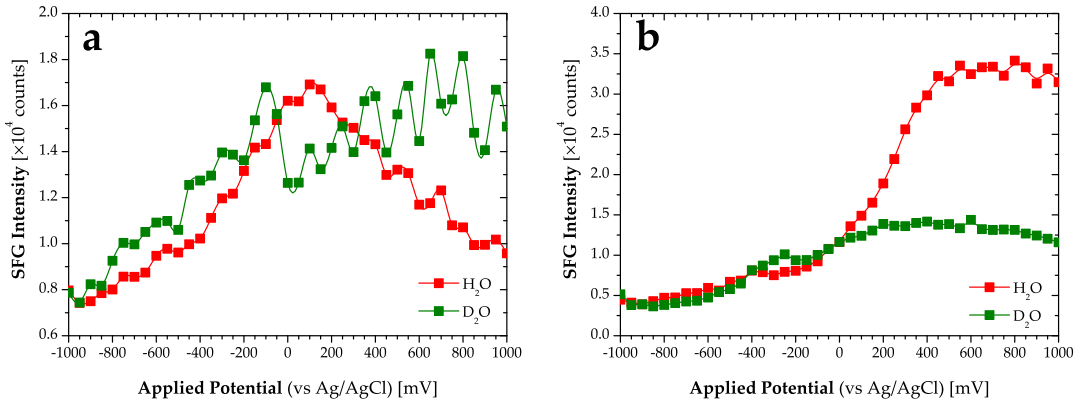

Fig. 3.20: Comparison of SFG intensity at maximum of D_2O and H_2O as function of applied potential in the 3150 and 3400 cm^{-1} water spectral regions. (a) 3150 cm^{-1}, (b) 3400 cm^{-1}. In both regions, the SFG signal of D_2O has been rescaled to that of H_2O.

SFG signal for some salts appears rather disperse and erratic. Nevertheless, with the exception of NaI whose behavior remains unclear, the salts can be categorized in three groups according to their response relative to that of H_2O. A first group concerns salts with a response similar to that of H_2O such as Na_2SO_4, Na_2HPO_4, $NaNO_3$, and to some extent Na_2CO_3. A second group which includes salts like $NaClO_4$ and NaSCN have a larger SFG response with respect to H_2O. The remaining group includes all salts that have an intermediary response relative to the two other groups. This group includes halogenated salts such as NaCl and NaBr. In addition, the latter salts show already the onset of corrosion effects around 200 mV. In contrast, in the 3400 cm^{-1} region, the SFG response for each salt appears much less noisy but still follows the same kind of trend observed in the 3150 cm^{-1} region with the $NaClO_4$ and NaSCN salts having the largest SFG response. These results taken together would suggests that hard ions like Na_2CO_3, Na_2SO_4, Na_2HPO_4 have little to no affinity for the ITO surface, whereas soft ions such as $NaClO_4$ and NaSCN have a much stronger affinity. Following the law of matching water affinities, this would imply that at positive potentials the surface groups of ITO would behave also as soft ions since soft/soft interactions are energetically favored. A possible candidate of a soft surface group would be to have a doubly protonated OH group, which would mean to consider the ITO surface as positively charged in this potential range.

3.2.2.2.3 Cationic salt solutions

The SFG response of water as function of applied potential was also measured at the ITO/aqueous solution interface for a series of 10 mM cationic Cl^- salt solutions in the bonded-OH spectral regions at $\sim 3150\ cm^{-1}$ (Figs. 3.40–3.46) and $\sim 3400\ cm^{-1}$ (Figs. 3.47–3.53).

A comparison of the SFG responses of all cationic Cl^- salts and their dependency on the applied potential for both bonded-OH spectral regions is also given (Fig. 3.54). In both spectral regions, the SFG spectra have been plotted in an applied potential range from -800 to +400 mV, again to exclude potential faradaic effects as well as the corrosion effects inherent to the use of chloride salts. Similarly to the Na^+ salts in the 3150 cm^{-1} region, the SFG response of Cl^- salts indicates that some of them like RbCl, CsCl, and NH_4Cl increase the water signal while others such as LiCl, NaCl, and to some extent, $CaCl_2$ have no significant effect. This behavior is however not so apparent with these anions in the 3400 cm^{-1} region, where the SFG response of almost all ions does not deviate significantly for that of H_2O. A definite picture of the anions behavior at the ITO surface for this water species remains therefore unclear. Nevertheless, the results obtained in the 3150 cm^{-1} region still further suggest pairing between soft ions according to the law of matching water affinities. This however leads to the situation of having positive, soft ions (e.g. Rb^+, Cs^+ or NH_4^+) with high affinity for a positively charged ITO surface, which is highly unlikely. As such, the model previously developed to explain the behavior of anions cannot be applied in any way to the cations. Unfortunately, in the course of this work, no other physical model could be found that would describe satisfactorily the behavior of both anions and cations at the ITO surface.

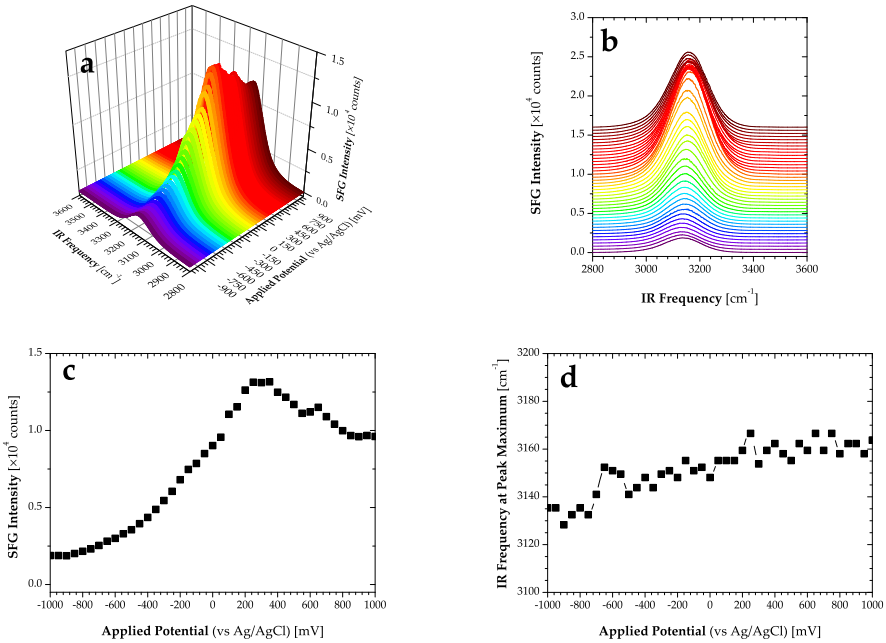

Fig. 3.21: SFG intensity of Na_2CO_3 salt solutions as function of applied potential in the 3150 cm^{-1} water spectral region. SFG intensity as function of potential in (a) 3D and (b) 2D representations, (c) SFG intensity at maximum as function of applied potential, and (d) IR frequency shift at maximum SFG intensity as function of applied potential.

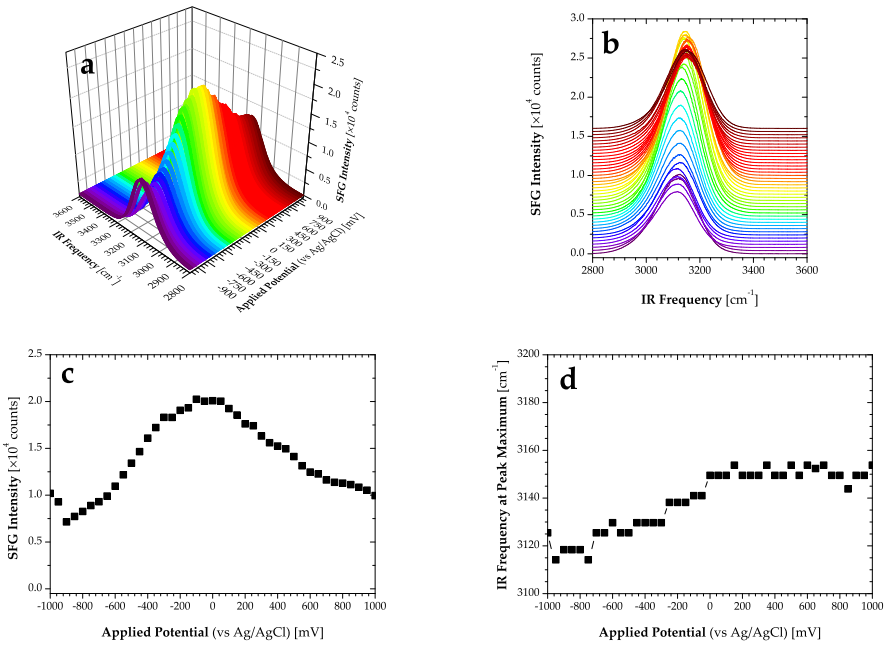

Fig. 3.22: SFG intensity of Na_2SO_4 salt solutions as function of applied potential in the 3150 cm^{-1} water spectral region. SFG intensity as function of potential in (a) 3D and (b) 2D representations, (c) SFG intensity at maximum as function of applied potential, and (d) IR frequency shift at maximum SFG intensity as function of applied potential.

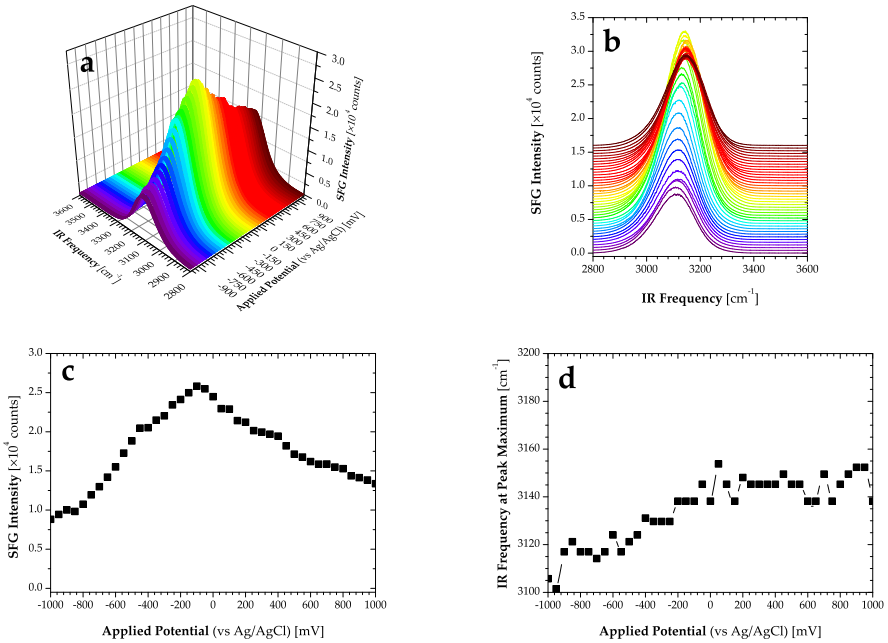

Fig. 3.23: SFG intensity of Na_2HPO_4 salt solutions as function of applied potential in the 3150 cm^{-1} water spectral region. SFG intensity as function of potential in (a) 3D and (b) 2D representations, (c) SFG intensity at maximum as function of applied potential, and (d) IR frequency shift at maximum SFG intensity as function of applied potential.

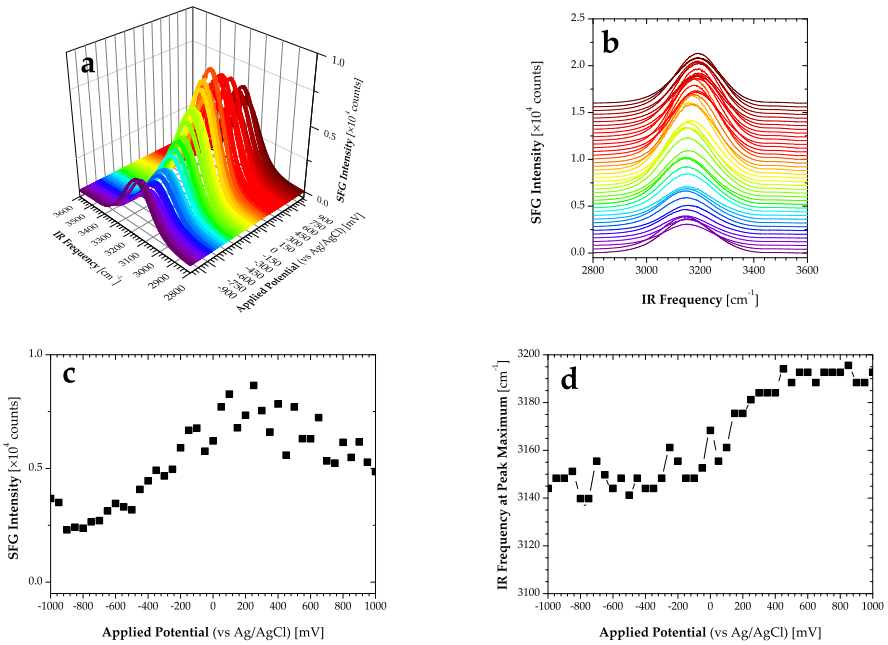

Fig. 3.24: SFG intensity of NaCl salt solutions as function of applied potential in the 3150 cm^{-1} water spectral region. SFG intensity as function of potential in (a) 3D and (b) 2D representations, (c) SFG intensity at maximum as function of applied potential, and (d) IR frequency shift at maximum SFG intensity as function of applied potential.

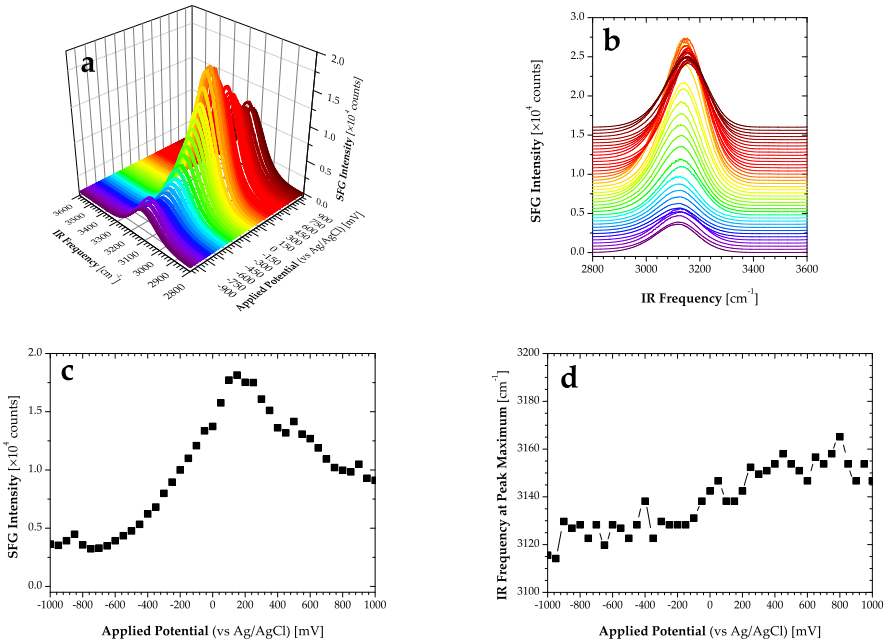

Fig. 3.25: SFG intensity of NaBr salt solutions as function of applied potential in the 3150 cm^{-1} water spectral region. SFG intensity as function of potential in (a) 3D and (b) 2D representations, (c) SFG intensity at maximum as function of applied potential, and (d) IR frequency shift at maximum SFG intensity as function of applied potential.

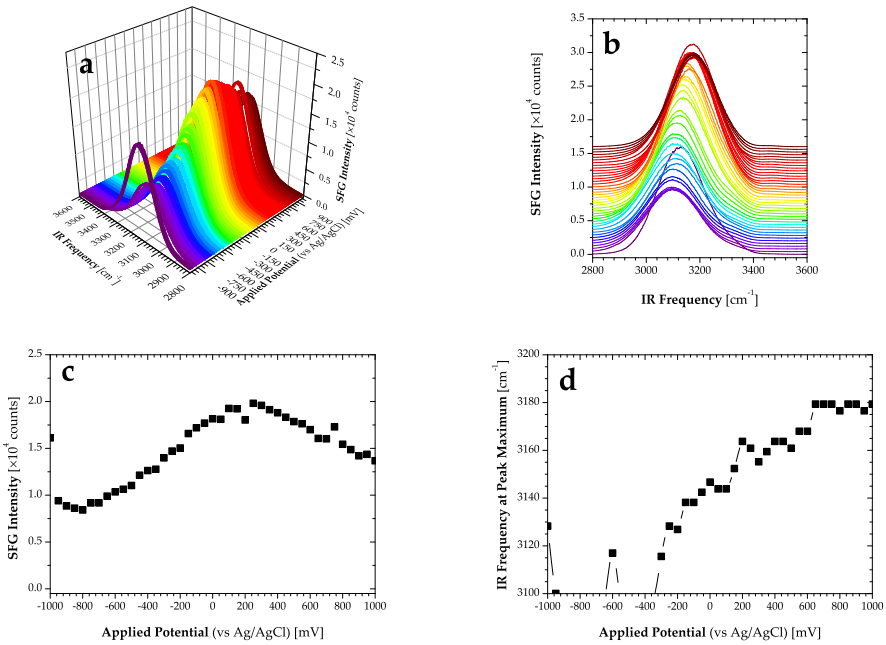

Fig. 3.26: SFG intensity of $NaNO_3$ salt solutions as function of applied potential in the 3150 cm^{-1} water spectral region. SFG intensity as function of potential in (a) 3D and (b) 2D representations, (c) SFG intensity at maximum as function of applied potential, and (d) IR frequency shift at maximum SFG intensity as function of applied potential.

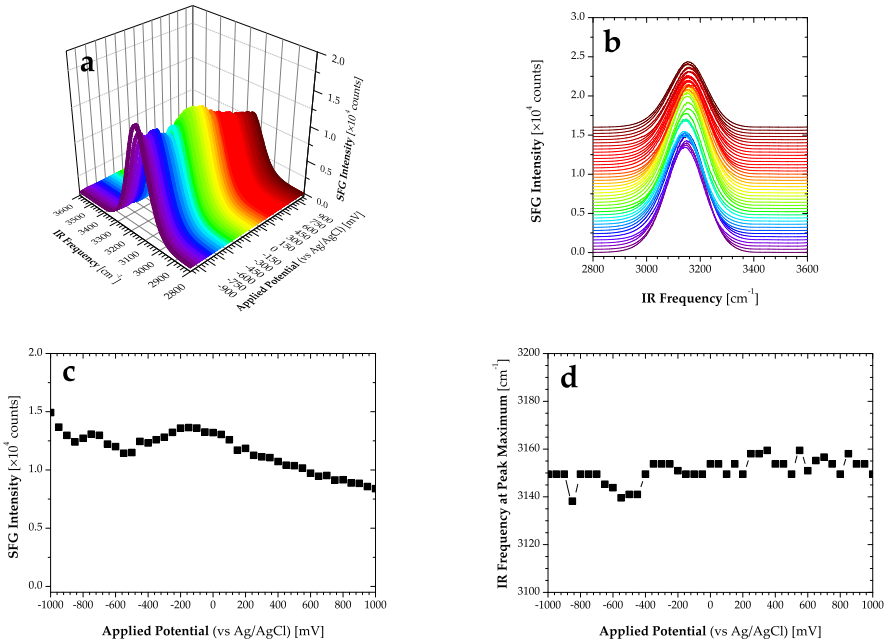

Fig. 3.27: SFG intensity of NaI salt solutions as function of applied potential in the 3150 cm^{-1} water spectral region. SFG intensity as function of potential in (a) 3D and (b) 2D representations, (c) SFG intensity at maximum as function of applied potential, and (d) IR frequency shift at maximum SFG intensity as function of applied potential.

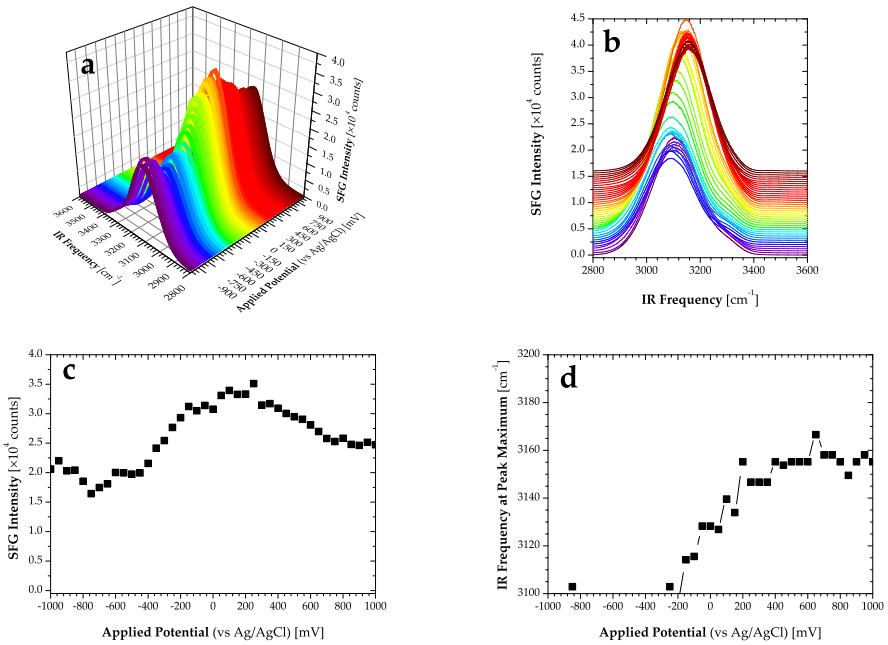

Fig. 3.28: SFG intensity of $NaClO_4$ salt solutions as function of applied potential in the 3150 cm^{-1} water spectral region. SFG intensity as function of potential in (a) 3D and (b) 2D representations, (c) SFG intensity at maximum as function of applied potential, and (d) IR frequency shift at maximum SFG intensity as function of applied potential.

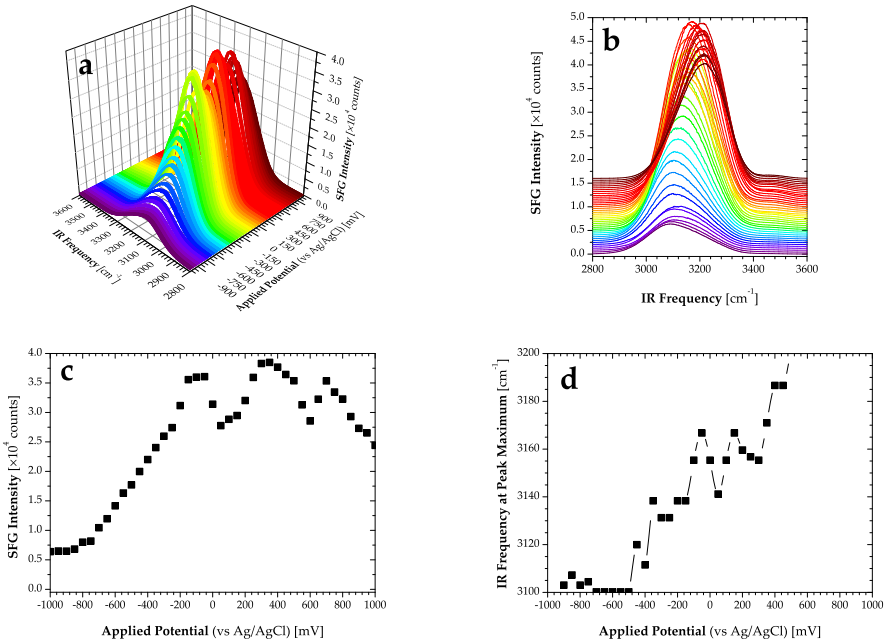

Fig. 3.29: SFG intensity of NaSCN salt solutions as function of applied potential in the 3150 cm^{-1} water spectral region. SFG intensity as function of potential in (a) 3D and (b) 2D representations, (c) SFG intensity at maximum as function of applied potential, and (d) IR frequency shift at maximum SFG intensity as function of applied potential.

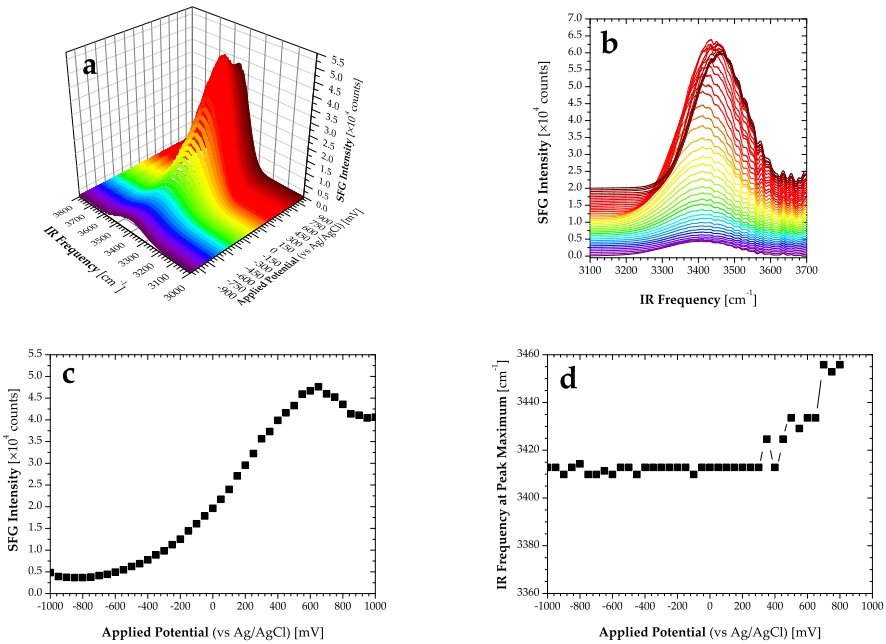

Fig. 3.30: SFG intensity of Na_2CO_3 salt solutions as function of applied potential in the 3400 cm^{-1} water spectral region. SFG intensity as function of potential in (a) 3D and (b) 2D representations, (c) SFG intensity at maximum as function of applied potential, and (d) IR frequency shift at maximum SFG intensity as function of applied potential.

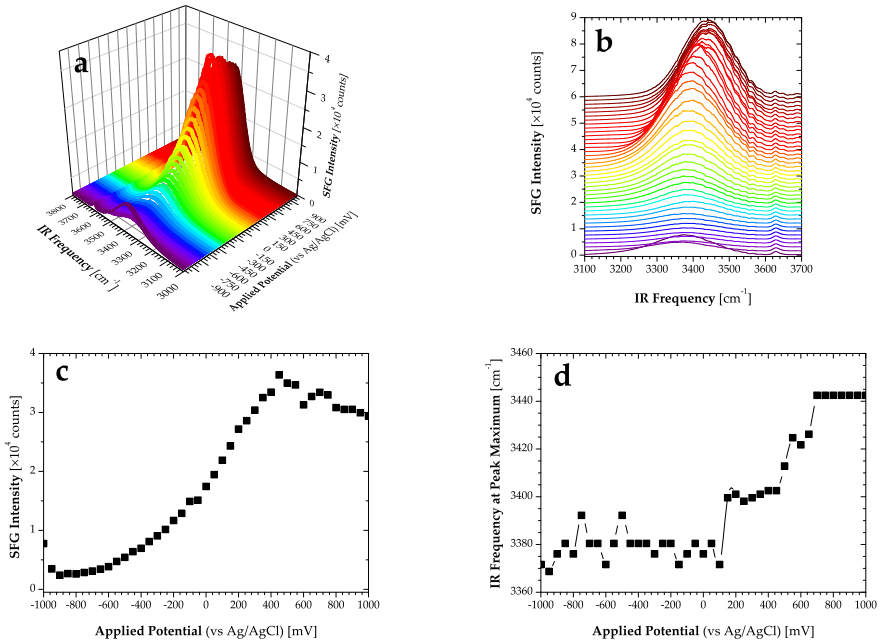

Fig. 3.31: SFG intensity of Na_2SO_4 salt solutions as function of applied potential in the 3400 cm^{-1} water spectral region. SFG intensity as function of potential in (a) 3D and (b) 2D representations, (c) SFG intensity at maximum as function of applied potential, and (d) IR frequency shift at maximum SFG intensity as function of applied potential.

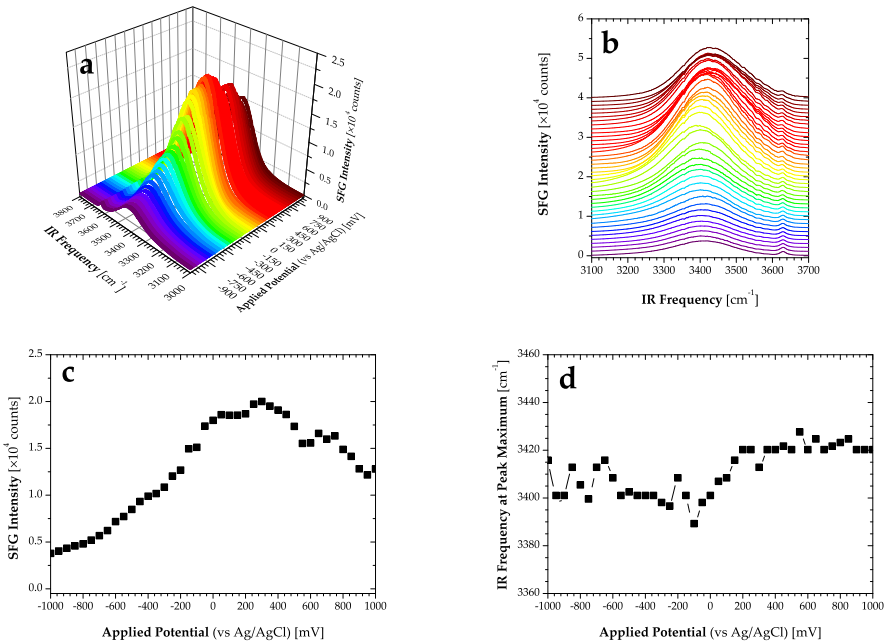

Fig. 3.32: SFG intensity of Na_2HPO_4 salt solutions as function of applied potential in the 3400 cm^{-1} water spectral region. SFG intensity as function of potential in (a) 3D and (b) 2D representations, (c) SFG intensity at maximum as function of applied potential, and (d) IR frequency shift at maximum SFG intensity as function of applied potential.

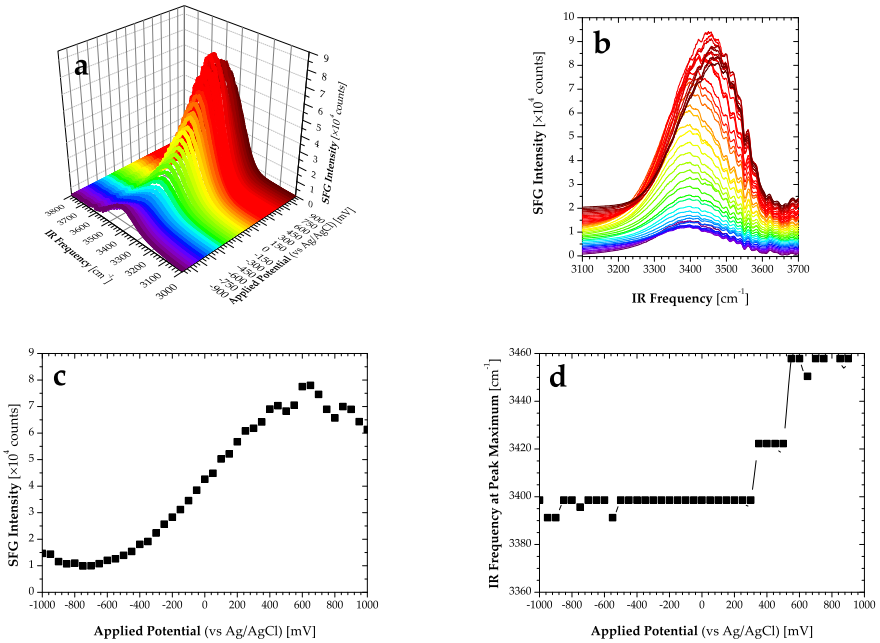

Fig. 3.33: SFG intensity of NaCl salt solutions as function of applied potential in the 3400 cm^{-1} water spectral region. SFG intensity as function of potential in (a) 3D and (b) 2D representations, (c) SFG intensity at maximum as function of applied potential, and (d) IR frequency shift at maximum SFG intensity as function of applied potential.

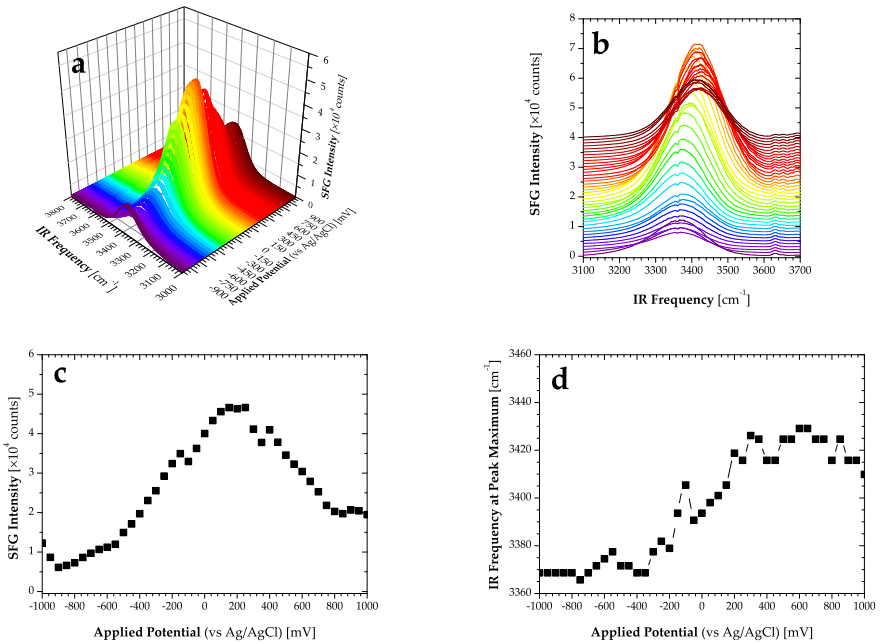

Fig. 3.34: SFG intensity of NaBr salt solutions as function of applied potential in the 3400 cm^{-1} water spectral region. SFG intensity as function of potential in (a) 3D and (b) 2D representations, (c) SFG intensity at maximum as function of applied potential, and (d) IR frequency shift at maximum SFG intensity as function of applied potential.

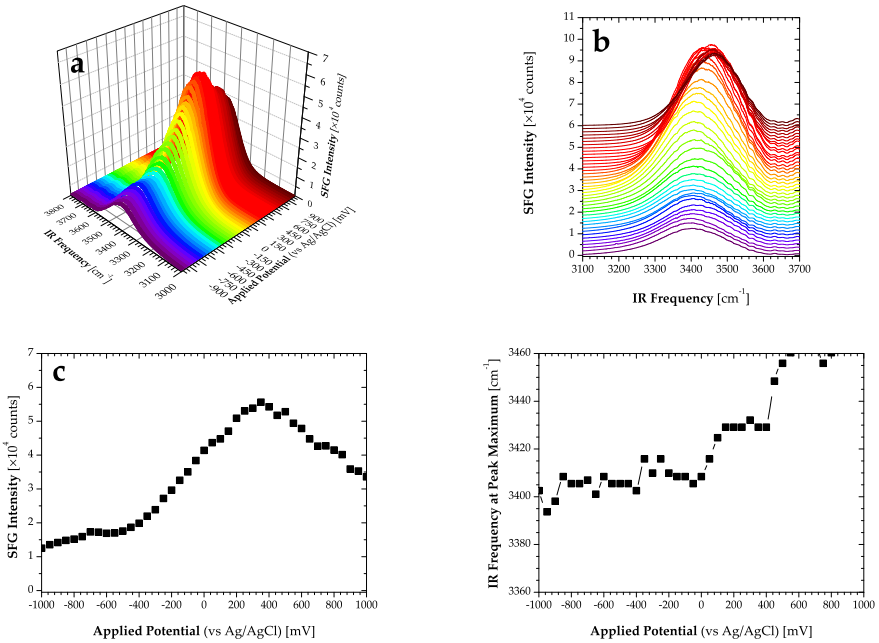

Fig. 3.35: SFG intensity of $NaNO_3$ salt solutions as function of applied potential in the 3400 cm^{-1} water spectral region. SFG intensity as function of potential in (a) 3D and (b) 2D representations, (c) SFG intensity at maximum as function of applied potential, and (d) IR frequency shift at maximum SFG intensity as function of applied potential.

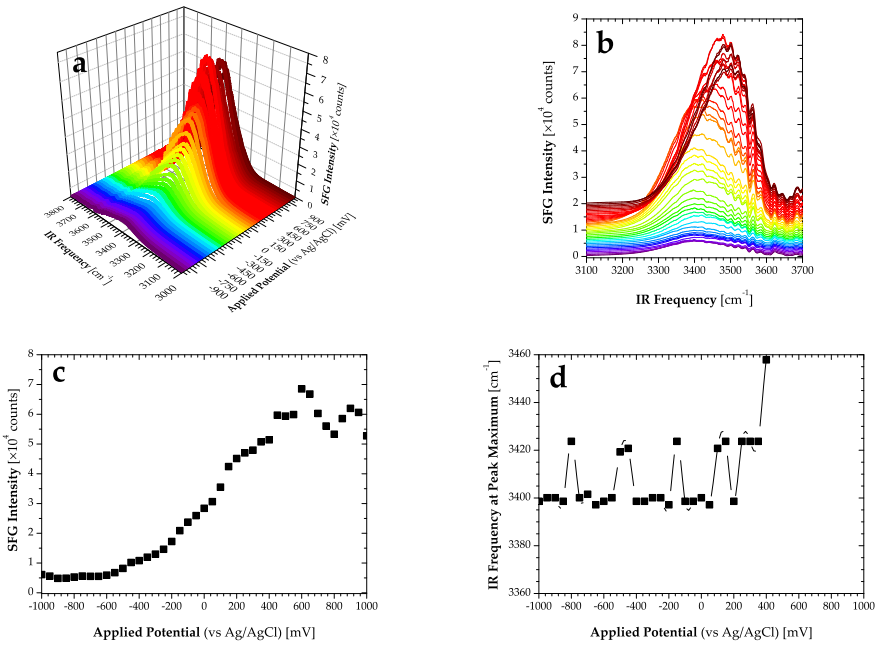

Fig. 3.36: SFG intensity of NaI salt solutions as function of applied potential in the 3400 cm^{-1} water spectral region. SFG intensity as function of potential in (a) 3D and (b) 2D representations, (c) SFG intensity at maximum as function of applied potential, and (d) IR frequency shift at maximum SFG intensity as function of applied potential.

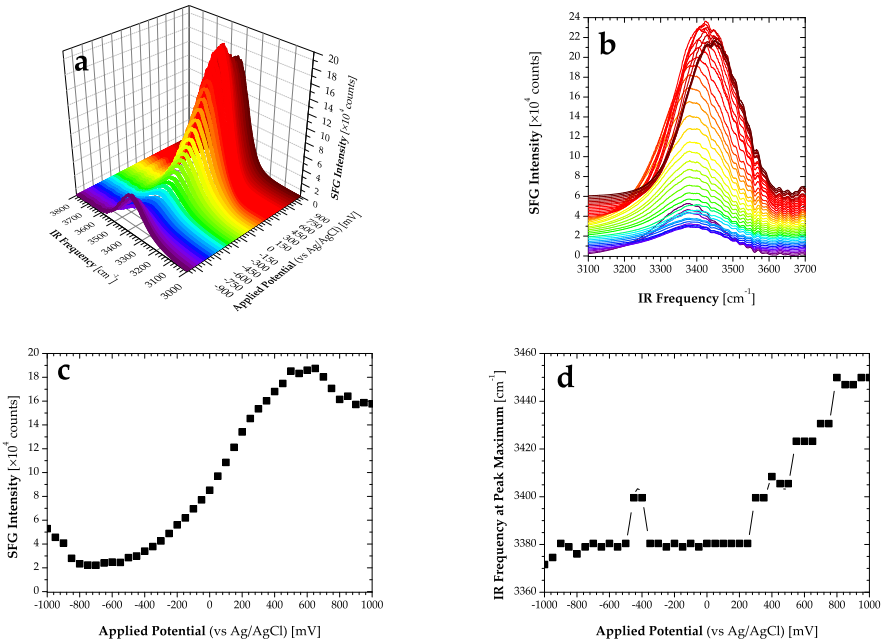

Fig. 3.37: SFG intensity of $NaClO_4$ salt solutions as function of applied potential in the 3400 cm^{-1} water spectral region. SFG intensity as function of potential in (a) 3D and (b) 2D representations, (c) SFG intensity at maximum as function of applied potential, and (d) IR frequency shift at maximum SFG intensity as function of applied potential.

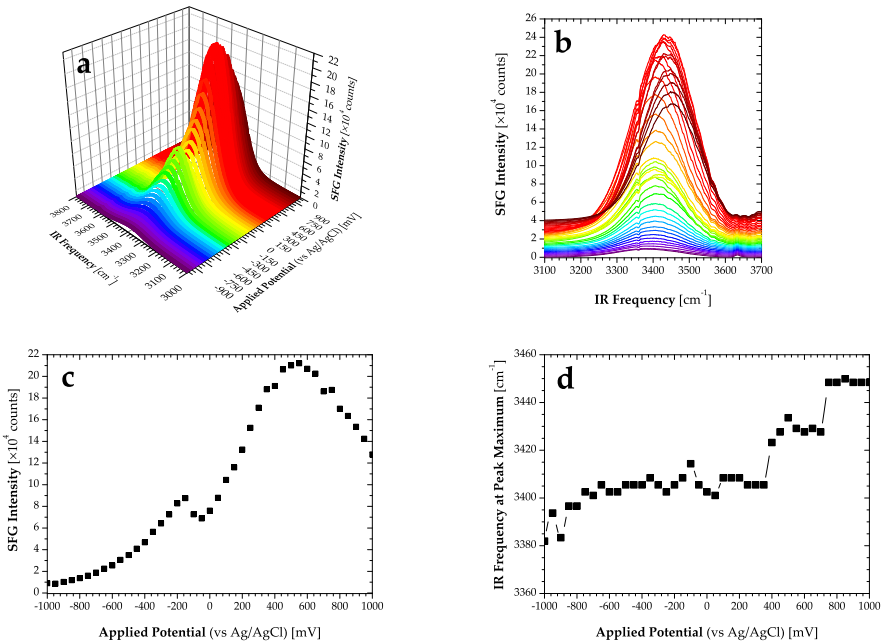

Fig. 3.38: SFG intensity of NaSCN salt solutions as function of applied potential in the 3400 cm^{-1} water spectral region. SFG intensity as function of potential in (a) 3D and (b) 2D representations, (c) SFG intensity at maximum as function of applied potential, and (d) IR frequency shift at maximum SFG intensity as function of applied potential.

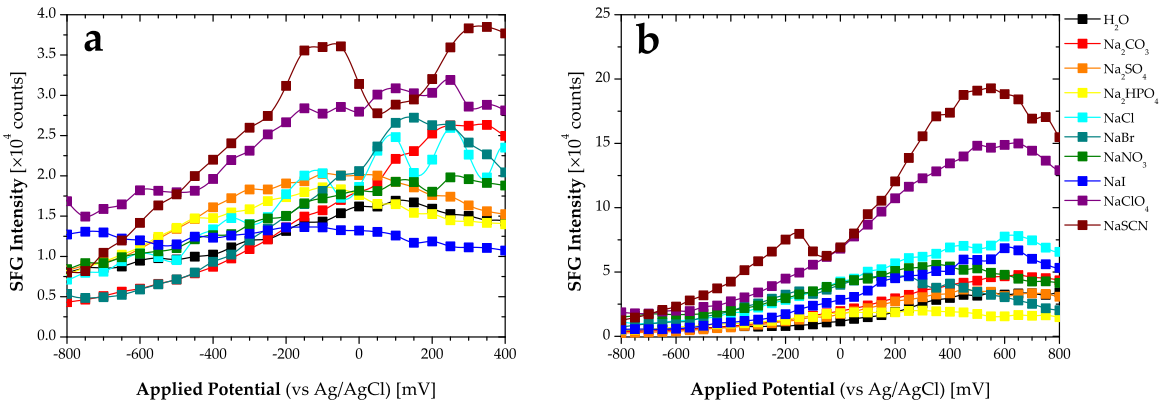

Fig. 3.39: Comparison of SFG intensity at maximum of H_2O and 10 mM anionic Na^+ salt solutions as function of applied potential in the 3150 and 3400 cm^{-1} water spectral regions. (a) 3150 cm^{-1}, (b) 3400 cm^{-1}. In both regions, the SFG spectra of $NaClO_4$ and NaSCN have been rescaled to that of H_2O.

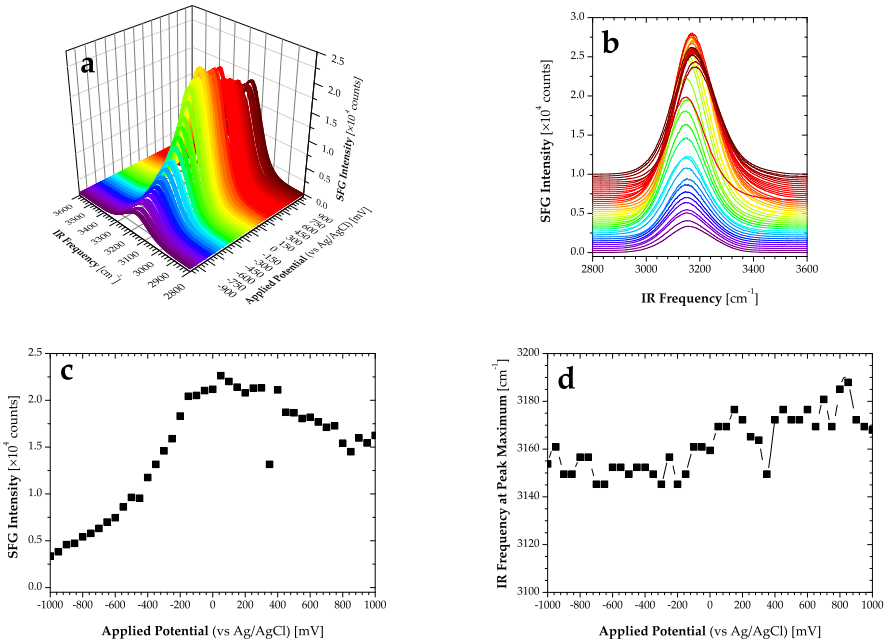

Fig. 3.40: SFG intensity of $CaCl_2$ salt solutions as function of applied potential in the 3150 cm^{-1} water spectral region. SFG intensity as function of potential in (a) 3D and (b) 2D representations, (c) SFG intensity at maximum as function of applied potential, and (d) IR frequency shift at maximum SFG intensity as function of applied potential.

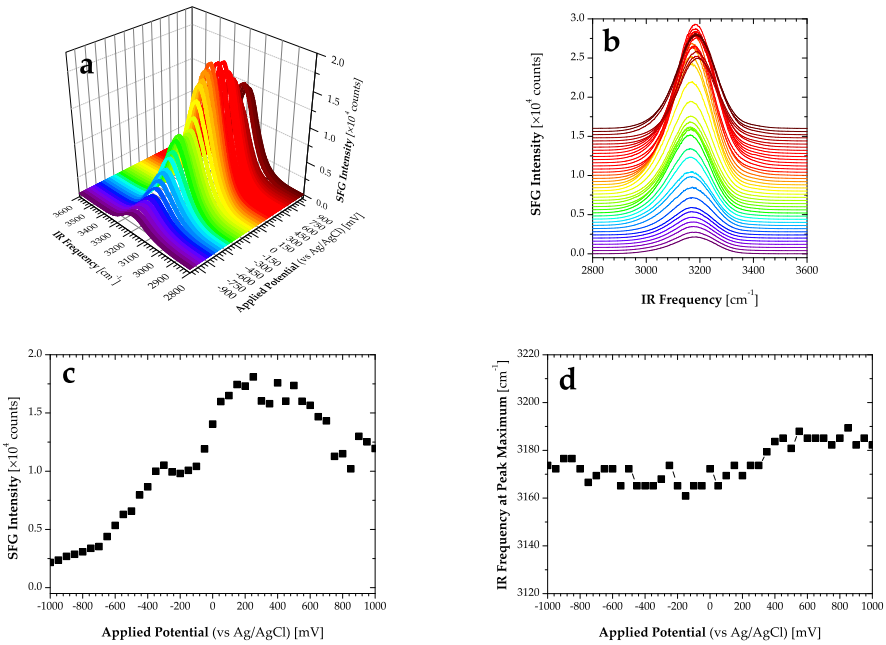

Fig. 3.41: SFG intensity of LiCl salt solutions as function of applied potential in the 3150 cm^{-1} water spectral region. SFG intensity as function of potential in (a) 3D and (b) 2D representations, (c) SFG intensity at maximum as function of applied potential, and (d) IR frequency shift at maximum SFG intensity as function of applied potential.

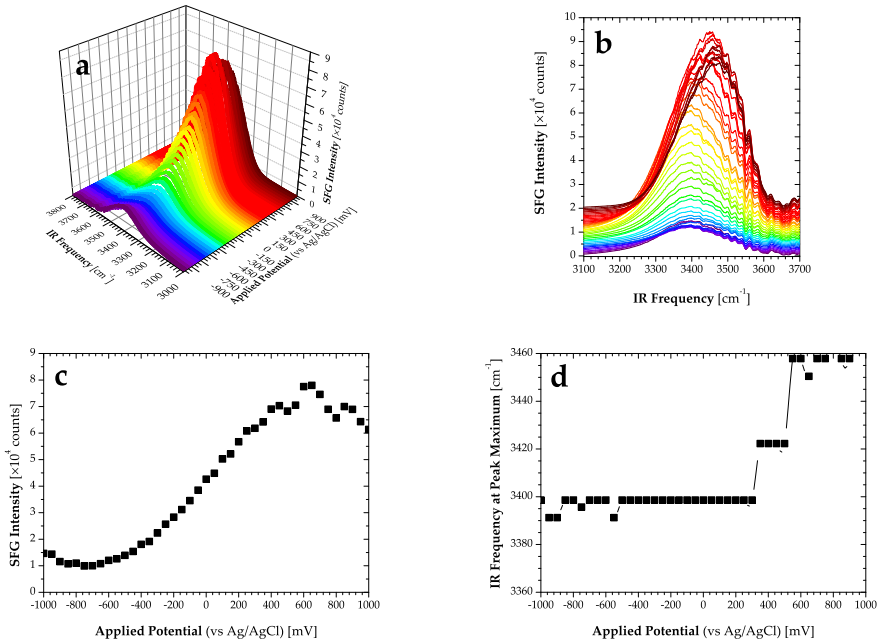

Fig. 3.42: SFG intensity of NaCl salt solutions as function of applied potential in the 3400 cm^{-1} water spectral region. SFG intensity as function of potential in (a) 3D and (b) 2D representations, (c) SFG intensity at maximum as function of applied potential, and (d) IR frequency shift at maximum SFG intensity as function of applied potential.

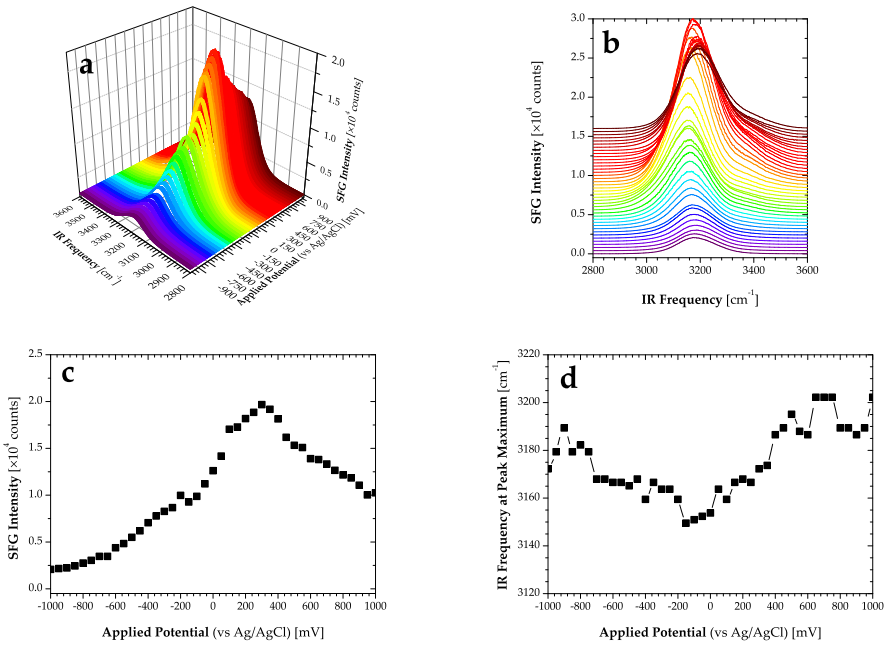

Fig. 3.43: SFG intensity of KCl salt solutions as function of applied potential in the 3150 cm^{-1} water spectral region. SFG intensity as function of potential in (a) 3D and (b) 2D representations, (c) SFG intensity at maximum as function of applied potential, and (d) IR frequency shift at maximum SFG intensity as function of applied potential.

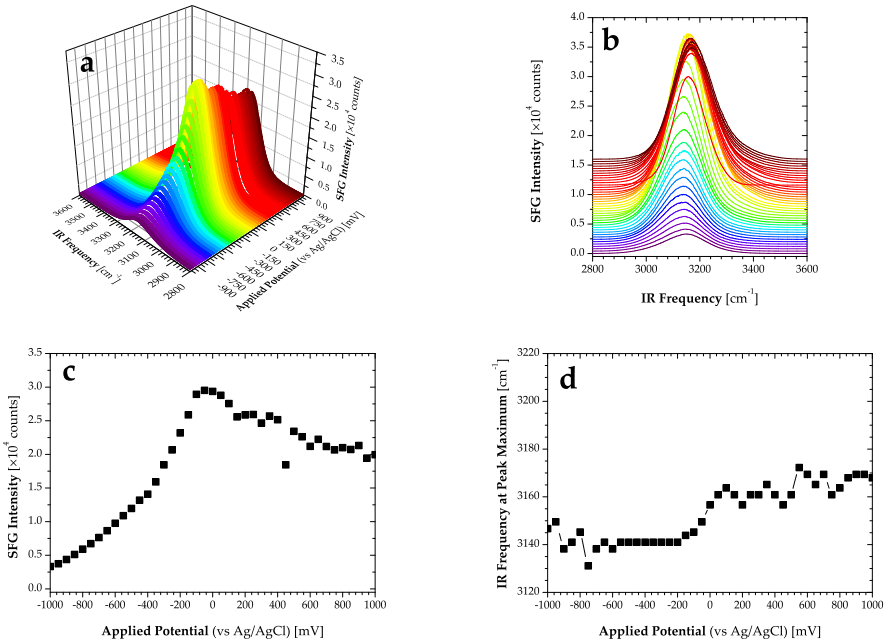

Fig. 3.44: SFG intensity of RbCl salt solutions as function of applied potential in the 3150 cm^{-1} water spectral region. SFG intensity as function of potential in (a) 3D and (b) 2D representations, (c) SFG intensity at maximum as function of applied potential, and (d) IR frequency shift at maximum SFG intensity as function of applied potential.

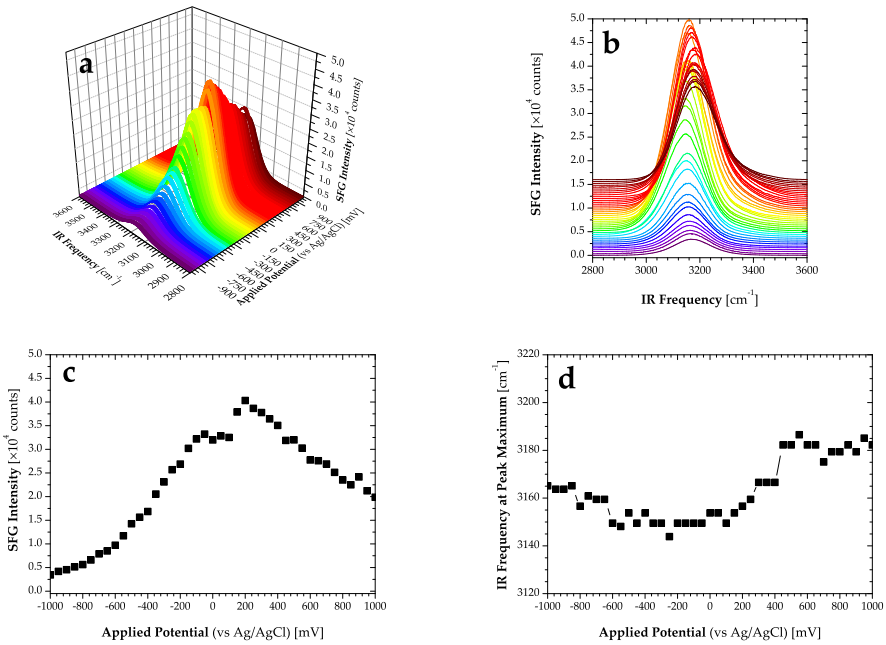

Fig. 3.45: SFG intensity of CsCl salt solutions as function of applied potential in the 3150 cm^{-1} water spectral region. SFG intensity as function of potential in (a) 3D and (b) 2D representations, (c) SFG intensity at maximum as function of applied potential, and (d) IR frequency shift at maximum SFG intensity as function of applied potential.

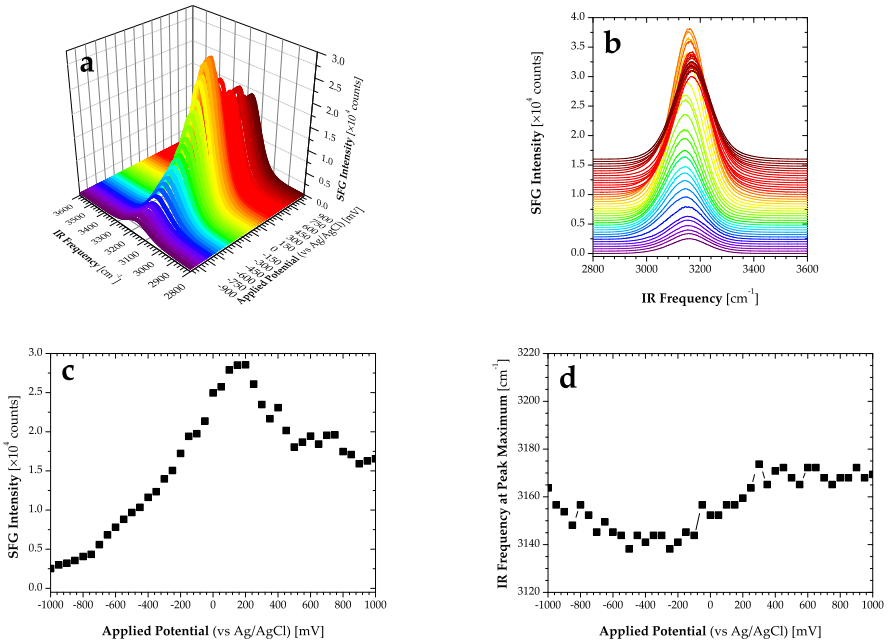

Fig. 3.46: SFG intensity of NH_4Cl salt solutions as function of applied potential in the 3150 cm^{-1} water spectral region. SFG intensity as function of potential in (a) 3D and (b) 2D representations, (c) SFG intensity at maximum as function of applied potential, and (d) IR frequency shift at maximum SFG intensity as function of applied potential.

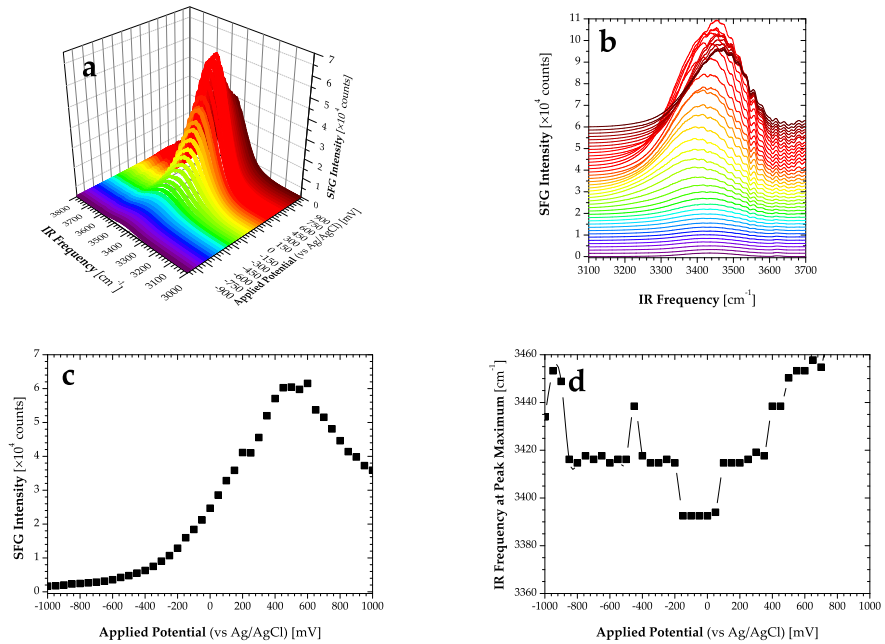

Fig. 3.47: SFG intensity of $CaCl_2$ salt solutions as function of applied potential in the 3400 cm^{-1} water spectral region. SFG intensity as function of potential in (a) 3D and (b) 2D representations, (c) SFG intensity at maximum as function of applied potential, and (d) IR frequency shift at maximum SFG intensity as function of applied potential.

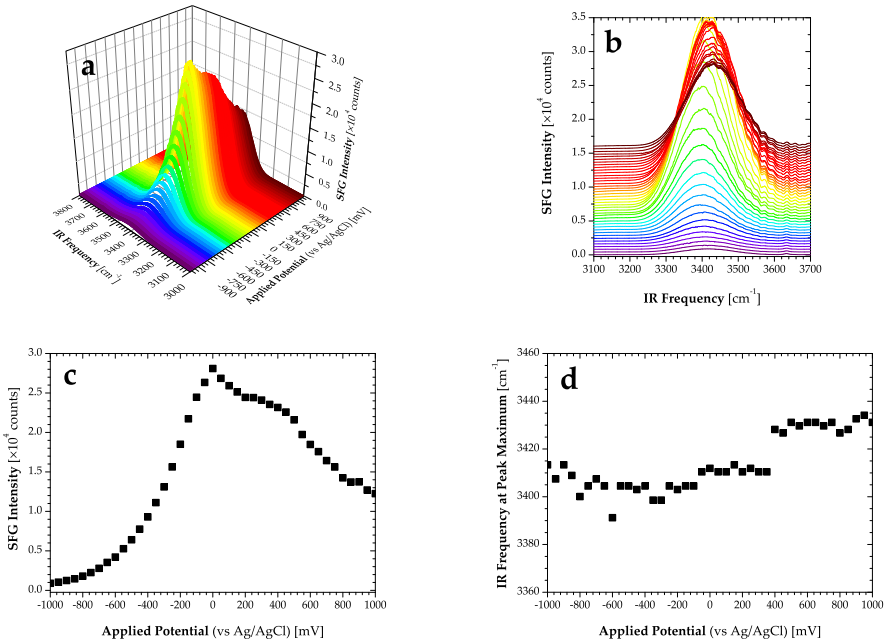

Fig. 3.48: SFG intensity of LiCl salt solutions as function of applied potential in the 3400 cm^{-1} water spectral region. SFG intensity as function of potential in (a) 3D and (b) 2D representations, (c) SFG intensity at maximum as function of applied potential, and (d) IR frequency shift at maximum SFG intensity as function of applied potential.

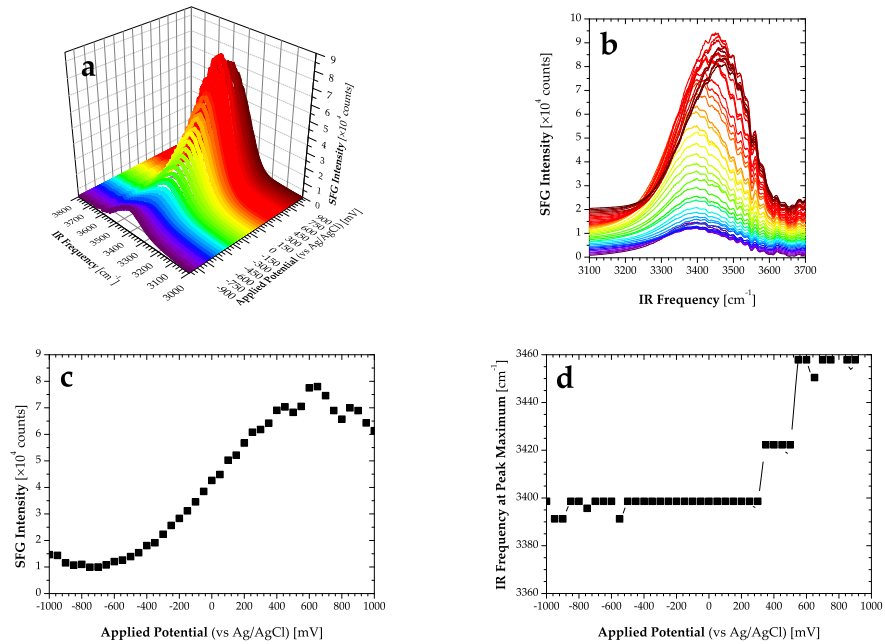

Fig. 3.49: SFG intensity of NaCl salt solutions as function of applied potential in the 3400 cm^{-1} water spectral region. SFG intensity as function of potential in (a) 3D and (b) 2D representations, (c) SFG intensity at maximum as function of applied potential, and (d) IR frequency shift at maximum SFG intensity as function of applied potential.

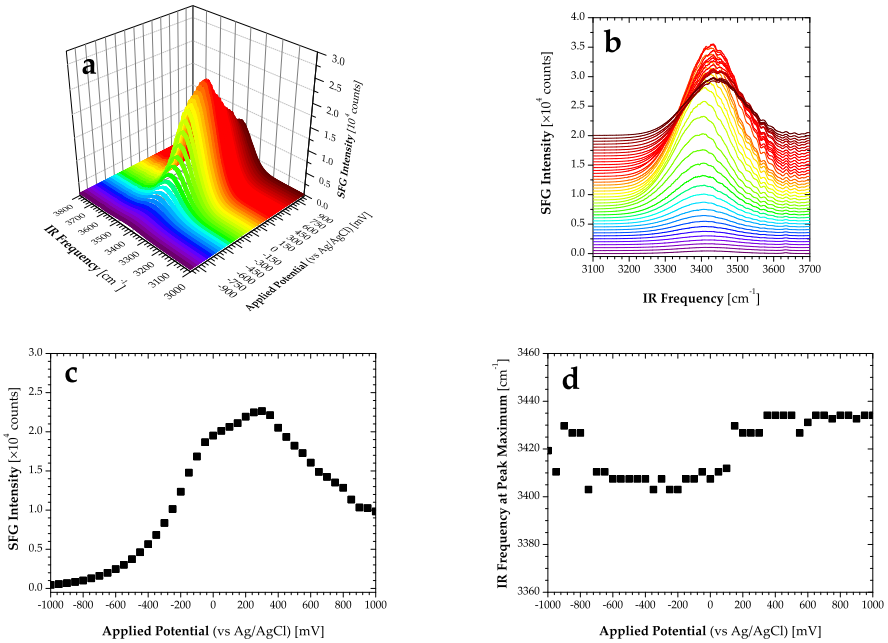

Fig. 3.50: SFG intensity of KCl salt solutions as function of applied potential in the 3400 cm^{-1} water spectral region. SFG intensity as function of potential in (a) 3D and (b) 2D representations, (c) SFG intensity at maximum as function of applied potential, and (d) IR frequency shift at maximum SFG intensity as function of applied potential.

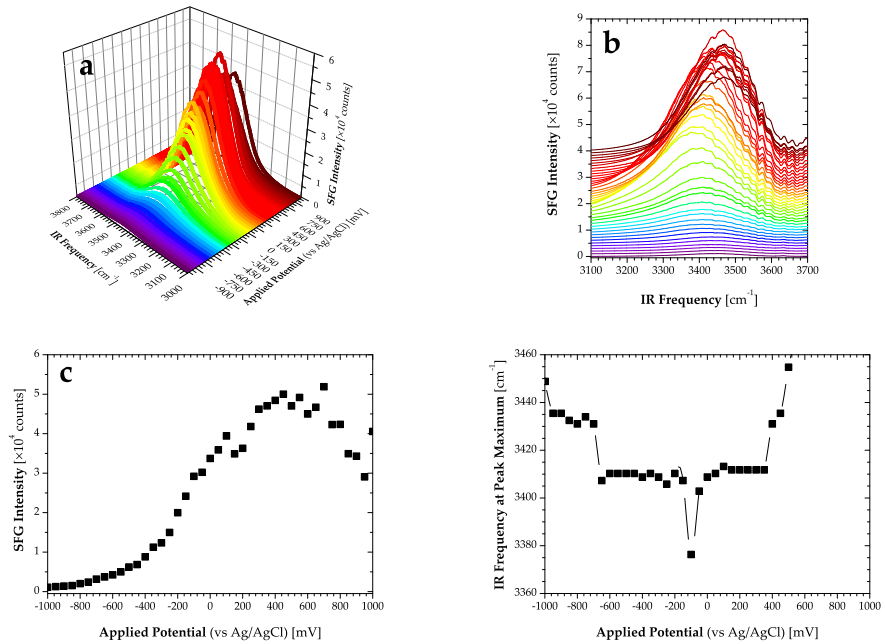

Fig. 3.51: SFG intensity of RbCl salt solutions as function of applied potential in the 3400 cm^{-1} water spectral region. SFG intensity as function of potential in (a) 3D and (b) 2D representations, (c) SFG intensity at maximum as function of applied potential, and (d) IR frequency shift at maximum SFG intensity as function of applied potential.

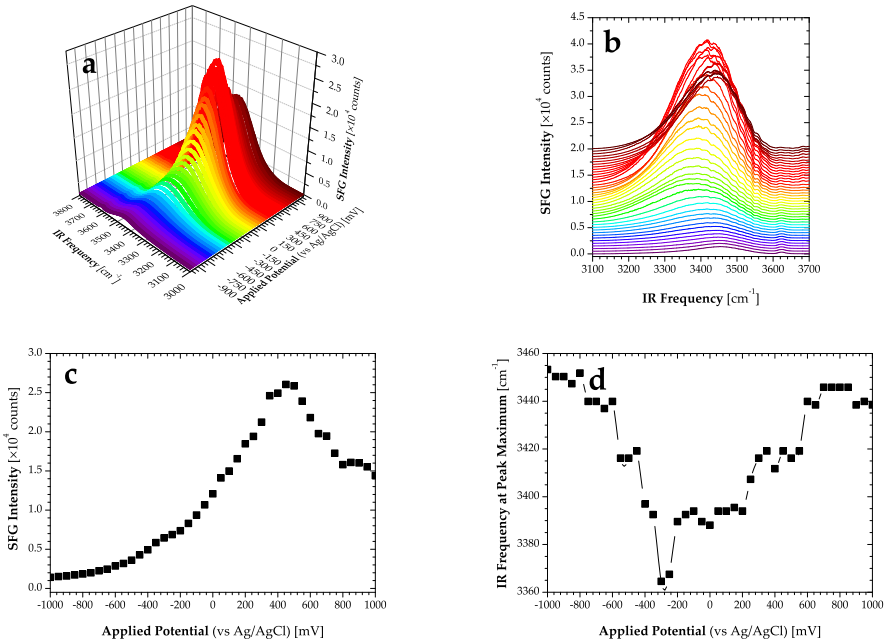

Fig. 3.52: SFG intensity of CsCl salt solutions as function of applied potential in the 3400 cm^{-1} water spectral region. SFG intensity as function of potential in (a) 3D and (b) 2D representations, (c) SFG intensity at maximum as function of applied potential, and (d) IR frequency shift at maximum SFG intensity as function of applied potential.

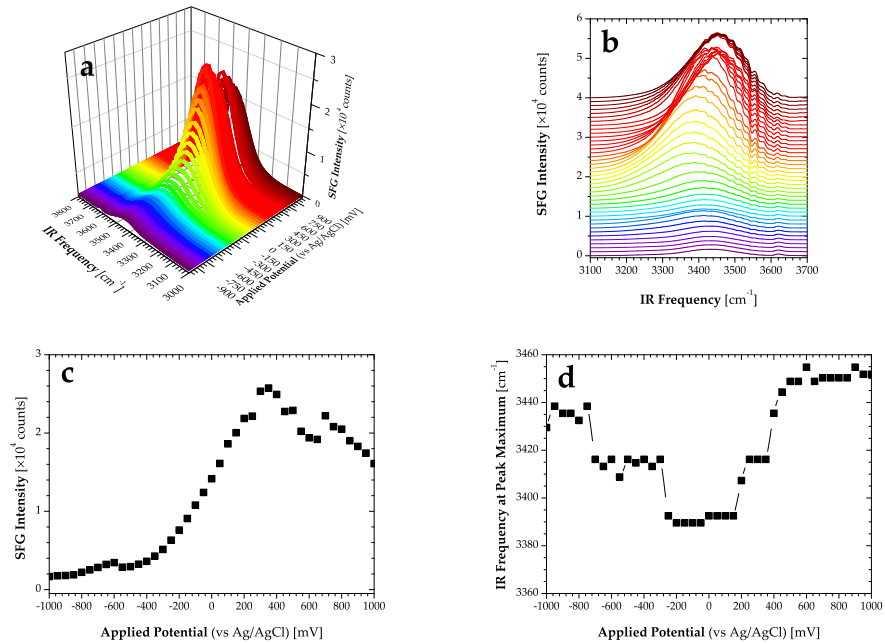

Fig. 3.53: SFG intensity of NH_4Cl salt solutions as function of applied potential in the 3400 cm^{-1} water spectral region. SFG intensity as function of potential in (a) 3D and (b) 2D representations, (c) SFG intensity at maximum as function of applied potential, and (d) IR frequency shift at maximum SFG intensity as function of applied potential.

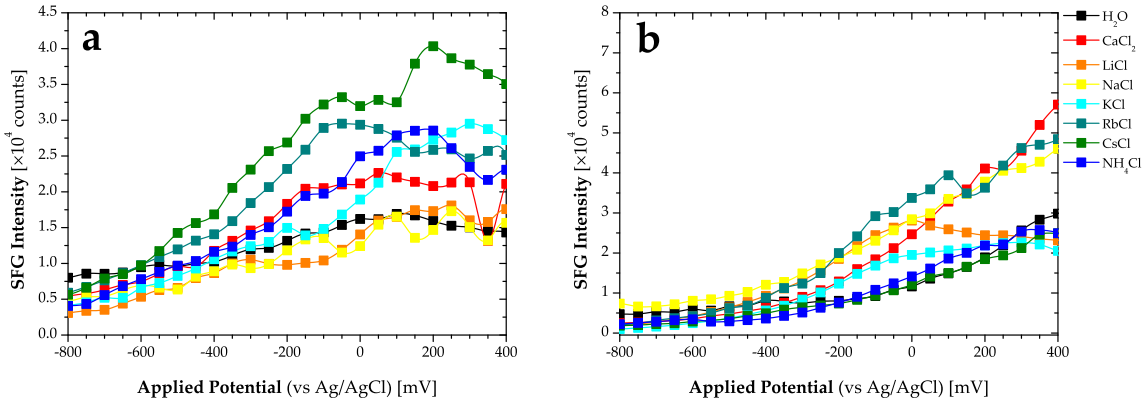

Fig. 3.54: Comparison of SFG intensity at maximum of H_2O and 10 mM cationic aqueous salt solutions as function of applied potential in the 3150 and 3400 cm^{-1} water spectral regions. (a) 3150 cm^{-1}, (b) 3400 cm^{-1}.

4

Conclusion and Outlook

In this thesis, the construction and implementation of an adaptable, vibrational SFG spectroscopy setup which enables *in situ* investigation at various interfaces under several experimental configurations and conditions was demonstrated. The inclusion of a sample stage area that allows easier manipulation and accommodates the application of various measuring cells for vibrational SFG spectroscopy was also highlighted. A measuring cell that permits *in situ* probing of the metal oxide/aqueous solution interfaces in the TIR geometry by using an IR-transparent prism was designed and constructed. An extension of this cell towards a three-electrode spectroelectrochemical measuring cell that allows simultaneous spectroscopic and voltammetric measurements was also shown. Through its working electrode coated directly on the basal face of the prism, this cell enables a direct voltammetric control (rather than a pH control as done traditionally) of the surface charging. For this purpose, a transparent, semiconducting metal oxide, namely ITO, was chosen as assay material for the working electrode because of its good chemical stability, low electrical resistivity, and transparency in the VIS and NIR spectral ranges. The ITO electrode was sputter-deposited and annealed on the IR-transparent prism and its quality (i.e., its structural, chemical, electrical, and optical properties) was assessed and found conform to similarly prepared films reported in literature.

The investigation of the surface charging through applied potential at the ITO/water interface on water ordering was first assayed by measuring the SFG response of deuterated and normal water in the bonded-OH spectral region (3100–3500 cm^{-1}) under different externally applied potentials. To cover this region, the SFG measurement were performed separately in two spectral regions located at ~ 3150 and ~ 3400 cm^{-1}, respectively. The control SFG measurement done with deuterated water revealed that ITO generates a large second-order NR response (and possibly a potential-dependent, third-order nonlinear response) which could potentially dominate any resonant response coming from adsorbed water molecules. The SFG measurement with normal water showed that the obtained SFG response behaves similarly to that of D_2O up to a given applied potential value, above which the two responses differ. However, a strict quantitative comparison of both responses could not be done since both experiments were performed and normalized separately with two different REF signals. As such, the predominance of one of these SFG response over the other in the given potential range could not be ruled out. Surface current density measurements were also simultaneously performed and revealed little to no faradaic currents, except at high potentials where gas evolution happens. Complementary streaming potential measurements made by acid/base titration showed that ITO exhibits a very low isoelectric point ($pH_{iep} \approx 3$) which makes its surface negatively

charged under normal pH conditions.

The influence of ions on interfacial water ordering at the ITO/aqueous solution interface was also investigated by measuring the SFG response of low concentrated (10 mM) anionic and cationic salt solutions in the bonded-OH spectral region (3100–3500 cm^{-1}) under different externally applied potentials. Although all experiments were conducted separately, the similarity of the SFG responses enabled to do a semi-quantitative comparison between most of the salt solutions. For both ion series, the obtained SFG response did not show any distinct ion-specific effects on water ordering at the ITO surface. However, two types of SFG responses could be observed from these experiments. Indeed, it was found that soft or poorly hydrated ions such as ClO_4^-, SCN^-, Rb^+ or Cs^+ exhibit a stronger affinity for the ITO surface in comparison to hard or strongly hydrated ions like SO_4^{2-}, HPO_4^{2-} or Li^+. This trend was found for both water spectral regions and for both ion series, with the exception of the cationic series at 3400 cm^{-1}. However, this trend could not be explained on the basis of the law of matching water affinities for both anions and cations. Surface current density measurements were also performed and revealed, besides the usual gas evolution, the occurrence of corrosion effects at positive applied potentials, especially significant for halogenated salts. In contrast to vibrational SFG spectroscopy, streaming potential measurements done on cationic salt solutions demonstrated the dependency of the zeta potential on the ion concentration as well as on the ion type. However, like SFG spectroscopy, it was found that at low concentrations soft cations have greater propensity for the ITO surface than hard cations. This result is again in contradiction with the law of matching water affinities and could only be explained by taking into account the ion size.

In view of these ambivalent results and remaining open questions, and in the perspective of a further use of ITO in vibrational SFG spectroscopy either as reference or as a working electrode material, one needs to address the problem of its large nonlinear bulk response. One possibility would be to further reduce the amount of material deposited as it was shown elsewhere that the SHG response of ITO is dependent on the film thickness. Another possibility would be to determine whether or not, angular conditions could be found for which the ITO response would be minimal. This would require, in a first step, determining accurately the optical constants of ITO in a range of wavelengths relevant to SFG spectroscopy and, in a second step, simulating the geometrical factors for the CaF_2-ITO-H_2O layered system which could provide some insights on the effect of material absorption, beam incident angles and polarization, on the nonlinear response of ITO.

Provided that the aforementioned problem could be overcome or at least minimized, comparative experimental investigations by SFG spectroscopy and voltammetry of normal and deuterated water as well as with a small set of cationic salt solutions, preferably non-halogenated, should be again attempted. Concerning streaming potential studies with ITO, further measurements should be done to complete the cationic salt series, especially with heavier cations (Rb^+, Cs^+). Other measurements should also include a small set of anionic salt solutions since it has been shown on other metal oxide surfaces that anions have curiously a weaker influence than cations on the SFG response of water. Some of these measurements are currently in progress.

As for the SFG spectroscopy setup as well as the three-electrode measuring cell, future instrumental developments and improvements could include, for example: (1) an upgrade

of the SFG spectrometer from the actual 100 fs mode to the 35 fs mode which would allow to record in a single spectrum the entire bonded-OH region, (2) a modernization of the electrochemical equipment (e.g., transition from an analog to a digital potentiostat) that would enable an automation of the voltammetric measurement and offer the possibility of getting other types of voltammetric data (e.g. cyclic voltamogram), (3) the inclusion of a liquid pump coupled to a degassing unit which would allow to flow in real time water or any series of aqueous solutions in a closed circuit without the need to remove the IR-transparent prism; without the possible change of optical alignment, this would also permit using the same reference for all solutions investigated, and (4) a redesign of the spectroelectrochemical cell, more specifically, the transformation of the solution reservoir into a channel that allows flowing the aqueous solutions. It is worth to mention that some of these improvements (potentiostat, pump) have recently been implemented.

Bibliography

[1] W. Stumm, "Chemistry of the Solid-Water Interface: Processes at the Mineral-Water and Particle-Water Interface in Natural Systems", John Wiley & Sons, New York, 448 p. (1992).

[2] G. E. Brown, Jr., V. E. Henrich, W. H. Casey, D. L. Clark, C. Eggleston, A. Felmy, D. W. Goodman, M. Grätzel, G. Maciel, M. I. McCarthy, K. H. Nealson, D. A. Sverjensky, M. F. Toney, J. M. Zachara, "Metal oxide surfaces and their interactions with aqueous solutions and microbial organisms", *Chem. Rev.* **99**, 77 (1999).

[3] G. E. Brown, Jr., "How minerals react with water", *Science* **294**, 67 (2001).

[4] H. A. Al-Abadleh, V. H. Grassian, "Oxide surfaces as environmental interfaces", *Surf. Sci. Rep.* **52**, 63 (2003).

[5] B. Li, B. E. Logan, "Bacterial adhesion to glass and metal-oxide surfaces", *Colloids Surf. B* **36**, 81 (2004).

[6] T. A. Oleson, N. Sahai, "Oxide-dependent adsorption of a model membrane phospholipid, dipalmitoylphosphatidylcholine: Bulk adsorption isotherms", *Langmuir* **24**, 4865 (2008).

[7] M. J. Stevens, L. J. Donato, S. K. Lower, N. Sahai, "Oxide-dependent adhesion of the Jurkat line of T lymphocytes", *Langmuir* **25**, 6270 (2009).

[8] R. J. Watts, M. D. Udell, S. Kong, S. W. Leung, "Fenton-like soil remediation catalyzed by naturally occurring iron minerals", *Environ. Eng. Sci.* **16**, 93 (1999).

[9] J.-f. Peng, Y.-h. Song, P. Yuan, X.-y. Cui, G.-l. Qiu, "The remediation of heavy metals contaminated sediment", *J. Hazard. Mater.* **161**, 633 (2009).

[10] W.-y. Shi, H.-b. Shao, H. Li, M.-a. Shao, S. Du, "Progress in the remediation of hazardous heavy metal-polluted soils by natural zeolite", *J. Hazard. Mater.* **170**, 1 (2009).

[11] R. A. Bunn, R. D. Magelky, J. N. Ryan, M. Elimelech, "Mobilization of natural colloids from an iron oxide-coated sand aquifer: Effect of pH and ionic strength", *Environ. Sci. Technol.* **36**, 314 (2002).

[12] G. A. Waychunas, C. S. Kim, J. F. Banfield, "Nanoparticulate iron oxide minerals in soils and sediments: unique properties and contaminant scavenging mechanisms", *J. Nanopart. Res.* **7**, 409 (2005).

[13] D. Buerge-Weirich, R. Hari, H. Xue, P. Behra, L. Sigg, "Adsorption of Cu, Cd, and Ni on goethite in the presence of natural groundwater ligands", *Environ. Sci. Technol.* **36**, 328 (2002).

[14] K. Pirkanniemi, M. Sillanpää, "Heterogeneous water phase catalysis as an environmental application: A review", *Chemosphere* **48**, 1047 (2002).

[15] H. Y. Chen, O. Zahraa, M. Bouchy, "Inhibition of the adsorption and photocatalytic degradation of an organic contaminant in an aqueous suspension of TiO_2 by inor-

ganic ions", *J. Photochem. Photobiol. A* **108**, 37 (1997).

[16] C. Guillard, H. Lachheb, A. Houas, M. Ksibi, E. Elaloui, J. M. Hermann, "Influence of chemical structure of dyes, of pH and of inorganic salts on their photocatalytic degradation by TiO_2 comparison of the efficiency of powder and supported TiO_2", *J. Photochem. Photobiol. A* **158**, 27 (2003).

[17] O. Seven, B. Dindar, S. Aydenir, D. Metin, M. A. Ozinel, S. Icli, "Solar photocatalytic disinfection of a group of bacteria and fungi aqueous suspensions with TiO_2, ZnO and Sahara desert dust", *J. Photochem. Photobiol. A* **165**, 103 (2004).

[18] M. N. Chong, B. Jin, C. W. K. Chow, C. Saint, "Recent developments in photocatalytic water treatment technology: A review", *Water Res.* **44**, 2997 (2010).

[19] M. Ni, M. K. H. Leung, D. Y. C. Leung, K. Sumathy, "Review and recent developments in photocatalytic water-splitting using TiO_2 for hydrogen production", *Renew. Sust. Energ. Rev.* **11**, 401 (2007).

[20] R. M. Navarro, F. del Valle, J. A. Villoria de la Mano, M. C. Álvarez-Galvána, J. L. G. Fierro, "Photocatalytic water splitting under visible light: Concept and catalysts development", *Adv. Chem. Eng.* **36**, 111 (2009).

[21] Y. Zhang, Y. Chen, P. Westerhoff, K. Hristovski, J. C. Crittenden, "Stability of commercial metal oxide nanoparticles in water", *Water Res.* **42**, 2204 (2008).

[22] I. Chowdhury, Y. Hong, S. L. Walker, "Container to characterization: Impacts of metal oxide handling, preparation, and solution chemistry on particle stability", *Colloids Surf. A* **368**, 91 (2010).

[23] A. A. Keller, H. Wang, D. Zhou, H. S. Lenihan, G. Cherr, B. J. Cardinale, R. Miller, Z. Ji, "Stability and aggregation of metal oxide nanoparticles in natural aqueous matrices", *Environ. Sci. Technol.* **44**, 1962 (2010).

[24] C. P. Tso, C. M. Zhung, Y. H. Shih, Y. M. Tseng, S. C. Wu, R. A. Doong, "Stability of metal oxide nanoparticles in aqueous solutions", *Water Sci Technol.* **61**, 127 (2010).

[25] S. E. Truesdail, J. Lukasik, S. R. Farrah, D. O. Shah, R. B. Dickinson, "Analysis of bacterial deposition on metal (hydr)oxide-coated sand filter media", *J. Colloid Interface Sci.* **203**, 369 (1998).

[26] M. Gabi, A. Larmagnac, P. Schulte, J. Vörös, "Electrically controlling cell adhesion, growth and migration", *Colloids Surf. B* **79**, 365 (2010).

[27] S. Glab, A. Hulanicki, G. Edwall, F. Ingman, "Metal-metal oxide and metal oxide electrodes as pH sensors", *Crit. Rev. Anal. Chem.* **21**, 29 (1989).

[28] P. Kurzweil, "Metal oxides and ion-exchanging surfaces as pH sensors in liquids: State-of-the-art and outlook", *Sensors* **9**, 4955 (2009).

[29] D. W. Fuerstenau, Pradip, "Zeta potentials in the flotation of oxide and silicate minerals", *Adv. Colloid Interface Sci.* **114**, 9 (2005).

[30] Z. Y. Tao, T. W. Chu, W. J. Li, J. Z. Du, X. X. Dai, Y. J. Gu, "Cation adsorption of NpO_2^+, UO_2^{2+}, Zn^{2+}, Sr^{2+}, Yb^{3+}, and Am^{3+} onto oxides of Al, Si, and Fe from aqueous solution: Ionic strength effect", *Colloids Surf. A* **242**, 39 (2004).

[31] P. N. Pathak, G. R. Choppin, "Sorption of neptunyl(V) cations on suspended silicate: Effects of pH, ionic strength, complexing anions, humic acid, and metal ions", *J. Radioanal. Nucl. Chem.* **274**, 53 (2007).

[32] K. Müller, H. Foerstendorf, V. Brendler, G. Bernhard, "Sorption of Np(V) onto TiO_2, SiO_2, and ZnO_2: An ATR-FTIR spectroscopic study", *Environ. Sci. Technol.* **43**, 7665

(2009).

[33] W. Kunz (ed.), "Specific Ion Effects", World Scientific Publishers, 325 p. (2010).

[34] J. Lyklema, "Fundamentals of Interface and Colloid Science", vol. 2, Academic Press, 768 p. (1995).

[35] G. Sposito, "On points of zero charge", *Environ. Sci. Technol.* **32**, 2815 (1998).

[36] M. Kosmulski, "The pH-dependent surface charging and the points of zero charge", *J. Colloid Interface Sci.* **253**, 77 (2002).

[37] H. Schulze, "Schwefelarsen in wässriger Lösung", *J. Prakt. Chemie* **25**, 431 (1882).

[38] W. B. Hardy, "A preliminary investigation of the conditions which determine the stability of irreversible hydrosols", *Proc. R. Soc. Lond.* **66**, 110 (1899).

[39] Uber die Koagulationsgeschwindigkeit des $Al(OH)_3$-Sols, *Kolloidchemie Beihefte* **8**, 63 (1916).

[40] H. B. Weiser, E. B. Middleton, "Adsorption by precipitates. II – Adsorption by hydrous ferric oxide", *J. Phys. Chem.* **24**, 30 (1920).

[41] H. B. Weiser, E. B. Middleton, "Adsorption by precipitates. III – The adsorption of precipitating ions by hydrous aluminum oxide", *J. Phys. Chem.* **24**, 630 (1920).

[42] H. B. Weiser, "Hydrous oxides. III – Hydrous chromic oxide", *J. Phys. Chem.* **26**, 30 (1922).

[43] M. Kosmulski, "Surface Charging and Point of Zero Charge", Surfactant Science Series, vol. 145, CRC Press, Boca Raton, 1064 p. (2009).

[44] H. S. Posselt, F. J. Anderson, W. J. Weber, "Cation sorption on colloidal hydrous manganese dioxide", *Environ. Sci. Technol.* **2**, 1097 (1968).

[45] W. Stumm, C. P. Huang, S. R. Jenkins, "Specific chemical interactions affecting the stability of dispersed systems", *Croat. Chem. Acta* **42**, 223 (1970).

[46] J. W. Murray, "The interaction of metal ions at the manganese dioxide-solution interface", *Geochim. Cosmochim. Acta* **39**, 505 (1975).

[47] M. J. Gray, M. A. Malati, "Adsorption from aqueous solution by δ-manganese dioxide II. Adsorption of some heavy metal cations", *J. Chem. Technol. Biotechnol.* **29**, 135 (1979).

[48] T. F. Tadros, J. Lyklema, "Adsorption of potential-determining ions at the silica-aqueous electrolyte interface and the role of some cations on the ionic adsorption sequences", *J. Electroanal. Chem. Interfacial Electrochem.* **17**, 267 (1968).

[49] R. P. Abendroth, "Behavior of a pyrogenic silica in simple electrolytes", *J. Colloid Interface Sci.* **34**, 591 (1970).

[50] M. A. Malati, R. J. Mazza, A. J. Sherren, D. R. Tomkins, "The mechanism of adsorption of alkali metal ions on silica", *Powder Technol.* **9**, 107 (1974).

[51] X. K. Wang, W. M. Dong, H. X. Zhang, Z. Y. Tao, "A multitracer study on the adsorption of 36 elements on a silica: Effects of pH and fulvic acid", *J. Radioanal. Nucl. Chem.* **250**, 491 (2001).

[52] G. V. Franks, "Zeta potentials and yield stresses of silica suspensions in concentrated monovalent electrolytes: Isoelectric point shift and additional attraction", *J. Colloid Interface Sci.* **249**, 44 (2002).

[53] Y. G. Bérubé, P. L. de Bruyn, "Adsorption at the rutile-solution interface. II. Model of the electrochemical double layer", *J. Colloid Interface Sci.* **28**, 92 (1968).

[54] M. A. Malati, A. E. Smith, "The adsorption of the alkaline earth cations on titanium dioxide", *Powder Technol.* **22**, 279 (1979).

[55] F. Dumont, J. Warlus, A. Watillon, "Influence of the point of zero charge of titanium dioxide hydrosols", *J. Colloid Interface Sci.* **148**, 543 (1990).

[56] N. Kallay, M. Colić, D. W. Fuerstenau, H. M. Jang, E. Matijević, "Lyotropic effect in surface charge, electrokinetics, and coagulation of a rutile dispersion", *Colloid Polym. Sci.* **272**, 554 (1994).

[57] R. Sprycha, "Surface charge and adsorption of background electrolyte ions at anatase/ electrolyte interface", *J. Colloid Interface Sci.* **102**, 173 (1984).

[58] S. K. Milonjić, Z. E. Ilić, M. M. Kopecni, "Sorption of alkali cations at the zirconium oxide/aqueous electrolyte interface", *Colloids Surf.* **6**, 167 (1983).

[59] F. Dumont, P. Verbeiren, C. Buess-Herman, "Adsorption sequence of the alkali cations at the tungsten trioxide–water interface", *Colloids Surf. A* **154**, 149 (1999).

[60] Y. Y. Petrov, S. Y. Avvakumova, M. P. Sidorova, L. E. Ermakova, O. M. Merkushev, "Electrosurface properties of tungsten(VI) oxide in electrolyte solutions", *Colloid J.* **72**, 663 (2010).

[61] L. Blok, P. L. de Bruyn, "The ionic double layer at the ZnO/solution interface : III. Comparison of calculated and experimental differential capacities", *J. Colloid Interface Sci.* **32**, 533 (1970).

[62] R. Sprycha, "Electrical double layer at alumina/electrolyte interface: I. Surface charge and zeta potential", *J. Colloid Interface Sci.* **127**, 1 (1989).

[63] M. R. Das, J. M. Borah, W. Kunz, B. W. Ninham, S. Mahiuddin, "Ion specificity of the zeta potential of α-alumina, and of the adsorption of *p*-hydroxybenzoate at the α-alumina-water interface", *J. Colloid Interface Sci.* **344**, 482 (2010).

[64] A. Breeuwsma, J. Lyklema, "Interfacial electrochemistry of haematite (α-Fe_{203})", *Discuss. Faraday Soc.* **52**, 324 (1971).

[65] F. Dumont, D. Van Tan, A. Watillon, "Study of ferric oxide hydrosols from electrophoresis, coagulation, and peptization measurements", *J. Colloid Interface Sci.* **55**, 678 (1976).

[66] J. Lyklema, "Lyotropic sequences in colloid stability revisited", *Adv. Colloid Interface Sci.* **100-102**, 1 (2003).

[67] J. Lyklema, "Simple Hofmeister series", *Chem. Phys. Lett.* **467**, 217 (2009).

[68] L. Gierst, L. Vandenberghen, E. Nicolas, A. Fraboni, "Ion pairing mechanisms in electrode processes", *J. Electrochem. Soc.* **113**, 1025 (1966).

[69] K. D. Collins, "Charge density-dependent strength of hydration and biological structure", *Biophys. J.* **72**, 65 (1997).

[70] K. D. Collins, "Ions from the Hofmeister series and osmolytes: eVects on proteins in solution and in the crystallization process", *Methods* **34**, 300 (2004).

[71] D. F. Parsons, M. Bostrmöm, T. J. Maceina, A. Salis, B. W. Ninham, "Why direct or reversed Hofmeister series? Interplay of hydration, non-electrostatic potentials, and ion size", *Langmuir* **26**, 3323 (2010).

[72] Y. Marcus, "Effects of ions on the structure of water: Structure making and breaking", *Chem. Rev.* **109**, 1346 (2009).

[73] R. Zangi, "Can salting-in/salting-out ions be classified as chaotropes/kosmotropes?", *J. Phys. Chem. B* **114**, 643 (2010).

[74] J. Lyklema, "Specificity in the statics and dynamics of surface-confined ions", *Mol. Phys.* **100**, 3177 (2002).

[75] Y. Marcus, "Ion Solvation", John Wiley & Sons, 306 p. (1985).

[76] J. Lyklema, S. Rovillard, J. De Coninck, "Electrokinetics: The properties of the stagnant layer unraveled", *Langmuir* **14**, 5659 (1998).

[77] S. B. Johnson, G. V. Franks, P. J. Scales, T. W. Healy, "The binding of monovalent electrolyte ions on α-alumina. II. The shear yield stress of concentrated suspensions", *Langmuir* **15**, 2844 (1999).

[78] R. W. Gurney, "Ionic Processes in Solution", McGraw-Hill, 284 p. (1953).

[79] R. G. Pearson, "Hard and soft acids and bases, HSAB, part 1: Fundamental principles", *J. Chem. Educ.* **45**, 581 (1968).

[80] R. G. Pearson, "Hard and soft acids and bases, HSAB, part II: Underlying theories", *J. Chem. Educ.* **45**, 643 (1968).

[81] R. A. Robinson, R. H. Stokes, "Electrolyte Solutions", Dover Publications, 590 p. (2003).

[82] A. Serr, R. R. Netz, "Polarizabilities of hydrated and free ions derived from DFT calculations", *Int. J. Quant. Chem.* **106**, 2960 (2006).

[83] J. Janeček, R. R. Netz, "Interfacial water at hydrophobic and hydrophilic surfaces: depletion versus adsorption", *Langmuir* **23**, 8417 (2007).

[84] F. Sedlmeier, J. Janeček, C. Sendner, L. Bocquet, R. R. Netz, D. Horinek, "Water at polar and nonpolar solid walls", *Biointerphases* **3**, FC23 (2008).

[85] S. Kerisit, D. J. Cooke, A. Marmier, S. C. Parker, "Atomistic simulation of charged iron oxyhydroxide surfaces in contact with aqueous solution", *Chem. Comm.* **24**, 3027 (2005).

[86] S. Kerisit, E. S. Ilton, S. C. Parker, "Molecular dynamics simulations of electrolyte solutions at the (100) goethite surface", *J. Phys. Chem. B* **110**, 20491 (2006).

[87] S. Kerisit, D. J. Cooke, D. Spagnoli, S. C. Parker, "Molecular dynamics simulations of the interactions between water and inorganic solids", *J. Mater. Chem.* **15**, 1454 (2005).

[88] D. Spagnoli, D. J. Cooke, S. Kerisit, S. C. Parker, "Molecular dynamics simulations of the interaction between the surfaces of polar solids and aqueous solutions", *J. Mater. Chem.* **16**, 1997 (2006).

[89] M. Předota, A. V. Bandura, P. T. Cummings, J. D. Kubicki, D. J. Wesolowski, A. A. Chialvo, M. L. Machesky, "Electric double layer at the rutile (110) surface. 1. Structure of surfaces and interfacial water from molecular dynamics by use of ab initio potentials", *J. Phys. Chem. B* **108**, 12049 (2004).

[90] M. Předota, Z. Zhang, P. Fenter, D. J. Wesolowski, P. T. Cummings, "Electric double layer at the rutile (110) surface. 2. Adsorption of ions from molecular dynamics and X-ray experiments", *J. Phys. Chem. B* **108**, 12061 (2004).

[91] Z. Zhang, P. Fenter, L. Cheng, N. C. Sturchio, M. J. Bedzyk, M. Předota, A. Bandura, O J. D. Kubicki, S. N. Lvov, P. T. Cummings, A. A. Chialvo, M. K. Ridley, P. Bénézeth, L. Anovitz, D. A. Palmer, M. L. Machesky, D. J. Wesolowski, "Ion adsorption at the rutile-water interface: Linking molecular and macroscopic properties", *Langmuir* **20**, 4954 (2004).

[92] P. Fenter, "Applications of synchrotron radiation in low-temperature geochemistry

and environmental science", *Rev. Mineral. Geochem.* **49**, 149 (2002).

[93] M. J. Bedzyk, L. Cheng, "X-ray standing wave studies of minerals and mineral surfaces: Principles and applications", *Rev. Mineral. Geochem.* **49**, 221 (2002).

[94] K. B. Eisenthal, "Second harmonic spectroscopy of aqueous nano- and microparticle interfaces", *Chem. Rev.* **106**, 1462 (1996).

[95] P. L. Hayes, J. N. Malin, D. S. Jordan, F. M. Geiger, "Get charged up: Nonlinear optical voltammetry for quantifying the thermodynamics and electrostatics of metal cations at aqueous/oxide interfaces", *Chem. Phys. Lett.* **499**, 183 (2010).

[96] J. Wang, M. Caffrey, M. J. Bedzyk, T. L. Penner, "Direct profiling and reversibility of ion distribution at a charged membrane/aqueous interface: An X-ray standing wave study", *Langmuir* **17**, 3671 (2001).

[97] T. P. Trainor, A. S. Templeton, G. E. Brown, Jr., G. A. Parks, "Application of the long-period X-ray standing wave technique to the analysis of surface reactivity: Pb(II) sorption at α-Al_2O_3/aqueous solution interfaces in the presence and absence of Se(VI)", *Langmuir* **18**, 5782 (2002).

[98] P. Fenter, L. Cheng, S. Rihs, M. Machesky, M. J. Bedzyk, N. C. Sturchio, "Electrical double-layer structure at the rutile–water interface as observed *in situ* with small-period X-ray standing waves", *J. Colloid Interface Sci.* **225**, 154 (2000).

[99] Z. Zhang, P. Fenter, L. Cheng, N. C. Sturchio, M. J. Bedzyk, M. L. Machesky, D. J. Wesolowski, "Model-independent X-ray imaging of adsorbed cations at the crystal–water interface", *Surf. Sci.* **554**, L95 (2004).

[100] Z. Zhang, P. Fenter, S. D. Kelly, J. G. Catalano, A. V. Bandura, J. D. Kubicki, J. O. Sofo, D. J. Wesolowski, M. L. Machesky, N. C. Sturchio, M. J. Bedzyk, "Structure of hydrated Zn^{2+} at the rutile TiO_2 (110)-aqueous solution interface: Comparison of X-ray standing wave, X-ray absorption spectroscopy, and density functional theory results", *Geochim. Cosmochim. Acta* **70**, 4039 (2006).

[101] Z. Zhang, P. Fenter, L. Cheng, N. C. Sturchio, M. J. Bedzyk, M. L. Machesky, L. M. Anovitz, D. J. Wesolowski, "Zn^{2+} and Sr^{2+} adsorption at the TiO_2 (110)–electrolyte interface: Influence of ionic strength, coverage, and anions", *J. Colloid Interface Sci.* **295**, 50 (2006).

[102] S. Kneip, C. McGuffey, J. L. Martins, S. F. Martins, C. Bellei, V. Chvykov, F. Dollar, R. Fonseca, C. Huntington, G. Kalintchenko, A. Maksimchuk, S. P. D. Mangles, T. Matsuoka, S. R. Nagel, C. A. J. Palmer, J. Schreiber, K. Ta Phuoc, A. G. R. Thomas, V. Yanovsky, L. O. Silva, K. Krushelnick, Z. Najmudin, "Bright spatially coherent synchrotron X-rays from a table-top source", *Nature Phys.* **6**, 980 (2010).

[103] S. Ong, X. Zhao, K. B. Eisenthal, "Polarization of water molecules at a charged interface: second harmonic studies of the silica/water interface", *Chem. Phys. Lett.* **191**, 327 (1992).

[104] V. Ostroverkhov, G. A. Waychunas, Y. R. Shen, "Vibrational spectra of water at water/α-quartz (0001) interface", *Chem. Phys. Lett.* **386**, 327 (2004).

[105] S. Kataoka, M. C. Gurau, F. Albertorio, M. A. Holden, S.-M. Lim, R. D. Yang, P. S. Cremer, "Investigation of water structure at the TiO_2/aqueous interface", *Langmuir* **20**, 1662 (2004).

[106] K. C. Jena, D. K. Hore, "Variation of ionic strength reveals the interfacial water structure at a charged mineral surface", *J. Phys. Chem. C* **113**, 15364 (2009).

[107] Z. Yang, Q. Li, K. C. Chou, "Structures of water molecules at the interfaces of aque-

ous salt solutions and silica: Cation effects", *J. Phys. Chem. C* **113**, 8201 (2009).

[108] Q. Du, E. Freysz, Y. R. Shen, "Vibrational spectra of water molecules at quartz/water interfaces", *Phys. Rev. Lett.* **72**, 238 (1994).

[109] M. S. Yeganeh, S. M. Dougal, H. S. Pink, "Vibrational spectroscopy of water at liquid/solid interfaces: Crossing the isoelectric point of a solid surface", *Phys. Rev. Lett.* **83**, 1179 (1999).

[110] I. Li, J. Bandara, M. J. Shultz, "Time evolution studies of the H_2O/quartz interface using sum frequency generation, atomic force microscopy, and molecular dynamics", *Langmuir* **20**, 10474 (2004).

[111] V. Ostroverkhov, G. A. Waychunas, Y. R. Shen, "New information on water interfacial structure revealed by phase-sensitive surface spectroscopy", *Phys. Rev. Lett.* **94**, 046102 (2005).

[112] P. L. Hayes, J. N. Malin, C. T. Konek, F. M. Geiger, "Interaction of nitrate, barium, strontium and cadmium ions with fused quartz/water interfaces studied by second harmonic generation", *J. Phys. Chem. A* **112**, 660 (2008).

[113] H. Asanuma, H. Noguchi, K. Uosaki, H.-Z. Yu, "Water structure at superhydrophobic quartz/water interfaces: A vibrational sum frequency generation spectroscopy study", *J. Phys. Chem. C* **113**, 21155 (2009).

[114] J. N. Malin, F. L. Hayes, F. M. Geiger, "Interactions of Ca, Zn, and Cd ions at buried solid/water interfaces studied by second harmonic generation", *J. Phys. Chem. C* **113**, 2041 (2009).

[115] L. Zhang, S. Singh, C. Tian, Y. R. Shen, Y. Wu, M. A. Shannon, C. J. Brinker, "Nanoporous silica-water interfaces studied by sum-frequency vibrational spectroscopy", *J. Chem. Phys.* **130**, 154702 (2009).

[116] J. P. Fitts, M. L. Machesky, D. J. Wesolowski, X. Shang, J. D. Kubicki, G. W. Flynn, T. F. Heinz, K. B. Eisenthal, "Second-harmonic generation and theoretical studies of protonation at the water/α-TiO2 (110) interface", *Chem. Phys. Lett.* **411**, 399 (2005).

[117] A. G. Stack, S. R. Higgins, C. M. Eggleston, "Point of zero charge of a corundum-water interface probed with optical Second Harmonic Generation (SHG) and Atomic Force Microscopy (AFM): New approaches to oxide surface charge", *Geochim. Cosmochim. Acta* **65**, 3055 (2001).

[118] J. P. Fitts, X. M. Shang, G. W. Flynn, T. F. Heinz, K. B. Eisenthal, "Electrostatic surface charge at aqueous/alpha-Al_2O_3 single-crystal interfaces as probed by optical second-harmonic generation", *J. Phys. Chem. B* **109**, 7981 (2005).

[119] M. J. Musorrafiti, C. T. Konek, P. L. Hayes, F. M. Geiger, "Interaction of chromium(VI) with the α-aluminum oxide-water interface", *J. Phys. Chem. C* **112**, 2032 (2008).

[120] B. Braunschweig, S. Eissner, W. Daum, "Molecular structure of a mineral/water interface: Effects of surface nanoroughness of α-Al_2O_3 (0001)", *J. Phys. Chem. C* **112**, 1751 (2008).

[121] L. Zhang, C. Tian, G. A. Waychunas, Y. R. Shen, "Structures and charging of α-alumina (0001)/water interfaces studied by sum-frequency vibrational spectroscopy", *J. Am. Chem. Soc.* **130**, 7686 (2008).

[122] M. Flörsheimer, K. Kruse, R. Polly, A. Abdelmonem, B. Schimmelpfennig, R. Klenze, T. Fanghänel, "Hydration of mineral surfaces probed at the molecular level", *Langmuir* **24**, 13434 (2008).

[123] I. V. Stiopkin, Z.-H. Zhang, K. B. Eisenthal, T. F. Heinz, "Determination of the point of zero charge of the hematite/water interface", APS Meeting Abstracts, Abstract Nr. 13.007 (2001).

[124] M. Sovago, R. Kramer Campen, G. W. H. Wurpel, M. Müller, H. J. Bakker, M. Bonn, "Vibrational response of hydrogen-bonded interfacial water is dominated by intramolecular coupling", *Phys. Rev. Lett.* **100**, 173901 (2008).

[125] J. Lützenkirchen, R. Zimmermann, T. Preočanin, A. Filby, T. Kupcik, D. Küttner, A. Abdelmonem, D. Schild, T. Rabung, M. Plaschke, F. Brandenstein, C. Werner, H. Geckeis, "An attempt to explain bimodal behaviour of the sapphire c-plane electrolyte interface", *Adv. Colloid Interface Sci.* **157**, 61 (2010).

[126] M. C. Gurau, G. Kim, S.-M. Lim, F. Albertorio, H. C. Fleisher, P. S. Cremer, "Organization of water layers at hydrophilic interfaces", *Chemphyschem* **4**, 1231 (2003).

[127] J. A. McGuire, Y. R. Shen, "Ultrafast vibrational dynamics at water interfaces", *Science* **313**, 1945 (2006).

[128] K. L. Chopra, S. Major, D. K. Pandya, "Transparent conductors — A status review", *Thin Solid Films* **102**, 1 (1983).

[129] D. S. Ginley, C. Bright, "Transparent Conducting Oxides", *MRS Bull.* **25**, 15 (2000).

[130] B. G. Lewis, D. C. Paine, "Applications and processing of transparent conducting oxides", *MRS Bull.* **25**, 22 (2000).

[131] T. Minami, "Transparent conducting oxide semiconductors for transparent electrodes", *Semicond. Sci. Technol.* **20**, S35 (2005).

[132] B. P. Kryzhanovskii, "Reflection of semiconducting indium oxide films in the infrared spectral region", *Opt. Spectr.-USSR* **10**, 359 (1961).

[133] R. Groth, "Untersuchungen an halbleitenden Indiumoxydschichten", *Phys. Status Solidi* **14**, 69 (1966).

[134] A. Kumar, C. Zhou, "The race to replace tin-doped indium oxide: Which material will win?", *ACS Nano* **4**, 11 (2010).

[135] J. Kim, J. Noh, D. Ihm, "Transparent multi-layer conductive electrode film prepared by DC sputter deposition and its flat panel display application", *Mol. Cryst. Liq. Cryst.* **377**, 41 (2002).

[136] U. Betz, M. Kharrazi Olsson, J. Marthy, M. F. Escolá, F. Atamny, "Thin films engineering of indium tin oxide: Large area flat panel displays application", *Surf. Coat. Tech.* **200**, 5751 (2006).

[137] C. W. Tang and S. A. Van Slyke, "Organic electroluminescent diodes", *Appl. Phys. Lett.* **12**, 913 (1987).

[138] J. S. Kim, M. Granström, R. H. Friend, N. Johansson, W. R. Salaneck, R. Daik, W. J. Feast, F. Cacialli, "Indium–tin oxide treatments for single- and double-layer polymeric light-emitting diodes: The relation between the anode physical, chemical, and morphological properties and the device performance", *J. Appl. Phys.* **84**, 6859 (1998).

[139] Y. Shen, D. B. Jacobs, G. G. Malliaras, G. Koley, M. G. Spencer and A. Ioannidis, "Modification of indium tin oxide for improved hole injection in organic light emitting diodes", *Adv. Mater.* **13**, 1234 (2001).

[140] J.-S. Kim, F. Cacialli, R. Friend, "Surface conditioning of indium-tin oxide anodes for organic light-emitting diodes", *Thin Solid Films* **445**, 358 (2003).

[141] T.-H. Chen, T. J. Wu, J. Y. Chen, Y. Liou, "Effects of metal-doped indium-tin-oxide buffer layers in organic light-emitting devices", *J. Appl. Phys.* **99**, 114515/1 (2006).

[142] C. G. Granqvist, "Transparent conductive electrodes for electrochromic devices: A review", *Appl. Phys. A* **57**, 19 (1993).

[143] C. G. Granqvist, "Electrochromic materials - out of a niche", *Nature Mater.* **5**, 89 (2006).

[144] C. G. Granqvist, G. A. Niklasson, A. Azens, "Electrochromics: Fundamentals and energy-related applications of oxide-based devices", *Appl. Phys. A* **89**, 29 (2007).

[145] K. S. Sree Harsha, K. J. Bachmann, P. H. Schmidt, E. G. Spencer, F. A. Thiel, "N-indium tin oxide/p-indium phosphide solar cells", *Appl. Phys. Lett.* **30**, 645 (1977).

[146] G. Cheek, N. Inoue, S. Goodnick, A. Genis, C. Wilmsen, J. B. Dubow, "Fabrication and characterization of indium tin oxide /ITO//polycrystalline silicon solar cells", *Appl. Phys. Lett.* **33**, 643 (1978).

[147] V. K. Jain, A. P. Kulshreshtha, "Indium-tin-oxide transparent conducting coatings on silicon solar cells and their "figure of merit"", *Sol. Energ. Mater.* **4**, 151 (1981).

[148] W. M. Sears, E. Fortin, J. B. Webb, "Indium tin oxide/Cu_2O photovoltaic cells, *Thin Solid Films* **103**, 303 (1983).

[149] S. Naseem, T. J. Coutts, "Indium tin oxide/gallium arsenide solar cells", *J. Appl. Phys.* **58**, 4463 (1985).

[150] S. K. Das, G. C. Morris, "Preparation and properties of electrodeposited indium tin oxide/SnO_2/CdTe and indium tin oxide/SnO_2/CdS/CdTe solar cells", *J. Appl. Phys.* **73**, 782 (1993).

[151] E. Fortunato, D. S. Ginley, H. Hosono, D. C. Paine, "Transparent conducting oxides for photovoltaics," *MRS Bulletin* **32**, 242 (2007).

[152] C. G. Granqvist, "Transparent conductors as solar energy materials: A panoramic review", *Sol. Energ. Mater. Sol. Cells* **91**, 1529 (2007).

[153] C. J. Brabec, "Organic photovoltaics: technology and market", *Solar. Ener. Mater. Solar Cells* **83**, 273 (2004).

[154] H. Hoppe, N. Serdar Sariciftci, "Organic solar cells: An overview", *J. Mater. Res.*, **19**, 1924 (2004).

[155] C. Waldauf, M. Morana, P. Denk, P. Schilinsky, K. Coakley, S. A. Choulis, C. J. Brabec, "Highly efficient inverted organic photovoltaics using solution based titanium oxide as electron selective contact", *Appl. Phys. Lett.* **89**, 233517 (2006).

[156] K. Schulze, B. Maennig, K. Leo, Y. Tomita, C. May, J. Hüpkes, E. Brier, E. Reinold, P. Bäuerle, "Organic solar cells on indium tin oxide and aluminum doped zinc oxide anodes", *Appl. Phys. Lett.* **91**, 073521 (2007).

[157] N. R. Armstrong, P. A. Veneman, E. Ratcliff, D. Placencia, M. Brumbach, "Oxide contacts in organic photovoltaics: Characterization and control of near-surface composition in indium-tin oxide (ITO) electrodes", *Acc. Chem. Res.* **42**, 1748 (2009).

[158] M. Grätzel, "Dye-sensitized solar cells", *J. Photochem. Photobio. C* **4**, 145 (2003).

[159] M. Grätzel, "Solar energy conversion by dye-sensitized photovoltaic cells", *Inorg. Chem.* **44**, 6841 (2005).

[160] S. Ngamsinlapasathian, T. Sreethawong, Y. Suzuki, S. Yoshikawa, "Doubled layered ITO/SnO_2 conducting glass for substrate of dye-sensitized solar cells", *Sol. Energ. Mater. Sol. Cells* **90**, 2129 (2006).

[161] J. E. Lyon, M. K. Rayan, M. M. Beerbom, R. Schlaf, "Electronic structure of the indium tin oxide/nanocrystalline anatase (TiO_2)/ruthenium-dye interfaces in dye-sensitized solar cells", *J. Appl. Phys.* **104**, 073714/1 (2008).

[162] S. Lee, J. H. Noh, S.-T. Bae, I.-S. Cho, J. Y. Kim, H. Shin, J.-K. Lee, H. S. Jung, K. S. Hong, "Indium-tin-oxide-based transparent conducting layers for highly efficient photovoltaic devices", *J. Phys. Chem. C* **113**, 7443 (2009).

[163] G. Sberveglieri, S. Groppelli, G. Coccoli, "Radio frequency magnetron sputtering growth and characterization of indium-tin oxide (ITO) thin films for NO_2 gas sensors", *Sens. Actuat.* **15**, 235 (1988).

[164] G. Sberveglieri, P. Benussi, G. Coccoli, S. Groppelli, P. Nelli, "Reactivity sputtered indium tin oxide polycrystalline thin films as NO and NO_2 gas sensors", *Thin Solid Films* **186**, 349 (1990).

[165] N. G. Patel, K. K. Makhija, C. J. Panchal, "Fabrication of carbon dioxide gas sensor and its alarm system using Indium Tin Oxide (ITO) thin films", *Sens. Actuat. B-Chem.* **21**, 193 (1994).

[166] N. G. Patel, K. K. Makhija, C. J. Panchal, D. B. Dave, V. S. Vaishnav, "Fabrication of carbon tetrachloride gas sensors using indium tin oxide thin films", *Sens. Actuat. B-Chem.* **23**, 49 (1995).

[167] H. Yumoto, T. Inoue, S. J. Li, T. Sako, K. Nishiyama, "Application of ITO films to photocatalysis", *Thin Solid Films* **345**, 38 (1999).

[168] T. Sako, A. Ohmi, H. Yumoto, K. Nishiyama, "ITO-film gas sensor for measuring photodecomposition of NO_2 gas", *Surf. Coat. Tech.* **142-144**, 781 (2001).

[169] N. G. Patel, P. D. Patel, V. S. Vaishnav, "Indium tin oxide (ITO) thin film gas sensor for detection of methanol at room temperature", *Sens. Actuat. B-Chem.* **96**, 180 (2003).

[170] V.S. Vaishnav, P.D. Patel, N.G. Patel, "Preparation and characterization of indium tin oxide thin films for their application as gas sensors", *Thin Solid Films* **487**, 277 (2005).

[171] V. S. Vaishnav, P. D. Patel, N. G. Patel, "Indium tin oxide thin film gas sensors for detection of ethanol vapours", *Thin Solid Films* **490**, 94 (2005).

[172] S.-Y. Oh, Y.-J. Yun, D.-Y. Kim, S.-H. Han, "Formation of a self-assembled monolayer of diaminododecane and a heteropolyacid monolayer on the ITO surface", *Langmuir* **15**, 4690 (1999).

[173] C. O. Kim, S.-Y. Hong, M. Kim, S.-M. Park, J. W. Park, "Modification of indium–tin oxide (ITO) glass with aziridine provides a surface of high amine density", *J. Colloid Interface Sci.* **277**, 499 (2004).

[174] S.-Y. Oh, Y.-J. Yun, K.-H. Hyung, S.-H. Han, "Self-assembled monolayers of diamine molecules and phosphomolybdic acid on an ITO surface", *New J. Chem.* **28**, 495 (2004).

[175] M. Carrara, F. Nüesch, L. Zuppiroli, "Carboxylic acid anchoring groups for the construction of self-assembled monolayers on organic device electrodes", *Synth. Met.* **121** 1633 (2001).

[176] N. R. Armstrong, C. Carter, C. Donley, A. Simmonds, P. Lee, M. Brumbach, B. Kippelen, B. Domercq, S. Yoo, "Interface modification of ITO thin films: Organic photovoltaic cells", *Thin Solid Films* **445**, 342 (2003).

[177] M. Cerruti, C. Rhodes, M. Losego, A. Efremenko, J.-P. Maria, D. Fischer, S. Franzen,

J. Genzer, "Influence of indium–tin oxide surface structure on the ordering and coverage of carboxylic acid and thiol monolayers", *J. Phys. D: Appl. Phys.* **40**, 4212 (2007).

[178] S. Besbes, A. Ltaief, K. Reybier, L. Ponsonnet, N. Jaffrezic, J. Davenas, H. Ben Ouada, "Injection modifications by ITO functionalization with a self-assembled monolayer in OLEDs", *Synth. Met.* **138**, 197 (2003).

[179] E. L. Hanson, J. Guo, N. Koch, J. Schwartz, S. L. Bernasek, "Advanced surface modification of indium tin oxide for improved charge injection in organic devices", *J. Am. Chem. Soc.* **127**, 10058 (2005).

[180] S. E. Koh, K. D. McDonald, D. H. Holt, C. S. Dulcey, J. A. Chaney, P. E. Pehrsson, "Phenylphosphonic acid functionalization of indium tin oxide: Surface chemistry and work functions", *Langmuir* **22**, 6249 (2006).

[181] S. A. Paniagua, P. J. Hotchkiss, S. C. Jones, S. R. Marder, A. Mudalige, F. S. Marrikar, J. E. Pemberton, N. R. Armstrong, "Phosphonic acid modification of indium-tin oxide electrodes: Combined XPS/UPS/contact angle studies", *J. Phys. Chem. C* **112**, 7809 (2008).

[182] H. Hillebrandt, M. Tanaka, "Electrochemical characterization of self-assembled alkylsiloxane monolayers on indium-tin oxide (ITO) semiconductor electrodes", *J. Phys. Chem. B* **105**, 4270 (2001).

[183] I. Markovich, D. Mandler, "Preparation and characterization of octadecylsilane monolayers on indium–tin oxide (ITO) surfaces", *J. Electroanal. Chem.* **500**, 453 (2001).

[184] J. Lee, B.-J. Jung, J.-I. Lee, H. Y. Chu, L.-M. Do, H.-K. Shim, "Modification of an ITO anode with a hole-transporting SAM for improved OLED device characteristics", *J. Mater. Chem.* **12**, 3494 (2002).

[185] V. M. Bermudez, A. D. Berry, H. Kim, A. Piqué, "Functionalization of indium tin oxide", *Langmuir* **22**, 11113 (2006).

[186] C. Yan, M. Zharnikov, A. Gölzhäuser, M. Grunze, "Preparation and characterization of self-assembled monolayers on indium tin oxide", *Langmuir* **16**, 6208 (2000).

[187] S. H. Brewer, D. A. Brown, S. Franzen, "Formation of thiolate and phosphonate adlayers on indium-tin oxide: Optical and electronic characterization", *Langmuir* **18**, 6857 (2002).

[188] N. Karsi, P. Lang, M. Chehimi, M. Delamar, G. Horowitz, "Modification of indium tin oxide films by alkanethiol and fatty acid self-assembled monolayers: A comparative study", *Langmuir* **22**, 3118 (2006).

[189] T. Daido, T. Akaike, "Electrochemistry of cytochrome c: influence of coulombic attraction with indium tin oxide electrode", *J. Electroanal. Chem.* **344**, 91 (1993).

[190] A. Fang, H. T. Ng, S. F. Y. Li, "Anchoring of self-assembled hemoglobin molecules on bare indium-tin oxide surfaces", *Langmuir* **17**, 4360 (2001).

[191] H. T. Ng, A. Fang, L. Huang, S. F. Y. Li, "Protein microarrays on ITO surfaces by a direct covalent attachment scheme", *Langmuir* **18**, 6324 (2002).

[192] K. Mitsubayashi, Y. Wakabayashi, S. Tanimoto, D. Murotomi, T. Endo, "Optical-transparent and flexible glucose sensor with ITO electrode", *Biosens. Bioelectr.* **19**, 67 (2003).

[193] D. H. Hedges, D. J. Richardson, D. A. Russell, "Electrochemical control of protein monolayers at indium tin oxide surfaces for the reagentless optical biosensing of

nitric oxide", *Langmuir* **20**, 1901 (2004).

[194] Y. Suemori, K. Fujii, M. Ogawa, Y. Nakamura, K. Shinohara, K. Nakagawa, M. Nagata, K. Iida, T. Dewa, K. Yamashita, M. Nango, "Molecular assembly of artificial photosynthetic antenna core complex on an amino-terminated ITO electrode", *Colloids Surf. B* **56**, 182 (2007).

[195] P. Vengadesh, S.V. Muniandy, W.H. Abd. Majid, "Fractal morphological analysis of bacteriorhodopsin (bR) layers deposited onto indium tin oxide (ITO) electrodes", *Mater. Sci. Eng. C* **29**, 1621 (2009).

[196] M. E. Napier, H. H. Thorp, "Modification of electrodes with dicarboxylate self-assembled monolayers for attachment and detection of nucleic acids", *Langmuir* **13**, 6342 (1997).

[197] P. M. Armistead, H. H. Thorp, "Modification of indium tin oxide electrodes with nucleic acids: Detection of attomole quantities of immobilized DNA by electrocatalysis", *Anal. Chem.* **72**, 3764 (2000).

[198] I. V. Yang, H. H. Thorp, "Repeat polynucleotides: Electrochemical detection of trinucleotide repeat expansion, *Anal. Chem.* **73**, 5316 (2001).

[199] J. Xu, J.-J. Zhu, Q. Huang, H.-Y. Chen, "A novel DNA-modified indium tin oxide electrode", *Electrochem. Comm.* **3**, 665 (2001).

[200] E. J. Moore, M. Curtin, J. Ionita, A. R. Maguire, G. Ceccone, P. Galvin, "Selective release of DNA from the surface of indium-tin oxide thin electrode films using thiol-disulfide exchange chemistry", *Anal. Chem.* **79**, 2050 (2007).

[201] S. Shah, A. Revzin, "Patterning cells on optically transparent indium tin oxide electrodes", *J. Vis. Exp.* **7**, 259 (2007).

[202] S. S. Shah, J. Y. Lee, S. Verkhoturov, N. Tuleuova, E. A. Schweikert, E. Ramanculov and A. Revzin, "Exercising spatiotemporal control of cell attachment with optically transparent microelectrodes", *Langmuir* **24**, 6837 (2008).

[203] S. S. Shah, M. C. Howland, L. J. Chen, J. Silangcruz, S. V. Verkhoturov, E. A. Schweikert, A. N. Parikh, A. M. Revzin, "Micropatterning of proteins and mammalian cells on indium tin oxide", *ACS Appl. Mater. Interfaces* **1**, 2592 (2009).

[204] D. R. Dunphy, S. B. Mendes, S. S. Saavedra, N. R. Armstrong, "The electroactive integrated optical waveguide: Ultrasensitive spectroelectrochemistry of submonolayer adsorbates", *Anal. Chem.* **69**, 3086 (1997).

[205] S. Vico, V. Carlier, C. Buess-Herman, "Spectroelectrochemical study of the influence of anions on the behaviour of poly(N-vinylcarbazole) films", *J. Electroanal. Chem.* **475**, 1 (1999).

[206] S. E. Ross, C. J. Seliskar, W. R. Heineman, "Spectroelectrochemical sensing based on multimode selectivity simultaneously achievable in a single device. 9. Incorporation of planar waveguide technology", *Anal. Chem.* **72**, 5549 (2000).

[207] N. Matsuda, J. H. Santos, A. Takatsu, K. Kato, "In situ observation of absorption spectra and adsorbed species of methylene blue on indium-tin-oxide electrode by slab optical waveguide spectroscopy", *Thin Solid Films* **445**, 313 (2003).

[208] J. Agrisuelas, D. Giménez-Romero, J.J. García-Jareño, F. Vicente, "Vis/NIR spectroelectrochemical analysis of poly-(Azure A) on ITO electrode", *Electrochem. Comm.* **8**, 549 (2006).

[209] S. Qiu, L. Sun, H. Chu, Y. Zou, F. Xu, N. Matsuda, "Study of adsorption behaviors of meso-tetrakis (4-N-Methylpyridyl) porphine p-Toluenesulfonate at indium–tin-

oxide electrode/solution interface by in-situ internal reflection spectroscopy and cyclic voltammetry", *Thin Solid Films* **517**, 2905 (2009).

[210] I. A. Rauf, "Low resistivity and high mobility tin-doped indium oxide films", *Mater. Lett.* **18**, 123 (1993).

[211] F. Hanus, A. Jadin, L. D. Laude, "Pulsed laser deposition of high quality ITO thin films", *Appl. Surf. Sci.* **96-98**, 807 (1996).

[212] D.-H. Kim, M.-R. Park, G.-H. Lee, "Preparation of high quality ITO films on a plastic substrate using RF magnetron sputtering", *Surf. Coat. Tech.* **201**, 927 (2006).

[213] Z. Chen, K. Yang, J. Wang, "Preparation of indium tin oxide films by vacuum evaporation", *Thin Solid Films* **162**, 305 (1988).

[214] T. Minami, S. Ida, T. Miyata, "High rate deposition of transparent conducting oxide thin films by vacuum arc plasma evaporation", *Thin Solid Films* **416**, 92 (2002).

[215] R. Banerjee, D. Das, S. Ray, A. K. Batabyal, A. K. Barua, "Characterization of tin doped indium oxide films prepared by electron beam evaporation", *Sol. Energ. Mater.* **13**, 11 (1986).

[216] M. Yamaguchi, A. Ide-Ektessabi, H. Nomura, N. Yasui, "Characteristics of indium tin oxide thin films prepared using electron beam evaporation", *Thin Solid Films* **447-448**, 115 (2004).

[217] P. C. Karulkar, M. E. McCoy, "D.C. magnetron sputter deposition of indium tin oxide films", *Thin Solid Films* **83**, 259 (1981).

[218] S. Bhagwat, R. P. Howson, "Use of the magnetron-sputtering technique for the control of the properties of indium tin oxide thin films", *Surf. Coat. Tech.* **111**, 163 (1999).

[219] F. Kurdesau, G. Khripunov, A. F. da Cunha, M. Kaelin, A. N. Tiwari, "Comparative study of ITO layers deposited by DC and RF magnetron sputtering at room temperature", *J. Non-Cryst. Solids* **352**, 1466 (2006).

[220] U. Betz, M. Kharrazi Olsson, J. Marthy, M. F. Escolá, "On the synthesis of ultra smooth ITO thin films by conventional direct current magnetron sputtering", *Thin Solid Films* **516**, 1334 (2008).

[221] J. P. Zheng, H. S. Kwok, "Preparation of indium tin oxide films at room temperature by pulsed laser deposition", *Thin Solid Films* **232**, 99 (1993).

[222] A. Suzuki, T. Matsushita, T. Aoki, A. Mori, M. Okuda, "Highly conducting transparent indium tin oxide films prepared by pulsed laser deposition", *Thin Solid Films* **411**, 23 (2002).

[223] H. L. Hartnagel, A. L. Dawar, A. K. Jain, C. Jagadish, "Semiconducting Transparent Thin Films", Institute of Physical Publishing, 358 p. (1995).

[224] C.-H. Yang, S.-C. Lee, T.-C. Lin, W.-Y. Z., "Effect of tin doping on the properties of indium-tin-oxide films deposited by radio frequency magnetron sputtering", *Mater. Sci. Eng. B* **138**, 271 (2007).

[225] D.-H. Kim, M.-R. Park, H.-J. Lee, G.-H. Lee, "Thickness dependence of electrical properties of ITO film deposited on a plastic substrate by RF magnetron sputtering", *Appl. Surf. Sci.* **253**, 409 (2006).

[226] C.-H. Liang, S.-C. Chen, X. Qi, C.-S. Chen, C.-C. Yang, "Influence of film thickness on the texture, morphology and electro-optical properties of indium tin oxide films", *Thin Solid Films* **519**, 345 (2010).

[227] K. J. Kumar, N. R. C. Raju, A. Subrahmanyam, "Thickness dependent physical and

photocatalytic properties of ITO thin films prepared by reactive DC magnetron sputtering", *Appl. Surf. Sci.* **257**, 3075 (2011).

[228] L.-j. Meng, M. P. dos Santos, "Properties of indium tin oxide (ITO) films prepared by r.f. reactive magnetron sputtering at different pressures", *Thin Solid Films* **303**, 151 (1997).

[229] L. R. Cruz, C. Legnani, I. G. Matoso, C. L. Ferreira, H. R. Moutinho, "Influence of pressure and annealing on the microstructural and electro-optical properties of RF magnetron sputtered ITO thin films", *Mater. Res. Bull.* **39**, 993 (2004).

[230] A. Salehi, "The effects of deposition rate and substrate temperature of ITO thin films on electrical and optical properties", *Thin Solid Films* **324**, 214 (1998).

[231] H. R. Fallah, M. Ghasemi, A. Hassanzadeh, H. Steki, "The effect of deposition rate on electrical, optical and structural properties of tin-doped indium oxide (ITO) films on glass at low substrate temperature", *Physica B: Cond. Mat.* **373**, 274 (2006).

[232] S. Honda, M. Watamori, K. Oura, "The effects of oxygen content on electrical and optical properties of indium tin oxide films fabricated by reactive sputtering", *Thin Solid Films* **281-282**, 206 (1996).

[233] D.-G. Kim, S. Lee, G.-H. Lee, S.-C. Kwon, "Effects of hydrogen gas on properties of tin-doped indium oxide films deposited by radio frequency magnetron sputtering method", *Thin Solid Films* **515**, 6949 (2007).

[234] H.-N. Cui, V. Teixeira, L.-J. Meng, R. Martins, E. Fortunato, "Influence of oxygen/argon pressure ratio on the morphology, optical and electrical properties of ITO thin films deposited at room temperature", *Vacuum* **82**, 1507 (2008).

[235] C. G. Choi, K. No, W.-J. Lee, H.-G. Kim, S. O. Jung, W. J. Lee, W. S. Kim, S. J. Kim, C. Yoon, "Effects of oxygen partial pressure on the microstructure and electrical properties of indium tin oxide film prepared by d.c. magnetron sputtering", *Thin Solid Films* **258**, 274 (1995).

[236] Rajesh Das, Koel Adhikary, Swati Ray, "The role of oxygen and hydrogen partial pressures on structural and optical properties of ITO films deposited by reactive rf-magnetron sputtering", *Appl. Surf. Sci.* **253**, 6068 (2007).

[237] L. Kerkache, A. Layadi, A. Mosser, "Effect of oxygen partial pressure on the structural and optical properties of dc sputtered ITO thin films", *J. Alloys Compd.* **485**, 46 (2009).

[238] H.-C. Lee, O. O. Park, "Behaviors of carrier concentrations and mobilities in indium–tin oxide thin films by DC magnetron sputtering at various oxygen flow rates", *Vacuum* **77**, 69 (2004).

[239] S. Li, X. Qiao, J. Chen, "Effects of oxygen flow on the properties of indium tin oxide films", *Mater. Chem. Phys.* **98**, 144 (2006).

[240] Y. J. Kim, S. B. Jin, S. I. Kim, Y. S. Choi, I. S. Choi, J. G. Han, "Effect of oxygen flow rate on ITO thin films deposited by facing targets sputtering", *Thin Solid Films* **518**, 6241 (2010).

[241] C. Guillén, J. Herrero, "Structural, optical and electrical characteristics of ITO thin films deposited by sputtering on different polyester substrates", *Mater. Chem. Phys.* **112**, 641 (2008).

[242] N. Manavizadeh, F. A. Boroumand, E. Asl-Soleimani, F. Raissi, S. Bagherzadeh, A. Khodayari, M. A. Rasouli, "Influence of substrates on the structural and morphological properties of RF sputtered ITO thin films for photovoltaic application", *Thin*

Solid Films **517**, 2324 (2009).

[243] L.-j. Meng, M. P. dos Santos, "Properties of indium tin oxide films prepared by rf reactive magnetron sputtering at different substrate temperature", *Thin Solid Films* **322**, 56 (1998).

[244] E. Terzini, P. Thilakan, C. Minarini, "Properties of ITO thin films deposited by RF magnetron sputtering at elevated substrate temperature", *Mater. Sci. Eng. B* **77**, 110 (2000).

[245] C. Nunes de Carvalho, A. M. Botelho do Rego, A. Amaral, P. Brogueira, G. Lavareda, "Effect of substrate temperature on the surface structure, composition and morphology of indium–tin oxide films", *Surf. Coat. Tech.* **124**, 70 (2000).

[246] J. N. Avaritsiotis, D. K. Sivridis, E. Roditi, "The effect of target erosion and RF substrate biasing on the properties of reactively sputtered ITO films", *Sol. Energ. Mater.* **15**, 485 (1987).

[247] H.-W. Zhang, W.-y. Xu, "Effect of bias and post-deposition vacuum annealing on structure and transmittance of ITO films", *Vacuum* **43**, 835 (1992).

[248] S. Calnan, H. M. Upadhyaya, S. E. Dann, M. J. Thwaites, A. N. Tiwari, "Effects of target bias voltage on indium tin oxide films deposited by high target utilisation sputtering", *Thin Solid Films* **515**, 8500 (2007).

[249] A. Antony, M. Nisha, R. Manoj, M. K. Jayaraj, "Influence of target to substrate spacing on the properties of ITO thin films", *Appl. Surf. Sci.* **225**, 294 (2004).

[250] D. J. You, S. K. Choi, H. S. Han, J. S. Lee, C. B. Lim, "Effect of the deposition geometry on the electrical properties within tin-doped indium oxide film deposited under a given RF magnetron sputtering condition", *Thin Solid Films* **401**, 229 (2001).

[251] G. Gonçalves, E. Elangovan, P. Barquinha, L. Pereira, R. Martins, E. Fortunato, "Influence of post-annealing temperature on the properties exhibited by ITO, IZO and GZO thin films", *Thin Solid Films* **515**, 8562 (2007).

[252] M. Marezio, "Refinement of the crystal structure of In_2O_3 at two wavelengths", *Acta Cryst.* **20**, 723 (1966).

[253] N. Nadaud, N. Lequeux, M. Nanot, J. Jové, T. Roisnel, "Structural studies of tin-doped indium oxide (ITO) and $In_4Sn_3O_{12}$", *J. Solid State Chem.* **135**, 140 (1998).

[254] O. N. Mryasov, A. J. Freeman, "Electronic band structure of indium tin oxide and criteria for transparent conducting behavior", *Phys. Rev. B* **64**, 233111 (2001).

[255] G. B. González, J. B. Cohen, J.-H. Hwang, T. O. Mason, J. P. Hodges, J. D. Jorgensen, "Neutron diffraction study on the defect structure of indium-tin oxide", *J. Appl. Phys.* **89**, 2550 (2001).

[256] O. P Agnihotri, A. K. Sharma, B. K. Gupta, R. Thangaraj, "The effect of tin additions on indium oxide selective coatings", *J. Phys. D: Appl. Phys.* **11**, 643 (1978).

[257] Y. Marcus, "Ion Properties", Marcel Dekker, 259 p. (1997).

[258] P. B. Paramonov, S. A. Paniagua, P. J. Hotchkiss, S. C. Jones, N. R. Armstrong, S. R. Marder, J.-L. Brédas, "Theoretical characterization of the indium tin oxide surface and of its binding sites for adsorption of phosphonic acid monolayers", *Chem. Mater.* **20**, 5131 (2008).

[259] C. Donley, D. Dunphy, D. Paine, C. Carter, K. Nebesny, P. Lee, D. Alloway, N. R. Armstrong, "Characterization of indium-tin oxide interfaces using X-ray photoelectron spectroscopy and redox processes of a chemisorbed probe molecule: Effect of

surface pretreatment conditions", *Langmuir* **18**, 450 (2002).

[260] C. F. Baes, Jr., R. E. Mesmer, "The Hydrolysis of Cations", Krieger Publishing, 489 p. (1986).

[261] J. S. Kim, F. Cacialli, M. Granström, R. H. Friend, N. Johansson, W. R. Salaneck, R. Daik, W. J. Feast, "Characterisation of the properties of surface-treated indium-tin oxide thin films", *Synth. Met.* **101**, 111 (1999).

[262] S. Besbes, H. Ben Ouada, J. Davenas, L. Ponsonnet, N. Jaffrezic, P. Alcouffe, "Effect of surface treatment and functionalization on the ITO properties for OLEDs", *Mater. Sci. Eng. C* **26**, 505 (2006).

[263] A. Abderrahmen, F. F. Romdhane, H. Ben Ouada, A. Gharbi, "Indium–tin oxide surface treatments: Effects on the performance of liquid crystal devices", *Mater. Sci. Eng. C* **26**, 538 (2006).

[264] R. F. Bianchi, A. J. F. Carvalho, M. A. Pereira-da-Silva, D. T. Balogh, R. M. Faria, "Characterization of indium-tin-oxide films treated by different procedures: effect of treatment time in aqua regia solution", *Mater. Sci. Eng. C* **24**, 595 (2004).

[265] E. S. Lee, J. H. Choi, H. K. Baik, "Surface cleaning of indium tin oxide by atmospheric air plasma treatment with the steady-state airflow for organic light emitting diodes", *Surf. Coat. Technol.* **201**, 4973 (2007).

[266] M.-H. Jung, H.-S. Choi, "Surface treatment and characterization of ITO thin films using atmospheric pressure plasma for organic light emitting diodes", *J. Colloid Interface Sci.* **310**, 550 (2007).

[267] S. Major, Satyendra Kumar, M. Bhatnagar, and K. L. Chopra, "Effect of hydrogen plasma treatment on transparent conducting oxides", *Appl. Phys. Lett.* **49**, 394 (1986).

[268] K. Furukawa, Y. Terasaka, H. Ueda, M. Matsumura, "Effect of a plasma treatment of ITO on the performance of organic electroluminescent devices", *Synth. Met.* **91**, 99 (1997).

[269] J. S. Kim, P. K. H. Ho, D. S. Thomas, R. H. Friend, F. Cacialli, G. -W. Bao, S. F. Y. Li, "X-ray photoelectron spectroscopy of surface-treated indium-tin oxide thin films", *Chem. Phys. Lett.* **315**, 307 (1999).

[270] J. A. Chaney, S. E. Koh, C. S. Dulcey, P. E. Pehrsson, "Surface chemistry of carbon removal from indium tin oxide by base and plasma treatment, with implications on hydroxyl termination", *Appl. Surf. Sci.* **218**, 259 (2003).

[271] Zhong Zhi You, Jiang Ya Dong, "Effect of oxygen plasma treatment on the surface properties of tin-doped indium oxide substrates for polymer LEDs", *J. Colloid Interface Sci.* **300**, 697 (2006).

[272] T. Kawai, Y. Maekawa, M. Kusabiraki, "Plasma treatment of ITO surfaces to improve luminescence characteristics of organic light-emitting devices with dopants", *Surf. Sci.* **601**, 5276 (2007).

[273] M. G. Mason, L. S. Hung, C. W. Tang, S. T. Lee, K. W. Wong, M. Wang, "Characterization of treated indium–tin–oxide surfaces used in electroluminescent devices", *J. Appl. Phys.* **86**, 1688 (1999).

[274] W. Song, S. K. So, D. Wang, Y. Qiu, L. Cao, "Angle dependent X-ray photoemission study on UV-ozone treatments of indium tin oxide", *Appl. Surf. Sci.* **177**, 158 (2001).

[275] T. Hu, F. Zhang, Z. Xu, S. Zhao, X. Yue, G. Yuan, "Effect of UV–ozone treatment on ITO and post-annealing on the performance of organic solar cells", *Synth. Met.* **159**,

754 (2009).

[276] X.-Y. Lin, E. Farhi, H. Arribart, "Determination of the isoelectric point of planar oxide surfaces by a particle adhesion method", *J. Adhesion* **51**, 181 (1995).

[277] J. Stotter, Y. Show, S. Wang, G. Swain, "Comparison of the electrical, optical, and electrochemical properties of diamond and indium tin oxide thin-film electrodes", *Chem. Mater.* **17**, 4880 (2005).

[278] Y. Wang, W. P. Chen, K. C. Cheng, "Optical degradation of indium tin oxide thin films induced by hydrogen-related room temperature reduction", *Jpn. J. Appl. Phys.* **42**, L546 (2003).

[279] J. E. A. M. van den Meerakker, P. C. Baarslag, M. Scholten, "On the mechanism of ITO etching in halogen acids: The influence of oxidizing agents", *J. Electrochem. Soc.* **142**, 2321 (1995).

[280] G. Folcher, H. Cachet, M. Froment, J. Bruneaux, "Anodic corrosion of indium tin oxide films induced by the electrochemical oxidation of chlorides" *Thin Solid Films* **301**, 242 (1997).

[281] P. M. S. Monk, C. M. Man, "Reductive ion insertion into thin-film indium tin oxide (ITO) in aqueous acidic solutions: the effect of leaching of indium from the ITO", *J. Mater. Sci.: Mater. Electron.* **10**, 101 (1999).

[282] A. J. Bard, R. Parsons, J. Jordan (eds.), "Standard Potentials in Aqueous Solutions", Marcel Dekker, 848 p. (1985).

[283] E. Matveeva, "Electrochemistry of the indium-tin oxide electrode in 1 M NaOH electrolyte", *J. Electrochem. Soc.* **152**, H138 (2005).

[284] A. Suzuki, T. Matsushita, T. Aoki, Y. Yoneyama, M. Okuda, "Pulsed laser deposition of transparent conducting indium tin oxide films in magnetic field perpendicular to plum", *Jap. J. Appl. Phys.* **40**, L401 (2001).

[285] A. Kono, Z. Feng, N. Nouchi, F. Shoji, "Fabrication of low resistivity tin-doped indium oxide films with high electron carrier densities by a plasma sputtering method", *Vacuum* **83**, 548 (2008).

[286] G. Frank, H. Köstlin, "Electrical properties and defect model of tin-doped indium oxide layers", *Appl. Phys. A* **27**, 197 (1982).

[287] G. B. González, T. O. Mason, J. P. Quintana, O. Warschkow, D. E. Ellis, J.-H. Hwang, J. P. Hodges, J. D. Jorgensen, "Defect structure studies of bulk and nano-indium-tin oxide", *J. Appl. Phys.* **96**, 3912 (2004).

[288] J. C. C. Fan, J. B. Goodenough, "X-ray photoemission spectroscopy studies of Sn-doped indium-oxide films", *J. Appl. Phys.* **48**, 3524 (1977).

[289] I. Hamberg, C. G. Granqvist, "Evaporated Sn-doped In_2O_3 films: Basic optical properties and applications to energy-efficient windows", *J. Appl. Phys.* **60**, R123 (1986).

[290] J. A. Dobrowolski, L. Li, J. N. Hilfiker, "Long-wavelength cutoff filters of a new type", *Appl. Opt.* **38**, 4891 (1999).

[291] A. Hjortsberg, I. Hamberg, C. G. Granqvist, "Preparation and characterization transparent and heat-reflecting indium tin oxide films prepared by reactive electron beam evaporation", *Thin Solid Films* **90**, 323 (1982).

[292] S. H. Brewer, S. Franzen, "Optical properties of indium tin oxide and fluorine-doped tin oxide surfaces: correlation of reflectivity, skin depth, and plasmon fre-

quency with conductivity", *J. Alloys Compd.* **338**, 73 (2002).

[293] S. H. Brewer, S. Franzen, "Indium tin oxide plasma frequency dependence on sheet resistance and surface adlayers determined by reflectance FTIR spectroscopy", *J. Phys. Chem. B* **106**, 12986 (2002).

[294] D. Dubreuil, J.-P. Ganne, G. Berginc, F. Terracher, "Optical and electrical properties between 0.4 and 12 μm for Sn-doped In_2O_3 films by pulsed laser deposition and cathode sputtering", *Appl. Opt.* **46**, 5709 (2007).

[295] F. Ghebremichael, C. Poga, M. G. Kuzyk, "Optical second harmonic characterization of spontaneous symmetry-breaking at polymer/transparent conductor interfaces", *Appl. Phys. Lett.* **66**, 139 (1995).

[296] W. Wang, J. Xu, X. Liu, Y. Jiang, G. Wang, X. Lu, "Second harmonic generation investigation of indium tin oxide thin films", *Thin Solid Films* **365**, 116 (2000).

[297] J. L. Humphrey, D. Kuciauskas, "Optical susceptibilities of supported indium tin oxide thin films", *J. Appl. Phys.* **100**, 113123 (2006).

[298] J. Kim, K. C. Chou, G. A. Somorjai, "Investigations of the potential-dependent structure of phenylalanine on the glassy carbon electrode by infrared-visible sum frequency generation", *J. Phys. Chem. B* **106**, 9198 (2002).

[299] D. L. Smith, "Thin-film Deposition: Principles and Practice", Irwin/McGraw-Hill, 616 p. (1995).

[300] K. S. Sree Harsha, "Principles of Physical Vapor Deposition of Thin Films", Elsevier Science & Technology, 1176 p. (2006).

[301] R. K. Waits, "Planar magnetron sputtering", *J. Vac. Sci. Technol.* **15**, 179 (1978).

[302] J. F. Watts, J. Wolstenholme, "An Introduction to Surface Analysis by XPS and AES", John Wiley & Sons, 224 p. (2003).

[303] J. H. Scofield, "Hartree-Slater subshell photoionization cross-sections at 1254 and 1487 eV", *J. Electron. Spectrosc. Rel. Phenom.* **8**, 129 (1976).

[304] M. Birkholz, "Thin film Analysis by X-Ray Scattering: Techniques for Structural Characterization", Wiley-VCH Verlag, 378 p. (2005).

[305] R. F. Egerton, "Physical Principles of Electron Microscopy: An Introduction to TEM, SEM, and AEM", Springer Verlag, 202 p. (2008).

[306] L. Reimer, P.W. Hawkes, "Scanning Electron Microscopy", Springer Verlag, 527 p. (2010).

[307] R. Bowen, N. Hilal, "Atomic Force Microscopy in Process Engineering: An Introduction to AFM for Improved Processes and Products", Butterworth Heinemann, 304 p. (2009).

[308] P. Eaton, P. West, "Atomic Force Microscopy", Oxford University Press, 288 p. (2010).

[309] D. K. Schroder, "Semiconductor material and device characterization", 3rd ed., Wiley-IEEE Press, 800 p. (2006).

[310] J. Albers, H. L. Berkowitz, "An alternative approach to the calculation of four-probe resistances on nonuniform structures", *J. Electrochem. Soc.* **132**, 2453 (1985).

[311] R. A. Weller, "An algorithm for computing linear four-point probe thickness correction factors", *Rev. Sci. Instrum.* **72**, 3580 (2001).

[312] L. B. Valdes, "Resistivity measurements on germanium for transistors", *Proc. IRE* **42**, 420 (1954).

[313] F. M. Smits, "Measurements of sheet resistivities with the four-point probe", *Bell Syst. Tech. J.* **37**, 711 (1958).

[314] H. Fujiwara, "Spectroscopic Ellipsometry: Principles and Applications", John Wiley & Sons, 388 p (2007).

[315] S. Huard, "Polarization of Light", Wiley-VCH Verlag, 348 p. (1996).

[316] R. M. A. Azzam, N. M. Bashara, "Ellipsometry and Polarized Light", North Holland, 529 p. (1977).

[317] H. C. Grinter, H.-H. Perkampus, "UV-VIS Spectroscopy and its Applications", Springer-Verlag, (1992).

[318] O. Stenzel, "The Physics of Thin Film Optical Spectra: An Introduction", Springer-Verlag, 277 p. (2005).

[319] P. R. Griffiths, J. A. De Haseth, J. D. Winefordner, "Fourier Transform Infrared Spectrometry", John Wiley & Sons, 560 p. (2007).

[320] P. Franken, A. E. Hill, C. W. Peters, G. Weinreich, "Generation of optical harmonics", *Phys. Rev. Lett.* **7**, 118 (1961).

[321] M. Bass, P. A. Franken, A. E. Hill, C. W. Peters, G. Weinreich, "Optical mixing", *Phys. Rev. Lett.* **8**, 18 (1962).

[322] P. D. Maker, R. W. Terhune, M. Nisenoff, C. M. Savage , "Effects of dispersion and focusing on the production of optical harmonics", *Phys. Rev. Lett.* **8**, 21 (1962).

[323] R. W. Terhune, P. D. Maker, C. M. Savage, "Optical harmonic generation in calcite", *Phys. Rev. Lett.* **8**, 404 (1962).

[324] J. A. Armstrong, N. Bloembergen, J. Ducuing, P. S. Pershan, "Interactions between light waves in a nonlinear dielectric", *Phys. Rev.* **127**, 1918 (1962).

[325] N. Bloembergen, P. S. Pershan, "Light waves at the boundary of nonlinear media", *Phys. Rev.* **128**, 606 (1962).

[326] J. H. Hunt, P. Guyot-Sionnest, Y. R. Shen, "Observation of C-H stretch vibrations of monolayers of molecules optical sum-frequency generation", *Chem. Phys. Lett.* **133**, 189 (1987).

[327] X. D. Zhu, H. Suhr, Y. R. Shen, "Surface vibrational spectroscopy by infrared-visible sum frequency generation", *Phys. Rev. B* **35**, 3047 (1987).

[328] P. Guyot-Sionnest, J. H. Hunt, Y. R. Shen, "Sum-frequency vibrational spectroscopy of a Langmuir film: Study of molecular orientation of a two-dimensional system", *Phys. Rev. Lett.* **59**, 1597 (1987).

[329] A. L. Harris, C. E. D. Chidsey, N. J. Levinos, D. N. Loiacono, "Monolayer vibrational spectroscopy by infrared-visible sum generation at metal and semiconductor surfaces", *Chem. Phys. Lett.* **141**, 350 (1987).

[330] M. B. Raschke, Y. R. Shen, "Nonlinear optical spectroscopy of solid interfaces", *Curr. Opin. Solid State Mater. Sci.* **8**, 343 (2004).

[331] H. C. Allen, N. N. Casillas-Ituarte, M. R. Sierra-Hernandez, X. Chen, C. Y. Tang, "Shedding light on water structure at air-aqueous interfaces: ions, lipids, and hydration", *Phys. Chem. Chem. Phys.* **11**, 5538 (2009).

[332] C. S. Tian, Y. R. Shen, "Sum-frequency vibrational spectroscopic studies of water/vapor interfaces," *Chem. Phys. Lett.* **470**, 1 (2009).

[333] V. Vogel, "Air/liquid interfaces and adsorbed molecular monolayers studied with nonlinear optical techniques", *Annu. Rev. Mater. Sci.* **21**, 515 (1991).

[334] K. B. Eisenthal, "Equilibrium and dynamic processes at interfaces by second harmonic and sum frequency generation", *Ann. Rev. Phys. Chem.* **43**, 627 (1992).

[335] Y. R. Shen, P. B. Miranda, "Liquid interfaces: a study by sum-frequency vibrational spectroscopy", *J. Phys. Chem. B* **103**, 3292 (1999).

[336] M. J. Shultz, C. Schnitzer, D. Simonelli, S. Baldelli, "Sum-frequency generation spectroscopy of the aqueous interface: ionic and soluble molecular solutions", *Int. Rev. Phys. Chem.* **19**, 123 (2000).

[337] S. Gopalakrishnan, D. F. Liu, H. C. Allen, M. Kuo, M. J. Shultz, "Vibrational spectroscopic studies of aqueous interfaces: Salts, acids, bases, and nanodrops", *Chem. Rev.* **106**, 1155 (2006).

[338] G. L. Richmond, "Molecular bonding and interactions at aqueous surfaces as probed by vibrational sum frequency spectroscopy", *Chem. Rev.* **102**, 2693 (2002).

[339] M. A. Leich, G. L. Richmond, "Recent experimental advances in studies of liquid/liquid interfaces", *Faraday Discuss.* **129**, 1 (2005).

[340] A. J. Hopkins, C. L. McFearin, G. L. Richmond, "Investigations of the solid-aqueous interface with vibrational sum-frequency spectroscopy", *Curr. Opin. Solid State Mater. Sci.* **9**, 19 (2005).

[341] F. M. Geiger, "Second harmonic generation, sum frequency generation, and $\chi^{(3)}$: Dissecting environmental interfaces with a nonlinear optical swiss army knife", *Ann. Rev. Phys. Chem.* **60**, 61 (2009).

[342] Z. Chen, Y. R. Shen, G. A. Somorjai, "Studies of polymer surfaces by sum frequency generation vibrational spectroscopy", *Ann. Rev. Phys. Chem.* **53**, 437 (2002).

[343] Z. Chen, "Understanding surfaces and buried interfaces of polymer materials at the molecular level using sum frequency generation vibrational spectroscopy", *Polym. Int.* **56**, 577 (2007).

[344] H. Rangwalla, A. Dhinojwala, "Probing hidden polymeric interfaces using IR-visible sum-frequency generation spectroscopy", *J. Adhesion* **80**, 37 (2004).

[345] Z. Chen, "Investigating buried polymer interfaces using sum frequency generation vibrational spectroscopy", *Prog. Polym. Sci.* **35**, 1376 (2010).

[346] A. Tadjeddine, A. Peremans, P. Guyot-Sionnest, "Vibrational spectroscopy of the electrochemical interface by visible-infrared sum-frequency generation", *Surf. Sci.* **335**, 210 (1995).

[347] S. Baldelli, A. A. Gewirth, "Sum Frequency Generation Studies of the Electrified Solid/Liquid Interface" *In*: "Advances in Electrochemical Science and Engineering" (R. C. Alkire, D. M. Kolb, j. Lipkowski, P. N. Ross, eds.), vol. 9, chap. 5, Wiley-VCH Verlag, pp. 163–198 (2006).

[348] Y. R. Shen, "Optical second harmonic generation at interfaces", *Ann. Rev. Phys. Chem.* **40**, 327 (1989).

[349] C. D. Bain, "Sum-frequency vibrational spectroscopy of the solid/liquid interface", *J. Chem. Soc. Faraday Trans.* **91**, 1281 (1995).

[350] J. F. McGilp, "A review of optical second-harmonic and sum-frequency generation at surfaces and interfaces", *J. Phys. D Appl. Phys.* **29**, 1812 (1996).

[351] M. Buck, M. Himmelhaus, "Vibrational spectroscopy of interfaces by infrared–visible sum frequency generation", *J. Vac. Sci. Technol. A* **19**, 2717 (2001).

[352] A. J. Moad, G. J. Simpson, "A unified treatment of selection rules and symmetry

relations for sum-frequency and second harmonic spectroscopies", *J. Phys. Chem. B* **108**, 3548 (2004).

[353] A. G. Lambert, P. B. Davies, "Implementing the theory of sum frequency generation vibrational spectroscopy: A tutorial review", *Appl. Spectrosc. Rev.* **40**, 103 (2005).

[354] F. Vidal, A. Tadjeddine, "Sum-frequency generation spectroscopy of interfaces", *Rep. Prog. Phys.* **68**, 1095 (2005).

[355] H. Arnolds, M. Bonn, "Ultrafast surface vibrational dynamics", *Surf. Sci. Rep.* **65**, 45 (2010).

[356] T. F. Heinz, "Second-order Nonlinear Optical Effects at Surfaces and Interfaces", *In*: "Nonlinear Surface Electromagnetic Phenomena" (G. I. Stegeman, H. E. Ponath, eds.), Modern Problems in Condensed Matter Sciences, vol. 29, North-Holland pp. 353-–416 (1991).

[357] Y. R. Shen, "Surface Spectroscopy by Nonlinear Optics", *In*: "Proceedings of the International School of Physics Enrico Fermi, Course CXX: Frontiers in Laser Spectroscopy" (T. W. Hänsch, M. Ignuscio, eds.), North-Holland, pp. 139-–165 (1994).

[358] G. A. Reider, T. F. Heinz, "Second-Order Nonlinear Optical Effects at Surfaces and Interfaces: Recent Advances", *In*: "Photonic Probes of Surfaces: Electromagnetic Waves" (P. Halevi, ed.), vol. 2, chap. 9, Elsevier, pp. 413–378 (1995).

[359] J. I. Dadap, T. F. Heinz, "Nonlinear Optical Spectroscopy of Surfaces and Interfaces", *In*: "Encyclopedia of Chemical Physics and Physical Chemistry" (J. H. Moore, N. D. Spencer, eds.), Taylor & Francis, chap. B1.5, pp. 1–48 (2001).

[360] M. J. Shultz, "Sum Frequency Generation: An Introduction with Recent Developments and Current Issues" *In*: "Advances in Multiphoton Processes and Spectroscopy" (S. H. Lin, A. A. Villaeys, A. Fujimura, eds.), vol. 18, chap. 4, pp. 133–199 (2004).

[361] M. B. Raschke, Y. R. Shen, "PHYSICAL APPLICATIONS OF LASERS/Sum-frequency generation at surfaces" *In*: "Encyclopedia of Modern Optics" (R. D. Guenther, D. G. Steel, L. Bayvel, eds.), vol. 4, Academic Press, pp. 184–189 (2005).

[362] A. McClelland, Z. Chen, "Sum Frequency Generation Spectroscopy", *In*: "Encyclopedia of Analytical Chemistry: Applications, Theory, and Instrumentation" (R. A. Meyers, ed.), John Wiley & Sons, pp. 1–40 (2008).

[363] H. Motschmann, P. Koelsch, "Linear and Non-linear Optical Techniques to Probe Ion Profiles at the Air-Water Interface", *In*: "Specific Ion Effects" (W. Kunz, ed.), Chap. 4, World Scientific Publishers, pp. 109–147 (2010).

[364] Y. R. Shen, "Principles of Nonlinear Optics", John Wiley & Sons, 563 p. (1984).

[365] J. F. McGilp, "Epioptics: Linear and Nonlinear Optical Spectroscopy of Surfaces and Interfaces" (C. H. Patterson, D. L. Weaire, eds.), Springer-Verlag, 230 p. (1995).

[366] S. Mukamel, "Principles of Nonlinear Optical Spectroscopy" (2nd ed.), Oxford University Press, 576 p. (1999).

[367] R. L. Sutherland, "Handbook of Nonlinear Optics" (2nd ed.), Marcel Dekker, 971 p. (2003).

[368] R. W. Boyd, "Nonlinear Optics" (3rd ed.), Academic Press, 613 p. (2008).

[369] W. Demtröder, "Laser Spectroscopy" (4th ed.), vol. 1 (Basic Principles)/vol. 2 (Instrumentation), Springer-Verlag, 1500 p. (2009).

[370] H. Jayathilake, "Vibrational Sum Frequency Generation Spectroscopy: Basics, Con-

cepts, Method Development and Applications", Verlag Dr. Müller, 190 p. (2010).

[371] Y. R. Shen, "Surface contribution versus bulk contribution in surface nonlinear optical spectroscopy", *Appl. Phys. B* **68**, 295 (1999).

[372] X. Wei, S.-C. Hong, A. I. Lvovsky, H. Held, Y. R. Shen, "Evaluation of surface vs bulk contributions in sum-frequency vibrational spectroscopy using reflection and transmission geometries", *J. Phys. Chem. B* **104**, 3349 (2000).

[373] H. Held, A. I. Lvovsky, X. Wei, Y. R. Shen, "Bulk contribution from isotropic media in surface sum-frequency generation", *Phys. Rev. B* **66**, 205110 (2002).

[374] J. E. Sipe, "New Green-function formalism for surface optics", *J. Opt. Soc. Am. B* **4**, 481 (1987).

[375] V. Mizrahi, J. E. Sipe, "Phenomenological treatment of surface second-harmonic generation", *J. Opt. Soc. Am. B* **5**, 660 (1988).

[376] D.-S. Zheng, Y. Wang, A.-A. Liu, H.-F. Wang, "Microscopic molecular optics theory of surface second harmonic generation and sum-frequency generation spectroscopy based on the discrete dipole lattice model", *Int. Rev. Phys. Chem.* **27**, 629 (2008).

[377] P. N. Prasad, D. J. Williams, "Introduction to Nonlinear Optical Effect in Molecules and Polymers" (3rd. ed.), John Wiley & Sons, 320 p. (1991).

[378] C. Hirose, "Formulas for the analysis of the surface SFG spectrum and transformation coefficients of cartesian SFG tensor components", *Appl. Spectrosc.* **46**, 1051 (1992).

[379] L. Dreesen, C. Humbert, M. Celebi, J. J. Lemaire, A. A. Mani, P. A. Thiry, A. Peremans, "Influence of the metal electronic properties on the sum-frequency generation spectra of dodecanethiol self-assembled monolayers on Pt (111), Ag (111) and Au (111) single crystals", *Appl. Phys. B* **74**, 621 (2002).

[380] A. Tadjeddine, A. Le Rille, O. Pluchery, F. Vidal, W. Q. Zheng, A. Peremans, "Sum and difference frequency generation at the electrochemical interface", *Phys. Stat. Solidi A* **175**, 89 (1999).

[381] A. V. Petukhov, "Sum-frequency generation on isotropic surfaces: General phenomenology and microscopic theory for jellium surfaces", *Phys. Rev. B* **52**, 16901 (1995).

[382] K. C. Jena, P. A. Covert, D. K. Hore, "The effect of salt on the water structure at a charged solid surface: Differentiating second- and third-order nonlinear contributions", *J. Phys. Chem. Lett.* **2**, 1056 (2011).

[383] L. J. Richter, T. P. Petralli-Mallow, J. C. Stephenson, "Vibrationally resolved sum-frequency generation with broad-bandwidth infrared pulses", *Opt. Lett.* **23**, 1594 (1998).

[384] E. Hommel, H. C. Allen, "Broadband sum frequency generation with two regenerative amplifiers: Temporal overlap of femtosecond and picosecond light pulses", *Anal. Sci.* **17**, 137 (2001).

[385] A. Lagutchev, S. A. Hambir, D. D. Dlott, "Nonresonant background suppression in broadband vibrational sum-frequency generation spectroscopy", *J. Phys. Chem. C* **111**, 13645 (2007).

[386] G. Xia, B. Li, L. Liu, Z. Wu, J. Chen, "Time delay of Fabry-Perot filters to short optical pulses", *J. Opt. Commun.* **22**, 87 (2001).

[387] A. J. Bard, L. R. Faulkner, "Electrochemical Methods: Fundamentals and Applications" (2nd ed.), John Wiley & Sons, 833 p. (2001).

[388] A. W. C. Lin, N. R. Armstrong, T. Kuwana, "X-ray photoelectron/Auger electron spectroscopic studies of tin and indium metal foils and oxides", *Anal. Chem.* **49**, 1228 (1977).

[389] D. C. Harris, "Quantitative Chemical Analysis", W. H. Freeman, 750 p. (2003).

[390] Y. S. Jung, S. S. Lee, "Development of indium tin oxide film texture during DC magnetron sputtering deposition", *J. Cryst. Growth* **259**, 343 (2003).

[391] Y. Hu, X. Diao, C. Wang, W. Hao, T. Wang, "Effects of heat treatment on properties of ITO films prepared by rf magnetron sputtering", *Vacuum* **75**, 183 (2006).

[392] C. Guillén, J. Herrero, "Polycrystalline growth and recrystallization processes in sputtered ITO thin films", *Thin Solid Films* **510**, 260 (2006).

[393] L. Kerkache, A. Layadi, E. Dogheche, D. Rémiens, "Physical properties of RF sputtered ITO thin films and annealing effect", *J. Phys. D* **39**, 184 (2006).

[394] W.-F. Wu, B.-S. Chiou, "Effect of annealing on electrical and optical properties of RF magnetron sputtered indium tin oxide films", *Appl. Surf. Sci.* **68**, 497 (1993.

[395] R. Bel Hadj Tahar, T. Ban, Y. Ohya, Y. Takahashi, "Tin doped indium oxide thin films: Electrical properties", *J. Appl. Phys.* **83**, 2631 (1998).

[396] Z. Qiao, D. Mergel, "Dielectric modeling of transmittance and ellipsometric spectra of thin In2O3:Sn films", *Phys. Status Solidi A* **207**, 1543 (2010).

[397] D. F. Bezuidenhout, "Calcium fluoride (CaF_2)" *In*: "Handbook of Optical Constants of Solids" (E. D. Palik, ed.), vol. II, Academic Press, pp. 815–835 (1991).

[398] J. A. Woollam, W. A. McGahan, B. Johs, "Spectroscopic ellipsometry studies of indium tin oxide and other flat panel display multilayer materials", *Thin Solid Films* **241**, 44 (1994).

[399] T. Gerfin, M. Grätzel, "Optical properties of tin-doped indium oxide determined by spectroscopic ellipsometry", *J. Appl. Phys.* **79**, 1722 (1996).

[400] M. Losurdo, M. Giangregorio, P. Capezzuto, G. Bruno, R. De Rosa, F. Roca, C. Summonte, J. Plá, R. Rizzoli, "Parametrization of optical properties of indium–tin–oxide thin films by spectroscopic ellipsometry: Substrate interfacial reactivity", *J. Vac. Sci. Technol. A* **20**, 37 (2002).

[401] R. A. Synowicki, "Spectroscopic ellipsometry characterization of indium tin oxide film microstructure and optical constants", *Thin Solid Films* **313–314**, 394 (1998).

[402] M. T. Bhatti, A. M. Rana, A. F. Khan, "Characterization of rf-sputtered indium tin oxide thin films", *Mater. Chem. Phys.* **84**, 126 (2004).

[403] S. Boycheva, A. Krasilnikova Sytchkova, A. Piegari, "Optical and electrical characterization of r.f. sputtered ITO films developed as art protection coatings", *Thin Solid Films* **515**, 8474 (2007).

[404] S. Yoshida, "Efficiency of Drude mirror-type selective transparent filters for solar thermal conversion", *Appl. Opt.* **17**, 145 (1978).

[405] G. A. Parks, "The isoelectric points of solid oxides, solid hydroxides, and aqueous hydroxo complex systems", *Chem. Rev.* **65**, 177 (1965).

[406] A. Carre, F. Roger, C. Varinot, "Study of acid/base properties of oxide, oxide glass, and glass-ceramic surfaces", *J. Colloid Interface Sci.* **154**, 174 (1992).

[407] M. Kosmulski, "Pristine points of zero charge of gallium and indium oxides", *J.*

Colloid Interface Sci. **238**, 225 (2001).

[408] J. Sun, B. V. Velamakanni, W. W. Gerberich, L. F. Francis, "Aqueous latex/ceramic nanoparticle dispersions: colloidal stability and coating properties", *J. Colloid Interface Sci.* **280**, 387 (2004).

[409] M. A. Bos, Z. Shervani, A. C. I. Anusiem, M. Giesbers, W. Norde, J. M. Kleijn, "Influence of the electric potential of the interface on the adsorption of proteins", *Colloids Surf. B* **3**, 91 (1994).

[410] C. L. Wirth, P. J. Sides, D. C. Prieve, "The imaging ammeter", *J. Colloid Interface Sci.* **357**, 1 (2011).

[411] C. Goebbert, R. Nonninger, M. A. Aegerter, H. Schmidt, "Wet chemical deposition of ATO and ITO coatings using crystalline nanoparticles redispersable in solutions", *Thin Solid Films* **351**, 79 (1999).

[412] J. U. Brehm, M. Winterer, H. Hahn, "Indium tin oxide nanoparticles prepared by chemical vapor synthesis", *Mater. Res. Soc. Symp. Proc.* **704**, W5.3/1 (2002).

[413] W. J. Tseng, F. Tzeng, "Effect of ammonium polyacrylate on dispersion and rheology of aqueous ITO nanoparticle colloids", *Colloids Surf. A* **276**, 34 (2006).

[414] R. Pan, K. Liew, L. Xu, Y. Gao, J. Zhou, H. Zhou, "A new approach for the determination of the iso-electric point of nanoparticles", *Colloids Surf. A* **305**, 17 (2007).

[415] C. Q. Peng, Y. S. Thio, R. A. Gerhardt, "Conductive paper fabricated by layer-by-layer assembly of polyelectrolytes and ITO nanoparticles", *Nanotechnology* **19**, 505603 (2008).

[416] S. Trasatti, "Systematic trends in the crystal face specificity of interfacial parameters: the cases of Ag and Au", *J. Electroanal. Chem.* **329**, 237 (1992).

[417] K. Sugiyama, H. Ishii, Y. Ouchi, K. Seki, "Dependence of the indium-tin-oxide work function on surface cleaning method as studied by ultraviolet and x-ray photoemission spectroscopies", *J. Appl. Phys.* **87**, 295 (2000).

Sworn statement

I hereby certify that the submitted dissertation is original and that no other sources other than those listed here have been used. Moreover, I certify that it has not been submitted in one or any other form to another faculty nor did it undergo any other examination procedure.

Dominique Verreault

Heidelberg, May 20$^{\text{th}}$ 2011

Eidesstattliche Erklärung

Ich erkläre hiermit, dass ich die vorgelegte Dissertation selbst verfasst und mich keiner anderen als der von mir ausdrücklich bezeichneten Quellen und Hilfen bedient habe. Ausserdem, habe ich an keiner anderen Stelle ein Prüfungsverfahren beantragt bzw. die Dissertation in dieser oder anderer Form bereits anderweitig als Prüfungsarbeit verwendet oder einer anderen Fakultät als Dissertation vorgelegt.

Dominique Verreault

Heidelberg, den 20ten Mai 2011